



Provided by the author(s) and University of Galway in accordance with publisher policies. Please cite the published version when available.

Title	Analysis and design of high frequency gapped transformers and planar transformers in LLC resonant converters
Author(s)	Zhang, Jun
Publication Date	2015-05-27
Item record	http://hdl.handle.net/10379/5048

Downloaded 2024-05-12T07:23:24Z

Some rights reserved. For more information, please see the item record link above.





OÉ Gaillimh
NUI Galway

Analysis and Design of High Frequency Gapped Transformers and Planar Transformers in LLC Resonant Converters

by

Jun Zhang

B.E. and M.S., Zhejiang University, China

in fulfilment of the requirements for the degree of

Doctor of Philosophy

in the subject of

Electrical and Electronic Engineering

Supervisor

Prof. William Gerard Hurley

Co-supervisors

Dr. Maeve Duffy

Prof. Werner Wölfle

Power Electronics Research Centre
School of Electrical and Electronic Engineering
College of Engineering and Informatics
National University of Ireland, Galway

May 2015

Table of Contents

Table of Contents	i
Abstract	iv
Acknowledgements	v
Declaration	vi
List of Figures	vii
List of Tables	xii
Nomenclature	xiii
Abbreviations	xix
Chapter 1 Introduction	1
1.1 High Frequency DC-DC Converters	3
1.2 Design Issues for Transformers in High Frequency DC-DC Converters	11
1.2.1. <i>High Frequency Winding Loss</i>	11
1.2.2. <i>Magnetic Core Loss</i>	18
1.2.3. Leakage Inductance and Stray Capacitance	19
1.3 Planar Magnetics and Design Considerations	20
1.3.1. <i>Introduction of Planar Magnetic Technologies</i>	20
1.3.2. <i>Planar Magnetics Design Considerations</i>	22
1.3.3. <i>Planar Transformers for LLC Resonant Converters</i>	26
1.4 Objectives and Outline of the Thesis	28
1.5 List of Publications	32
Chapter 2 Design Parameters in LLC Resonant Converters	33
2.1 Operation of LLC Resonant Converters	33
2.1.1 <i>Steady State Waveforms of LLC Resonant Converters</i>	35
2.1.2 <i>Fundamental Frequency Analysis</i>	38
2.1.3 <i>Parameters Influence Based on k, Q Factors</i>	40
2.2 Power Loss Modelling of LLC Resonant Converters	43
2.2.1 <i>Switches Losses</i>	43
2.2.2 <i>Magnetic Components Losses</i>	44
2.3 Trade-off Design of the Main Parameters	45

2.4	Design Results of the 240 W, 105 kHz LLC Resonant Converter	47
2.5	Experimental Results of the 240 W LLC Resonant Converter	52
2.6	Conclusions	54
Chapter 3 Design Methodology for a Gapped Conventional Transformer		55
3.1	Gapped Transformer Operation Principle	55
3.2	Design Considerations for the Gapped Transformer	57
3.2.1	<i>Multiple Windings Consideration</i>	57
3.2.2	<i>Magnetizing Inductance Consideration</i>	58
3.2.3	<i>Losses Consideration</i>	60
3.2.4	<i>Thermal Considerations</i>	62
3.3	Design Methodology of the Gapped Transformer	62
3.4	Design Results of Conventional Gapped Transformer	65
3.4.1	<i>Design Specifications of Gapped Transformer</i>	66
3.4.2	<i>Design Results for the Gapped Transformer</i>	66
3.4.3	<i>Magnetizing Inductance Due to Gap Effect</i>	68
3.4.4	<i>Losses in the Gapped Transformer</i>	69
3.4.5	<i>Parameters Verification</i>	69
3.5	Experimental Results of the Gapped Conventional Transformer	70
3.6	Conclusions	70
Chapter 4 Parasitic Parameters in Conventional Transformers		71
4.1.	Leakage Inductance at High Frequency	71
4.2.	Frequency Dependent Leakage Inductance Analysis	75
4.3.	Leakage Inductance with Interleaving Windings	80
4.4.	Experimental Verifications for High Frequency Leakage Inductance	81
4.4.1	<i>Simulations and Measurements of Leakage Inductances</i>	81
4.4.2	<i>Leakage Inductances of Different Interleaved Configurations</i>	84
4.5.	Stray Capacitances in the Conventional Transformer	87
4.6.	Conclusions	93
Chapter 5 Analysis and Modelling of Planar Transformers		94
5.1	Planar Cores	95
5.2	Winding Loss Modelling of Planar Transformers	98
5.2.1	<i>Winding Loss for Strip Conductors</i>	99
5.2.2	<i>Winding Loss for Circular Conductors</i>	101
5.2.3	<i>Winding Loss with Phase Shifted Excitations</i>	109
5.3	Stray Capacitances of Planar Transformer	111
5.4	Leakage Inductance of Planar Transformer with Magnetic Shunt	116
5.5	Conclusions	127
Chapter 6 Gapped Planar Transformer in LLC Resonant Converters		128
6.1	Planar Core Selection	128
6.2	Gap and Winding Design	130
6.3	Windings Optimization	131
6.4	Experimental Results of Gapped Planar Transformer	136
6.5	Conclusions	140
Chapter 7 Conclusions and Future Work		141

7.1 Introduction	141
7.2 Contributions to Gapped and Planar Transformers in LLC Resonant Converters	141
7.3 Future Work	142
Appendix A Planar EE and ER Cores	144
Appendix B Fundamental Frequency Analysis of LLC Resonant Converters	149
Appendix C Design Equations for Gapped Transformers	160
Appendix D Planar Winding Loss of Circular Conductors	165
Appendix E Publications	168
References	173

Abstract

The LLC resonant converter is particularly applicable for power supplies applications since soft switching is easily achieved. The dual objectives in power supply are higher switching frequencies and higher power densities. The analysis and design of the LLC resonant converter, especially the magnetic components needs further investigation and the related research has enormous practical significance.

In this thesis, the design methodology for the LLC resonant converter is proposed based on the circuit analysis and the loss calculations with soft switching conditions and input voltage variations considered. The gapped transformer employed in the resonant converter is deeply investigated. The transformer was treated as the multi-winding inductor and a new design methodology is proposed. The parasitic parameters in the transformer involving high frequency leakage inductance and stray capacitance are studied, and reliable evaluation formulas are presented.

With the purpose of introducing the planar transformer in the LLC resonant converter, the detailed modelling of planar transformer including the winding loss calculation, the stray capacitance and the leakage inductance for the integrated planar structure incorporating the low permeability magnetic shunt is carried out. Combing the analytical results of the gapped transformer design method and modelling of the planar transformer, the gapped planar transformer for the LLC resonant converter is designed and fabricated. Comparison with the conventional transformer shows that successful operation is possible with the low profile core.

Acknowledgements

Time flies and the most beautiful time flies quicker. In the season of harvesting, I would like to sincerely thank my supervisor, Prof. Ger Hurley for his direction and the supports of both my studying and daily life. I would never forget the most wonderful days that I worked with him, learned from him during these four years in this beautiful city and lovely country.

I also would like to thank Dr. Maeve Duffy and Prof. Werner Wöfle for kindly helping my project. I would like to appreciate Prof. Mark Dehong Xu of Zhejiang University, China for his kindly help and advices. I would like to acknowledge Dr. Ziwei Ouyang of DTU for the valuable advice and memorable visiting to DTU, Denmark.

To all those who have worked with me in Power Electronics Research Centre – Martin Burke, Myles Meehan, David Newell, Fearghal Kineavy, Migle Makelyte and Prathamesh Shard Dhanpalwar, thanks for all your help and fun at the break time. Special thanks to Ciarán Feeney who always shared his ideas and always willing to pass on valuable information. Extend heartfelt thanks to Chengrui Du, years of friendship and memorable days when he was in Ireland.

To my parents and sister, thank you for your constant encouragement and support. Wenwen, thanks you for the long time waiting, your support and understanding. That's the most powerful force which is always with me.

Thanks for the funding supported by Convertec Ltd., Wexford, Ireland and Chinese Scholarship Council (CSC, supporting no. 2010632015).

Declaration

I, **Jun Zhang**, hereby declare that this thesis titled “**Analysis and Design of High Frequency Gapped Transformers and Planar Transformers in LLC Resonant Converters**” and the work presented in it are my own. I confirmed that the work contained in this thesis has not been submitted by me in pursuance of any other degree.

Signature: _____

Jun Zhang

List of Figures

Fig. 1.1	Typical configuration of the power supply including DC-DC	2
Fig. 1.2	Configurations of half bridge and full bridge PWM converters	4
Fig. 1.3	Topologies of half bridge resonant converters with centre-tapped rectifier	6
Fig. 1.4	Summary of soft switching DC-DC converters (input voltage: around 300 V ~ 400 V; output voltage: 5 V ~ 50 V; output power: 100 W ~ 2 kW)	10
Fig. 1.5	Skin effect and eddy current in a round conductor	12
Fig. 1.6	Proximity effect of adjacent round conductors and long copper foil	13
Fig. 1.7	Foil windings in the transformer and eddy current based on 1-D Dowell's equation	14
Fig. 1.8	Fringing field and winding loss in conductors near the air gap	16
Fig. 1.9	Different types of air gaps and reluctance models	17
Fig. 1.10	Typical patterns of planar windings (a) PCB windings; (b) copper foils	23
Fig. 1.11	Distinguished planar windings (a) planar litz wire; (b) planar winding for stacked I-cores	24
Fig. 1.12	Edge effect on winding loss	25
Fig. 1.13	Integrated planar transformers for LLC resonant converters	27
Fig. 1.14	Planar transformers for LLC resonant converters	28
Fig. 2.1	Topology of half bridge LLC resonant converter with the synchronous rectifier	34
Fig. 2.2	Typical waveforms of LLC resonant converters	35

Fig. 2.3	Switching states with current path highlighted for the LLC resonant converter with the synchronous rectifier	37
Fig. 2.4	Normalized output voltage versus normalized switching frequency for different values of k with output power from 10% to 100% of rated power	41
Fig. 2.5	Rms currents through the primary and secondary winding for different values of k	42
Fig. 2.6	Normalized output voltage versus normalized switching frequency for different values of Q with $k = 7$	42
Fig. 2.7	Selection of L_m based on the calculated total power loss	46
Fig. 2.8	Flow chart of trade-off design procedure for the LLC resonant converter	48
Fig. 2.9	Calculated power loss versus L_m	49
Fig. 2.10	Relation between M_{\max} and M_{req}	50
Fig. 2.11	Selection of k and Q	51
Fig. 2.12	Winding configurations of the conventional wire wound transformer	53
Fig. 2.13	Photo of the tested power supply with the LLC resonant converter	53
Fig. 2.14	Efficiency of the LLC resonant converter with conventional transformer	54
Fig. 3.1	Gapped transformer in the LLC resonant converter	56
Fig. 3.2	Gap placed in the EE core sets and the dimensions of the gap	59
Fig. 3.3	Flow chart of the design methodology for the gapped transformer	63
Fig. 3.4	Structure of designed gapped transformer with ETD39 core set	68
Fig. 4.1	Leakage flux distributed in the transformer with half-core demonstrated	73
Fig. 4.2	MMF curve along x axis at low and high frequencies	74
Fig. 4.3	Transformer cross section and magnetic field boundary in generalized n^{th} layer	74
Fig. 4.4	Calculated leakage inductances versus frequencies for different conductor thicknesses	79

Fig. 4.5	Full interleaved winding configuration and the winding portion	80
Fig. 4.6	FEA simulations of H field along the winding width direction	82
Fig. 4.7	Leakage inductance measured by HP-4294A	83
Fig. 4.8	Comparisons of calculated, FEA simulated and measured leakage inductance at different frequencies	83
Fig. 4.9	Four transformer configurations with different interleaved windings	85
Fig. 4.10	FEA simulations results of H field in the window area	86
Fig. 4.11	Winding configuration and dimensions of the studied wire wound transformer	88
Fig. 4.12	Distributed stray capacitance model	91
Fig. 4.13	Voltage distributed on the windings	91
Fig. 4.14	Simulation model for the capacitor across P_a and S_a	93
Fig. 5.1	Data fitting of thermal resistances versus planar core volume	96
Fig. 5.2	Winding configurations assembled with planar EE and ER cores	96
Fig. 5.3	Differences between winding losses of planar EE and ER cores	98
Fig. 5.4	Planar windings for strip conductors and circular conductors	99
Fig. 5.5	Equivalent transformation for narrow strip conductor	100
Fig. 5.6	Simulated and calculated results of R_{ac} / R_{dc} for strip conductors	101
Fig. 5.7	Boundary conditions of the n^{th} primary layer	102
Fig. 5.8	Comparisons of calculated and simulated AC winding resistance	104
Fig. 5.9	Comparisons of simulated and calculated current density distribution within one circular conductor	105
Fig. 5.10	FEA simulated AC conductor resistance of primary winding with interleaved and non-interleaved winding configurations at 100 kHz	107
Fig. 5.11	Simulated and calculated results of R_{ac} / R_{dc} for circular conductor	108
Fig. 5.12	Simulated and calculated results of P_{ac} / P_{dc} for different phase shift angles between primary and secondary currents	110
Fig. 5.13	Planar transformer for the capacitance calculation	112

Fig. 5.14	Detailed cross section and insulation layers of planar transformer	114
Fig. 5.15	Assembly of the planar transformer with magnetic shunt	116
Fig. 5.16	Cross section of planar transformer with magnetic shunt and simplified analytical scheme of MMF distribution	117
Fig. 5.17	Schematic diagram for the number of turns in each layer	118
Fig. 5.18	MMF distribution in vicinity of the n^{th} layer	118
Fig. 5.19	Reluctances distributed in the integrated planar transformer	121
Fig. 5.20	Reluctance model of the integrated planar transformer	121
Fig. 5.21	Simulated magnetic intensity in the planar transformer with $\mu_r = 10$, $t_{\text{sh}} = 0.4$ mm	123
Fig. 5.22	Comparisons of the calculated and simulated results for the leakage inductance in the integrated planar transformer	124
Fig. 5.23	PCB windings and planar core applied in the experimental test	124
Fig. 5.24	Photo of planar transformer with magnetic shunt (Trans1)	126
Fig. 5.25	Comparisons of the calculated and experimental results of the leakage inductance	126
Fig. 6.1	Simulation results of winding loss in the gapped planar transformer with different thicknesses and distances away from the gap	134
Fig. 6.2	Fabrication and assembly for the primary winding	134
Fig. 6.3	Cutting patterns of the secondary winding	135
Fig. 6.4	Assembly drawing of the gapped planar transformer	135
Fig. 6.5	Planar transformer fabricated based on the design results	137
Fig. 6.6	Test set-up for the gapped planar transformer in the LLC resonant converter	137
Fig. 6.7	Typical experimental waveforms	138
Fig. 6.8	Temperature rise of the gapped planar transformer tested at different places on the core surface	138
Fig. 6.9	Efficiencies of the LLC resonant converter incorporating designed planar gapped transformer and conventional gapped transformer	139

Fig. 6.10	Side view of the designed planar gapped transformer and conventional transformer	139
Fig. A.1	Shapes of planar E core and ER core	144
Fig. B.1	Half-bridge LLC resonant converter with the uncontrolled rectifier	150
Fig. B.2	Equivalent circuit of the LLC resonant converter based on FFA	151
Fig. B.3	DC voltage gain of the LLC resonant converter	153
Fig. B.4	Waveforms of the LLC resonant converter	154
Fig. B.5	Equivalent circuits of the LLC resonant converter	155

List of Tables

TABLE 1.1	SPECIFICATIONS OF THE INVESTIGATED DC-DC CONVERTERS	3
TABLE 1.2	BASIC FULL-WAVE RECTIFIER TOPOLOGIES AND COMPARISONS [6]	5
TABLE 1.3	SUMMARY OF PLANAR TRANSFORMERS OF LLC RESONANT CONVERTERS	29
TABLE 2.1	DESIGN SPECIFICATIONS OF THE LLC RESONANT CONVERTER	49
TABLE 2.2	APPLIED PARAMETERS AND VALUES DURING THE DESIGN PROCESS	50
TABLE 3.1	SPECIFICATIONS OF THE GAPPED TRANSFORMER	66
TABLE 3.2	SPECIFICATIONS OF THE MAGNETIC MATERIAL EPCOS N87	67
TABLE 3.3	PARAMETERS OF SELECTED ETD39 CORE	67
TABLE 4.1	PARAMETERS OF THE TRANSFORMER FOR VERIFICATIONS	82
TABLE 4.2	CALCULATED AND SIMULATED RESULTS OF LEAKAGE INDUCTANCES FOR FOUR DIFFERENT WINDING CONFIGURATIONS	86
TABLE 4.3	MEASURED LEAKAGE INDUCTANCES AT 10 HZ AND 1 MHZ	86
TABLE 5.1	VOLUMES AND THERMAL RESISTANCES OF PLANAR CORES	95
TABLE 5.2	SYMBOLS APPLIED IN CAPACITANCE CALCULATIONS	115
TABLE 5.3	SPECIFICATIONS OF THE PLANAR TRANSFORMER WITH SHUNT	123
TABLE 5.4	SPECIFICATIONS OF TESTED PLANAR TRANSFORMERS	125
TABLE 6.1	DESIGN SPECIFICATIONS OF THE PLANAR TRANSFORMER	129
TABLE 6.2	DIMENSIONS AND PARAMETERS OF PLANAR EER 41/7.6/32 CORE	130
TABLE 6.3	LOSSES BREAKDOWN OF THE PLANAR TRANSFORMER	136

Nomenclature

The following is a list of symbols used in this thesis.

a	Turns ratio of the transformer
a_R	Reluctance ratio, defined in Equation 5.41
A_1, A_2	Complex constants
A_c	Cross-sectional area of magnetic core (m^2)
A_L	Inductance per turn ($H/turn^2$)
A_p	Product of window winding area \times cross-sectional area of core (m^4)
b_w	Width of the core window (m)
B_{max}	Maximum flux density (T)
B_{sat}	Saturation flux density of core material (T)
C_{oss}	Output capacitance of the switch in the bridge (F)
C_{pasa}	Capacitance between terminals Pa and Sa (F)
C_r	Resonant capacitance (F)
d_g	Distance from the winding to the gap (m)
F_{R1}	Eddy current factor for foil windings
F_{R2}	Skin effect factor for round conductor
f	Frequency in hertz (Hz)
f_n	Normalized switching frequency defined in Equation (2.3)
f_r	Resonant frequency of L_r and C_r defined in Equation (2.1) (Hz)
f_{rm}	Resonant frequency of $L_r + L_m$ and C_r defined in Equation (2.1) (Hz)
f_s	Switching frequency of semiconductor devices (Hz)
g	Air gap length (m)

g^b	Air gap length defined in Fig. 1.9(a) (m)
g_d	Depth of air gap (m)
g_r	Radius of air gap (m)
g_w	Width of air gap (m)
g_w^b	Width of air gap defined in Fig. 1.9(a) (m)
h^b	Height of the core leg, defined in Fig. 1.9(a) (m)
h_{leg}	Core window dimension shown in Fig. 3.2 (m)
h_w	Height of windings (m)
h_{wc}	Height of core window (m)
i_{Lm}	Magnetizing current through L_m (A)
i_p	Current through the primary winding of ideal transformer (A)
i_r	Resonant current through L_r (A)
i_{s1}	Current through the secondary winding 1 (A)
i_{s2}	Current through the secondary winding 2 (A)
I_o	DC output current (A)
I_{Lm_pk}	Peak value of the magnetizing current (A)
I_{Lm_rms}	RMS value of the magnetizing current (A)
I_p, I_s	Currents through the primary winding and the secondary winding (A)
I_{r_pk}	Peak value of the resonant current (A)
I_{r_rms}	RMS value of the resonant current (A)
I_{s1_rms}	RMS value of the current through secondary winding 1 (A)
J_0	Current density (A/m^2)
k	Factor defined as Equation (2.3)
k_u	Window utilization factor
k_{up}	Window utilization factor of the primary winding
K_c	Magnetic material parameter used in Steinmetz equation
K_{ic}	Improved Steinmetz parameter, defined in Equation 3.15
K_t	Constant, 48.2×10^3
l_c	Magnetic path length of the core (m)
l_w	Winding length (m)

L_{lk}	Leakage inductance (H)
L_m	Magnetizing inductance (H)
L_m^f	Magnetizing inductance with fringing effect considered
L_r	Resonant inductance (H)
m_p, m_s	Number of turns in each layer of the primary winding and secondary winding, respectively
M	DC voltage gain of the LLC resonant converter
M_{max}	Maximum value of DC voltage gain of the LLC resonant converter
M_{req}	Required minimum value of M_{max}
MLT	Mean length of a turn (m)
n_p, n_s	Number of layers in the primary winding and secondary winding, respectively
n_{Lp}, n_{Ls}	Number of turns in each layer of the primary winding and secondary winding, respectively
n_{pp}, n_{ps}	Number of layers in each primary winding portion and secondary winding portion, respectively
n_{wp}, n_{ws}	Number of winding portions in the primary winding and secondary winding, respectively
N_p	Number of turns in the primary winding
N_{s1}	Number of turns in the secondary winding 1
p	Number of layers
P_c	Transformer core loss (W)
P_{cu_ac}	AC winding loss (W)
P_{cu_dc}	DC winding loss (W)
P_{cu_p}	DC winding loss of the primary winding (W)
P_{fe}	Magnetic core loss per unit volume (W/m ³)
P_{Lr}	Power loss of the resonant inductor (W)
P_{max}	Maximum allowed power loss (W)
P_o	Output power (W)
P_{sr}	Losses of switches in the synchronous rectifier (W)
P_{s_dr}	Driving loss of switches in the bridge (W)
P_{s_off}	Turn off loss of switches in the bridge (W)

P_{s_on}	Conducting loss of switches in the bridge (W)
P_{trafo}	Total power loss of the transformer (W)
P_{total}	Total power loss of the LLC resonant converter (W)
P_T	Power loss of the transformer (W)
P_w	Transformer winding loss (W)
Q	Factor defined as Equation (2.3)
Q_{gs}	Gate-source charge of the switch in the bridge (C)
Q_{gs_sr}	Gate-source charge of the switch in the synchronous rectifier (C)
r	Radius of the conductor with round cross section (m)
R_{ac}	AC resistance of a winding with sinusoidal excitation (Ω)
R_{dc}	DC resistance of a winding (Ω)
R_g	Reluctance of an air gap (A/Wb)
R_{gc}	Reluctance of the air gap in the centre leg without fringing flux (A/Wb)
R_{gc}^f	Reluctance of the air gap in the centre leg with fringing flux (A/Wb)
R_g^b	Reluctance of an air gap in basic geometry shown in Fig. 1.9(a) (A/Wb)
R_i, R_o	Inner and outer radius of the core window area, shown in Fig. 5.7 (m)
R_L	Load resistance (Ω)
R_{Lr}	Resistance of the inductor winding (Ω)
R_{p_dc}	DC resistance of the primary winding (Ω)
R_{s_on}	Conducting resistance of the switch in the bridge (Ω)
R_{s1_dc}	DC resistance of the secondary winding 1 (Ω)
R_{sr_on}	Conducting resistance of the switch in the synchronous rectifier (Ω)
R_{T_p}	Resistance of the primary winding of the transformer (Ω)
R_{T_s}	Resistance of each secondary winding of the transformer (Ω)
R_{wi}, R_{wo}	Inner and outer radius of the circular conductor (m)
R_θ	Thermal resistance of core ($^{\circ}C/W$)
t	Thickness of the conductor with rectangular cross section (m)
t_d	Dead time (s)
t_f	Turn off time of the switch in the bridge (s)
t_{ins}	Thickness of insulation (m)

t_p, t_s	Conductor thickness of the primary winding and secondary winding, respectively (m)
t_{sh}	Thickness of the magnetic shunt (m)
$t_{\Delta p}, t_{\Delta s}$	Insulation thickness inside the primary winding and secondary winding, respectively (m)
T_a	Ambient temperature ($^{\circ}\text{C}$)
T_r	Resonant period corresponding to f_r (s)
T_{rm}	Resonant period corresponding to f_{rm} (s)
T_s	Switching period (s)
v_{Cr}	Voltage of the resonant capacitor C_r (V)
v_p	Voltage across the primary winding of the transformer (V)
v_{tank}	Voltage supplied to the resonant tank (V)
V_c	Core volume (m^3)
V_{gs}	Driving voltage of the switch in the bridge (V)
V_{gs_sr}	Driving voltage of the switch in the synchronous rectifier (V)
V_{in}	DC input voltage (V)
V_{in_max}	Maximum input voltage (V)
V_{in_min}	Minimum input voltage (V)
V_o	DC output voltage (V)
V_o^n	Normalized output voltage
w_c	Core depth, shown in Fig. 5.2 (m)
w_w	Width of strip conductors (m)
W_a	Window winding area of core (m^2)
α, β	Magnetic material parameter used in Steinmetz equation
α_{20}	Temperature coefficient of resistivity at 20°C
δ_0	Skin depth (m)
Δ	Depth ratio, defined in Equation 1.3, Equation 4.17 and Equation 5.15
ΔT	Temperature rise ($^{\circ}\text{C}$)
φ	Phase angle shown in Fig. 2.2
ϕ_p	Flux built by the primary current i_p (Wb)
ϕ_{s1}	Flux built by the secondary current i_{s1} (Wb)

ϕ_{s2}	Flux built by the secondary current i_{s2} (Wb)
θ_{ps}	Phase shift angle
γ	Factor defined in Equation 3.19
ϵ_r	Relative permittivity of kapton tape
λ	Complex propagation constant
μ_0	Magnetic permeability for free space (H/m)
μ_{eff}	Effective relative permeability
μ_{eff}^f	Effective relative permeability with fringing flux considered
μ_{opt}	Optimum relative permeability (H/m)
μ_r	Relative permeability of core
μ_s	Relative permeability of the magnetic shunt
η	Porosity factor
ρ_{20}	Electrical resistivity at 20 °C ($\Omega \cdot m$)
ρ_w	Electrical resistivity ($\Omega \cdot m$)
σ	Electrical conductivity (S/m)
σ_r	Fringing factor defined in Equation 3.12
σ_x, σ_y	Fringing factor defined in Equation 3.9

Abbreviations

EMI	Electromagnetic Interference
FEA	Finite Element Analysis
FFA	Fundamental Frequency Analysis
GaN	Gallium Nitride
GSE	Generalized Steinmetz Equation
GTO	Gate Turn-off Thyristor
iGSE	Improved GSE
i ² GSE	Improved iGSE
IGBT	Insulated Gate Bipolar Thyristor
ISP ³	Integrated Spiral Planar Power Passive
LTCC	Low Temperature Co-fired Ceramic
MMF	Magneto-motive Force
MOSFET	Metal-Oxide-Semiconductor Field-Effect Transistor
PCB	Printed Circuit Board
PFC	Power Factor Correction
PFM	Pulse Frequency Modulation
PRC	Parallel Resonant Converter
PwrSoC	Power Supply on Chip
PWM	Pulse Width Modulation
RMS	Root-mean-square
SRC	Series Resonant Converter
ZVS	Zero Voltage Switching

1

Introduction

Power Electronics is the technology associated with the efficient conversion, control and conditioning of electric power by static means from its available input into the desired electrical output [1]. The main target of power electronics is to control the energy from a power source to an electrical load with high efficiency of power transfer, high reliability of system operation, small size and light weight of the circuit system. With the rapid development of power semiconductor devices since 1970's and 1980's, when the power metal-oxide-semiconductor field-effect transistor (MOSFET), the gate turn-off thyristor (GTO) and the insulated gate bipolar (IGBT) were introduced [2], the power level and the operation frequency of power electronics circuit has been greatly promoted. Nowadays, power electronics system can be found in almost every electronics product and is continuously expanding its applications through new developing and innovative industries, for example renewable energy, electrical vehicles, lighting and wireless power transfer.

Among all power electronics applications, the DC-DC converter is one group of electronic circuits in which DC input voltage is converted to a DC output voltage having a larger or smaller magnitude, possibly with opposite polarity or with isolation between input and output ground references [3]. They are normally employed in distributed power systems for computers and servers in telecommunication systems, adapters for laptops and chargers for consumer electronics [4]-[6]. For the typical power supply connected with the AC grid, DC-DC converter is generally applied as

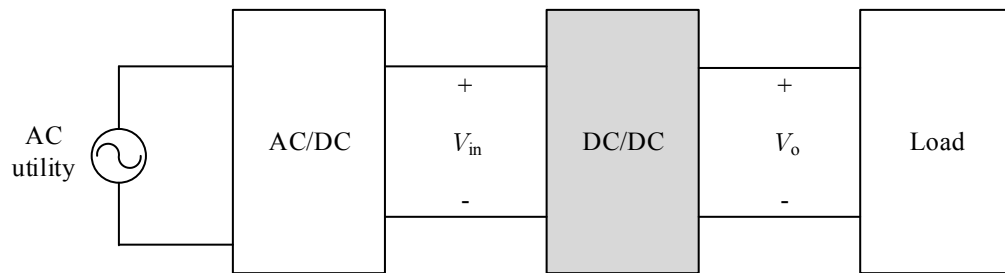


Fig. 1.1 Typical configuration of the power supply including DC-DC converter

the second conversion stage following an AC-DC power rectifier which can generate the DC voltage from the public utility with high power factor and high efficiency. The configuration of one power supply is shown in Fig. 1.1 [7].

In the DC-DC stage of the power supply, higher switching frequency is always the persistent pursuit because of the smaller volume of passive components, i.e. inductors, transformers and capacitors, can be realized. Higher power density, on account of smaller components, means lower cost of the converter and allows more units to be accommodated in the infrastructure where the space is limited. However, the switching loss of semiconductor devices is directly related to the switching frequency and the permissible temperature rise of switching components will limit the operation frequency. In an effort to reduce the switching loss, soft-switching technology was introduced and a number of main topologies have been proposed to approach higher operation frequency. The associated topologies of DC-DC converters with the output power range from 100 W to 2 kW will be summarised in Section 1.1.

On the other hand, miniaturization of the magnetic components operating at high frequency will create other challenges. For wire wound inductors or transformers, the winding loss caused by the skin effect, the proximity effect and the fringing effect due to the air gap will increase significantly. In consequence, the design methodology for magnetic components should be further investigated with high frequency effects. Meanwhile, the parasitic parameters, such as the leakage inductance and the stray capacitance for the transformer, will play more significant roles in the circuit operation under higher switching frequency operation. All these design issues will be introduced and reviewed in Section 1.2.

TABLE 1.1 SPECIFICATIONS OF THE INVESTIGATED DC-DC CONVERTERS

Parameters	Symbols	Values
Input voltage	V_{in}	300 V to 400 V
Output voltage	V_o	5 V to 50 V
Output power	P_o	100 W to 2 kW
Maximum ambient temperature	T_a	50 °C

Another trend of magnetic components leads to lower profile and integration within the circuit board. Thus, the planar magnetics consisting of printed circuit board (PCB) or flat copper foil is extensively used in modern DC-DC power converters because of the advantages achieved in terms of low profile, excellent thermal characteristic and extremely good repeatability [8]. The manufacturing technologies and associated design considerations for planar magnetics applied in DC-DC converters will be introduced and discussed in Section 1.3.

1.1 High Frequency DC-DC Converters

The DC-DC converter stage as part of the power supply unit shown in Fig. 1.1, adapts the bus voltage from $V_{in} = 300 \text{ V} \sim 400 \text{ V}$ to $V_o = 5 \text{ V} \sim 50 \text{ V}$. For regular power supplies, the output power range is generally from 100 W to 2 kW. The ambient temperature of the power supply under normal operation does not exceed 50 °C. The following investigation of DC-DC converters are principally based on the specifications given in Table 1.1. Furthermore, the electrical isolation between the input and output is commonly required for safety considerations which means the transformer is implemented in the converter.

The topologies involved in soft-switching isolated DC-DC converters following the specifications shown in Table 1.1 need further elaborations. The soft-switching DC-DC converters can be divided into pulse-width-modulated (PWM) converters and resonant converters. Depending on the number of main switches in the topology, PWM converters have three categories, single switch converters, half bridge

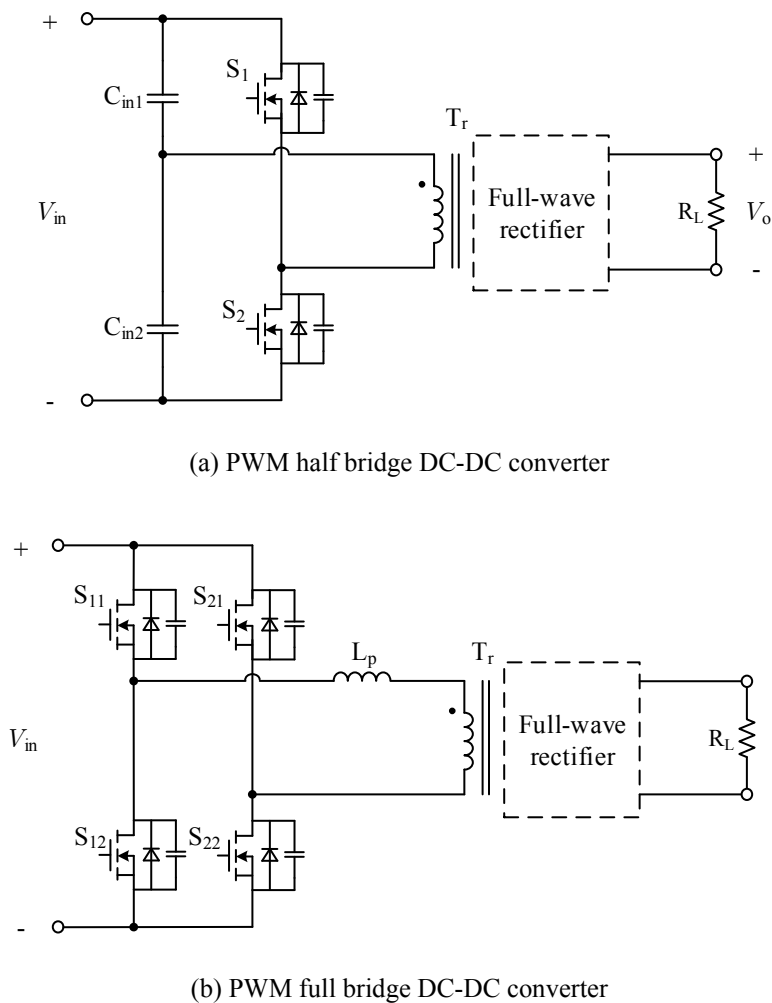
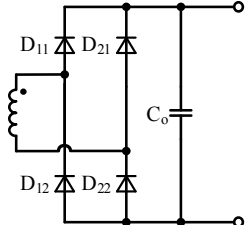
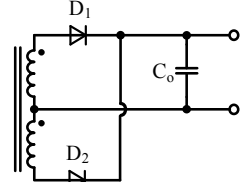
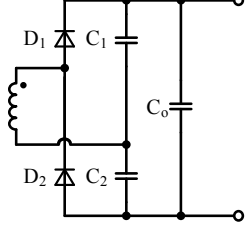
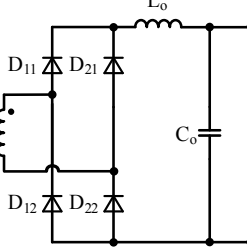
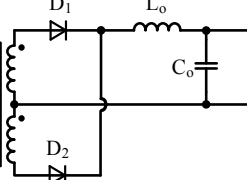
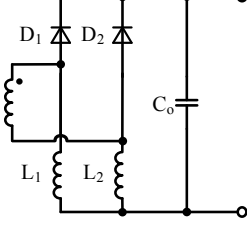


Fig. 1.2 Configurations of half bridge and full bridge PWM converters

converters and full bridge converters. For the half bridge or full bridge converters, a full-wave rectifier will be connected to the secondary windings of the transformer as shown in Fig. 1.2. In [6], different configurations of full-wave rectifiers have been investigated. Table 1.2 lists the advantages and disadvantages of each topology. The diodes in rectifiers can be replaced by controllable active switching devices, such as the synchronous rectifier or the bidirectional power converter.

For resonant converters, half bridge or full bridge could be realised in the main topology. However, the significant feature to distinguish two resonant converters is the resonant tank, which is a dual-port circuit network between the output of the switching bridge and the isolation transformer. According to the components in the

TABLE 1.2 BASIC FULL-WAVE RECTIFIER TOPOLOGIES AND COMPARISONS [6]

Full-wave rectifier topologies	Advantages	Disadvantages
 <p>Voltage output bridge rectifier</p>	<p>Simple assembly of the transformer with only one secondary winding</p>	<p>(1) High conduction loss (2) High current ripple (3) Larger filter capacitor required</p>
 <p>Voltage centre-tapped rectifier</p>	<p>(1) Only two diodes needed (2) Well adapted for high current output</p>	<p>Two secondary windings in the transformer resulting in complex implementation</p>
 <p>Voltage output doubler rectifier</p>	<p>Suitable for high voltage output applications</p>	<p>For high current output, the capacitors will be bulky for the demand output voltage ripple.</p>
 <p>Current output bridge rectifier</p>	<p>Better filter characteristic</p>	<p>(1) Added inductor increases the loss and complexity (2) Blocking voltage of diodes increased (3) High conduction loss</p>
 <p>Current centre-tapped rectifier</p>	<p>(1) Only two diodes needed (2) Better filter characteristic</p>	<p>Two secondary windings in the transformer resulting in complex implementation</p>
 <p>Current output doubler rectifier</p>	<p>Suitable for high current output applications</p>	<p>Two added inductors resulting in higher power loss and complexity</p>

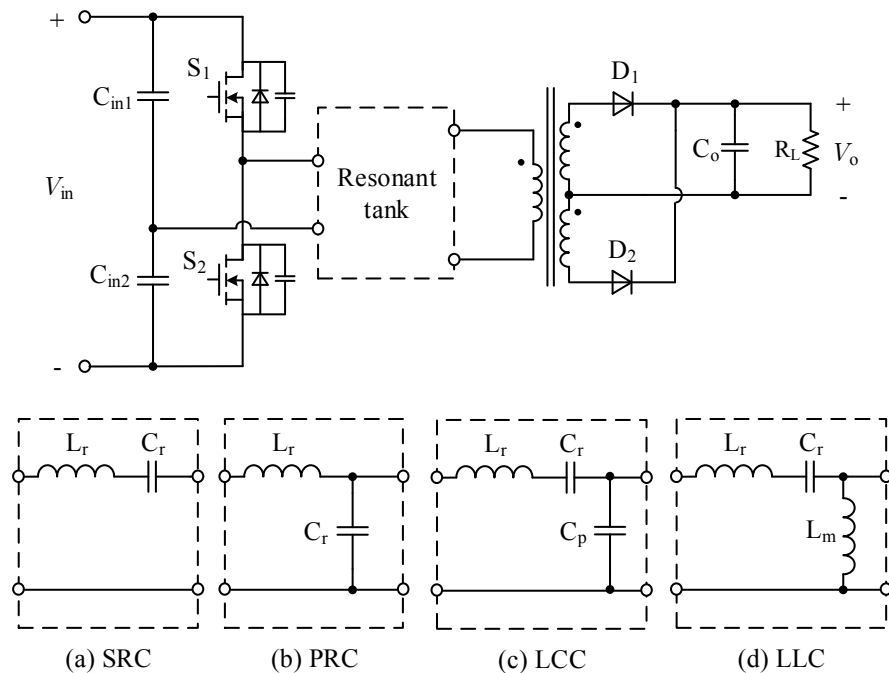


Fig. 1.3 Topologies of half bridge resonant converters with centre-tapped rectifier: (a) series resonant converter (SRC), (b) parallel resonant converter (PRC), (c) LCC resonant converter, (d) LLC resonant converter

resonant tank, there will be four basic resonant converters, series resonant converters (SRC), parallel resonant converters (PRC), LCC resonant converters and LLC resonant converters shown in Fig. 1.3. The characteristics of each topology and the previous research related to the circuit will be described next.

PWM Single Switch Converters The basic isolated DC-DC converters with one switch including flyback and forward converters, are widely used in low power applications below 100 W [6]. Auxiliary circuit is complemented with the single switch converter to achieve soft switching operation [9]-[11]. Therefore, the circuit is getting complex. Worst of all, the voltage stress of switches is typically twice the input voltage and high performance commercial MOSFETs with voltage capability of 600 V are not available.

PWM Half Bridge Converters With two switches in one bridge, shown in Fig. 1.2(a), the control signal will be symmetrical if the turn-on time for the upper switch equals the conduction time of the bottom one. As the symmetric control strategy is

assigned, the soft switching can only be realized if the active switches or auxiliary circuits are added. The bidirectional control for the half bridge converter with the mirrored bridge connected with the secondary side of the transformer is employed in [12]. The three-level three-phase half bridge converter was proposed in [13]. In this case, the voltage drop on each switch is reduced, however the scale of the circuit and the control system is significantly increased.

The other more interesting control method for high bridge converters is asymmetrical. With the help of the leakage inductance in the transformer, soft switching is feasible. The asymmetric half bridge converters with passive components, for instance, inductor, capacitor or coupled inductors have been reported in [14]-[18].

The auxiliary circuit and active components were introduced in [19] and [20] to meet the hold-up time requirement when the converter is disconnected from the public utility and to improve the efficiency, respectively. Approaching power levels up to 1 kW, interleaved-, three-level- and two series- asymmetric half bridge converters were developed in [21]-[23].

PWM Full Bridge Converters Each switch in the full bridge converter, shown in Fig. 1.2(b), will be turned on for half of the total switching period and driving signals for two bridges have a certain phase-shift to guarantee the soft switching. This kind of phase-shift controlled full bridge converters is popular in power supplies [24]-[28]. The leakage inductance of the transformer can be implemented to achieve the zero voltage switching (ZVS) of switches in bridge circuit. The improved topologies based on the PWM full bridge converter were also investigated in former publications, such as the series structure [29], [30], the multilevel topology [31] and bidirectional power flowing converters [32], [33].

The main drawback of this topology is that the soft switching is difficult to realize in light load operation. For soft switching, the energy stored in the series inductor should be bigger than the charging energy to the capacitors which are paralleled with the switches. The range of soft switching, which depends on the load condition, can be adjusted by the inductance. However, larger inductance will result in larger energy

circulating through the switching bridge and the primary winding of the transformer. This means the conduction loss will increase. One method to overcome this disadvantage is connecting a saturated inductor in series with the transformer as proposed in [34], [35]. The other commonly applied approaches include more advanced control strategies [36]-[40] and extra active commutation auxiliary circuits [41], [42].

Series Resonant Converters (SRC) In the resonant converter, the impedance of the resonant tank, as shown in Fig. 1.3, can be changed with the varied switching frequency, f_s . Consequently, the DC output voltage is maintained the same value for different load conditions by varying f_s . Among all resonant converters, the most significant advantage is that the current through the resonant tank is almost purely sinusoidal which will allow the inductor and transformer to perform at higher efficiency without higher-order harmonics. But the output voltage of the SRC will be out of control in cases of light load and no load conditions because the output voltage gain will be constant if the impedance of the resonant tank is much higher than the load resistance [43]. This topology was utilized to generate 48 V from around 400 V of 700 W in [44] and 2.9 kW in [45]. An improved structure with the series primary windings and secondary windings in parallel with two transformers was proposed in [46]. A SRC of 35 W with a switching frequency of 2.63 MHz was carried out in [47].

Parallel Resonant Converters (PRC) In the PRC, the capacitor is in parallel with the primary winding of the transformer. Compared to the SRC, the PRC operates without light load or no load regulation issues and it can even work with a short circuit load. However, the considerable limitation is the circulating energy in the resonant tank since the current is almost independent at the load and the efficiency at light load condition is very low. The PRC was reported in applications of power suppliers in [48], [49]. The three-level PRC was implemented with the power level as high as 30 kW in [50], [51].

LCC Resonant Converters LCC resonant converter (in some cases, called series-parallel resonant converter) has a series inductor, a series capacitor and a parallel capacitor connected with the transformer winding (can be in either primary side or

secondary side) to consist its resonant tank as shown in Fig. 1.3. Actually LCC resonant converter combines the SRC and the PRC, so it overcomes the main disadvantages of the SRC and the PRC, such as the light load or no load regulation issues.

In research papers, LCC resonant converters have been designed to achieve 48 V or 50 V output voltage ([52] with output power 1 kW, [53] with output power 3 kW, [54] with output power 2.3 kW). However, the LCC resonant converter is particularly suitable for high voltage and high power level applications ([55] with output power 100 kW, [56] with output 20 kW and voltage 20 kV, [57] with output voltage 3.8 kV, [58] and [59] with output voltage 10 kV).

LLC Resonant Converters This topology was first proposed by Bat in 1990 [60]. Because of the similarity to the SRC, it was neglected for years. The difference between the LLC resonant converter and the SRC is the inductor in parallel with the primary winding of the transformer which is normally integrated with the transformer by the non-ideal magnetizing inductor. Since Yang revealed its superior characteristics in 2002 [61], LLC resonant converters have been further studied and several modified topologies as well as modelling, control and performance improvement methodologies were investigated. In this topology, low switching loss and low circulating energy in the resonant tank can be easily achieved. It is possible to regulate the output voltage over a wide range of the input voltage and load variations with a relatively small variation of the switching frequency. The significant advantage is that the stray capacitances of the switching devices, the leakage inductance and the magnetizing inductance of the transformer are suitable for the soft switching. Nowadays, the LLC resonant converter is treated as one of the most popular topologies in commonly applied power supplies. It is difficult to find an easy method to model and control the LLC resonant converter since the switching frequency varies to maintain the output voltage under different circuit conditions, i.e., different input voltages and different loads. A large number of research publications devoted themselves to the application and improvement of the LLC resonant converter in recent years. The output voltages of 12 V, 24 V and 48 V converted from the input voltage of around 400 V based on the regular LLC resonant converter were reported in [61]-[78] and the highest

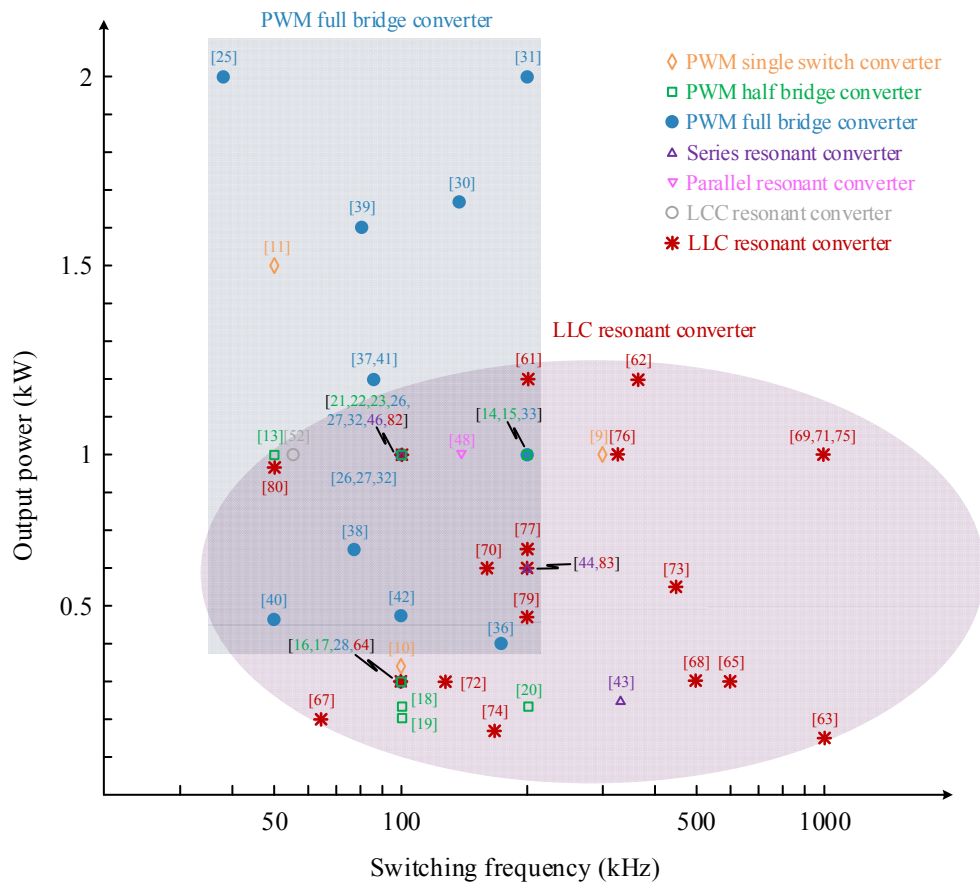


Fig. 1.4 Summary of soft switching DC-DC converters (input voltage: around 300 V ~ 400 V; output voltage: 5 V ~ 50 V; output power: 100 W ~ 2 kW)

operation frequency has approached 1 MHz. The modified LLC resonant converters were proposed for power supply applications including the three-level topology [79], [80], the capacitor-diode clamped converter [81], the bidirectional [82] and interleaved structures [83].

According to the specifications listed in Table 1.1, key soft switching DC-DC converters for power supply applications with different topologies are summarised in Fig. 1.4 based on the output power and the switching frequency. It is shown that the PWM full bridge converter and the LLC resonant converter are the two mostly applied topologies for power supply applications within a wide range of output power levels and switching frequencies. Besides, the switching frequencies of LLC resonant converters in the research papers are higher than the other topologies and it is definitely the most popular circuit for power supplies in recent years.

Previous papers discussed the modelling, design methodology, control strategy and light-load efficiency improvement for LLC resonant converters, however the research on the transformer, which is supposed to occupy large volume of the whole circuit, is not available to date. It is meaningful to investigate the design issues of the transformer in the LLC resonant converter operated at high frequency, in which the magnetizing inductor is integrated. The related topics of the transformer applied in high frequency DC-DC converters will be introduced in the following section.

1.2 Design Issues for Transformers in High Frequency DC-DC Converters

High efficiency is the aim of power electronics circuits, so the power loss of the transformer needs to be low. The losses of one transformer consists of the loss in windings (represented as P_w) and the loss in the magnetic core (represented as P_c) if a magnetic core is employed to construct the component. With increasing switching frequency, the currents through the windings of the transformers in DC-DC converters will cause extra winding loss compared to the low frequency case. The AC resistance R_{ac} is commonly introduced to evaluate the high frequency effect on the winding loss. The DC resistance R_{dc} correspondingly represents the winding resistance at low operation frequency. In summary, the main consequences of high frequencies include the skin effect and proximity effect in the windings and increased eddy current and hysteresis losses in the core [84].

1.2.1. High Frequency Winding Loss

With AC current flowing in an isolated conductor, an alternating magnetic field will be induced to cancel the field generated by the original current and eddy currents. The result is that the current density near the surface of the conductor will be higher than in the centre, and this phenomenon is called skin effect. The equivalent conduction area for the current flowing gets smaller and the loss increases. Fig. 1.5 shows the eddy currents in one isolated round conductor and the current density in the conductor based on Finite Element Analysis (FEA) simulations. The distance from the outer radius of the conductor to the position where the electromagnetic wave traveling in a

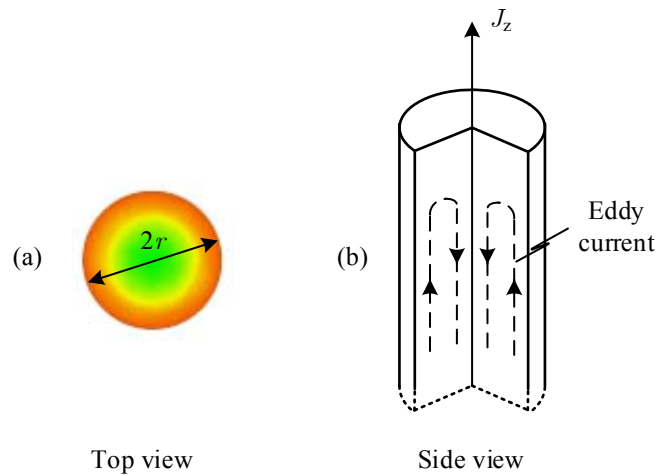


Fig. 1.5 Skin effect and eddy current in a round conductor: (a) cross-sectional view of the round conductor and current distribution; (b) eddy current inside the round conductor

lossy conductor is reduced to $1/e$ of the original value is named as the skin depth (e is the base of the natural logarithm),

$$\delta_0 = \frac{1}{\sqrt{\pi f \mu_0 \sigma}}, \quad (1.1)$$

where μ_0 is the magnetic permeability of free space with the value of $4\pi \times 10^{-7}$ H/m for a conductor with conductivity σ and operating at frequency f .

Several winding turns will appear in the inductor or transformer and the current in one conductor is influenced by the magnetic field generated by the current in the other conductor. The current densities of two adjacent round conductors and two long copper foils which are carrying currents with the same magnitude and same/opposite directions are shown in Fig. 1.6. The results show that the current density distribution in the conductors is altered and the winding loss will vary compared to DC operation condition. This phenomenon is called the proximity effect.

The skin effect and proximity effect are collectively known as the eddy current effect of winding loss because there are eddy currents due to both skin effect and proximity effect at high frequency. Lots of efforts have been carried out for quantitative calculations and a related review can be found in [85]. The particular investigation for the eddy current loss calculation of one transformer with foil windings or equivalent

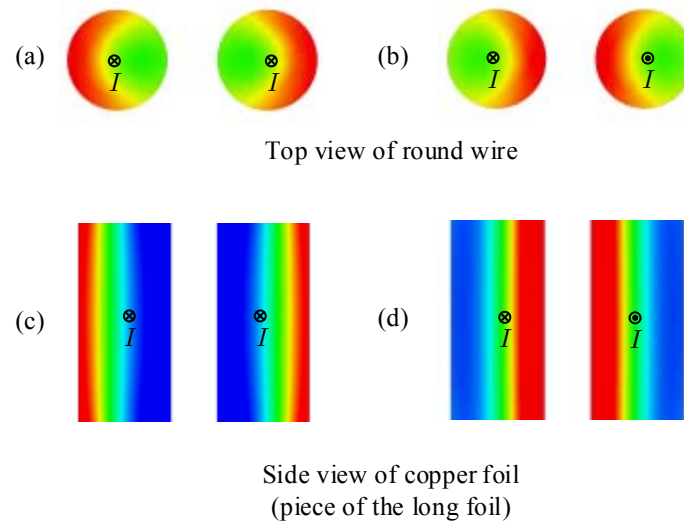


Fig. 1.6 Proximity effect of adjacent round conductors and long copper foils (a) two round conductors carrying currents in same direction; (b) two round conductors carrying currents in opposite directions; (c) two copper foils carrying currents in same direction; (d) two copper foils carrying currents in opposite directions

foil conductors for round wires in the same layer was presented by Dowell in [86]. The work is a 1-D solutions of the equation incorporating proper assumptions. Based on Dowell's equation, the loss in multilayers solenoid windings was solved in [87]. In [88] and [89], loss under the condition of non-sinusoidal excitation currents was considered. These previous Dowell-based work was synthetically applied in [90]. For arbitrary current waveforms, Hurley proposed the method to optimize the conductor thickness without the need of Fourier coefficients calculations in [91]. Basically, the Dowell's result can be illustrated with the winding structure of the transformer shown in Fig. 1.7. The eddy current factor for windings with p layers is calculated by

$$F_{R1} = \frac{R_{ac}}{R_{dc}} = \Delta \left[\frac{\sinh 2\Delta + \sin 2\Delta}{\cosh 2\Delta - \cos 2\Delta} + \frac{2(p^2 - 1)}{3} \frac{\sinh \Delta - \sin \Delta}{\cosh \Delta + \cos \Delta} \right], \quad (1.2)$$

with

$$\Delta = \frac{t}{\delta_0}, \quad (1.3)$$

where t is the thickness of the layer.

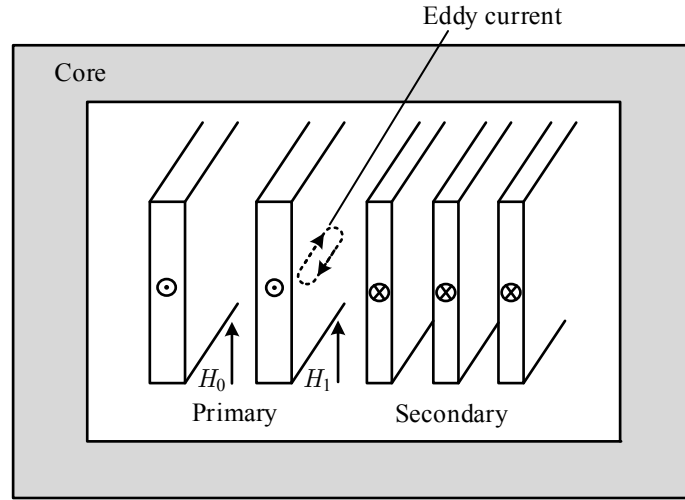


Fig. 1.7 Foil windings in the transformer and eddy current based on 1-D Dowell's equation

Another calculation method for round conductors based on Bessel-functions was given in [92]. In [93], Ferreira found the orthogonality between the skin effect and the proximity effect. Some other Bessel-function-based calculations include [94] and [95]. The expression of the skin effect factor for an isolated round conductor with the radius r was given as

$$F_{R2} = \frac{R_{ac}}{R_{dc}} = \frac{\xi}{2} \frac{\text{ber}\xi \text{bei}'\xi - \text{bei}\xi \text{ber}'\xi}{\text{ber}'^2\xi + \text{bei}'^2\xi}, \quad (1.4)$$

with

$$\xi = \frac{\sqrt{2}r}{\delta_0}. \quad (1.5)$$

However, [96] declared that both the Dowell's equation and Ferreira's method based on Bessel-function will generate huge error for non-isolated conductors with finite length. Some calculation methods incorporating 2-D considerations have been carried out in an effort to improve accuracy. FEA tools are commonly used in the inductor or transformer windings design and the calculation of high frequency winding loss based on FEA, also called "semi-empirical" method, were proposed in [97], [98] and [99]. In [100], the static field simulations in conjunction with semi-empirical expressions were applied to obtain the winding loss under arbitrary current excitation conditions and the resistance matrix was used. These 2-D methods are mainly obtained based on case studies, hence the generality of the results is not very strong. In [101], Sullivan

proposed the squared-field-derivation method for calculating the eddy current losses in round wire or litz wire transformer and inductor windings. Another calculation methodology employed the complex permeability model and transferred the eddy current loss into the hysteresis loss of equivalent material [102], [103]. This method was extended to attain the winding loss for litz wire in [104], [105].

Litz wire and interleaving windings are two common solutions. Litz wire is a group of stranded wires with each strand insulated. The optimum design and the cost analysis for litz wire can be found in [106]-[108]. Considering the cost and the implementation complexity of the transformer, the interleaving method in the transformer with round wire or copper foils windings is generally used to eliminate the eddy current effect. The difference between the interleaved and conventional winding arrangements was introduced in [109]. In [110], the interleaving transformer for high voltage applications and the insulation method were described. The equivalent circuit model for the transformer with windings interleaved and the mathematical analysis were presented in [111]. In order to reduce the eddy current loss and the leakage inductance, the new method for partially interleaving the windings was introduced in [112].

Another main factor that will increase the winding loss at high frequency is the air gap in the magnetic core of the inductor or the transformer in which the magnetizing inductance is relatively small, for example, the transformer in the LLC resonant converter. As shown in Fig. 1.8, for an inductor simulation model in 2-D in the X-Y coordinate system, the fringing field will exist around the air gap and it results in extra winding loss due to the induced current in the winding. This effect is extremely significant for the inductor with a relative large air gap and the inductance of the structure will vary depending on the fringing field.

The fringing effect to the quantity of inductance was comprehensively investigated and a good review for evaluation methods based on different gap implementations was summarised in [113]. One of the approaches to obtain the precise inductance with air gap is the method of the conformal Schwarz-Christoffel transformation. The related solutions were introduced in [114]. Basically, these methods will lead to very complex calculations. An alternative approach to solve the issue is to treat the air gap by

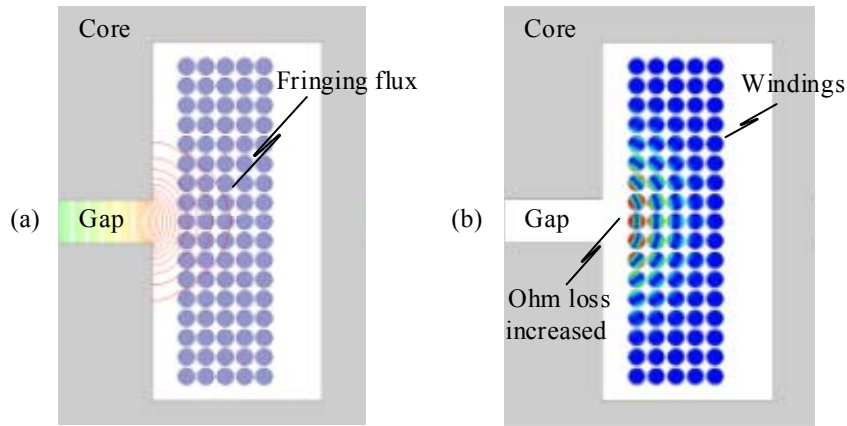


Fig. 1.8 Fringing field and winding loss in conductors near the air gap: (a) magnetic flux around the air gap; (b) ohm loss distribution in the windings

increasing the actual cross-sectional area (A_c) [115]. In [116] and also mentioned in [84], the reluctance of an air gap with length g , width g_w and depth g_d can be calculated as

$$R_g = \frac{g}{\mu_0 (g_w + g)(g_d + g)}. \quad (1.6)$$

In [113], the reluctances for different air gap implementations with 2-D consideration were proposed as shown in Fig. 1.9 and the reluctance of the air gap was given by

$$R_g^b = \frac{1}{\mu_0 \left[\frac{g_w^b}{2g^b} + \frac{2}{\pi} \left(1 + \ln \frac{\pi h^b}{4g^b} \right) \right]}, \quad (1.7)$$

where the parameters are illustrated in Fig. 1.9. Finally, the actual 3-D air gap is treated by combining 2-D results for different coordinate planes. In [113], the reluctance model for the air gap with round cross-sectional area was also presented.

The fringing effect to the winding loss will be remarkable with a large air gap placed in the magnetic core or the windings lose. A simple and accurate closed formula to calculate the winding loss due to the fringing effect is not available.

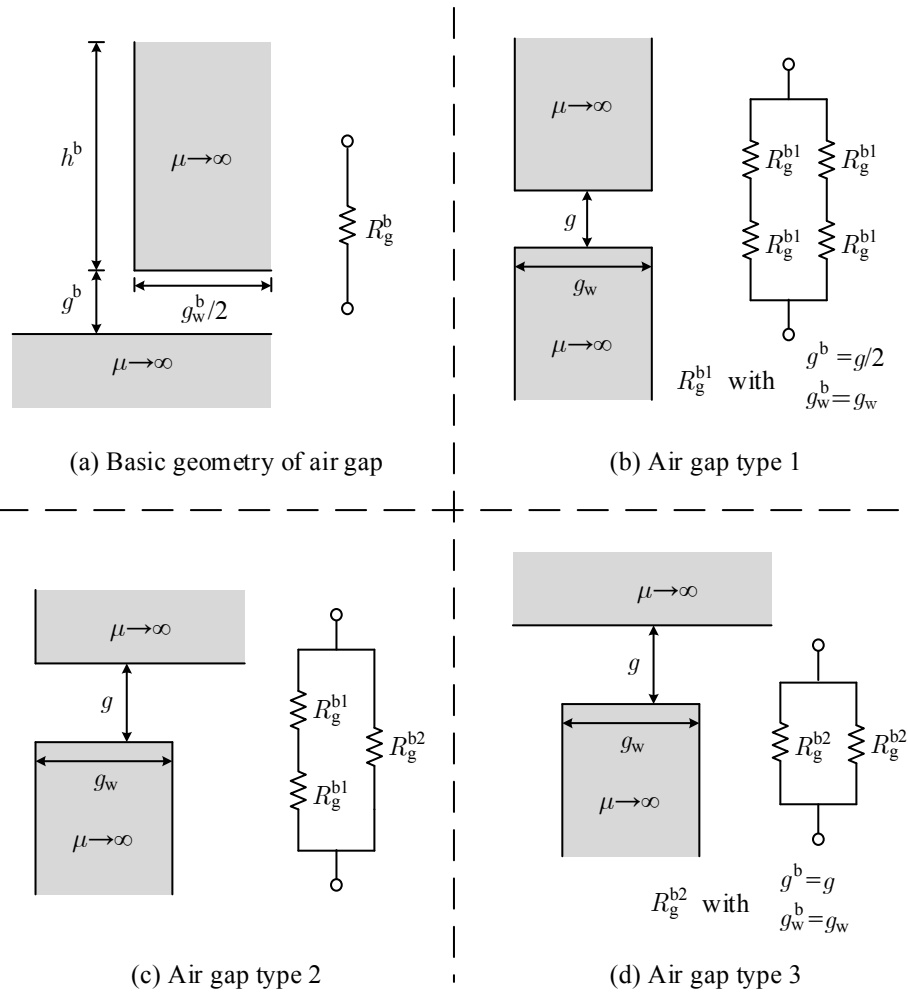


Fig. 1.9 Different types of air gaps and reluctance models

The equivalent current pole or current sheet was effectively utilized to replace the physical air gap [113], [117], and [118]. Based on this equivalent method, the mirroring/images analysis can be applied to gain the winding loss [119]. In [113], the small air gap was replaced by one current pole and the whole winding is mirrored. However, the current sheet would be better applied to replace the relatively large air gap and the associated calculation methodologies for winding losses with round wires and foils were presented in [118]. In [120], the current sheet with improved cambered shape was applied and the images method was used to evaluate the winding loss. Another calculation method was studied by Roshen [121]-[123]. Firstly, the 2-D field formulas around the air gap were obtained and then the winding loss was calculated supposing that the self-field of currents through windings will not affect the fringing field. In [124], the fringing effect was solved based on the equivalent permeability

analysis method. Furthermore, FEA simulations were also reported to investigate the fringing effect [125] and the data fit method was presented in [126]. Generally, a simple formula is difficult to obtain. In [113], the approximate formula of AC resistance per unit length of foil windings with single air gap was given. However, the formula can only be used if the tips of the foil windings are very close to the magnetic core and the air gap is relatively small compared to the distance from the innermost foil to the air gap and also the foil thickness is much smaller than the skin depth.

Some implementations were designed to reduce the fringing effect. The winding was placed away from the air gap [127] or shaped in order to make sure that there is no conductor around the air gap [128]-[130]. The mounting strap could be placed around the air gap to decrease the winding loss [125], [131]. The other frequently applied method to reduce fringing loss is using the distributed gap in the core or a uniformly lower permeability core to replace the discrete large air gap [126], [132], [133].

1.2.2. Magnetic Core Loss

Another main power loss of the magnetic component comes from the magnetic core. In general, the evaluation of the core loss can be done through three main methods, the hysteresis model, loss separation approach and empirical models [8]. The hysteresis model was introduced in [134]-[136] and the core loss separation approach divides the total core loss into three parts, which are static hysteresis loss, eddy current loss and excess eddy current loss [137]. In empirical models, the core loss is fitted based on abundant measurement results which might be provided by the manufacturer.

The most popular used method to calculate the core loss is the Steinmetz equation [138], in which three constants (K_c , α , β) for each core material could be found by the data obtained from measurements. The expression of the Steinmetz equation is given by

$$P_{fe} = K_c f^\alpha B_{max}^\beta, \quad (1.8)$$

where P_{fe} is the time-average core loss per unit volume, B_{max} is the peak value of the flux density with sinusoidal excitation at the frequency f .

However, [139] found that the core loss with non-sinusoidal excitations can result in a far larger value compared to the Steinmetz equation. For the purpose of adapting the Steinmetz equation with a wide variety of excitations, lots of efforts have been carried out to improve the method including modified Steinmetz expression [140], generalized Steinmetz expression (GSE) [141], improved GSE (iGSE) [142], improved iGSE (i^2 GSE) [143], natural Steinmetz expression [144], equivalent elliptical loop [145] and waveform coefficient Steinmetz expression [146].

1.2.3. Leakage Inductance and Stray Capacitance

In magnetic components, such as the transformer, the flux generated by one winding will not completely couple all the other windings and some of these fluxes will leak through the conductors or the air space. The leakage inductance is introduced to represent the imperfect coupling between windings. On one hand, the leakage inductance of the transformer can be used to limit the current changing slope through the switching device, plays the role of the inductive component in the circuit to guarantee the soft switching in the full bridge phase shift converter, and acts as the resonant inductance in resonant converters. On the other hand, the energy stored in the leakage inductance would cause the voltage spikes on the main switches which may damage the components, and it could also affect the unpredictable operation of the circuit because the value of leakage inductance is normally difficult to estimate accurately. It is extremely significant to obtain an accurate value of the leakage inductance at high frequency.

The leakage inductance of the transformer can be derived from the stored energy inside the window area of the magnetic core with excitations of the primary winding and the secondary winding cancelling each other. The magneto-motive force (MMF) and the magnetic intensity are normally associated to get the leakage energy [147]. In practice, a more accurate method will be with the help of FEA simulations.

In the case of higher operating frequency, the current distribution in the windings will change and the corresponding stored leakage energy will vary. In [148], the detailed calculation methodology for the leakage inductance in the transformer with a toroidal core was presented. As proposed in Dowell's paper [86], the decreased leakage

inductance due to high frequencies for 1-D calculation for the structure shown in Fig. 1.7 can be estimated by

$$\frac{L_{1kac}}{L_{1kdc}} = \frac{3}{2p^2\Delta} \left[\frac{\sinh 2\Delta - \sin 2\Delta}{\cosh 2\Delta - \cos 2\Delta} + \frac{2(p^2 - 1)}{3} \frac{\sinh \Delta + \sin \Delta}{\cosh \Delta + \cos \Delta} \right]. \quad (1.9)$$

Furthermore, the capacitance in transformer or inductor windings is of interest in the switching converters because the capacitance may provide a short path to a step change in voltage which can frequently appear. Meanwhile, the stray capacitance could resonate with the inductance and it will give rise to the unexpected resonant operation stage in the circuit.

A review of calculating the stray capacitance in transformer windings has been done in [149]. The stray capacitance calculations are basically based on the static layer-to-layer capacitance and different models can be used to get the stray capacitance for different windings arrangements including the parallel-plate capacitor model, the cylindrical capacitor model and several analytic capacitance models for orthogonal windings and orthocyclic windings [150]-[152]. For some special winding structures, i.e., the planar windings, the analysis of the stray capacitance was presented in [153].

1.3 Planar Magnetics and Design Considerations

The high frequency DC-DC converter incorporating planar magnetics is the trend for higher power density and convenient manufacturing. However, new design issues including calculation of the winding loss and leakage inductance will appear in planar magnetics. The current distribution in the planar winding is different from the traditional winding because the width of the planar winding is generally much larger than the thickness of the conductor. In particular, the planar magnetics applied in the LLC resonant converter has an air gap in the magnetic core and the design must take this into account.

1.3.1. Introduction of Planar Magnetic Technologies

Basically, there are five main advantages for employing planar magnetics including:

Low profile The height of the planar component is lower than the wire-wound component due to the fabrication process [8].

Automatic fabrication The manufacturing process of the planar magnetics is simplified as the complex wire wrapping and bobbin mounting are avoided. Typically, the planar winding fabricated by PCB technology can be merged into the main circuit manufacturing process.

Better thermal characteristic The surface area of the planar core is much bigger and it can be easier to transfer the heating generated by the winding loss and core loss. In addition, other heat-dissipating methods including the sink and forced cooling are easily realized for planar cores.

Predictable parasitic parameters In wire-wound components, the windings are varying in their shapes and routings. The parasitic parameters including the leakage inductance and stray capacitance are extremely difficult to predict, and on the contrary, the precise and consistent planar windings bring in the possibility to obtain relatively accurate calculations. This advantage is especially important for high frequency applications.

Easy interleaving Interleaving windings can be implemented if the multi-layer PCB is incorporated.

The main disadvantages of planar magnetics are the relatively larger footprint compared to the conventional magnetics and the number of turns in the planar magnetics will be limited by the cost of the fabrications.

The fabrication technologies may be generally classified as PCB, copper foil, thick film, low temperature co-fired ceramic (LTCC) and thin film [84]. PCB and copper foil are normally applied in relatively high power applications [154]-[157]. The other three technologies are generally used to manufacture miniature components which may applied in low power and extremely high frequency applications, i.e., power supply on chip (PwrSoC).

The printed circuit board (PCB) is frequently employed to incorporate the planar windings including the multi-layer PCB, the flexible PCB and the hybrid of PCB and copper foils. Integrated PCB magnetics can also be applied and achieved by integrating the core and windings so that the magnetic core is formed during the PCB process. The disadvantage of the PCB is that the window utilization factor is quite low due to thick insulation material.

In the interest of improving current handling performance, copper foil is normally introduced for planar windings. After the proper pattern is cut by laser technology, the kapton tape should be attached to both sides of the foil to make sure the windings are well isolated. External connections will be needed to achieve layers interconnections.

Thick film can integrate passive RLC components and printed conductor through-holes in alumina substrates have been developed. This allows double-sides solenoidal-type inductors to be manufactured, with the substrate acting as the interlayer dielectric [84], [158]. A screen printing process is employed to fabricate thick film circuits. In the process of LTCC technology, all layers of the circuit including the conductors and isolations are treated separately, then they are fired together at the proper temperature. Nowadays, the trend towards PwrSoC prompts the applications of thin film technology [159]. The typical applicable power range is lower than 1 W and the frequency is higher than 10 MHz.

For planar magnetics in power supply applications, the best choices of fabrication technologies are PCB and copper foils when the cost and the current handling capacity are considered.

1.3.2. Planar Magnetics Design Considerations

During the design of planar magnetics, the same approaches as the wire-wound components described in Section 1.2 should be fully considered. Besides, there will be other particular design issues in planar magnetics [160], [161].

Planar Core and Windings On the survey of commercial planar cores manufactured, typical planar cores include planar EE or EI cores, planar ER cores and other low

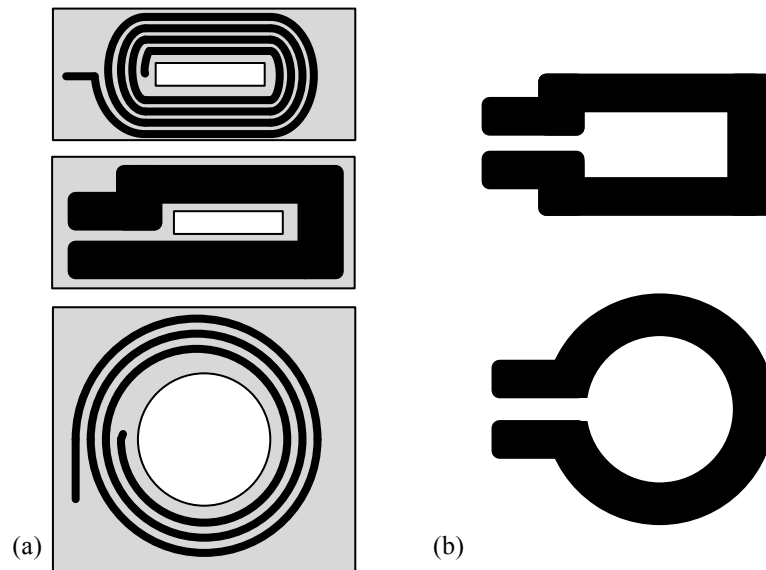


Fig. 1.10 Typical patterns of planar windings (a) PCB windings; (b) copper foils

profile versions of standard core such as RM, PQ and pot cores. The widely used EE and ER planar cores made by Ferroxcube [162] and TDK EPCOS [163] are listed in Appendix A. In particular, the high performance planar core can be achieved by custom cores [164]. The centre leg of the cores are mostly rectangular and circular. The shape of the centre leg will affect the arrangement of planar windings. It must be pointed out that the planar component may have no magnetic core and only planar windings are involved for some specific applications with extremely high operation frequency.

With the different types of cores, planar windings may have different pattern made by PCB tracks or copper foils, as shown in Fig. 1.10. Basically, in PCB windings it is easy to implement more turns than copper foil, and on the contrary, the thickness of copper foil can be larger. Besides, there are some distinguishing planar windings reported such as the planar litz wire [165] and the planar winding for stacked I-cores [166], as shown in Fig. 1.11.

For the first step in the design for planar magnetics, the proper planar core should be selected and the size of the core is determined based on the proper design procedure.

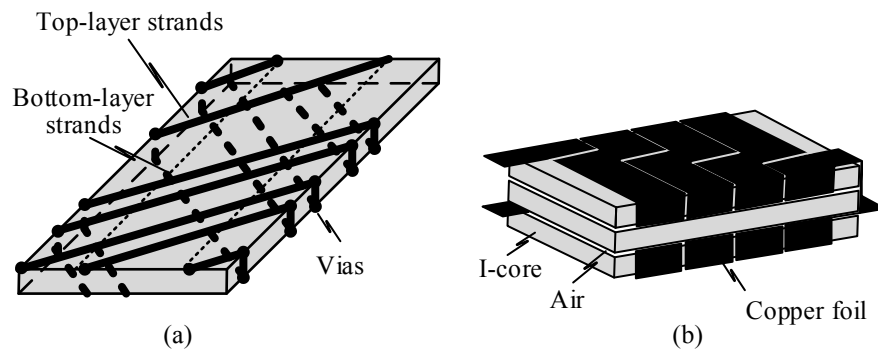


Fig. 1.11 Distinguished planar windings (a) planar litz wire; (b) planar winding for stacked I-cores

High Frequency Planar Winding Loss As the assembly method of planar windings differs from the traditional wire-wound windings, the high frequency winding loss needs further investigation.

Dowell's equation is widely used to calculate the high frequency winding loss for magnetic components with wire wound or perpendicular copper foil windings. For the planar windings implemented with small wires or litz wire, the approximate 1-D calculation method or the improved methods mentioned in Section 1.1 can be extended to calculate the winding loss. However, for planar windings fabricated by PCB or copper foils, the ratio of width to height of conductors could be large, resulting in quite complex current distributions. As the window utilization of the conductor is relatively small for planar components, the 2-D edge effect in the winding loss will be increased with the thick conductor. These issues must be treated seriously during the design of planar magnetics.

In [167]-[169], uniform current distribution for cylindered plate windings was considered. Based on the proposed current distribution at lower frequency, Maxwell equations were solved. The precise formulas for winding loss, self-inductance and mutual inductance for planar magnetics with three magnetic core structures, air core, substrate core and sandwich core were presented. The FEA was employed to obtain the accurate winding loss of planar structures in [170]-[172]. The detailed lumped modelling for planar magnetics based on "1-D" and "Magneto-Quasi-Static" assumptions has been proposed in [173].

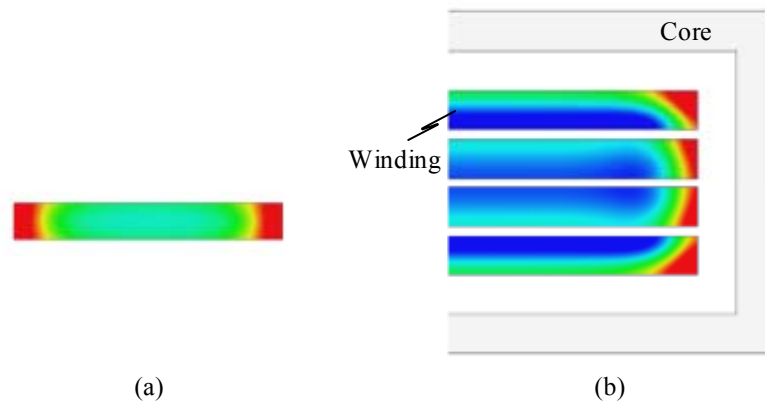


Fig. 1.12 Edge effect on winding loss: (a) a thick conductive strip in free space; (b) multi-layer windings away from the core

In order to handle large current in planar magnetics, the parallel connection of multi-layer conductors is generally applied. The current in one layer would be different from the other due to the high frequency AC resistances of each layer. The extra winding loss caused by the circulating current needs further consideration [174]-[176].

Another issue for the winding loss in planar magnetics is called the “Edge Effect” if the edge of the conductor is away from the magnetic core. Fig. 1.12 shows the current distribution for a thick conductive strip in free space and the multi-layer windings away from the core. Without regard to the skin effect and the proximity effect, the edge effect is due to the magnetic field at the end of the conductor which is perpendicular to the conductor. In [177], the edge effect was solved by approximate equivalent elliptical cross-sections for a strip conductor. Based on the estimated DC boundary condition of each conductor, an improved 2-D method was proposed to calculate the high frequency winding loss for small winding porosity factor in [178]. The research in [179] pointed out the edge effect can be ignored if the distance between the conductor and the core is smaller than the thickness of the conductor.

Leakage Inductance Calculation and Design One of the advantages of planar magnetics is that the leakage inductance can be predicted precisely. The leakage inductance based on 1-D assumption was carried out in [147] by calculating the leakage energy. Compared to the conventional wire wound transformer, the leakage inductance of planar transformer is larger because the longer mean turn length (MLT)

of planar windings appears [180]. The interleaved winding technology is commonly used to minimize the leakage inductance in planar magnetics, which can also reduce the winding loss at the same time.

However, for cases of replacing the discrete inductor by the leakage inductance of the transformer, large leakage inductance is required. The best way to increase the leakage inductance is inserting a magnetic shunt, a lower permeability magnetic material, inside the window area to provide a magnetic flux path [15], [181]. The associated analysis of the leakage inductance for the transformer cooperating the magnetic shunt is given in [182].

1.3.3. Planar Transformers for LLC Resonant Converters

According to the summary and conclusion in the Section 1.1, the LLC resonant converter shows great promise in high frequency DC-DC converters for power supplies. Combining the advantages of planar magnetics, the idea of replacing the conventional wire wound components is very appealing.

The development of an electromagnetic model for a resonant integrated spiral planar power passive (ISP³) structure was presented by Wyk in [15], [183] and [184]. The series resonant ISP³ LLCT structure is shown in Fig. 1.13(a). The structure consists of an LC series resonant structure as primary winding (realizing the required series capacitance). A standard planar spiral winding is separated from the primary by a low permeability “leakage layer” that shunts some of the flux between the windings and thereby reducing the coupling between windings, thus realizing (most of) the leakage (or resonant) inductance.

Cove described the methodology for determining parametric models for leakage and magnetizing inductance, inter and intra-winding capacitances, and winding resistance of small planar transformers using a variety of winding arrangements based on the PCB planar transformer structure shown in Fig. 1.13(b), and the planar Ferroxcube ER18/3.2/10-3F3 core set was selected [170], [185]. The models were employed to shape the winding design to control parasitic elements in order to optimize soft-switching and resonant converters.

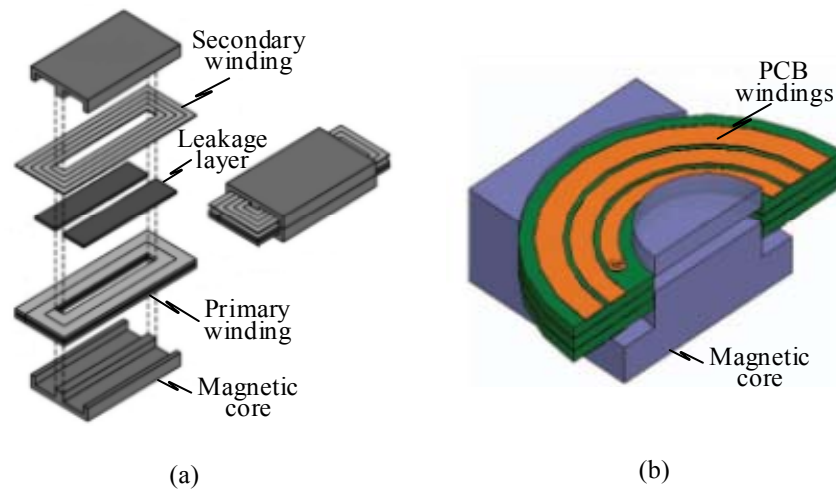


Fig. 1.13 Integrated planar transformers for LLC resonant converters: (a) Wyk's ISP³ LLCT structure; (b) Cove's PCB windings with ER18/3.2/10-3F3 core

D. Kim proposed the structure of a slim-type transformer composed of copper wire on the bobbin as the primary winding and PCB winding on the outer layer as the secondary winding shown in Fig. 1.14(a) [186]. In the slim-type transformer, the insulation between the primary and the secondary winding uses a considerable portion of the window area when the windings are stacked. However, when the primary and secondary windings are positioned inside and outside, respectively, the volume of insulation between them can be greatly decreased. The saved area can contribute to the conductive cross-sectional area, and the conduction loss can be reduced. Also, the utilization of the primary winding is easier due to the use of the bobbin. The planar transformer proposed by Eun-Soo Kim shown in Fig. 1.14(b) can increase the leakage inductance without inserting a leakage layer or I shaped magnetic core [187], [188]. The EE core of the transformer and EE core of the inductor side are combined into one core. In [189], Fu proposed several novel concepts to reveal the essence of the transformer design, as shown in Fig. 1.14(c). In order to minimize the winding loss, several winding structures were proposed and compared. Wang used the ferrite mosaic structured core which is finished after cutting, laminating and assembling the ferrite mosaics. It consists of a supporting plate and ferrite units with small size stuck on it, as shown in Fig. 1.14(d) [190]. As the centralized gap was distributed into several small gaps, the fringing field caused by adjacent gaps was avoided. The core loss was also be reduced.

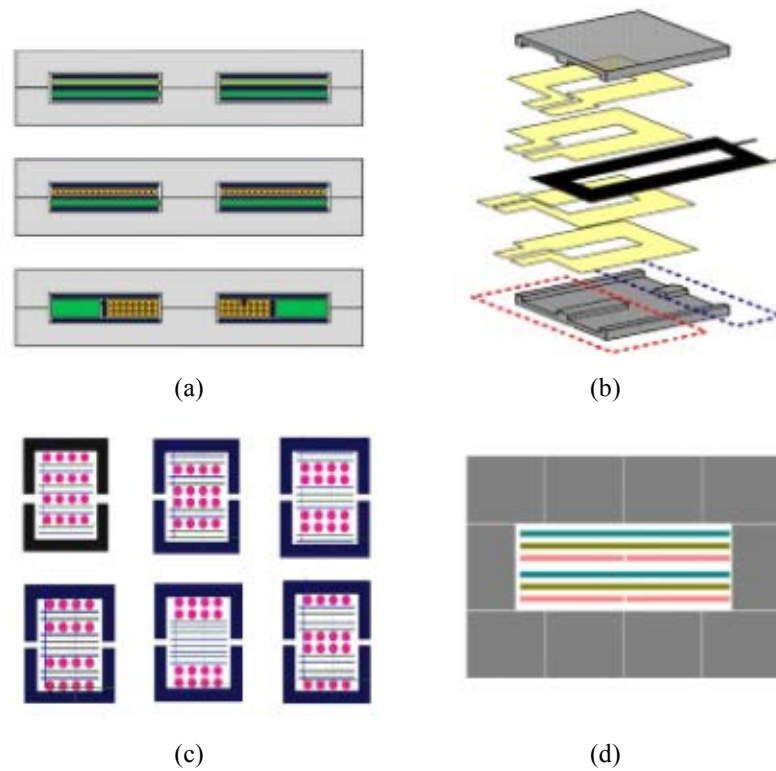


Fig. 1.14 Planar transformers for LLC resonant converters: (a) D. Kim's structure; (b) Eun-Soo Kim's structure; (c) Fu's structure; (d) Wang's structure

Comparing and summarizing these proposed planar transformer structures, conclusions can be drawn, based on the core types, the primary and secondary winding implementations as well as the gap arrangement, as shown in Table 1.3.

1.4 Objectives and Outline of the Thesis

Based on the literature review, the LLC resonant converter stands out due to its remarkable advantages for the power supply applications. The parameters including the resonant components and the dead time will affect the circuit operation. Thus, the design methodology for the main parameters in the LLC resonant converter should be investigated.

On the other hand, the magnetic components, especially the transformer in the LLC resonant converter, play significant roles in the main circuit. The design of the transformer which has an air gap in the magnetic core to implement the required magnetizing inductance will bring new issues. The existing design methodology for

TABLE 1.3 SUMMARY OF PLANAR TRANSFORMERS OF LLC RESONANT CONVERTERS

Structure	Core	Primary winding	Secondary winding	Air gap
Wyk's LLCT structure	Planar EE	Copper spiral	Copper spiral	None
Cove's structure	Planar ER	PCB spiral	PCB spiral	Lumped
D. Kim's structure	Planar EE	Copper wire	PCB	Lumped
Eun-Soo Kim's structure	Novel Planar EE	Copper wire	Copper foil	Lumped
Fu's structure	Planar EE	Litz wire	PCB	Lumped
Wang's structure	Planar EE	PCB	PCB	Distributed

the conventional transformer cannot be applied to design the gapped transformer because the magnetizing inductance is integrated in the transformer. The operation principle of the gapped transformer needs to be investigated and proper design procedures need to be developed.

Lots of efforts have been carried out to evaluate the high frequency winding loss according to the literature review, the leakage inductance of the high frequency transformer were rarely mentioned. It is significant to obtain the method of calculating the leakage inductance at high operating frequency as it will affect the circuit operation, especially the LLC resonant converter.

For applying the planar transformer in the LLC resonant converter, different structures of planar transformers were carried out in the literature. However, the detailed design method and optimization strategy were not covered. The comprehensive modelling of the planar magnetics should be carried out. The high frequency winding loss and the leakage inductance of the planar transformer are the main design considerations. The planar transformer employed in the LLC resonant converter, the air gap and the phase shift between the primary current and the secondary current will affect the design result. Furthermore, the integrated planar transformer was applied in the LLC resonant converter in the literature. Nevertheless, the modelling for the leakage inductance in the integrated planar transformer was not presented.

According to the literature review, the objectives of this thesis may be summarised as follows:

- (1) To develop a design methodology for the selections of the main parameters in the LLC resonant converter including the resonant inductance, the resonant capacitance and the magnetizing inductance;
- (2) To analyse the operation of the gapped transformer applied in the LLC resonant converter and propose the design procedure based on the specifications;
- (3) To illustrate the calculation methodology for the winding loss of the planar transformer fabricated by PCB windings or copper foils and investigate the stray capacitances of the planar transformers;
- (4) To discuss the phase shift effect in the winding loss of the planar transformer and illustrate the optimization design methodology of the planar transformer applied to the LLC resonant converter.

In Chapter 2, the design methodology for the parameters in LLC resonant converters will be described. Based on the operation analysis and calculation of the circuit, the main power losses of the LLC resonant converter will be obtained. Combining the efficiency, the no load operation and the input voltage range requirements, the trade-off design method will be presented.

In Chapter 3, the operation and design procedure for the conventional gapped transformer in the LLC resonant converter will be described. The design example and results for the transformer applied in the LLC resonant converter will be discussed.

Chapter 4 mainly focuses on the leakage inductance calculation for the transformer operated at high frequency and the stray capacitances. The leakage inductances for different interleaving structures will be analysed.

Chapter 5 focuses on the modelling of the planar transformer. The planar cores and high frequency winding loss calculations will be illustrated. In addition, the

calculation method for the leakage inductance of the planar transformer with a magnetic shunt will be discussed.

Due to the fact that the air gap may need to be placed in the planar core and the currents through the primary and secondary windings are not in phase, the issues relating to the design of the planar transformer in LLC resonant converters and the optimized design results for the gapped planar transformer will be studied in Chapter 6. The planar transformer applied in a 240 W LLC resonant converter has been fabricated and the experimental results will be presented.

Chapter 7 presents the conclusions of the thesis and describes possible work in this area.

In summary, the novelties of this thesis include:

- A new design methodology for the main parameters in the LLC resonant converter including the resonant inductance, magnetizing inductance, resonant capacitance and dead time has been proposed with the efficiency, zero voltage switching, input voltage variation and light load operation taken into account. A full analysis of the losses in the LLC resonant converter will be included. (published in IEEE APEC 2013)
- A new design methodology for the conventional and planar gapped transformer applied in the resonant converter will be presented, taking into account the role of the magnetizing inductance and the gap in the transformer. (published in IEEE Transactions on Industry Applications)
- Leakage inductance will be investigated for planar integrated transformers including the role of a magnetic shunt to increase the leakage inductance and to provide consistent values of leakage inductance. (published in IEEE Transactions on Industry Applications)

1.5 List of Publications

- [1] C. Zhu, D. Xu, L. Zhang and **J. Zhang**, *Transformers and Inductors for Power Electronics – Theory, Design and Applications (Chinese Translation Version)*, Beijing: China Machine Press, 2014.
- [2] **J. Zhang**, Z. Ouyang, M. C. Duffy, M. A. E. Andersen and W. G. Hurley, “Leakage inductance calculation for planar transformers with a magnetic shunt,” *IEEE Trans. Ind. Appl.*, vol. 50, no. 6, pp. 4107-4112, Nov.-Dec. 2014.
- [3] **J. Zhang**, W. G. Hurley and W. H. Wolfle, “Gapped transformer design methodology and implementation for LLC resonant converters,” *IEEE Trans. Ind. Appl.*, 2015. (Under minor modifications)
- [4] Z. Ouyang, **J. Zhang** and W. G. Hurley, “Calculation of leakage inductance for high frequency transformers,” *IEEE Trans. Power Electron.*, PP(99):1. (In press)
- [5] C. Feeney, **J. Zhang** and M. Duffy, “Ac winding loss of phase-shifted coupled windings,” *IEEE Trans. Power Electron.*, 2015. (In press)
- [6] W. G. Hurley, M. C. Duffy, **J. Zhang**, I. Lope, B. Kunz and W. H. Wölfle, “A unified approach to the calculation of self- and mutual- inductance for coaxial coils in air,” *IEEE Trans. Power Electron.*, 2015. (In press)
- [7] **J. Zhang**, W. G. Hurley, W. H. Wolfle and M. C. Duffy, “Optimized design of LLC resonant converters incorporating planar magnetics,” in *Proc. IEEE Appl. Power Electron. Conf. Expo. (APEC)*, 2013, pp. 1683-1688.
- [8] **J. Zhang**, Z. Ouyang, M. C. Duffy, M. A. E. Andersen and W. G. Hurley, “Leakage inductance calculation for planar transformers with a magnetic shunt,” in *Proc. IEEE Energy Convers. Congr. Expo. (ECCE)*, 2013, pp. 643-648.
- [9] **J. Zhang**, W. G. Hurley and W. H. Wolfle, “Gapped transformer design methodology and implementation for LLC resonant converters,” in *Proc. IEEE Appl. Power Electron. Conf. Expo. (APEC)*, 2014, pp. 726-731.
- [10] **J. Zhang**, W. G. Hurley and W. H. Wolfle, “Design of the planar transformer in llc resonant converters for micro-grid applications,” in *Proc. IEEE Power Electron. Distributed Generation Systems (PEDG)*, 2014, pp. 1-7.
- [11] I. Lope, W. G. Hurley and **J. Zhang**, “Common-mode choke design considerations applied to domestic induction heating,” in *Proc. Int. Universities' Power Eng. Conf. (UPEC)*, 2013, pp. 1-5.

2

Design Parameters in LLC Resonant Converters

In this chapter, the design methodology of the main parameters in LLC resonant converters, including selection of the resonant inductance, the resonant capacitance, the magnetizing inductance and the dead-time of the drive signals for the main switches in the bridge will be presented. Based on the analysis of the circuit operation, the main power losses of the LLC resonant converter will be calculated. In an attempt to meet the requirements of constant output, the varying input voltage and the no load operation, the trade-off design for the LLC resonant converter is introduced in this chapter. Finally, a 105 kHz, 240 W LLC resonant converter is built to evaluate the methods as described.

2.1 Operation of LLC Resonant Converters

The typical topology of the half bridge LLC resonant converter with synchronous rectifier is shown in Fig. 2.1. The synchronous rectifier is employed to overcome the shortage of discrete diodes taking advantage of low conduction loss. If the diodes were used to implement the full wave rectifier, the large voltage drop in the diodes will cause large power loss in the secondary side because the current through secondary windings is high. In the LLC resonant converter, the resonant tank consists of three components, L_r , C_r and L_m . In practice, L_r and C_r are discrete components and L_m is

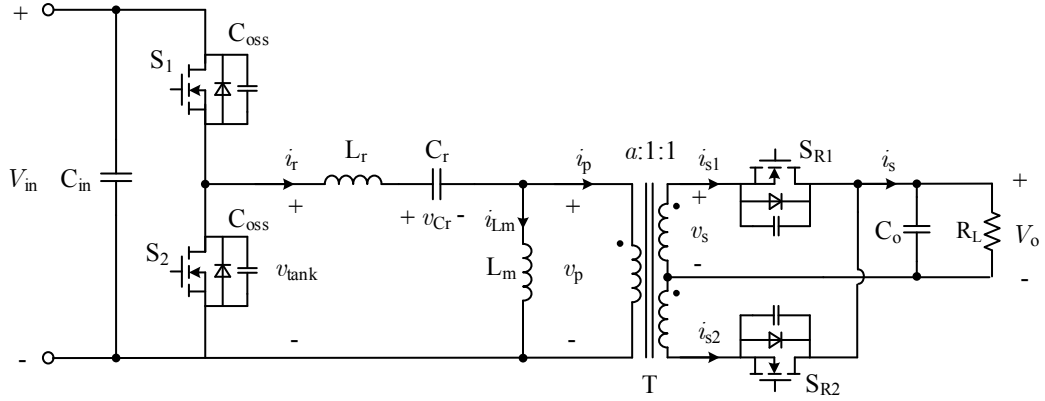


Fig. 2.1 Topology of half bridge LLC resonant converter with the synchronous rectifier

the magnetizing inductor of the isolating transformer T. The pulse frequency modulation (PFM) controller is generally used in the LLC resonant converter and the duty cycle in each switching period is almost 0.5. Due to the complementary conduction of the two main switches (S_1 and S_2) in the bridge, the output voltage of the bridge, which is the same as the voltage supplied to the resonant tank v_{tank} , is a square waveform if the dead-time is ignored. The isolation transformer has two centre-tapped secondary windings and the full-wave rectifier is established with two controlled switches S_{R1} and S_{R2} . In the operation process of the circuit, different components in the resonant tank will achieve resonance and two associated resonant frequencies are defined to simplify the analysis which are given by

$$f_r = \frac{1}{2\pi\sqrt{L_r C_r}}, \quad f_{rm} = \frac{1}{2\pi\sqrt{(L_r + L_m) C_r}}. \quad (2.1)$$

The corresponding periods are represented by T_r and T_{rm} , respectively. With proper assumptions, the resonant current i_r may be treated as approximately pure sinusoidal. Thus, the fundamental frequency analysis (FFA) can be introduced to examine the characteristics of LLC resonant converters and the detailed investigation is presented in Appendix B. Depending on the switching frequency f_s , different operation modes are possible for $f_s \leq f_{rm}$, $f_{rm} < f_s \leq f_r$ or $f_s > f_r$. Referring to previous work [191], the condition of switching frequency $f_{rm} < f_s \leq f_r$ is chosen because ZVS is possible under all load conditions. In the following description, f_s is set in this range.

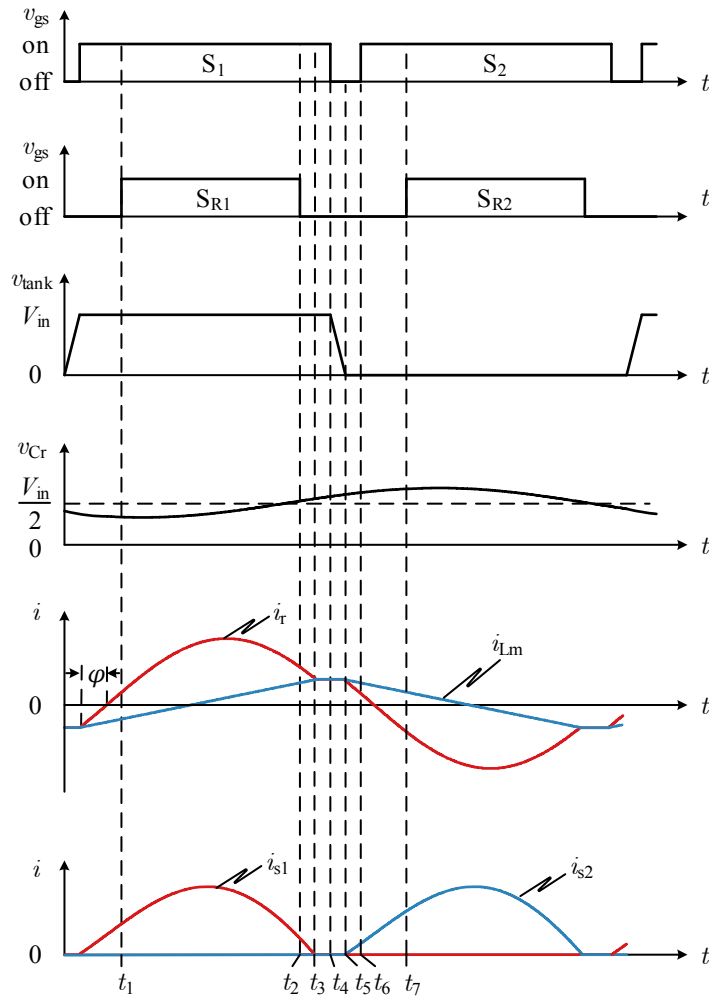
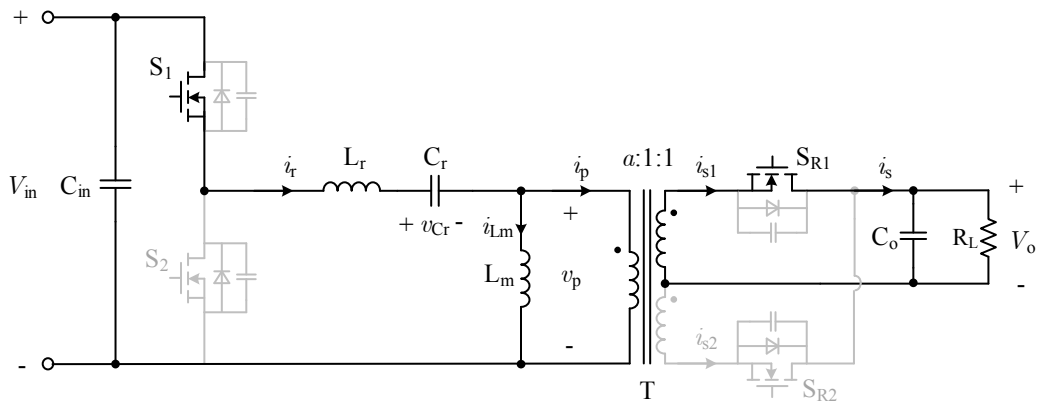


Fig. 2.2 Typical waveforms of LLC resonant converters

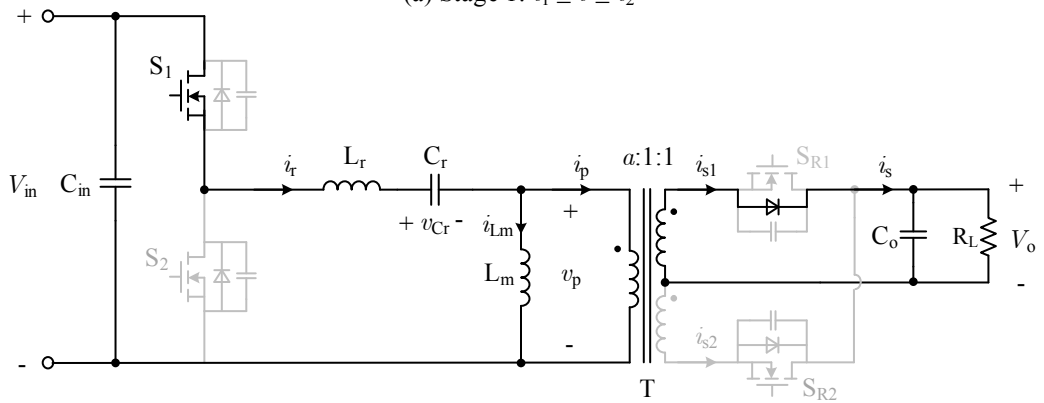
2.1.1 Steady State Waveforms of LLC Resonant Converters

Basically, there are six main switching stages of LLC resonant converters in steady state during half of the total switching period. The typical waveforms and highlighted current paths for each state are shown in Fig. 2.2 and Fig. 2.3. Operation stages in half switching period ($t_1 \leq t \leq t_7$) are introduced as follows.

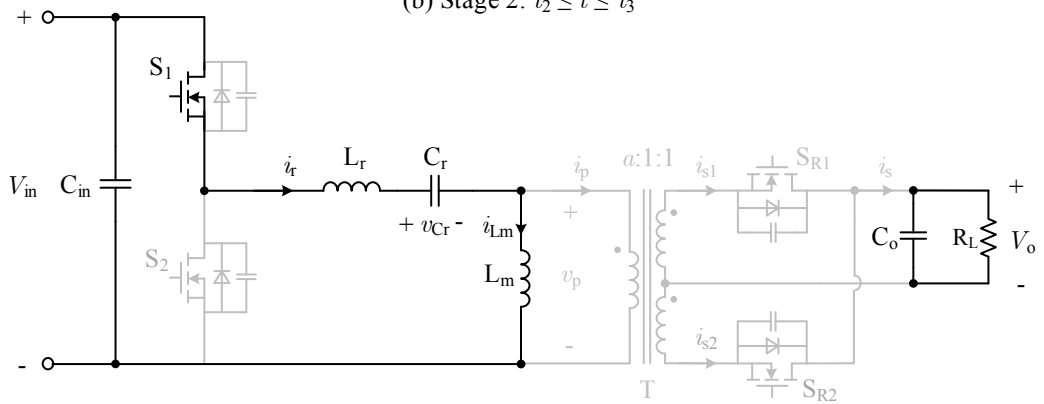
Stage 1 ($t_1 \leq t \leq t_2$, Fig. 2.3(a)) Before time t_1 , the resonant current flows through S_1 and the resonant tank in the primary side. The switch S_2 is off. In the synchronous rectifier, the body diode in S_{R1} conducts the secondary current i_{s1} . At t_1 ,



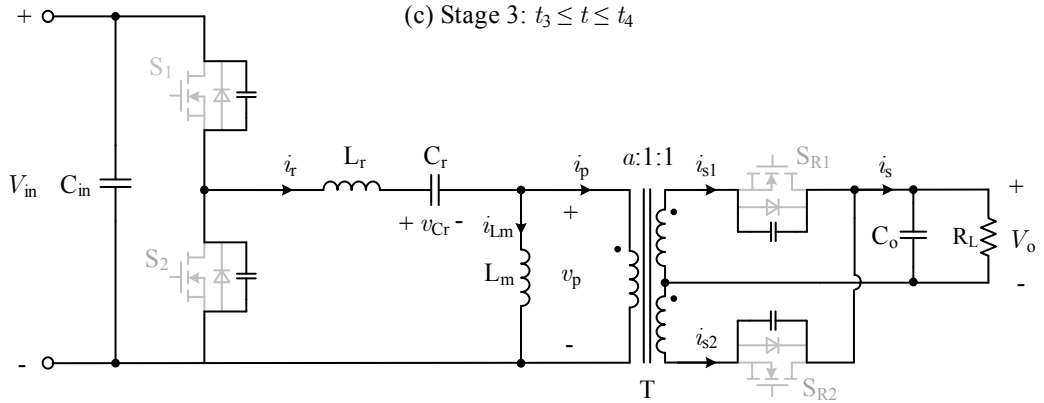
(a) Stage 1: $t_1 \leq t \leq t_2$



(b) Stage 2: $t_2 \leq t \leq t_3$



(c) Stage 3: $t_3 \leq t \leq t_4$



(d) Stage 4: $t_4 \leq t \leq t_5$

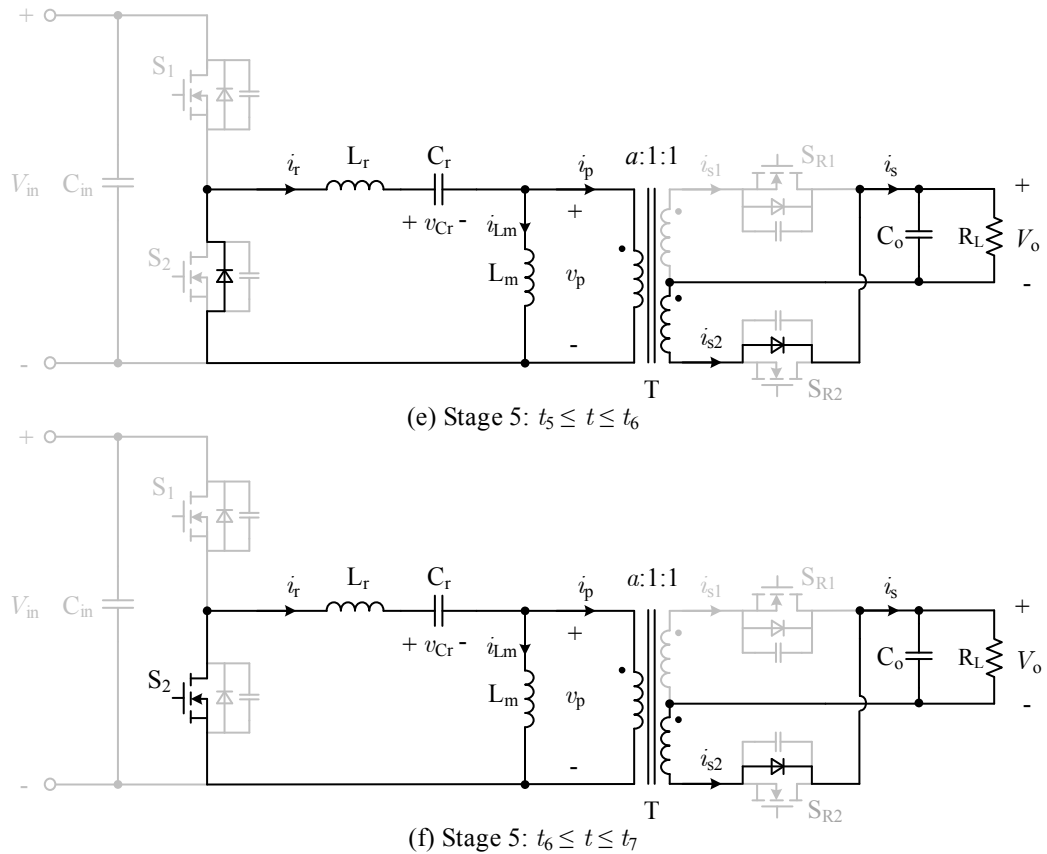


Fig. 2.3 Switching states with current path highlighted for the LLC resonant converter with the synchronous rectifier

S_{R1} is turned on and i_{s1} is transferred from the body diode to S_{R1} . The voltage of the magnetizing inductor L_m is constant which is directly related to the output voltage. The magnetizing current i_{L_m} increases linearly. On the other hand, L_r and C_r are in resonance, resulting in i_r as a sinusoidal waveform (the switching frequency is selected close to the resonant frequency). The secondary current is in direct proportion to $(i_r - i_{L_m})$.

Stage 2 ($t_2 \leq t \leq t_3$, Fig. 2.3(b)) S_{R1} is turned off at t_2 . The body diode in S_{R1} will be forward biased with current i_{s1} . The operation of the primary side is the same as in Stage 1. This stage will end when i_r equals i_{L_m} .

Stage 3 ($t_3 \leq t \leq t_4$, Fig. 2.3(c)) At t_3 , i_r is resonating back to the quality of i_{L_m} . At this moment, the current through the primary winding of the ideal transformer,

represented by i_p in Fig. 2.2, equals to zero. It will make the body diode of S_{R1} naturally turned-off. In this stage, L_r , C_r and L_m build up the resonant tank. Generally, the inductance of L_m will be much bigger than L_r , thus i_r is taken to be constant during this stage.

Stage 4 ($t_4 \leq t \leq t_5$, Fig. 2.3(d)) The switch S_1 is turned off at time t_4 and i_r will charge the output capacitor of S_1 and discharge the output capacitor of S_2 . Meanwhile, the output capacitors of S_{R1} and S_{R2} will be charging and discharging, respectively.

Stage 5 ($t_5 \leq t \leq t_6$, Fig. 2.3(e)) By the end of Stage 4, at time t_5 , capacitors in two switches in the half bridge complete the charging and discharging processes. The voltage across S_2 decreases to zero and the body diode in S_2 is naturally forward biased. In this situation, the switch S_2 can achieve ZVS and the turn-on loss will be eliminated. The body diode of S_{R2} will conduct.

Stage 6 ($t_6 \leq t \leq t_7$, Fig. 2.3(f)) At time t_6 , S_2 will be turned on with ZVS. At the end of this stage, S_{R2} is turned on and i_{s2} will transfer from the body diode to S_{R2} .

In practical, the duration time from t_3 to t_6 is distinctly short compared to the switching period. The waveform of i_r is approximately sinusoidal and the fundamental frequency analysis (FFA) methodology can be applied to the model and the main characteristics of the LLC resonant converter may be calculated.

2.1.2 Fundamental Frequency Analysis

The design of LLC resonant converters is challenging because the selection of L_r , C_r , L_m and the dead-time of the driving signals for S_1 and S_2 (represented by t_d) are interdependent and can affect the operation and performance of the converter. Consequently, it is necessary to investigate relations between the characteristic of LLC resonant converters and these main parameters. In order to carry on the quantitative analysis, FFA is introduced. The detailed analysis and derivations are listed in

Appendix B. The key results, which would be applied during the design procedure, are presented in follows.

The DC voltage gain of the LLC resonant converter is given by

$$M = \frac{V_o}{V_{in}} = \frac{1}{2a \sqrt{\left[1 + \frac{1}{k} \left(1 - \frac{1}{f_n^2}\right)\right]^2 + \left[Q \left(f_n - \frac{1}{f_n}\right)\right]^2}}, \quad (2.2)$$

with

$$f_n = \frac{f_s}{f_r}, \quad k = \frac{L_m}{L_r}, \quad Q = \frac{\pi^2}{8a^2 R_L} \sqrt{\frac{L_r}{C_r}}, \quad (2.3)$$

where a represents the turns ratio of the transformer and R_L is the load resistance. In the LLC resonant converter, the switching frequency will vary to maintain the constant output voltage if the input voltage or the load is changing.

For the power loss calculation and semiconductor switches selections, root-mean-square (rms) values and peak values of currents in the resonant tank (i_r), the magnetizing inductor (i_{Lm}) and the secondary winding (i_{s1}) are required. Based on the formulas of currents in the time domain during half of the switching period, shown as (B.35) to (B.40), expressions for peak values and rms values of currents are given by

$$I_{r_pk} = \sqrt{\left(\frac{a V_o T_r}{4L_m}\right)^2 + \left(\frac{\pi I_o T_s}{2a T_r}\right)^2}, \quad I_{r_rms} = \sqrt{\left(1 - \frac{T_r}{2T_s}\right) \left(\frac{a V_o T_r}{4L_m}\right)^2 + \frac{1}{2} \left(\frac{\pi I_o T_s}{2a T_r}\right)^2}, \quad (2.4)$$

$$I_{Lm_pk} = \frac{a V_o T_r}{4L_m}, \quad I_{Lm_rms} = \frac{a V_o T_r}{4L_m} \sqrt{1 - \frac{2T_r}{3T_s}}, \quad (2.5)$$

$$I_{s1_rms} = \sqrt{\frac{(5\pi^2 - 48) a^2 V_o^2 T_r^3}{192\pi^2 L_m^2 T_s} + \frac{\pi^2 I_o^2 T_s}{16T_r}}. \quad (2.6)$$

2.1.3 Parameters Influence Based on k , Q Factors

From the formulas in Section 2.1.2, it is evident that the output voltage and currents in the circuit will be tightly dependent on the selection of L_r , C_r and L_m . Following the definitions of factors k and Q in (2.3), the relations among components in the resonant tank may be linked. In following discussions, the operation of LLC resonant converters, including the output voltage, the switching frequency variation and peak currents, will be investigated with different values of k, Q and load conditions (from 10% rated load to 100% rated load). In order to simplify the explanations, the normalized output voltage will be used

$$V_o^n = \frac{2a V_o}{V_{in}} = \frac{1}{\sqrt{\left[1 + \frac{1}{k} \left(1 - \frac{1}{f_n^2}\right)^2\right] + \left[Q \left(f_n - \frac{1}{f_n}\right)\right]^2}}. \quad (2.7)$$

Under normal operating conditions, the value of V_o^n will be 1. Fig. 2.4 shows the normalized output power characteristics with different values of k . The maximum output voltage is bigger with smaller k . This means that the larger variation range of V_{in} can be accommodated. For different load conditions, the switching frequency variation range will be narrower with smaller k from light load to rated load. Thus, the smaller L_m would be preferred with the determined L_r considering the variations of f_s and V_{in} .

The currents will also be affected by L_m . The smaller L_m will cause bigger rms values of i_r and i_{s1} based on (2.4) and (2.6). Fig. 2.5 presents the relations of I_{r_rms} and I_{s1_rms} versus k for different load conditions. It is indicated from Fig. 2.5(a) that the rms value of i_r is closely related to k . With the smaller k , I_{r_rms} increases and it will cause bigger power loss for components in the primary side. Nevertheless, the rms value of the secondary current is less dependent on the value of k . Consequently, the value of k should be selected by comprehensively considering the switching frequency variation, the input voltage variation and the power loss. All these effects will be included in the trade-off design methodology.

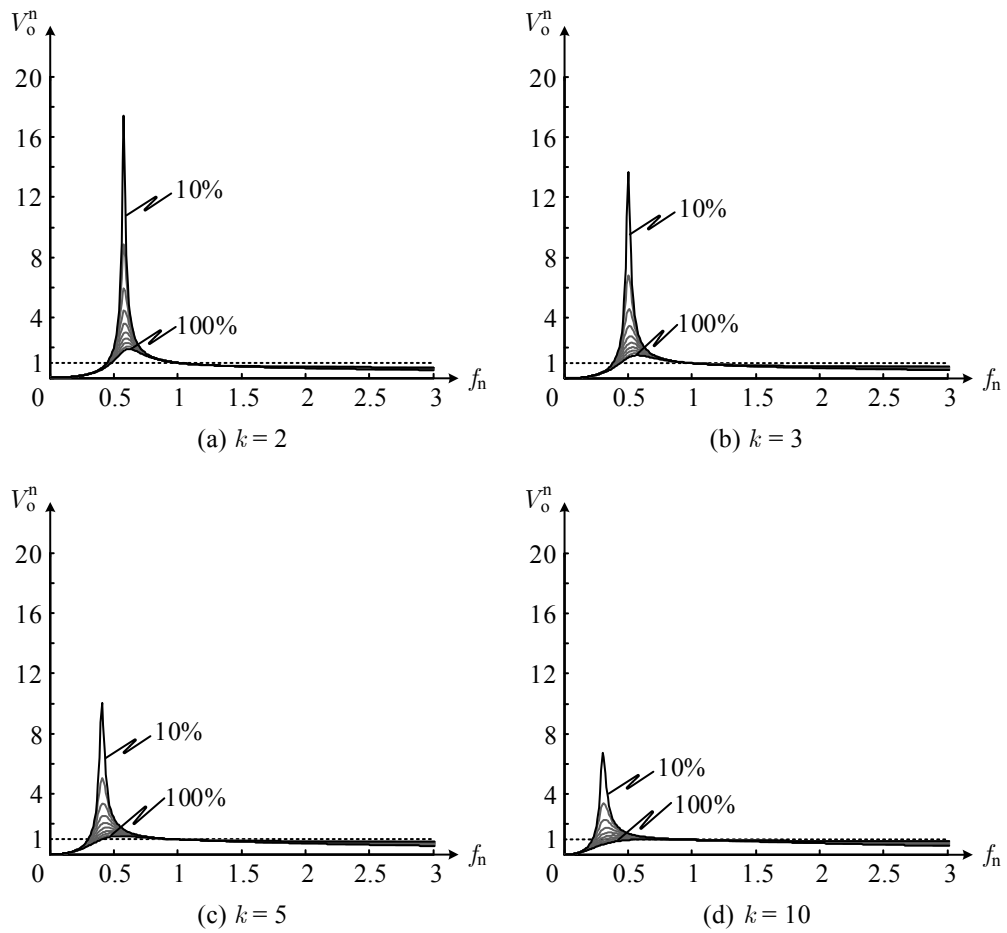
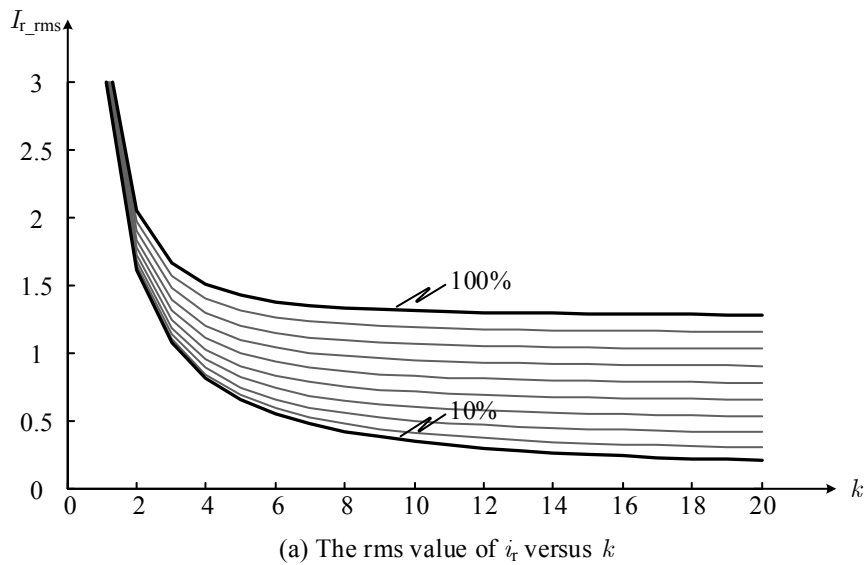


Fig. 2.4 Normalized output voltage versus normalized switching frequency for different values of k with output power from 10% to 100% of rated power



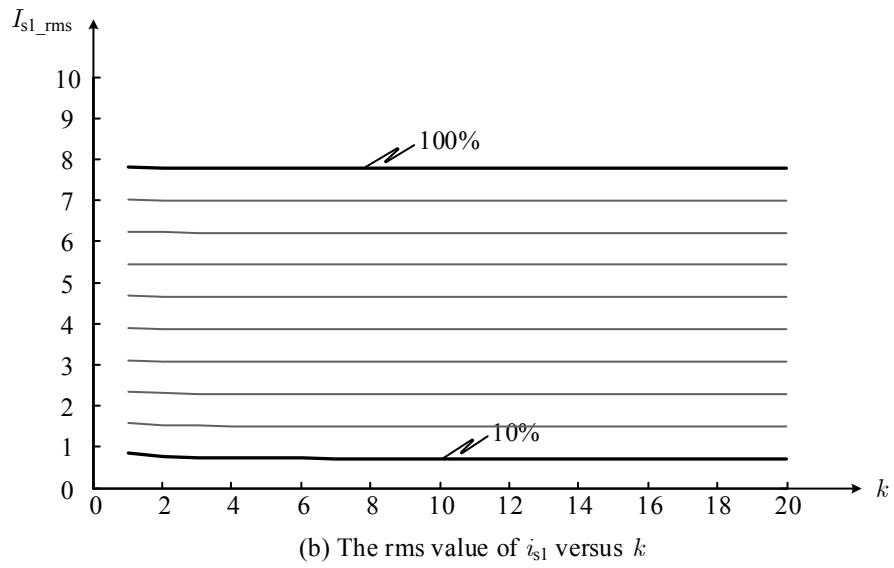


Fig. 2.5 Rms currents through the primary and secondary winding for different values of k

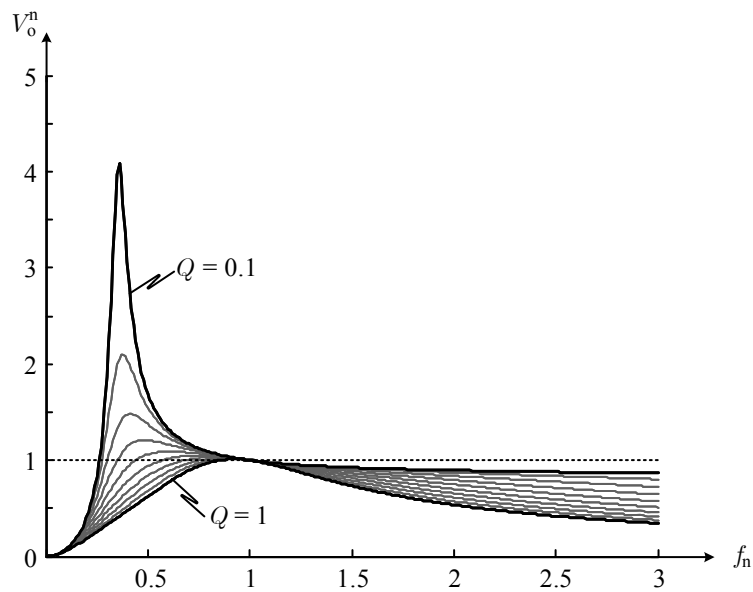


Fig. 2.6 Normalized output voltage versus normalized switching frequency for different values of Q with $k = 7$

The factor Q will also affect the output voltage based on (2.7). The values of V_o^n with fixed $k = 7$ versus different values of Q and f_n are shown in Fig. 2.6. The smaller value of Q will be preferred as the smaller variation of switching frequency and

bigger adaptive input voltage range can both be achieved. Thus, the values of k and Q should be properly determined during the design process.

2.2 Power Loss Modelling of LLC Resonant Converters

The total power losses of the LLC resonant converter contain the loss of the switches including the switches in the half bridge and the switches in the synchronous rectifier, the losses of the magnetic components including the resonant inductor and transformer, and the losses of the capacitors which are neglected here due to their small values for typical power supplies. Next, each component of the power losses will be calculated and the dependent parameters will also be described.

2.2.1 Switches Losses

The turn-on process of S_1 and S_2 is ZVS, therefore, the losses of S_1 and S_2 consist of the conduction loss P_{s_on} , turn-off loss P_{s_off} and driving loss P_{s_dr} . Supposing the conduction resistances of S_1 and S_2 are the same, represented as R_{s_on} , the conduction loss is calculated as

$$P_{s_on} = 2R_{s_on}I_r^2_{rms}. \quad (2.8)$$

Considering that the turn-off time is very short, i_r may be treated as constant during the turn-off process. Actually, i_r is equal to the peak value of i_{Lm} during the turn-off of S_1 and S_2 . We can assume that the current through S_1 is linearly reduced from I_{Lm_pk} to 0 in the turn-off time duration t_f . The turn off current is expressed as

$$i_{s1_off}(t) = I_{Lm_pk} \left(1 - \frac{t}{t_f} \right). \quad (2.9)$$

Supposing the currents through the output capacitors of S_1 and S_2 are identical, the voltage across S_1 during the turn-off process may be obtained by

$$v_{s1_off}(t) = \frac{I_{Lm_pk}}{4C_{oss}t_f} t^2, \quad (2.10)$$

where C_{oss} is the output capacitance of the MOSFET. Thus, the total turn-off loss of the two switches is calculated by

$$P_{s_off} = \frac{I_{Lm_pk}^2 t_f^2 f_s}{24C_{oss}}. \quad (2.11)$$

The driving loss of S₁ and S₂ is obtained from

$$P_{s_dr} = 2Q_{gs}V_{gs}f_s, \quad (2.12)$$

where Q_{gs} is the gate-source charge given by the manufacturer and V_{gs} is the driving voltage.

In the secondary synchronous rectifier, the dominating power loss contains the conduction loss and the driving loss of S_{R1} and S_{R2} if switches are assumed to be controlled perfectly. The calculation for losses of S_{R1} and S_{R2} is

$$P_{sr} = 2R_{sr_on}I_{s1_rms}^2 + 2Q_{gs_sr}V_{gs_sr}f_s, \quad (2.13)$$

where R_{sr_on} , Q_{gs_sr} and V_{gs_sr} represent the conducting resistance, gate-source charge and the driving voltage of S_{R1} and S_{R2}, respectively.

As the conducting time of the body diodes in S_{R1} and S_{R2} is relatively short under proper control strategy for the synchronous rectifier, conducting losses of the body diodes in S_{R1} and S_{R2} are neglected.

2.2.2 Magnetic Components Losses

The losses of the resonant inductor and the transformer, including the magnetic core loss and winding loss, are complex to carry out precisely. The related analysis and design of the transformer in the LLC resonant converter will be further discussed in Chapter 3. Aiming to select proper values of parameters in the main circuit, it is reasonable to simplify the issue at the beginning. The core loss is assumed to be equal to the winding loss which is related to the winding resistance and rms values of currents through windings. Thus, losses of the resonant inductor and the transformer are expressed by

$$P_{Lr} = 2R_{Lr}I_{r_rms}^2, \quad (2.14)$$

$$P_T = 2\left(R_{T_p}I_{r_rms}^2 + 2R_{T_s}I_{s1_rms}^2\right), \quad (2.15)$$

where R_{L_r} , R_{T_p} and R_{T_s} are the resistances of the inductor winding, the primary winding and single secondary winding of the transformer, respectively.

Combining the obtained loss in each part, the total power loss P_{total} can be calculated. With the selected switches and f_s , the power loss under rated output will only depend on T_r and L_m . Actually, the relationship between T_r and L_m can be built up by the requirement of ZVS which will be explained later.

2.3 Trade-off Design of the Main Parameters

In order to achieve ZVS of the primary MOSFETs, the energy stored in the output capacitor of the MOSFET, C_{oss} , should be released totally during the dead-time from t_4 to t_6 shown in Fig. 2.2. Referring to [192], the dead-time should meet the condition

$$t_d \geq \frac{8C_{\text{oss}}V_{\text{in}}L_m}{aV_oT_r}. \quad (2.16)$$

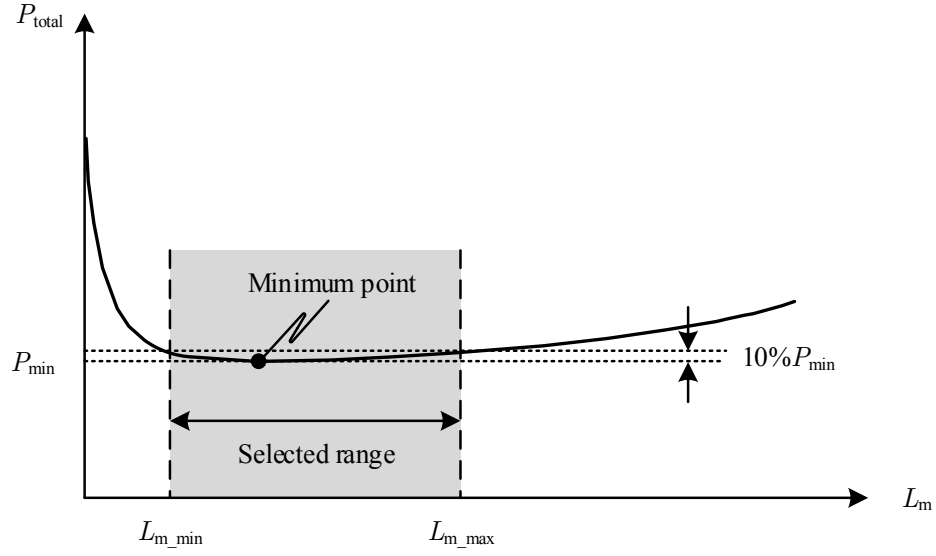
When the LLC resonant converter is operated at rated load, f_s is closed to f_r . Ideally we have

$$T_s = T_r + 2t_d. \quad (2.17)$$

With the critical dead-time selected, the relation between T_r and L_m can be derived by combing (2.16) and (2.17). The results is

$$T_r = \frac{1}{2} \left(T_s + \sqrt{T_s^2 - \frac{64C_{\text{oss}}V_{\text{in}}}{aV_o} L_m} \right). \quad (2.18)$$

Until now, the relation between L_m and T_r has been described and the total power loss can be treated as the function of L_m only. Fig. 2.7 shows the typical curves of P_{total} to L_m . From the result, there is one minimum point in the curve. However, we select the optimized range instead of the minimum point because some parameters in the power losses calculation are approximate. The allowable power loss would be set within 10% of the minimum calculated value. Under the overall considerations, the proper range of L_m can be firstly selected to be $[L_{m_min}, L_{m_max}]$.


 Fig. 2.7 Selection of L_m based on the calculated total power loss

Combing (2.1), (2.3) and (2.18), we have

$$L_m = \frac{4a^2 R_L T_r}{\pi^3} (kQ), \quad (2.19)$$

and

$$kQ = \frac{\pi^3 L_m}{2a^2 R_L} \frac{1}{T_s + \sqrt{T_s^2 - \frac{64C_{oss}V_{in}}{aV_o} L_m}}. \quad (2.20)$$

Thus, the proper set of (k, Q) can be obtained and represented to be $\{(k, Q)\}^A$. The values of k and Q will be further optimized by the following limitations and requirements.

Input Voltage Variation As illustrated in Fig. 2.4 and Fig. 2.5, the voltage gain for the designed LLC resonant converter has a maximum value (represented by M_{max}) which is related to k and Q . With fixed V_{in} and V_o , the proper f_s is adapted through the feedback controller and the value of M is determined. Nevertheless, the input voltage will be changed in practical circuits due to the voltage ripple or variations on loss of the utility voltage. In the hold-up time duration, V_{in} may be reduced to a lower

level, therefore a larger voltage gain must be satisfied. If the lowest input voltage is supposed to be V_{in_min} , the required minimum value of M_{max} will be

$$M_{req} = \frac{V_o}{V_{in_min}}. \quad (2.21)$$

Based on the relationship given by

$$M_{max}(k, Q) \geq M_{req}, \quad (2.22)$$

the adequate set of solutions can be obtained and expressed by $\{(k, Q)\}^B$. By now, the values of k and Q are limited within $\{(k, Q)\}^A \cap \{(k, Q)\}^B$.

Light Load Operation As mentioned in Section 2.1.3, a smaller k is preferred since the frequency variation due to light load operation can be narrowed. This factor should be considered during the trade-off design.

Peak Currents At last, the peak currents of the primary side and secondary side must be calculated to guarantee that the values do not exceed the capacity of the selected MOSFETs. On the other hand, the peak currents are related to the magnetic flux in the inductor and the transformer, therefore smaller values are preferred because of the lower core loss.

The flow chart of design procedure is shown in Fig. 2.8. In the following section, the main parameters of a 105 kHz, 240 W LLC resonant converter will be designed.

2.4 Design Results of the 240 W, 105 kHz LLC Resonant Converter

Based on the trade-off design methodology of the LLC resonant converter, one design example with the specifications listed in Table 2.1 was carried out. The turns ratio of the transformer is $a = 35:4:4$. The MOSFETs used in the primary bridge and the synchronous rectifier have the associated parameters, which will be used in the design process, listed in Table 2.2.

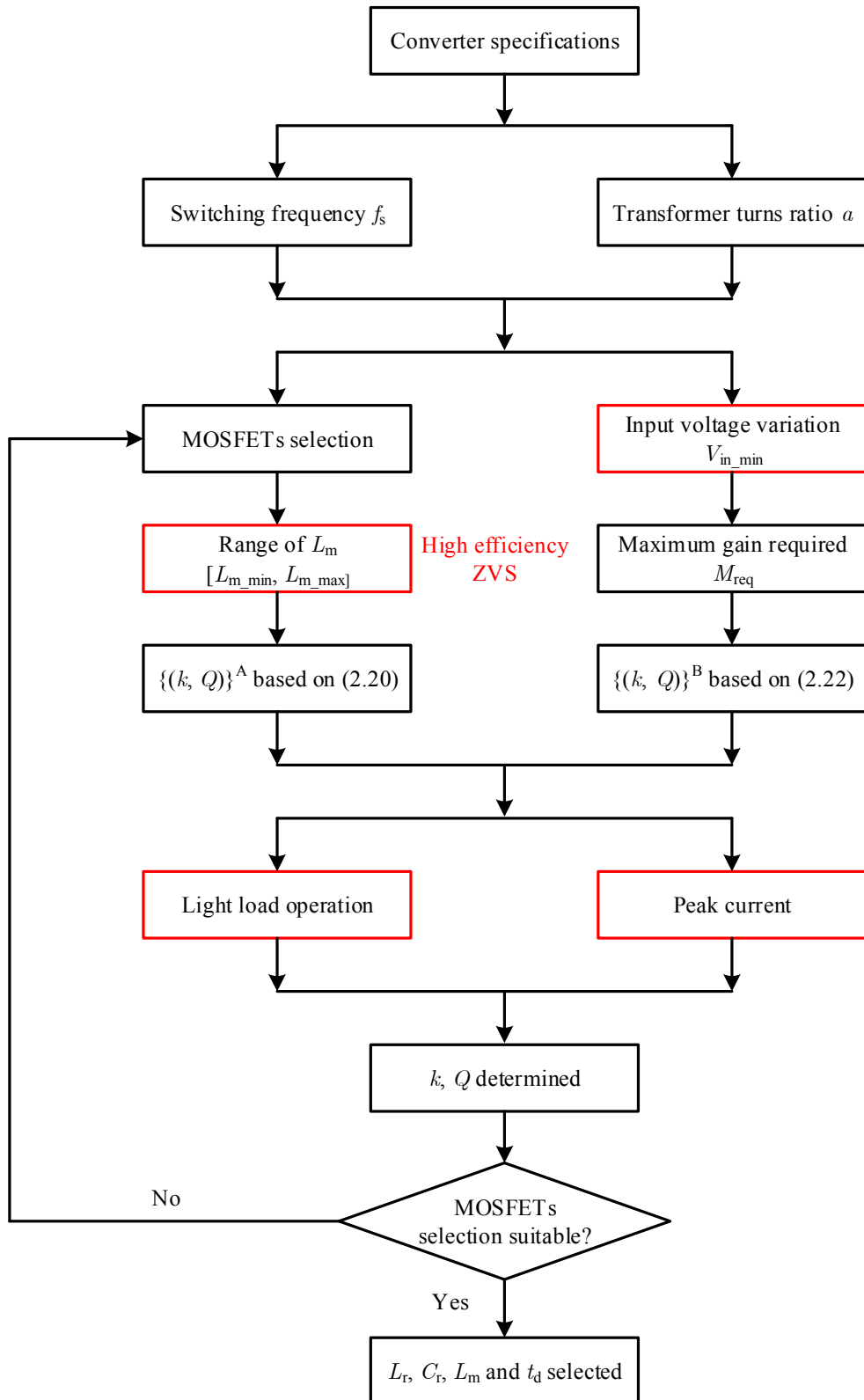


Fig. 2.8 Flow chart of trade-off design procedure for the LLC resonant converter

TABLE 2.1 DESIGN SPECIFICATIONS OF THE LLC RESONANT CONVERTER

Parameters	Symbols	Values
Normal input voltage	V_{in}	400 V
Minimum input voltage	V_{in_min}	350 V
Maximum input voltage	V_{in_max}	420 V
Output voltage	V_o	24 V
Rated output current	I_o	10 A
Switching frequency	f_s	105 kHz

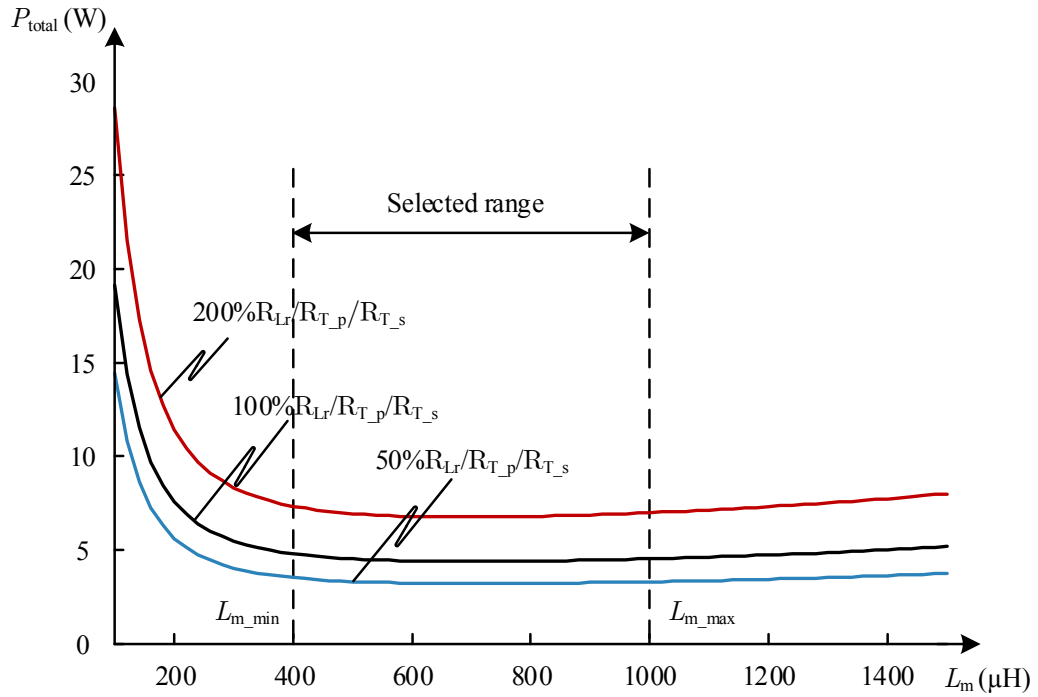


Fig. 2.9 Calculated power loss versus L_m

Fig. 2.9 shows the calculated power loss versus L_m . In order to consider the accuracy of approximate values for winding resistances in the inductor and the transformer, R_{Lr} , R_{Tp} and R_{Ts} are all varied by -50% to +100%. According to the results shown in Fig. 2.9, the selected range of L_m is from 400 μH to 1000 μH and it is insensitive to the resistances of magnetic components.

TABLE 2.2 APPLIED PARAMETERS AND VALUES DURING THE DESIGN PROCESS

Components	Parameters	Values
MOSFETs in the primary side	R_{s_on}	220 m Ω
	Q_{gs}	12.5 nC
	C_{oss}	330 pF
	t_f	90 ns
	V_{gs}	12 V
MOSFETs in the synchronous rectifier	R_{sr_on}	7.1 m Ω
	Q_{gs_sr}	10 nC
	V_{gs_sr}	12 V
Magnetic components	R_{Lr}	150 m Ω
	R_{T_p}	150 m Ω
	R_{T_s}	4 m Ω

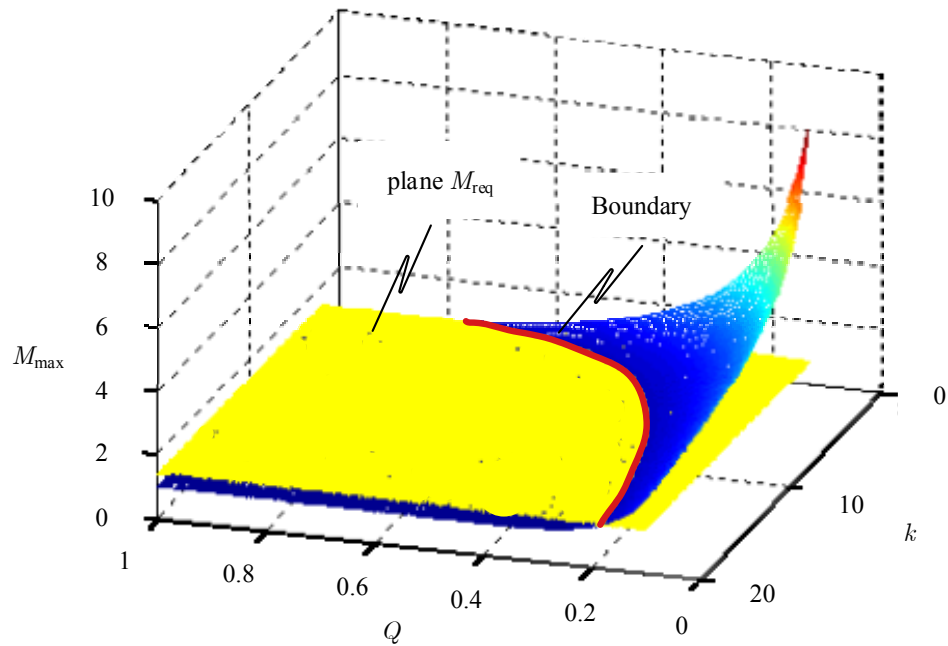
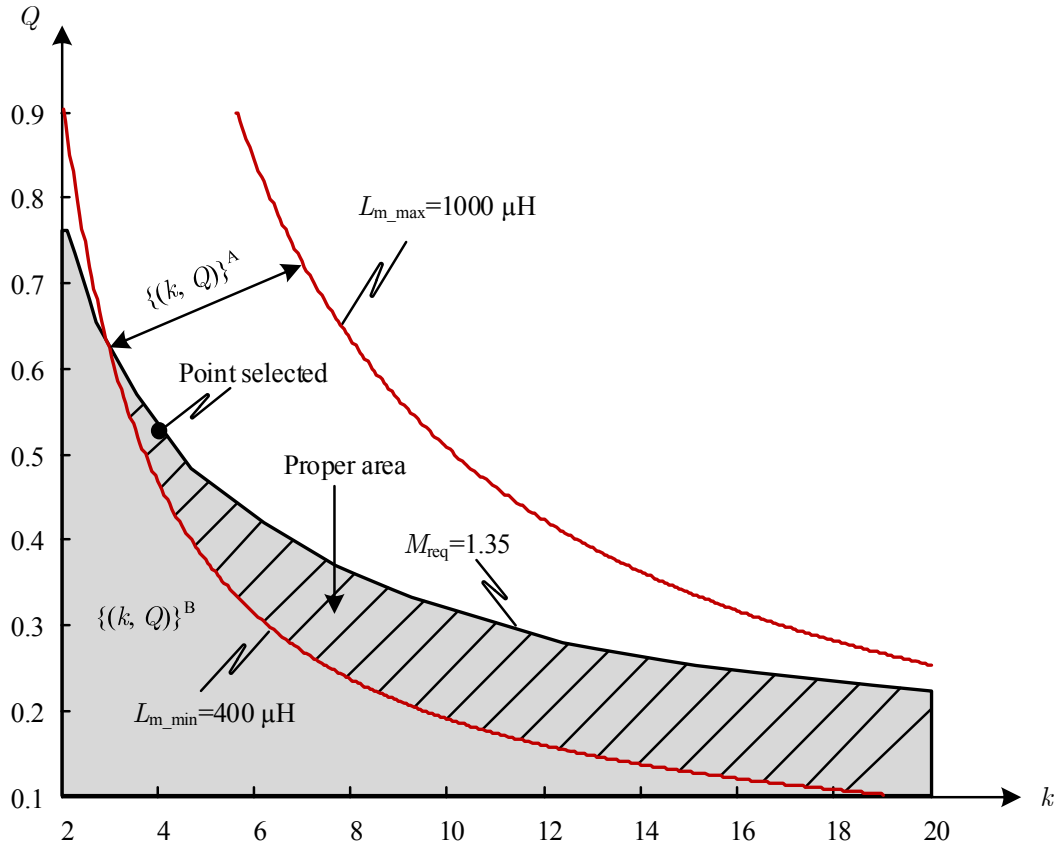


Fig. 2.10 Relation between M_{max} and M_{req}


 Fig. 2.11 Selection of k and Q

Under the design specifications, the maximum voltage gain should be bigger than 1.35 based on (2.21) with the allowance considered. The proper area and the boundary of (2.22) were obtained and the relation of M_{\max} and M_{req} for different k and Q are shown in Fig. 2.10.

In Fig. 2.11, the shaded area shows the proper groups of $\{(k, Q)\}^B$ which is determined by the requirement of input voltage variations. The hatched area shows the groups of $\{(k, Q)\}^A \cap \{(k, Q)\}^B$. The selected design point is shown and taken as $k = 4$, $Q = 0.52$. The resonant inductance is

$$L_r = \frac{L_m}{k} = 105 \mu\text{H}. \quad (2.23)$$

The value of the resonant capacitor is given by

$$C_r = \left(\frac{\pi^2}{8a^2 R_L Q} \right)^2 L_r = 17.5 \text{ nF}. \quad (2.24)$$

The final parameters are designed as

$$L_m = 420 \text{ } \mu\text{H}, L_r = 105 \text{ } \mu\text{H}, C_r = 20 \text{ nF}. \quad (2.25)$$

2.5 Experimental Results of the 240 W LLC Resonant Converter

With the selected parameters of the LLC resonant converter shown in (2.25), the rms values of i_r and i_{s1} are calculated by (2.4) and (2.6) as 1.562 A and 8.099 A, respectively. The phase angle φ shown in Fig. 2.2 is 31.2° . Based on the selected parameters, the prototype with $f_s = 105 \text{ kHz}$ and $P_o = 240 \text{ W}$ is carried out to verify the design results. The standard TDK PQ26/20 sets magnetic core with $A_L = 160 \text{ nH/N}^2$ is applied to implement the resonant inductor and the number of turns is 26.

The standard core ETD 39 with EPCOS N87 material is selected for making the transformer. A 0.5 mm gap was made in the centre leg in order to get the proper magnetizing inductance. The numbers of turns in the primary winding and each secondary winding are 35 and 4, respectively. The HF45 \times 0.1 mm litz wire is used in the primary winding. Each secondary winding uses 3 parallel wires of HF 30 \times 0.15 litz wire. The implementation of windings in the conventional wire wound gapped transformer and the windings arrangements are shown in Fig. 2.12. The detailed design issues and considerations for the transformer applied in the LLC resonant converter will be discussed in next chapter.

The LLC resonant converter along with the Boost PFC is tested and the photo of the power supply prototype is shown in Fig. 2.13. The efficiency of the LLC resonant converter is measured under different load conditions. The result is presented in Fig. 2.14. The experimental results show that the trade-off design methodology for the LLC resonant converter works well.

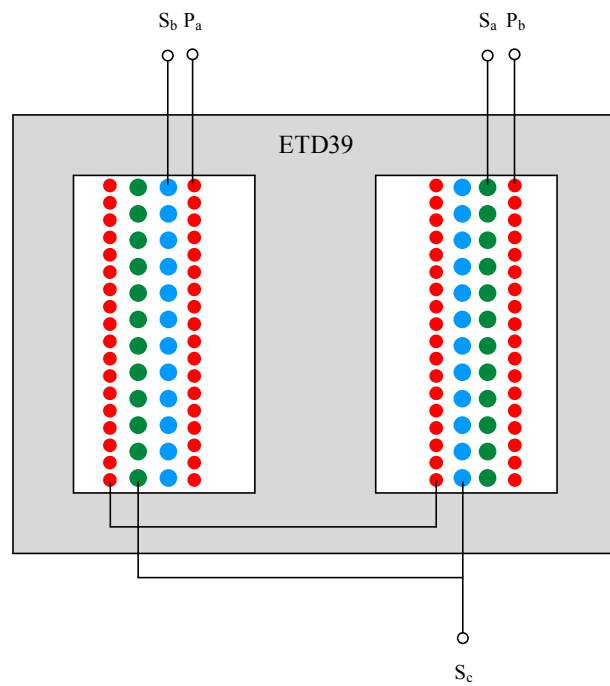


Fig. 2.12 Winding configurations of the conventional wire wound transformer



Fig. 2.13 Photo of the tested power supply with the LLC resonant converter

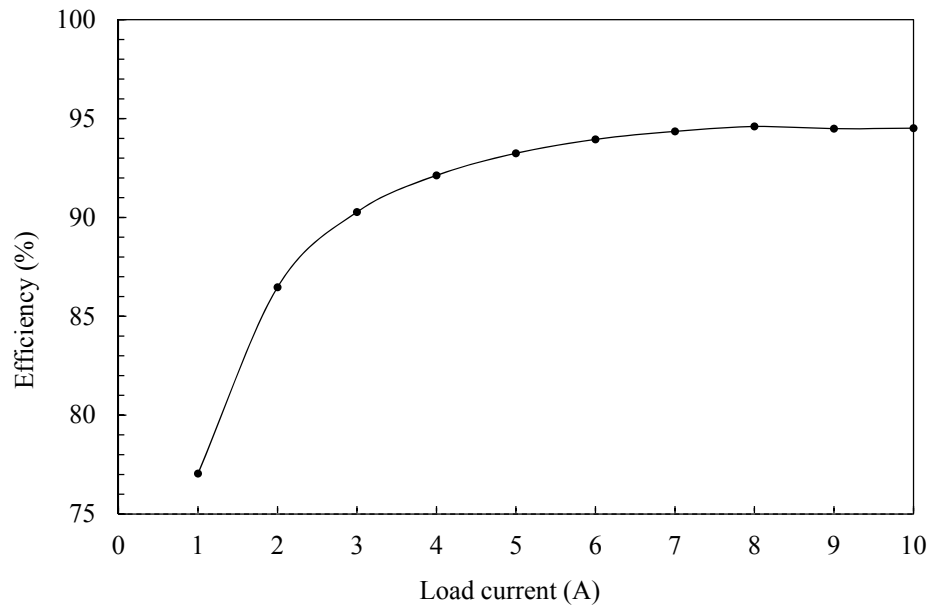


Fig. 2.14 Efficiency of the LLC resonant converter with conventional transformer

2.6 Conclusions

The LLC resonant converter is widely applied in the applications of power supplies and the main parameters need to be determined properly. In this chapter, the basic operations and analysis of the LLC resonant converter has been carried out by FFA. The output voltage and switching frequency will be affected by the resonant components and the specific relations were discussed. Based on the calculation of the main power losses in the circuit, the trade-off design procedure has been presented with the input voltage variation, light load operation and peak currents taken into account. The main parameters of LLC resonant converter with switching frequency 105 kHz and output power 240 W were determined.

3

Design Methodology for a Gapped Conventional Transformer

In the LLC resonant converter, the magnetizing inductance of the transformer should be reasonably selected and the air gap is normally placed in the magnetic core to implement the required value. The design methods of conventional transformers without the gap cannot be applied for this application for the reason that the gapped transformer integrates the magnetizing inductance within the conventional transformer. In this chapter, the operation of the gapped transformer and the design methodology based on given specification will be presented.

3.1 Gapped Transformer Operation Principle

For a conventional transformer, the magnetic inductance will be quite large and the flux in the magnetic core is easily built up by small current through the winding. However, the situation will be different for the transformer in the LLC resonant converter in which the magnetizing inductance is optimized to guarantee the performance of the circuit, described in Chapter 2, as shown in Fig. 3.1(a). The transformer can be treated as one magnetizing inductor L_m connected in parallel with the primary side of an ideal transformer. To determine the proper inductance of L_m , the air gap is normally placed in the core and the equivalent magnetic core with the permeability μ_{eff} can be applied to analyse the operation of the gapped transformer.

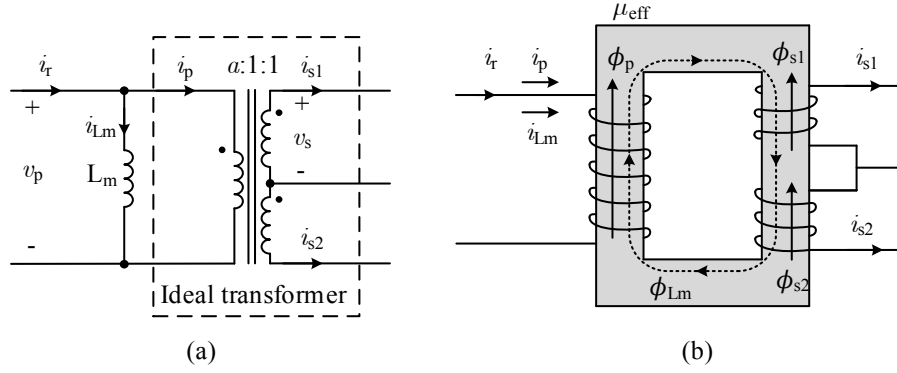


Fig. 3.1 Gapped transformer in the LLC resonant converter (a) circuit model; (b) simplified fabrication sketch of the gapped transformer

As shown in Fig. 3.1(b), three windings are wound around the core, they are the primary winding on the left side, the secondary 1 and secondary 2 windings on the right side.

The current through the primary winding is the resonant current i_r which is the sum of the magnetizing current i_{L_m} and the primary current through the ideal transformer i_p balancing the secondary load current. The two secondary currents are i_{s1} and i_{s2} and they are complementary. The waveforms and calculations for these currents have been introduced in Chapter 2. The comprehensive analysis of the role for each current in view of the magnetic flux must be carried out. Only in this way can the magnetic flux density, the core loss and the winding loss of the transformer be properly calculated.

The fluxes built by the primary current i_p and the secondary currents i_{s1} and i_{s2} in the ideal transformer are represented as ϕ_p , ϕ_{s1} and ϕ_{s2} , respectively in Fig. 3.1(b). For the ideal transformer, these fluxes will cancel each other. The magnetizing current i_{L_m} sets up the common flux linking all windings. The flux density in the core will be directly proportional to i_{L_m} . The maximum flux density in the core is given by

$$B_{\max} = \frac{\mu_0 \mu_{\text{eff}} N_p I_{L_m \text{pk}}}{l_c}, \quad (3.1)$$

where N_p is the number of turns in the primary winding, I_{Lm_pk} is the peak value of magnetizing current, μ_{eff} and l_c are the effective relative permeability and the magnetic path length of the core, respectively. Based on the flux density in the core, the core loss of the transformer may be solved and the final design result should guarantee that the maximum flux density is smaller than the saturation flux density of the core material.

On the other hand, the current through the primary winding is i_r which is the sum of i_p and i_{Lm} . Thus, it is the resonant current i_r that will be used to calculate the winding loss of the primary winding.

Based on the operation analysis of the gapped transformer, the design considerations will be discussed and then the design methodology will be established.

3.2 Design Considerations for the Gapped Transformer

There are three windings in the transformer, the design consideration of multiple windings should be taken into account. For the gapped transformer in the LLC resonant converter, the magnetizing inductance effected by the gap dimension must be considered. On the other hand, the temperature rise of the transformer operating at steady state is a significant specification in the practical application. Once the maximum allowed temperature rise is determined, the smaller size of the transformer is always pursued to achieve higher power density. Thus, the thermal characteristic of the magnetic core and the temperature rise related to the total power loss of the transformer must be discussed.

3.2.1 Multiple Windings Consideration

For multiple windings transformers, the optimum window utilization factor for the primary winding and secondary windings may be investigated by the DC winding loss. The total window utilization factor of all windings is defined as the ratio of the winding conduction area (W_c) to the window winding area of the core (W_a) and represented

as k_u . If the primary winding has the window utilization factor of k_{up} , the total winding loss of the transformer can be obtained by

$$P_{cu_dc} = \rho_w \left[\frac{N_p M L T}{k_{up} W_a} \cdot \frac{I_{r_rms}^2}{N_p} + 2 \cdot \frac{N_{s1} M L T}{(k_u - k_{up}) W_a} \cdot \frac{I_{s1_rms}^2}{2 N_{s1}} \right], \quad (3.2)$$

where ρ_w is the electrical resistivity of the winding, N_p and N_{s1} are the number of turns of the primary winding and the secondary winding 1.

The optimum value of P_{cu_dc} in relation to k_{up} is obtained by taking the partial derivative with respect to k_{up} and setting it to zero:

$$\frac{\partial P_{cu_dc}}{\partial k_{up}} = \frac{\rho_w M L T}{W_a} \left[-\frac{N_p^2 I_{r_rms}^2}{k_{up}^2} + \frac{4 N_{s1}^2 I_{s1_rms}^2}{(k_u - k_{up})^2} \right] = 0. \quad (3.3)$$

Thus, the window utilization factor of the primary winding is related to the total window utilization factor by

$$k_{up} = k_u \frac{1}{1 + \frac{2 I_{s1_rms}}{a I_{r_rms}}}. \quad (3.4)$$

3.2.2 Magnetizing Inductance Consideration

With the equivalent relative permeability of the gapped core μ_{eff} , the magnetizing inductance can be calculated by the basic inductance equation

$$L_m = \frac{\mu_0 \mu_{eff} N_p^2 A_c}{l_c}, \quad (3.5)$$

where A_c is the cross-sectional area of the core.

For typical EE core sets with gaps placed on the centre leg, as shown in Fig. 3.2, the basic relationship between g and μ_{eff} is

$$\mu_{eff} = \frac{\mu_r l_c}{g \mu_r + l_c}, \quad (3.6)$$

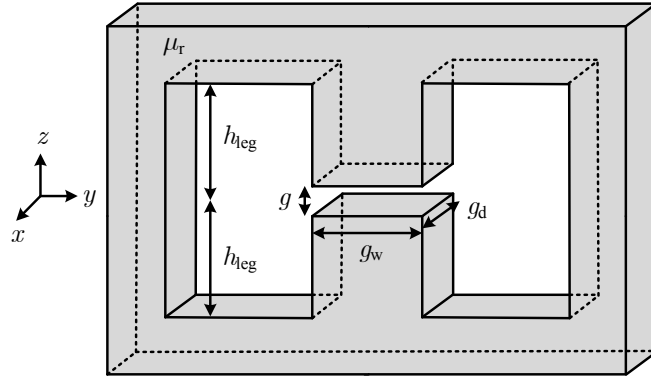


Fig. 3.2 Gap placed in the EE core sets and the dimensions of the gap

where μ_r is the relative permeability of the core material. However, the gap effect may cause significant change in the inductance with larger gap length. Thus, the final selected gap length should be verified to make sure that the obtained magnetizing inductance is in the allowable range. According to the review in Chapter 1, the calculation of the magnetizing inductance considering the fringing flux due to the air gap can follow the 3-D reluctance model proposed in [113]. For the gaps illustrated in Fig. 3.2, the reluctance of the air gap in the centre leg with the assumption of a homogenous flux density distribution in the gap without fringing flux can be calculated by

$$R_{gc} = \frac{g}{\mu_0 A_c}. \quad (3.7)$$

The reluctance of the air gap in the centre leg with 3-D fringing flux considered can be obtained by

$$R_{gc}^f = \sigma_x \sigma_y \frac{g}{\mu_0 A_c}, \quad (3.8)$$

where

$$\sigma_x = \frac{1}{1 + \frac{g}{\pi g_d} \left(1 + \ln \frac{\pi h_{leg}}{g} \right)}, \quad \sigma_y = \frac{1}{1 + \frac{g}{\pi g_w} \left(1 + \ln \frac{\pi h_{leg}}{g} \right)}. \quad (3.9)$$

Consequently, the effective permeability of the core with the fringing effect due to the air gap in the core is given by

$$\mu_{\text{eff}}^f = \frac{\mu_r l_c}{\sigma_x \sigma_y g \mu_r + l_c}. \quad (3.10)$$

For the air gap with round cross-section placed on the centre leg, such as the centre leg of ER sets, the reluctance of the air gap with 3-D consideration can be calculated as

$$R_{\text{gc}}^f = \sigma_r^2 \frac{g}{\mu_0 A_c}, \quad (3.11)$$

where

$$\sigma_r = \frac{1}{1 + \frac{g}{\pi g_r} \left(1 + \ln \frac{\pi h_{\text{leg}}}{2g} \right)}, \quad (3.12)$$

and g_r is the radius of the cross-sectional area. Thus, the effective permeability of the ER cores set with the fringing effect due to the air gap in the core is given by

$$\mu_{\text{eff}}^f = \frac{\mu_r l_c}{\sigma_r^2 g \mu_r + l_c}. \quad (3.13)$$

3.2.3 Losses Consideration

The total loss of the transformer consists of the core loss and the winding loss. The flux density in the gapped transformer in the LLC resonant converter is set by the magnetizing current. The general Steinmetz equation will involve some error in the calculation of the core loss since the waveform of flux density is not purely sinusoidal. As the dead-time between drive signals is very short, the waveform of the flux density is assumed to be triangular with the same rising and falling times. For this situation, the iGSE method is more suitable to obtain an accurate estimate of core loss. The expression of core loss per volume is given by

$$P_{\text{fe}} = \frac{1}{T} \int_0^T K_{\text{ic}} \left| \frac{dB}{dt} \right|^\alpha |B(t)|^{\beta-\alpha} dt, \quad (3.14)$$

with

$$K_{\text{ic}} = \frac{K_c}{(2\pi)^{\alpha-1} \int_0^{2\pi} |\cos \theta|^\alpha |\sin \theta|^{\beta-\alpha} d\theta}, \quad (3.15)$$

where K_c , α , β are the parameters of the material applied in the Steinmetz equation as shown in (1.8), $B(t)$ is the instantaneous flux density. For the gapped transformer in the LLC resonant converter, (3.14) can be rewritten by

$$P_{fe} = \frac{2}{T_s} \left(\frac{\mu_0 \mu_{eff} N_p}{l_c} \right)^\beta \int_0^{\frac{T_r}{2}} K_{ic} \left(\frac{a V_o}{L_m} \right)^\alpha \left| -\frac{a V_o T_r}{4 L_m} + \frac{a V_o}{L_m} t \right|^{\beta-\alpha} dt. \quad (3.16)$$

If the volume of the magnetic core is V_c , the core loss will be $P_c = V_c P_{fe}$.

On the other hand, the total winding loss of the transformer with the high frequency effects ignored and the DC winding loss can be obtained as

$$P_{cu_dc} = R_{p_dc} I_{r_rms}^2 + 2R_{s1_dc} I_{s1_rms}^2. \quad (3.17)$$

However, the switching frequency of the LLC resonant converter is quite high and the high frequency effect will cause bigger winding loss in practice. Based on the introduction of high frequency effects in Chapter 1, the eddy current effect and the air gap effect may be evaluated. The extra winding loss due to high frequency effects is represented by P_{cu_ac} . Thus, the total power loss of the transformer is

$$P_{trafo} = P_{cu_dc} + P_{cu_ac} + P_c. \quad (3.18)$$

As the high frequency effect in the winding loss is tightly dependent on the winding arrangements and the calculation of core loss is quite complex, the factor γ is introduced to simplify the total loss calculation and the definition is given by

$$P_{trafo} = (1 + \gamma) P_{cu_dc}. \quad (3.19)$$

Based on the factor γ , the total power loss will be linked to the DC winding loss which can be easily expressed as the function of magnetic core parameters as it is shown in (3.2). During the design process, the total power loss of the gapped transformer are calculated with the initially assumed value of γ . With the selected core and parameters of the windings, the core loss and high frequency winding loss will both be calculated and the final calculated value of γ will be confirmed. If the final calculated value is different from the initially assumed value, the new value is selected to replace the initial assumed value and the design process is repeated until the final calculated value is stable in an iteration process.

3.2.4 Thermal Considerations

For the transformer where the maximum temperature rise ΔT is limited, the maximum allowed power loss P_{\max} can be expressed as

$$P_{\max} = \frac{\Delta T}{R_{\theta}}, \quad (3.20)$$

where R_{θ} is the thermal resistance for the core assembly. This value is normally supplied by the manufacturer or obtained from empirical data [84]. In any case, the thermal resistance is related to the dimensions of the magnetic core. The approximation of R_{θ} based on empirical data is related to the volume of the core and given by [84]

$$R_{\theta} = \frac{0.06}{\sqrt{V_c}}. \quad (3.21)$$

In this empirical equation, is R_{θ} in $^{\circ}\text{C}/\text{W}$ for V_c in m^3 .

3.3 Design Methodology of the Gapped Transformer

For the gapped transformer, the maximum allowable power loss is determined by the temperature rise and the thermal resistance of the transformer as given by (3.20) which is related to the dimensions of the magnetic core. Besides, the relative permeability of the core should be selected based on the requirement of the magnetizing inductance within the limitation of the saturation flux density. Taking all the design considerations presented in Section 3.2, the design methodology for the gapped transformer in the LLC resonant converter can be implemented as outlined in Fig. 3.3. The specifications for the transformer will be assigned or calculated based on the main parameters of the LLC resonant converter. The A_p value will be introduced to select the proper core. A_p is defined as the product of the window winding area and the cross-sectional area of the magnetic core. The calculations for the minimum required A_p value and the corresponding selection of the relative permeability of the gapped core μ_{opt} and the current density J_0 are derived as shown in Appendix C. The main calculations and design procedure is as follows.

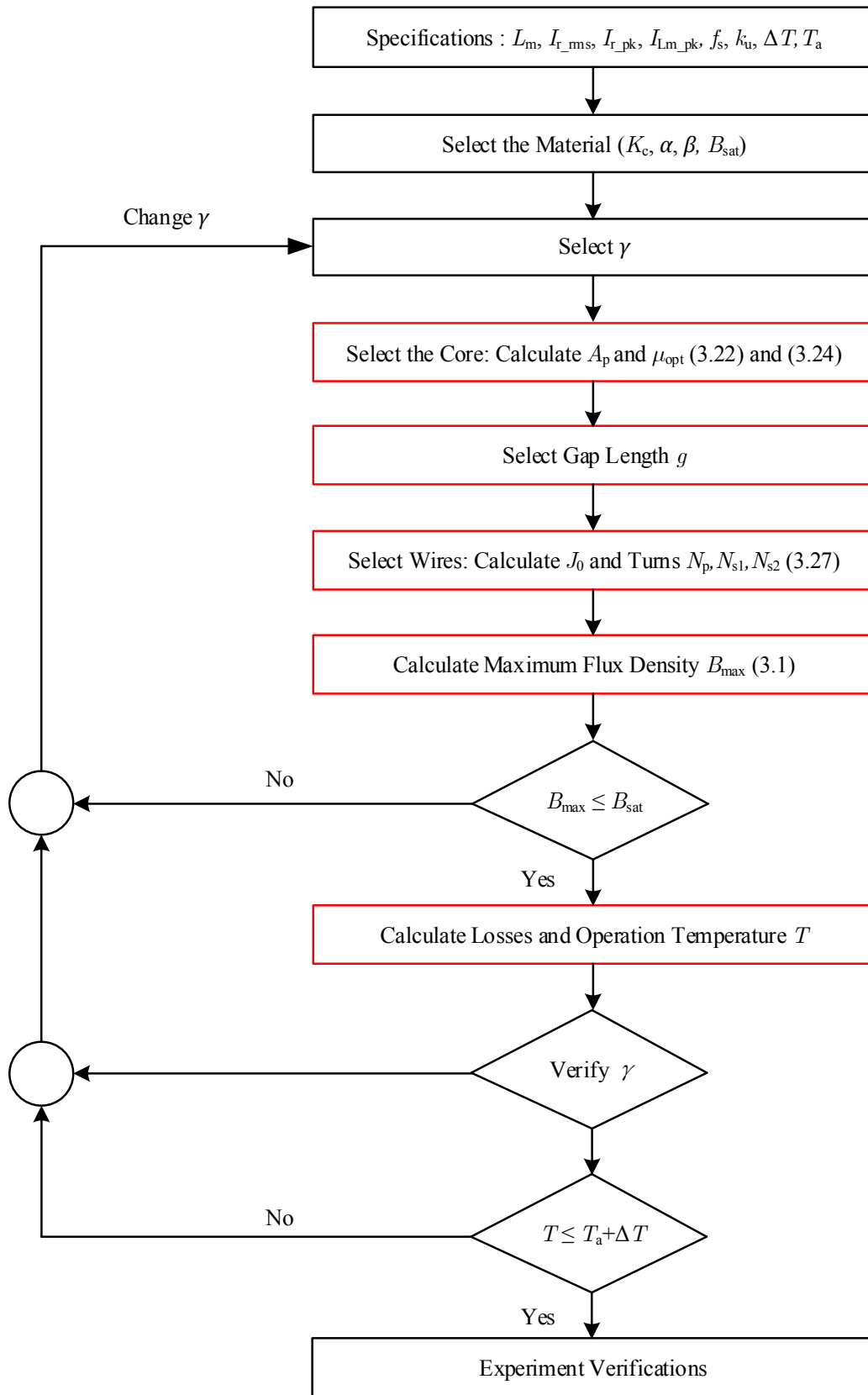


Fig. 3.3 Flow chart of the design methodology for the gapped transformer

Core Selection A_p is the product of the core window winding area W_a and the cross-sectional area A_c , the required minimum A_p value for the gapped transformer is expressed as

$$A_p = \left[\frac{\sqrt{k_u(1+\gamma)} L_m I_{r_rms} I_{Lm_pk}}{B_{max} k_{up} K_t \sqrt{\Delta T}} \right]^{\frac{8}{7}}, \quad (3.22)$$

where $K_t = 48.2 \times 10^3$ is a parameter based on the analysis of several core types and sizes [84] and the value of γ can be originally presumed and the value will be checked when the total design is completed. (3.22) is derived in Appendix C.

Gap Length Selection With the value of A_p from (3.22), the proper core may be chosen. The dimensions and parameters of the core are then available from the manufacturer. Based on the thermal resistance of the selected core and the allowable temperature rise, the DC copper loss of the primary winding P_{cu_p} is obtained by

$$P_{cu_p} = \frac{k_{up}}{k_u} \frac{\Delta T}{R_\theta (1+\gamma)}. \quad (3.23)$$

The optimum relative permeability is then given by

$$\mu_{opt} = \frac{B_{max} l_c}{\mu_0 \sqrt{\frac{P_{cu_p} k_{up} W_a}{\rho_w M L T}}} \frac{I_{r_rms}}{I_{Lm_pk}}. \quad (3.24)$$

See Appendix C for the derivation of (3.24). It is illustrated that the relative permeability is directly proportional with the maximum flux density in the core and inversely proportional to the square root of the winding loss. As the maximum flux density is limited by the saturation value of the core and the winding loss is limited by the maximum temperature rise, the relative permeability is balanced between the maximum flux density which is related to the core loss and the winding loss.

For an EE core with the gap placed on the centre leg of the core, the gap length could be found from (3.6) or the more accurately from (3.10) or (3.13) with the gap effect considered.

Numbers of Turns Once the proper gap length g is determined, the corresponding value of the inductance per turn, A_L , is calculated by

$$A_L = \frac{\mu_0 \mu_{\text{eff}} A_c}{l_c}, \quad (3.25)$$

The number of turns for the primary winding is

$$N_p = \sqrt{\frac{L_m}{A_L}}. \quad (3.26)$$

The number of turns in each secondary winding is $N_{s1} = N_{s2} = N_p / a$.

Windings of the Gapped Transformer The current density J_0 in windings should meet the requirement of the temperature rise and given as

$$J_0 = K_t \sqrt{\frac{\Delta T}{k_u (1 + \gamma)}} \frac{1}{\sqrt[3]{A_p}}, \quad (3.27)$$

where is $K_t = 48.2 \times 10^3$. The derivation is given in Appendix C.

The conduction areas of the conductors may be found and then the proper wires or copper foils can be selected.

Finally, the winding loss and the core loss should be calculated with the high frequency eddy current effect and fringing effect taken into account. The presumed value of γ must be checked.

3.4 Design Results of Conventional Gapped Transformer

The gapped transformer applied in the 240 W LLC resonant converter has been designed and tested to verify the proposed methodology. The input voltage and the output voltage of the LLC resonant converter are 400 V and 24 V, respectively. The switching frequency is around 105 kHz. In the resonant tank, the resonant inductance and the resonant capacitance are 105 μH and 20 nF, respectively, as designed in Chapter 2. The turns ratio of the gapped transformer is $a=35:4:4$ and the required magnetizing inductance of the transformer is around 420 μH .

TABLE 3.1 SPECIFICATIONS OF THE GAPPED TRANSFORMER

Parameters	Symbols	Values
Output power	P_o	240 W
Switching frequency	f_s	105 kHz
Magnetizing inductance	L_m	420 μ H
Turns ratio	a	35:4:4
Maximum temperature rise	ΔT	50 °C
Ambient temperature	T_a	40 °C
Rms value of resonant current	I_{r_rms}	1.562 A
Peak value of magnetizing current	I_{Lm_pk}	1.138 A
Rms value of each secondary current	I_{s1_rms}	8.099 A

3.4.1 Design Specifications of Gapped Transformer

The full specifications of the LLC resonant converter and the calculation results for currents which will be applied during the design process are given in Table 3.1. Furthermore, the total window utilization factor, k_u , is selected as 0.15 and will be check at the end of the design.

3.4.2 Design Results for the Gapped Transformer

For the application at 105 kHz, ferrite would normally be used. The material specifications for EPCOS N87 are listed in Tab 3.2. The saturation flux density is 0.32 T at 100 °C with $H = 250$ A/m. In the initial design, the maximum magnetic flux density B_{max} is selected as 0.1 T. The value of B_{max} is based on an iterative design and it was found that the value satisfies the constraint of the design while ensures that the maximum specifications not exceed.

At the first step, the value of γ is assumed to be 1.5 and will be checked later. The A_p parameter can be calculated with (3.22) and the result is 2.15 cm⁴. Thus, the ETD39 core is suitable. The core specifications are listed in Table 3.3. The optimum relative

TABLE 3.2 SPECIFICATIONS OF THE MAGNETIC MATERIAL EPCOS N87

Parameters	Symbols	Values
Steinmetz parameter	K_c	16.9
Steinmetz parameter	α	1.25
Steinmetz parameter	β	2.35
Saturation value of flux density	B_{sat}	0.32 T

TABLE 3.3 PARAMETERS OF SELECTED ETD39 CORE

Parameters	Symbols	Values
Cross-sectional area	A_c	1.25 cm ²
Magnetic path length	l_c	9.22 cm
Window winding area	W_a	1.77 cm ²
Area product parameter of the core	A_p	2.21 cm ⁴
Volume of the core	V_c	11.5 cm ³
Mean length of a turn	MLT	6.08 cm
Height of the window of an ER core	h_{leg}	12.53 mm
Radius of the centre leg	g_r	6.4 mm
Thermal resistance	R_{θ}	17.7 °C/W
Copper resistivity (20 °C)	ρ_{20}	1.72 μΩ-cm
Constant	α_{20}	0.00393

permeability will be obtained by (3.24) and the calculation result is 130. Therefore, the final gap length from (3.6) is selected as 0.5 mm. Finally, the numbers of turns for the primary winding and each secondary winding are 35 and 4, respectively given by (3.26).

The current density J_0 is calculated by (3.27) and the value is 505.8 A/cm². Thus, the cross-section area of the conductor for the primary winding is 0.31 mm². HF45 × 0.1 mm litz wires were selected for space considerations and the DC resistance is 0.049

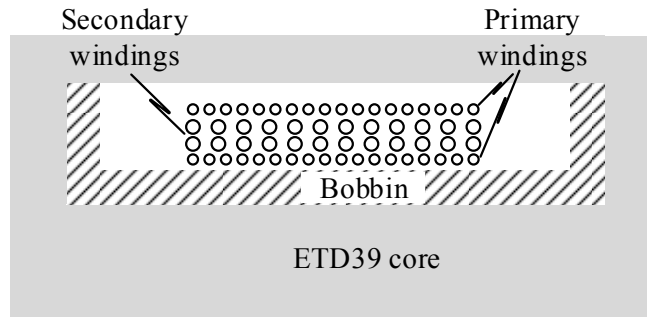


Fig. 3.4 Structure of designed gapped transformer with ETD39 core set

Ω/m at 20 °C. With the same calculation method, the cross-sectional area of the conductor for each secondary winding is 1.6 mm^2 . The 3 parallel litz wires of HF30 \times 0.15 mm meet this requirement. The total dc resistance is $0.011 \text{ }\Omega/\text{m}$ at 20 °C.

The magnetic core, gap length and windings were all determined through the calculation equations proposed in Section 3.2. In order to minimize the high frequency winding loss and the leakage inductance of the transformer, the primary winding and secondary windings are interleaved. The configuration is shown in Fig. 3.4.

3.4.3 Magnetizing Inductance Due to Gap Effect

Due to the gap placed in the core, the magnetizing inductance is calculated considering the fringing field around the gap. For the selected ETD39 core, the magnetizing inductance will be increased due to the fringing flux around the gap. The factor for the inductance variation caused by the fringing effect is calculated based on (3.13) and the result is

$$F_{L_m} = \frac{L_m^f}{L_m} = \frac{g\mu_r + l_c}{\sigma_r^2 g\mu_r + l_c} = 1.223. \quad (3.28)$$

Based on the chosen number of turns for the primary winding and the gap length, the magnetizing inductance is finally calculated to be $434 \text{ }\mu\text{H}$ which is acceptable. The original specification called for $420 \text{ }\mu\text{H}$.

3.4.4 Losses in the Gapped Transformer

For the designed gapped transformer, the value of B_{\max} based on (3.1) is 0.092 T which is in the allowable range for the magnetic material. The core loss based on iGSE calculation method is $P_c = 1.389$ W based on (3.16). Combing the DC resistances of windings and the rms values of currents through windings, the DC winding loss can be calculated as

$$\begin{aligned} R_{p_dc} &= 35 \times (60.8 \times 10^{-3}) \times 0.049 \times [1 + 0.00393 \times (90 - 20)] = 0.132 \, \Omega, \\ R_{s1_dc} &= 4 \times (60.8 \times 10^{-3}) \times 0.011 \times [1 + 0.00393 \times (90 - 20)] = 0.003 \, \Omega, \\ P_{cu_dc} &= R_{p_dc} I_{r_rms}^2 + 2R_{s1_dc} I_{s1_rms}^2 = 0.763 \, \text{W}. \end{aligned} \quad (3.29)$$

For the assembly of windings in the gapped transformer, the litz wires are implemented. As the skin depth at 105 kHz is 0.204 mm which is much larger than the diameter of litz wire, the extra AC winding loss due to high frequency effects may be neglected. The total loss of the gapped transformer is given by

$$P_{\text{trafo}} = P_c + P_{cu_dc} = 2.152 \, \text{W}. \quad (3.30)$$

Thus, the calculated temperature rise of the transformer is 37.6 °C which is smaller than the specified allowed value of 50 °C.

3.4.5 Parameters Verification

The assumed parameters applied during the design process must be verified including k_u and γ . Based on the selected windings and designed transformer, we have

$$k_u = \frac{35 \times (3.53 \times 10^{-7}) + 2 \times 4 \times (1.59 \times 10^{-6})}{1.77 \times 10^{-4}} = 0.142, \quad (3.31)$$

$$\gamma = \frac{P_{\text{trafo}} - P_{cu_dc}}{P_{cu_dc}} = 1.82. \quad (3.32)$$

These values are close to the initially assumed values which were applied to calculate A_p . Thus, the design of the gapped transformer is complete and the associated experiments should be carried out to verify the performance of the transformer.

3.5 Experimental Results of the Gapped Conventional Transformer

The gapped transformer based on the design results has been built to verify the presented methodology. The transformer is operated in the 240 W LLC resonant converter. The photo of the prototype is shown in Fig. 2.13 in Chapter 2. This is an entire power supply which consists of LLC converter and front-end power factor correction (PFC) converter. As mentioned in Chapter 2, the efficiency of the power converter at different load conditions was measured.

The temperature rise of the designed gapped conventional transformer under steady state operation is 31.8 °C. The power loss of the gapped transformer is 1.8 W. The experimental results show that the proposed design methodology for the gapped conventional transformer in LLC resonant converter works according to the design specifications.

3.6 Conclusions

This chapter distinguishes the design methodology for the gapped transformer in the LLC resonant converter from the traditional approach. In the design of the transformer, several significant aspects have been considered including the analysis of the role for each current across the transformer, the multiple windings optimization method, and the power loss with high frequency effects involved. The detailed design methodology and equations were presented. The gapped conventional transformer for a 240 W, 105 kHz LLC resonant converter has been designed based on the proposed method. The experimental results for the resonant converter and the transformer verified the design process. For future work a more detailed investigation of the fringing effect in the winding loss should be carried out.

4

Parasitic Parameters in Conventional Transformers

For the transformer, the leakage inductance has an essential role in the circuit operation, especially for the LLC resonant converter. The calculation of the leakage inductance of the transformer operated at high frequency will be presented in this chapter. The results for different interleaving winding structures of the transformer will also be discussed. On the other hand, the stray capacitance appearing between different windings can cause serious problems for the power switching circuit. The calculation of stray capacitances for a practical transformer has been completed in this chapter.

4.1. Leakage Inductance at High Frequency

Due to the deficient coupling between windings in the transformer, the magnetic flux could leak through the window area of the magnetic core. Leakage inductance is introduced to evaluate the value of the leakage flux. In circuits applied in switching mode power supplies, leakage inductance plays a critical function as mentioned in Section 1.2.3. The leakage inductance will not only limit the rate of switching current variation through the switching device, but also cause voltage spikes across the switches owing to the energy stored in the leakage inductance. In general, limitations including the increased switching loss, reduced the power efficiency and

electromagnetic interference (EMI) have been discussed [193]-[196]. With the help of new devices, such as Gallium Nitride (GaN) switches, the switching frequency is heading towards the mega-Hertz range and the size of the magnetic components can be reduced. Consequently, the leakage inductance of the transformer operated at high frequency should be accurately predicted for the circuit design applied in the switching mode power supply. The leakage inductance is especially significant for resonant converters to accurately predict the resonant frequency [189], [197].

The investigations of leakage inductances both in conventional and planar transformers have been carried out in many research papers including the analysis and the calculation methodologies [86], [148], [153], [198]-[200]. In [86], Dowell pointed out that the leakage inductance is frequency-dependent and the formula for the leakage inductance was presented. For different winding interleaving methods in the transformer, the effect of winding configurations on the leakage inductance was not discussed. Nevertheless, most of these papers focused on the leakage inductance calculations for different core types, including toroidal cores, EE core or planar cores, at relatively low frequency and the high frequency effects were ignored. These proposed formulas were frequency independent and basically derived assuming uniform current distribution in the conductor. According to eddy current effect at high frequency operation, the current gravitates towards the surface of conductors. Consequently, the excitation current distribution is non-uniform. This is better explained by a particular example.

As shown in Fig. 4.1, two windings sitting inside the window area of one EE core are represented by P and S, where P is the primary winding and S is the secondary winding. Assuming the primary winding carries an AC current with the reference direction flowing into the plane, is part of the generated flux leaks through the magnetic core and the window area, and this flux has no link with the secondary winding. If the secondary winding is shorted, the main flux in the magnetic core linking both windings is negligible because the magneto-motive force (MMF) of the primary side and secondary side will cancel. Thus, it is only the leakage flux that appears as shown in the figure. The leakage flux in the transformer is mainly through the window area including the conduction area and the insulation area between windings.

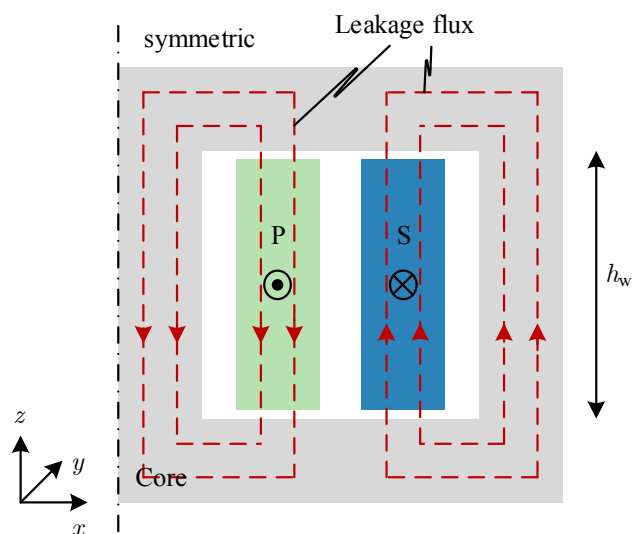


Fig. 4.1 Leakage flux distributed in the transformer with half-core demonstrated

In order to analysis and derive the analytical formula for leakage inductance, we assume that:

- (1) The magnetic core is ideal which means the permeability of the core material is infinite. This will guarantee the magnetic field intensity inside the core is zero.
- (2) The height of windings (represented by h_w) is close to the height of core window and the height of core window is much larger than the width of the window. Under this condition, the edge effect for windings can be ignored.

In consequence, the leakage flux in the window area is approximated to be parallel with the conductor surfaces. With the skin effect and proximity effect considered for excitations at high frequency, the current distribution in winding conductors will be non-uniform. Fig. 4.2 shows the MMF curves in the window area along the x axis for both low frequency and high frequency. It is clear that the area of the MMF curve at high frequency is smaller than that at low frequency, in which the current density is uniformly distributed in the conductor. Thus, the stored magnetic

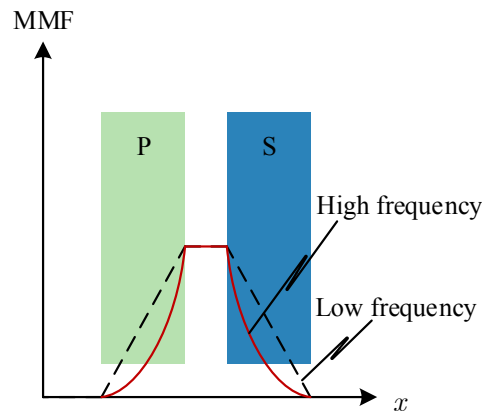


Fig. 4.2 MMF curve along x axis at low and high frequencies

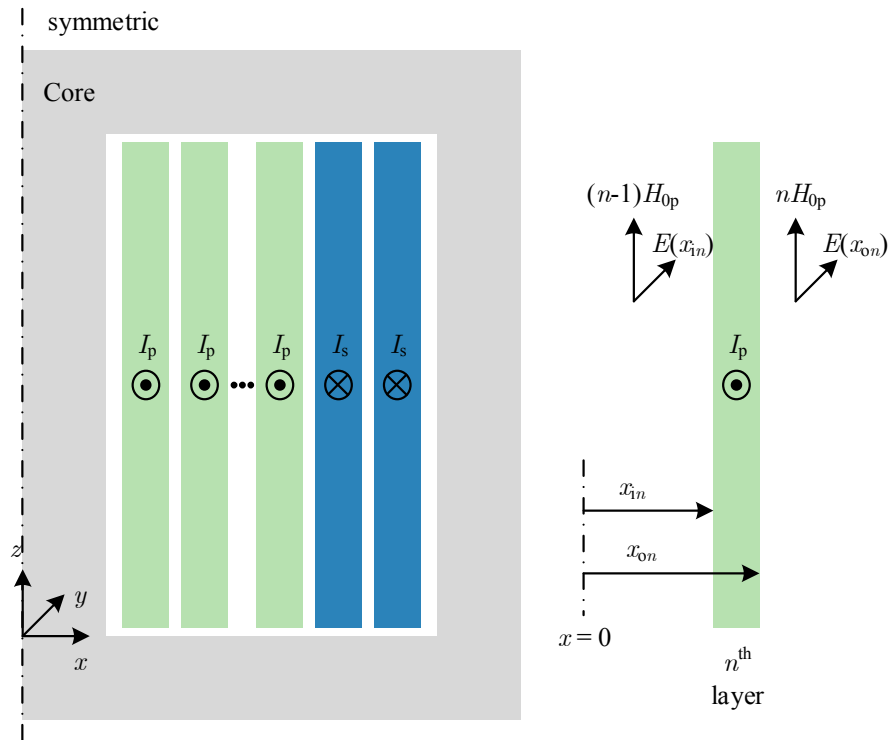


Fig. 4.3 Transformer cross section and magnetic field boundary in generalized n^{th} layer

field energy by the leakage inductance is reduced with high frequency operation. In an attempt to obtain the accurate value of leakage inductance at different frequencies, the following section will present the detailed calculations.

4.2. Frequency Dependent Leakage Inductance Analysis

With the assumptions made in Section 4.1, the 1-D analytical method can be employed to solve the magnetic field in the transformer, as shown in Fig. 4.3. The currents through the primary winding and the secondary winding are I_p and I_s , respectively. For linear homogeneous isotropic medium, Maxwell's equations are given for a magnetquasistatic system by

$$\nabla \times E = -\mu_0 \frac{\partial H}{\partial t}, \quad (4.1)$$

$$\nabla \times H = \sigma E. \quad (4.2)$$

In Cartesian coordinates shown in Fig. 4.3, the magnetic field can be easily solved and the derivation is partly referred to the calculations presented in [115]. The following identities will apply to the electric field intensity E and magnetic field intensity H in the conductor because of the symmetry,

$$E_x = 0, \quad E_z = 0, \quad \frac{\partial E_y}{\partial z} = 0, \quad (4.3)$$

$$H_x = 0, \quad H_y = 0, \quad \frac{\partial H_z}{\partial y} = 0. \quad (4.4)$$

For the steady state analysis, the equations can be written in phasor form as following because E and H contain only y and z components, respectively.

$$\frac{dE_y}{dx} = -j\omega\mu_0 H_z, \quad (4.5)$$

$$-\frac{dH_z}{dx} = \sigma E_y. \quad (4.6)$$

Combing (4.5) and (4.6), the one-dimensional diffusion equation will be yielded as,

$$\frac{d^2 H_z}{dx^2} = j\omega\mu_0\sigma H_z. \quad (4.7)$$

The general solution of the equation is given by

$$H_z(x) = H(x) = A_1 e^{\lambda x} + A_2 e^{-\lambda x}, \quad (4.8)$$

where A_1 and A_2 are complex constants determined by boundary conditions, and the complex propagation constant λ is defined as

$$\lambda = \sqrt{j\omega\mu_0\sigma} = \frac{1+j}{\delta_0}, \quad (4.9)$$

where δ_0 is the skin depth defined in (1.1).

Based on the structure shown in Fig. 4.3 and invoking Ampere's law, the inner and outer boundary conditions of H for the n^{th} layer will be obtained,

$$H(x_{in}) = (n-1)H_{0p}, \quad (4.10)$$

$$H(x_{on}) = nH_{0p}, \quad (4.11)$$

where x_{in} and x_{on} are distances from the inner surface and outer surface of the n^{th} layer to the inner surface of the innermost layer, respectively. H_{0p} is the magnetic field intensity of the outer surface of the innermost layer and given by

$$H_{0p} = \frac{m_p I_p}{h_w}, \quad (4.12)$$

where m_p is the number of turns in each layer of the primary winding. Substituting (4.10) and (4.11) into (4.8), A_1 and A_2 are derived by

$$A_1 = H_{0p} \frac{ne^{-\lambda x_{in}} - (n-1)e^{-\lambda x_{on}}}{2 \sinh(\lambda t_p)}, \quad (4.13)$$

$$A_2 = H_{0p} \frac{(n-1)e^{\lambda x_{on}} - ne^{\lambda x_{in}}}{2 \sinh(\lambda t_p)}, \quad (4.14)$$

where t_p is the conductor thickness of the primary winding and $t_p = x_{on} - x_{in}$. Introducing (4.13) and (4.14) into (4.8), the H field inside the n^{th} layer of the primary winding along x axis is obtained as

$$H(x) = H_{0p} \frac{n \sinh(\lambda x) + (n-1) \sinh[\lambda(t_p - x)]}{\sinh(\lambda t_p)}, \quad (4.15)$$

with $0 \leq x \leq t_p$ and x starts at the inner surface of the n^{th} layer which means the reference coordination is different from the coordination shown in Fig. 4.3 where the original point of x axis is at the middle of centre leg. The displacement of the reference coordination in (4.15) is x_{in} for the n^{th} layer.

Referring to the calculations given in [115] based on the Poynting vector, the magnetic field energy stored in the n^{th} primary layer is calculated by

$$E_{pn} = \frac{\mu_0 l_w (m_p I_p)^2}{8h_w} \delta_0 \left[\frac{\sinh(2\Delta) - \sin(2\Delta)}{\cosh(2\Delta) - \cos(2\Delta)} + 2n(n-1) \frac{\sinh \Delta + \sin \Delta}{\cosh \Delta + \cos \Delta} \right], \quad (4.16)$$

where l_w is the length of each layer, δ_0 is the skin depth and Δ is defined as

$$\Delta = \frac{t_p}{\delta_0}. \quad (4.17)$$

The total magnetic field energy stored in the primary winding is obtained by

$$E_p = \sum_{n=1}^{n_p} E_{pn} = \frac{\mu_0 l_w t_p n_p (m_p I_p)^2}{8h_w \Delta} \left[\frac{\sinh(2\Delta) - \sin(2\Delta)}{\cosh(2\Delta) - \cos(2\Delta)} + \frac{2(n_p^2 - 1)}{3} \frac{\sinh \Delta + \sin \Delta}{\cosh \Delta + \cos \Delta} \right], \quad (4.18)$$

where n_p is the number of layers in the primary winding and the total number of turns in the primary winding is $N_p = n_p m_p$. In a similar way, the total magnetic field energy stored in the conductors of secondary windings is given by

$$E_s = \sum_{n=1}^{n_s} E_{sn} = \frac{\mu_0 l_w t_s n_s (m_s I_s)^2}{8h_w \Delta} \left[\frac{\sinh(2\Delta) - \sin(2\Delta)}{\cosh(2\Delta) - \cos(2\Delta)} + \frac{2(n_s^2 - 1)}{3} \frac{\sinh \Delta + \sin \Delta}{\cosh \Delta + \cos \Delta} \right], \quad (4.19)$$

where n_s and t_s are the number of turns in each secondary layer and the conductor thickness of the secondary winding, respectively.

On the other hand, the magnetic field energy stored in the insulation between two adjacent layers should be considered. The H field in the insulation layer maintains a

constant value equal to the strength at the conductor outer surface. For instance, the magnetic field intensity of the insulation layer between n^{th} and $(n+1)^{\text{th}}$ layer of the primary winding is nH_{0p} . The total magnetic field energy stored in the insulations is calculated by

$$\begin{aligned} E_{\text{ins}} &= \frac{1}{2} \mu_0 l_w h_w t_{\text{ins}} \left(H_{0p}^2 \sum_{n=1}^{n_p} n^2 + H_{0s}^2 \sum_{n=1}^{n_s-1} n^2 \right) \\ &= \frac{\mu_0 l_w t_{\text{ins}}}{12h_w} \left[n_p (n_p + 1)(2n_p + 1)(m_p I_p)^2 + \right. \\ &\quad \left. n_s (n_s - 1)(2n_s - 1)(m_s I_s)^2 \right], \end{aligned} \quad (4.20)$$

where t_{ins} is the insulation thickness between two adjacent layers and it is assumed to be identical for all insulations in the transformer.

Finally, the total leakage inductance of the transformer referred to the primary side is derived as

$$L_{\text{lk}} = \frac{2(E_p + E_s + E_{\text{ins}})}{I_p^2}. \quad (4.21)$$

Assuming the number of turns in each conductor layer is $m_p = m_s = 1$ and the thickness of all conductors is the same as $t_s = t_p$, the total leakage inductance referred to the primary side calculated by (4.21) is given by

$$L_{\text{lk}} = \frac{\mu_0 l_w n_p (1+a)}{12h_w} \left[3t_p A_{\Delta} + 2t_p \left(\frac{1}{a} n_p^2 - 1 \right) B_{\Delta} + 2t_{\text{ins}} \left(\frac{2}{a} n_p^2 + 1 \right) \right], \quad (4.22)$$

with

$$A_{\Delta} = \frac{1}{\Delta} \frac{\sinh(2\Delta) - \sin(2\Delta)}{\cosh(2\Delta) - \cos(2\Delta)}, \quad (4.23)$$

$$B_{\Delta} = \frac{1}{\Delta} \frac{\sinh \Delta + \sin \Delta}{\cosh \Delta + \cos \Delta}, \quad (4.24)$$

where a is the turns ratio of the primary winding to the secondary winding.

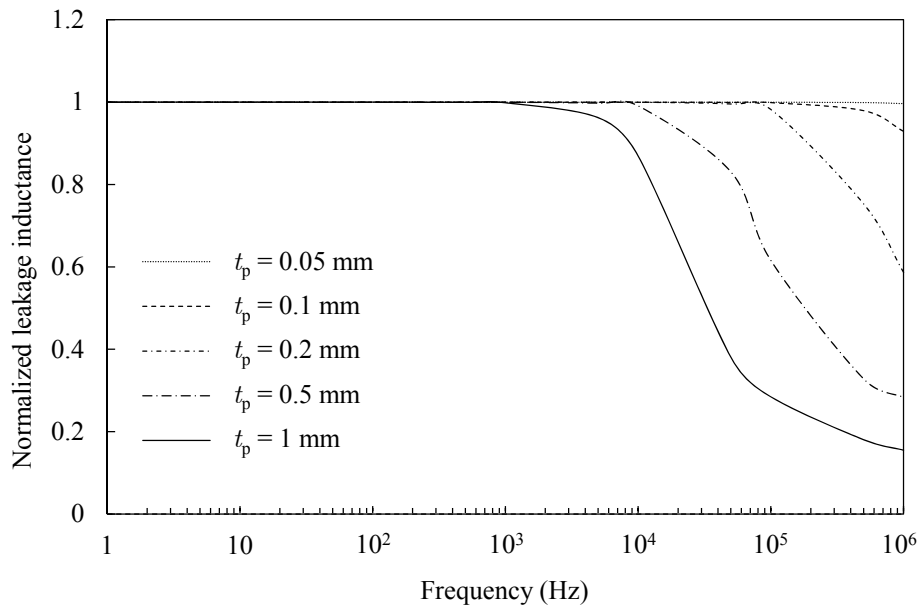


Fig. 4.4 Calculated leakage inductances versus frequencies for different conductor thicknesses

Calculations for leakage inductance at different frequencies have been carried out based on ETD39 core. The number of primary turns is fixed to be $N_p = 4$ and the turns ratio is $a = 1$. The thickness of conductors in the primary and secondary windings is selected to vary as five values, $t_p = 0.05$ mm, 0.1 mm, 0.2 mm, 0.5 mm, 1 mm. The height of windings is $h_w = 26$ mm. The length of windings is $l_w = 62.8$ mm. The insulation thickness is fixed as $t_{ins} = 0.1$ mm for different cases. The frequency range is selected from 1 Hz to 1 MHz.

Fig. 4.4 shows the curves of leakage inductances versus frequencies and conductor thicknesses. The leakage inductances at 1 Hz are applied to normalize the calculated results. In each case, the leakage inductance of the transformer reduces along with higher frequency. For the thicker conductor, the leakage inductance diminution will be more evident at relatively lower frequency. Considering high frequency effects on the winding loss and leakage inductance, the thinner conductor is preferred as expected.

The above calculation is based on the winding structure with no interleaving, in which the primary layers and secondary layers are placed totally separated from each other. In practical applications, the interleaved configuration of the primary winding and secondary winding is commonly used to reduce the winding loss due to proximity

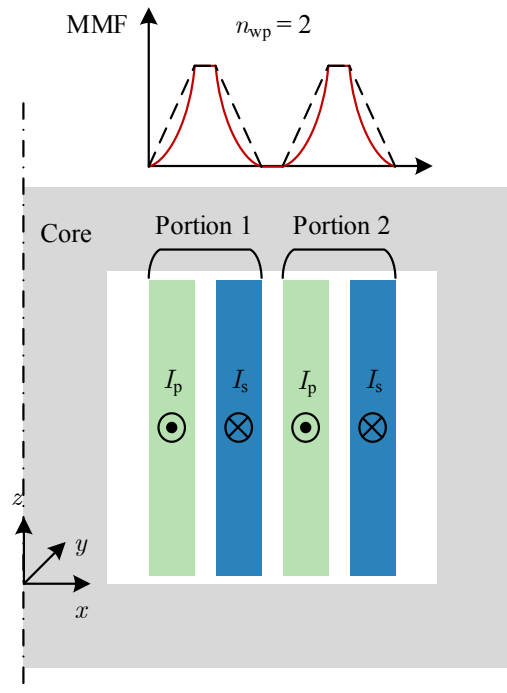


Fig. 4.5 Full interleaved winding configuration and the winding portion

effect. Thus, the high frequency leakage inductance should be investigated for interleaved windings and the following section will mainly focus on this issue.

4.3. Leakage Inductance with Interleaving Windings

The interleaving windings can be divided into several winding portions depending on interleaving level. In one winding portion, the primary winding and secondary winding are both included with no interleaving. Supposing the number of winding portions is represented by n_{wp} . For the winding arrangement in Fig. 4.3, $n_{wp} = 1$. The formula of leakage inductance calculation presented as (4.22) can be applied in each winding portion with the number of layers, n_p , replaced by the number of layers in one portion, n_{pp} .

Fig. 4.5 demonstrates the winding configuration with interleaving and the number of winding portions is 2. In each portion, there are one primary layer and one secondary layer. This kind of interleaving structure is named the full interleaved winding configuration. The other interleaving windings in which the number of primary or secondary layers more than one in each portion is called partially interleaved winding

configuration. The MMF distribution along the window width of low frequency and high frequency is presented in Fig. 4.5. The H field inside the primary conductor in whichever portion can be obtained by (4.15) with $n = 1$,

$$H(x) = H_{0p} \frac{\sinh(\lambda x)}{\sinh(\lambda t_p)}. \quad (4.25)$$

The leakage inductance in each portion of the full interleaved winding configuration can be found from (4.22) with $n_p = 1$ and $a = 1$,

$$L_{lkpp} = \frac{\mu_0 l_w}{2h_w} (t_p A_\Delta + 2t_{ins}). \quad (4.26)$$

The total leakage inductance for the interleaved winding with $m_p = m_s = 1$ is obtained by

$$L_{lk} = n_{wp} L_{lkpp} = \frac{\mu_0 n_{wp} l_w}{2h_w} (t_p A_\Delta + 2t_{ins}). \quad (4.27)$$

For partially interleaved windings, the similar calculation principle can be employed. The associated simulations and experimental verifications for different kinds of interleaved structures will be described next.

4.4. Experimental Verifications for High Frequency Leakage Inductance

4.4.1 Simulations and Measurements of Leakage Inductances

The experiments were carried out on the magnetic core ETD39. The results including calculations, FEA simulations and measurements are comprehensively compared. The parameters for the objective transformer are listed in Table 4.1.

Fig. 4.6 presents the H field distribution along the winding width direction for the winding configuration with no interleaving. At low frequency (around 100 kHz), the H field almost linearly distributes inside the conductor as expected. With the increasing frequency, the current due to the high frequency eddy current effect flows at the surface of the conductors and it causes distribution of H field to be non-

TABLE 4.1 PARAMETERS OF THE TRANSFORMER FOR VERIFICATIONS

Parameters	Symbols	Values
Number of turns in primary winding	N_p	6
Turns ratio	a	1
Conductor thickness of primary winding	t_p	0.2 mm
Conductor thickness of secondary winding	t_s	0.2 mm
Thickness of insulation layers	t_{ins}	0.25 mm
Magnetic core		ETD 39
Core material		Ferrite N87
Height of the core window area or windings	h_w	26 mm
<i>MLT</i> of windings	l_w	62.8 mm

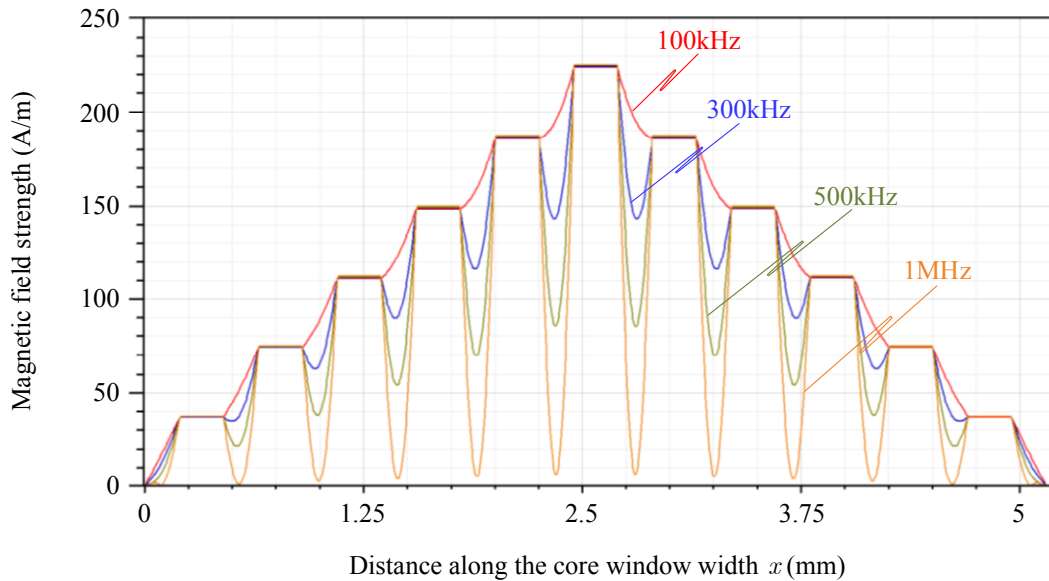


Fig. 4.6 FEA simulations of H field along the winding width direction

uniformly as shown. With more layers in the winding, the curve of the H field appears as “concave shape” and the shape becomes more concave because the proximity effect concentrates the current concentrating on the conductor surface. The leakage inductance at higher frequency is smaller than the value at low frequency.

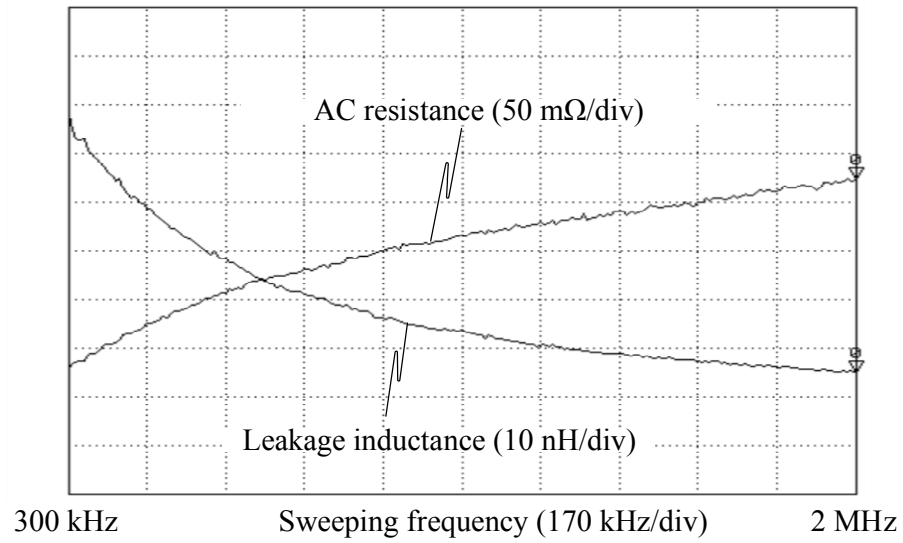


Fig. 4.7 Leakage inductance measured by HP-4294A

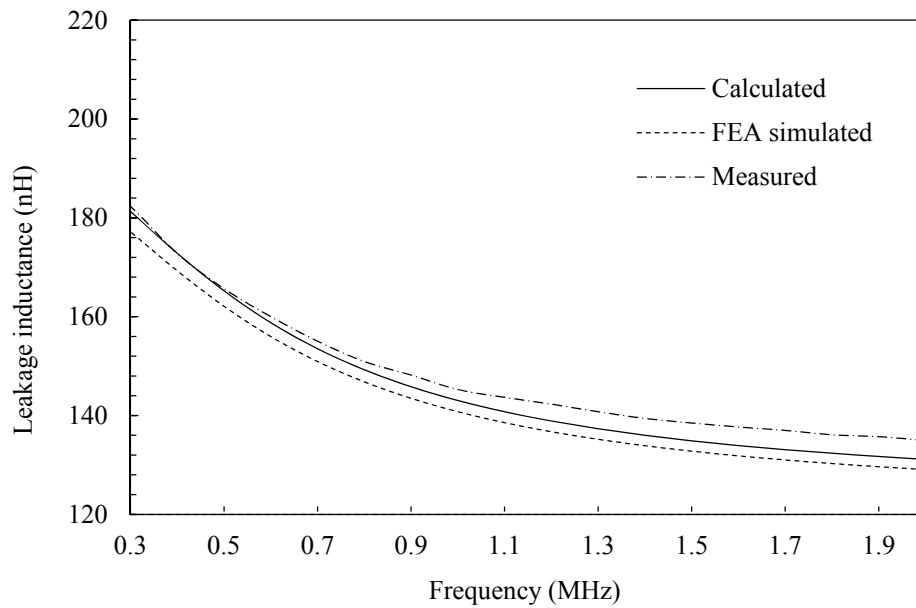


Fig. 4.8 Comparisons of calculated, FEA simulated and measured leakage inductance at different frequencies

The measurement results of leakage inductances and AC resistances versus different frequencies were carried out using the precision impedance analyser HP-4294A. The secondary winding of the transformer under test is shorted and the leakage inductance was measured at the primary side. One of measured results is shown in Fig. 4.7. It is obvious that the leakage inductance decreases with increasing frequency. The leakage

inductance at 300 kHz is 188 nH and the value is 134 nH at 2 MHz. Actually, the leakage inductance approximately reduces by 29%.

The leakage inductance calculated based on the proposed formula was compared with FEA simulations and the measurement results. The FEA simulations were carried out by Ansoft Maxwell. The comparisons in a wide range of frequencies (from 300 kHz to 2 MHz) are presented in Fig. 4.8. The results demonstrate the overall agreement between calculated, FEA simulated and experimental results.

4.4.2 Leakage Inductances of Different Interleaved Configurations

Interleaving of windings can eliminate the high frequency winding loss due to the weakened proximity effect. According to the presented calculation method, it is possible to evaluate the leakage inductances of transformers with different interleaved configurations. Basically, four cases of the winding structures were studied and they are shown in Fig. 4.9.

Case-A is the non-interleaved winding configuration. The primary winding and secondary winding are placed totally separated from each other and this structure only has one portion which consists of 6 primary layers and 6 secondary layers. Case-B shows partially interleaved windings and 3 portions can be found in this transformer. Each portion includes 2 layers of primary conductors and 2 layers of secondary conductors. Case-C and Case-D present two fully interleaved winding configurations and both of them have 6 portions. Single primary layer and single secondary layer are included in one portion.

The calculated and simulated results of leakage inductances at 1 MHz are listed in Table 4.2. Obviously, the leakage inductance of interleaved windings is reduced significantly compared to the non-interleaved structure as predicted.

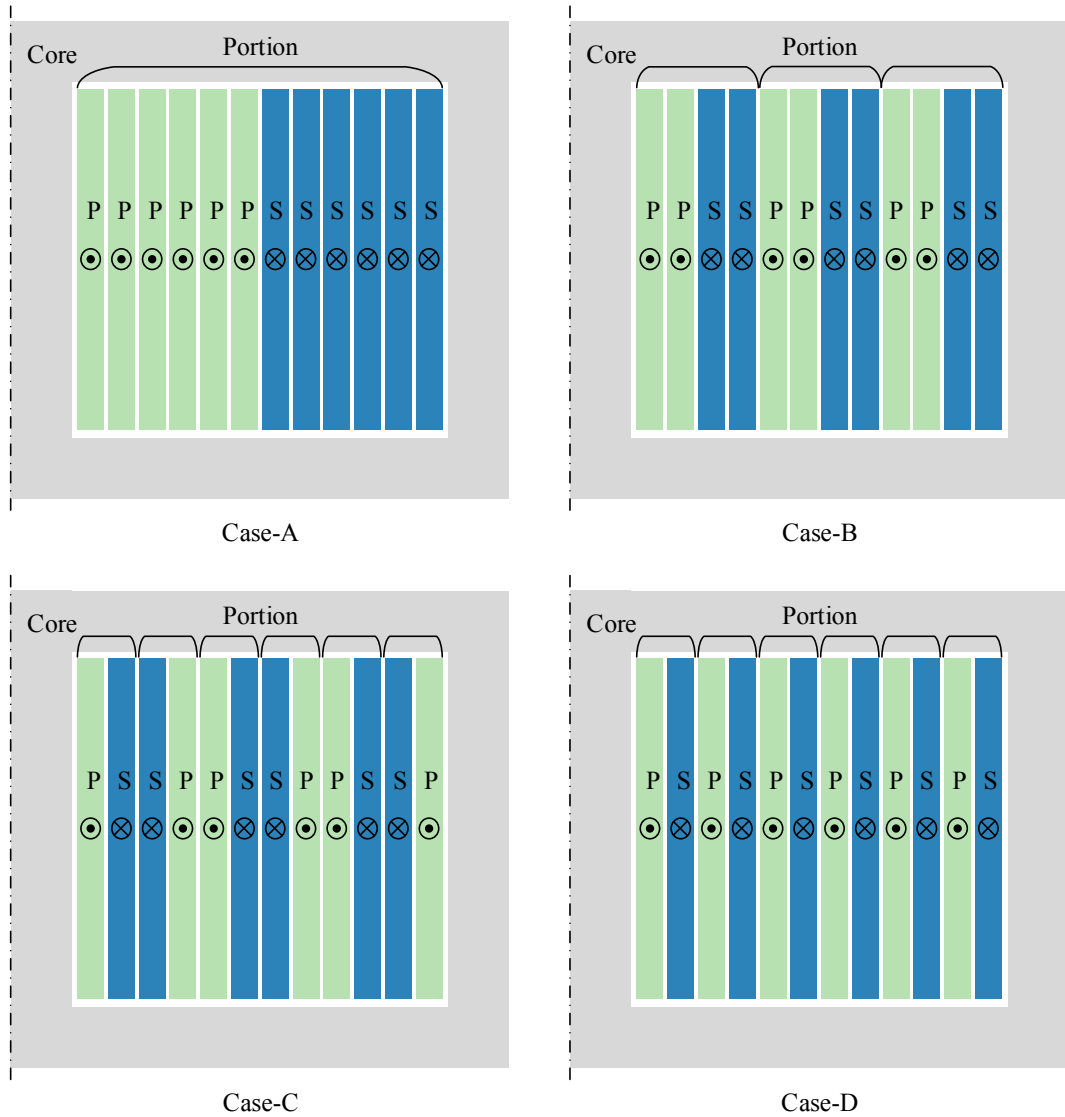


Fig. 4.9 Four transformer configurations with different interleaved windings

Table 4.3 lists the measurement results of leakage inductance at 10 Hz and 1 MHz for different cases. It is the non-interleaved case that has the most pronounced reduction of leakage inductance with increasing frequency. With more winding layers in one portion of non-interleaved winding configuration, the stronger proximity effect will force more H field distributed in the outer surface of the conductors.

The simulated results of leakage energy stored in the window area and MMF distribution for different cases are given in Fig. 4.10. As expected, the leakage energy shown in Case-D is dramatically reduced.

TABLE 4.2 CALCULATED AND SIMULATED RESULTS OF LEAKAGE INDUCTANCES FOR FOUR DIFFERENT WINDING CONFIGURATIONS

Cases	Leakage inductance (L_{lk})	Calculated	FEA simulated	Measured
Case-A	$\frac{\mu_0 l_w}{h_w} (3t_p A_\Delta + 70t_p B_\Delta + 146t_{ins})$	127 nH	140.8 nH	138 nH
Case-B	$\frac{\mu_0 l_w}{h_w} (3t_p A_\Delta + 6t_p B_\Delta + 18t_{ins})$	15.6 nH	17.3 nH	17.3 nH
Case-C	$\frac{3\mu_0 l_w}{h_w} (t_p A_\Delta + 2t_{ins})$	5.16 nH	5.74 nH	5.72 nH
Case-D	$\frac{3\mu_0 l_w}{h_w} (t_p A_\Delta + 2t_{ins})$	5.16 nH	5.71 nH	5.71 nH

TABLE 4.3 MEASURED LEAKAGE INDUCTANCES AT 10 HZ AND 1 MHz

Cases	Leakage inductance (10 Hz)	Leakage inductance (1 MHz)	Reduction
Case-A	216 nH	138 nH	36%
Case-B	23 nH	17.3 nH	25%
Case-D	6.88 nH	5.71 nH	17%

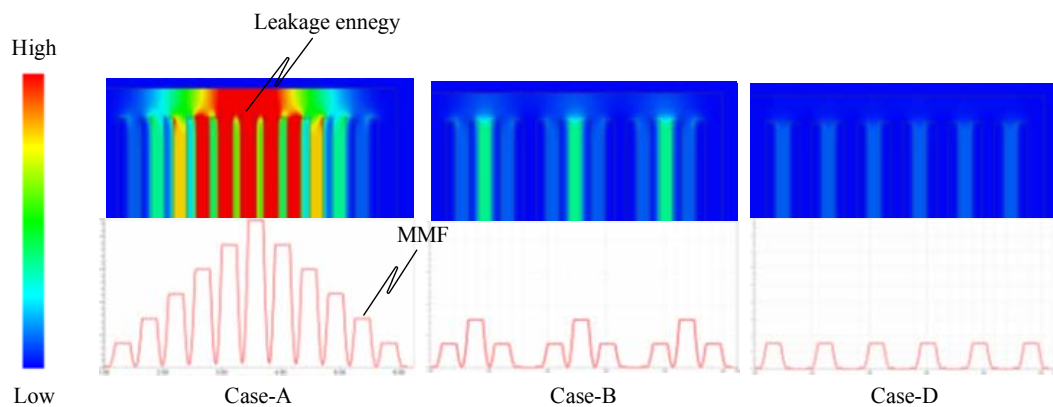


Fig. 4.10 FEA simulations results of H field in the window area

4.5. Stray Capacitances in the Conventional Transformer

In the wire wound transformer, the stray capacitances will appear between adjacent conductors in one layer and conductors in different adjacent layers if the capacitance between the winding and the magnetic core and the capacitance between the winding and the shield screen are ignored. Taking the transformer applied in the LLC resonant converter for example, the stray capacitance will be modelled based on the specific winding configuration as shown in Fig. 4.11.

The primary winding has two layers and two secondary windings are interleaved with the primary layers. The magnetic core is ETD 39. The diameters of the primary and secondary wires are 0.8 mm and 1.2 mm, respectively. There are $n_p = 18$ turns and $n_s = 12$ turns in each primary layer and secondary layer, respectively. The other dimensions are labelled in Fig. 4.11(b). In order to clearly demonstrate the constructions of the transformer windings, the proportion of Fig. 4.11 (b) is not to the scale.

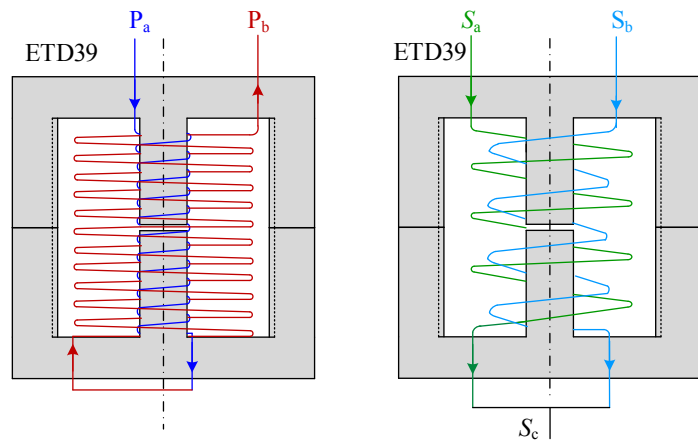
First of all, the equivalent relative permittivity of the air and insulation kapton tape between each two layers should be worked out. With the relative permittivity of kapton tape of $\epsilon_r = 3.8$, the equivalent relative permittivity between the primary and the secondary layers is calculated by

$$\epsilon_{ps} = \frac{\epsilon_r (d_{in1} + d_{air})}{d_{in1} + \epsilon_r d_{air}} = 2.235. \quad (4.28)$$

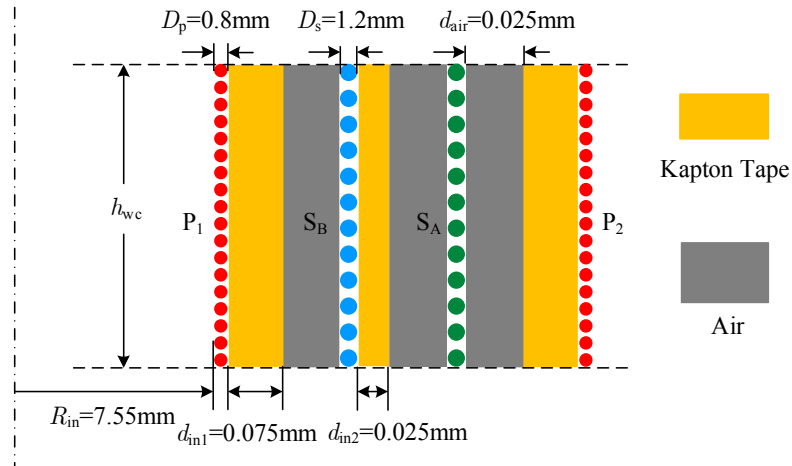
The equivalent relative permittivity between two secondary layers is

$$\epsilon_{ss} = \frac{\epsilon_r (d_{in2} + d_{air})}{d_{in2} + \epsilon_r d_{air}} = 1.583. \quad (4.29)$$

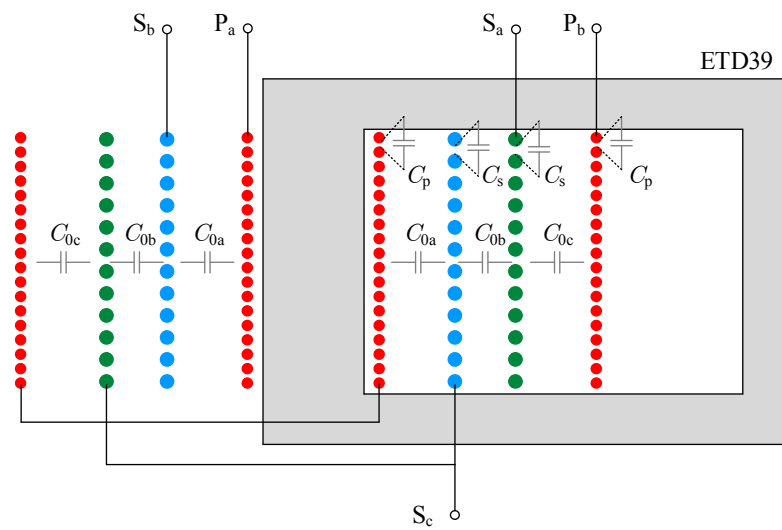
The relative permittivity of wire insulation between two adjacent turns in the same layer is $\epsilon_{in} = 2$. The parallel plate capacitor model will be applied to calculate the capacitance, since the radius of curvature is quite large.



(a) Winding configurations of examined wire wound transformer



(b) Dimensions of the transformer windings and insulations



(c) Winding connections and stray capacitance distribution

Fig. 4.11 Winding configuration and dimensions of the studied wire wound transformer

The height of each winding is calculated by

$$h_{pri} = n_p D_p = 14.4 \text{ mm}, \quad h_{sec} = n_s D_s = 14.4 \text{ mm}. \quad (4.30)$$

The inner and outer radii of each cylindrical layer are given as:

Layer P ₁	$R_{p1}^{in} = 7.55 \text{ mm}$	$R_{p1}^{out} = 8.35 \text{ mm}$
Layer S ₁	$R_{sB}^{in} = 8.45 \text{ mm}$	$R_{sB}^{out} = 9.65 \text{ mm}$
Layer S ₂	$R_{sA}^{in} = 9.7 \text{ mm}$	$R_{sA}^{out} = 10.9 \text{ mm}$
Layer P ₂	$R_{p2}^{in} = 11 \text{ mm}$	$R_{p2}^{out} = 11.8 \text{ mm}$

The distances between two successive turns for the primary and secondary windings are

$$d_{tp} = \frac{h_{wc} - n_p D_p}{n_p - 1} + D_p = 0.953 \text{ mm}, \quad d_{ts} = \frac{h_{wc} - n_s D_s}{n_s - 1} + D_s = 1.436 \text{ mm}, \quad (4.31)$$

where h_{wc} is the height of the core window. The effective distances between two adjacent layers are calculated by

$$\left\{ \begin{array}{l} d_{ps} = \frac{1}{2} \left(\begin{array}{l} D_s + d_{in1} + d_{air} - \frac{2.3D_p}{2} + 0.26d_{tp} + \\ D_s + d_{in1} + d_{air} - \frac{2.3D_s}{2} + 0.26d_{ts} \end{array} \right) = 2.606 \times 10^{-4} \text{ mm}, \\ d_{ss} = D_s + d_{in2} + d_{air} - \frac{2.3D_s}{2} + 0.26d_{ts} = 2.435 \times 10^{-4} \text{ mm}. \end{array} \right. \quad (4.32)$$

The effective distances between adjacent turns in the same layer of primary and secondary windings are obtained by

$$\left\{ \begin{array}{l} d_{Lp} = D_p + \frac{h_{wc} - n_p D_p}{n_p - 1} - \frac{2.3D_p}{2} + 0.26d_{tp} = 2.807 \times 10^{-4} \text{ mm} \\ d_{Ls} = D_s + \frac{h_{wc} - n_s D_s}{n_s - 1} - \frac{2.3D_s}{2} + 0.26d_{ts} = 4.298 \times 10^{-4} \text{ mm} \end{array} \right. \quad (4.33)$$

Consequently, the capacitance between layer P₁ and S_A and the capacitance between two adjacent turns in layer P₁ are calculated by

$$\begin{cases} C_{0a} = \frac{\varepsilon_0 \varepsilon_{ps} \pi (R_{pl}^{\text{out}} + R_{sB}^{\text{in}}) h_{pri}}{d_{ps}} = 57.69 \text{ pF} \\ C_{p1} = \frac{\varepsilon_0 \varepsilon_{in} \pi (R_{pl}^{\text{in}} + R_{pl}^{\text{out}}) D_p}{d_{Lp}} = 2.52 \text{ pF} \end{cases} \quad (4.34)$$

Based on the same calculation method, we obtained $C_{0b} = 50.38 \text{ pF}$, $C_{0c} = 50.38 \text{ pF}$, and $C_{sA} = 2.81 \text{ pF}$, $C_{sB} = 3.20 \text{ pF}$, $C_{p2} = 3.61 \text{ pF}$.

In order to obtain the comprehensive stray capacitance model, the capacitances distributed in the transformer with three windings and five terminals shown in Fig. 4.12 are required. Supposing the supplied voltages of the transformer windings are presented as shown in the figure, the stored electrical field energy can be calculated by

$$W_E = \frac{1}{2} \begin{bmatrix} C_1 V_1^2 + C_2 V_2^2 + C_3 V_3^2 + C_4 (V_2 + V_3)^2 + C_5 V_4^2 + \\ C_6 (V_1 - V_2 - V_3 - V_4)^2 + C_7 (V_3 + V_4)^2 + \\ C_8 (V_1 - V_3 - V_4)^2 + C_9 (V_2 + V_3 + V_4)^2 + C_{10} (V_1 - V_4)^2 \end{bmatrix} \quad (4.35)$$

Fig. 4.13 shows the voltage distribution on each winding. The voltage level at point P_b is assumed to be zero and then we have

$$\begin{aligned} V_{pa} &= V_1, & V_{pb} &= 0, & V_{pc} &= 0.5V_1, \\ V_{sa} &= V_2 + V_3 + V_4, & V_{sb} &= V_4, & V_{sc} &= V_3 + V_4. \end{aligned} \quad (4.36)$$

The voltage at position x on each layer is

$$\begin{cases} V_{pa}(x) = \left(1 + \frac{x}{h_{pri}}\right) \frac{V_1}{2} \\ V_{sa}(x) = V_3 + V_4 + \frac{x}{h_{sec}} V_2 \\ V_{sb}(x) = V_3 + V_4 - \frac{x}{h_{sec}} V_3 \\ V_{pb}(x) = \left(1 - \frac{x}{h_{pri}}\right) \frac{V_1}{2} \end{cases} \quad (4.37)$$

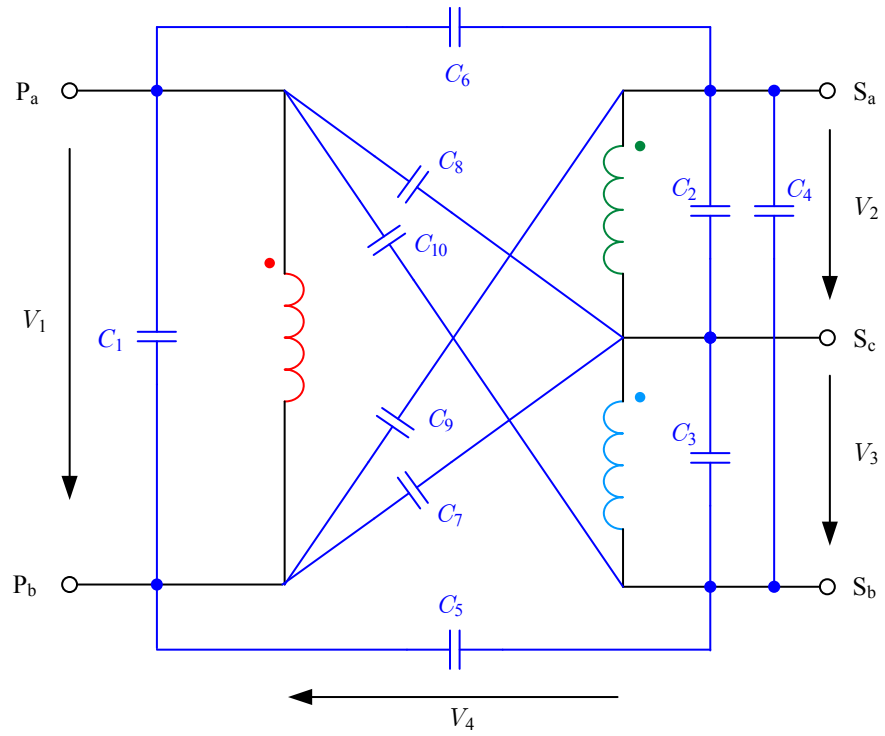


Fig. 4.12 Distributed stray capacitance model

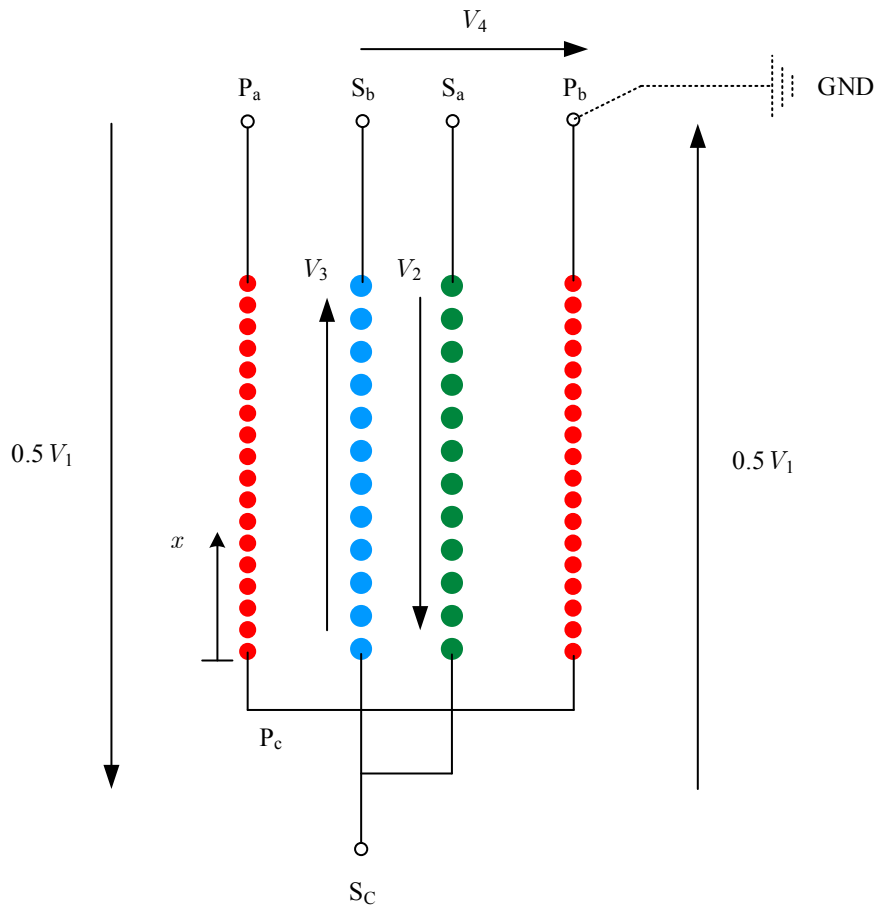


Fig. 4.13 Voltage distributed on the windings

For the area between layer P₁ and S_B, The electrical field energy is

$$W_{ps1} = \frac{1}{2} \frac{C_{0a}}{h_{pri}} \int_0^{h_{pri}} [V_{sb}(x) - V_{p1}(x)]^2 dx. \quad (4.38)$$

Thus,

$$W_{ps1} = \frac{1}{2} C_{0a} \left[\left(V_3 + V_4 - \frac{V_1}{2} \right)^2 - \left(V_3 + V_4 - \frac{V_1}{2} \right) \left(V_3 + \frac{V_1}{2} \right) + \frac{1}{3} \left(V_3 + \frac{V_1}{2} \right)^2 \right]. \quad (4.39)$$

According to the same principle, we can get

$$W_{ss} = \frac{1}{2} C_{0b} \left[\frac{1}{3} (V_2 + V_3)^2 \right], \quad (4.40)$$

$$W_{ps2} = \frac{1}{2} C_{0c} \left[\left(V_3 + V_4 - \frac{V_1}{2} \right)^2 + \left(V_3 + V_4 - \frac{V_1}{2} \right) \left(V_2 + \frac{V_1}{2} \right) + \frac{1}{3} \left(V_2 + \frac{V_1}{2} \right)^2 \right]. \quad (4.41)$$

The energies stored inside the self-capacitances of each layer are

$$\begin{aligned} W_{p1} &= \frac{17}{2} C_{p1} \left(\frac{1}{34} V_1 \right)^2, & W_{sa} &= \frac{11}{2} C_{sa} \left(\frac{1}{11} V_2 \right)^2, \\ W_{sb} &= \frac{11}{2} C_{sb} \left(\frac{1}{11} V_3 \right)^2, & W_{p2} &= \frac{17}{2} C_{p2} \left(\frac{1}{34} V_1 \right)^2. \end{aligned} \quad (4.42)$$

Combining these equations, each capacitance shown in Fig. 4.12 can be obtained and the values are

$$\begin{cases} C_1 = -22.1 \text{ pF}, & C_2 = -12.41 \text{ pF}, & C_3 = -9.47 \text{ pF}, \\ C_4 = 16.79 \text{ pF}, & C_5 = 4.81 \text{ pF}, & C_6 = 6.27 \text{ pF}, & C_7 = 34.69 \text{ pF}, \\ C_8 = 31.77 \text{ pF}, & C_9 = 31.34 \text{ pF}, & C_{10} = 24.04 \text{ pF}. \end{cases} \quad (4.43)$$

The simulation model for the LLC resonant converter with stray capacitors distributed in the transformer considered using PSIM. The simulated results show that the operation of the LLC resonant converter works well.

Based on the distributed stray capacitance model, the calculated capacitance between terminals P_a and S_a will be $C_{pasa} = 132.90 \text{ pF}$ with the other terminals open circuit.

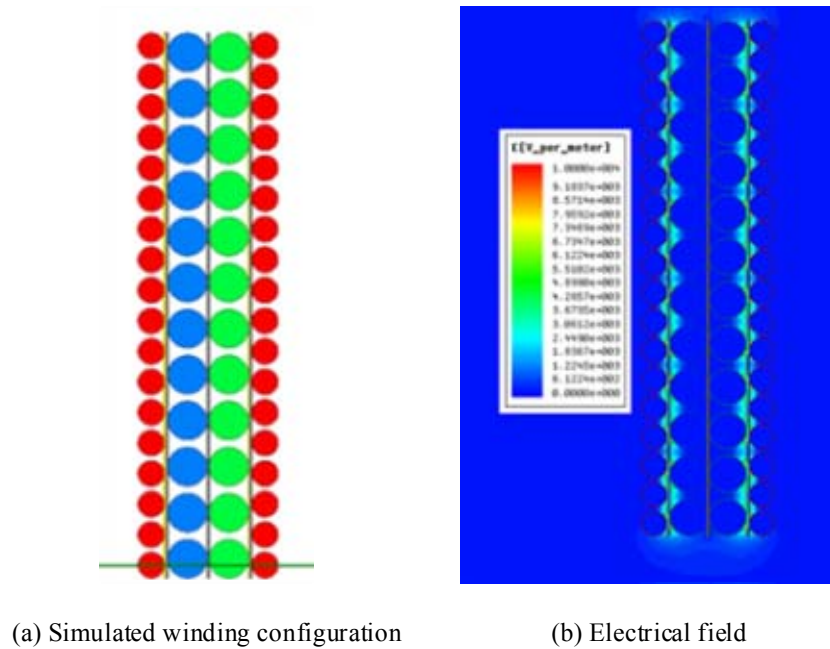


Fig. 4.14 Simulation model for the capacitor across P_a and S_a

The simulation has been carried out, as shown in Fig. 4.14 using Ansoft Maxwell. The simulation results is $C_{pasa} = 112.18\text{pF}$. The capacitance across terminals P_a and S_a was measured by the impedance analyser of Agilent 4395A with the other terminals open circuit and the test result is 119.63 pF which means the stray capacitance model is valid.

4.6. Conclusions

The high frequency operation of the transformer will cause a reduction in leakage inductance due to the eddy current effect. Based on the analysis, the proximity effect between adjacent layers exacerbates the reduction of leakage inductance. The formula for predicting the leakage inductance at high frequency was proposed in this chapter and the leakage inductances of different interleaving winding configurations were discussed. FEA simulation and measurement show good agreement with the predictions. On the other hand, the stray capacitance was modelled for the wire wound transformer and the detailed calculation process based on the transformer applied in LLC resonant converter has been carried out. The method was validated by both the simulation and measurements. The corresponding analysis for planar transformer will be considered in Chapter 5.

5

Analysis and Modelling of Planar Transformers

The planar transformer is now widely used in the converters for the low profile, automated manufacturing, high power density and consistently predictable parameters. For the planar core, the manufacturers have released lots of commercial products. Basically, planar cores have rectangular or circular cross section of the centre leg. On the other hand, planar windings implemented by PCB and copper foils are extensively employed in magnetic components for power supplies applications. The associated winding loss evaluation considering the high frequency effect is noteworthy for the planar transformer design. Meanwhile, the excitation currents in the primary winding and secondary winding of the transformer might not be in phase. The accurate prediction of winding loss with phase-shifted excitations should be investigated. Because the footprint of the planar transformer is bigger than the conventional transformer and the overlapping area of windings might be large, the stray capacitance of the planar transformer needs further discussion. For the advantage of implementing planar transformer windings under accurate control, the leakage inductance can be implemented. Consequently, the series inductor connected with the transformer in the circuit, for instance, the LLC resonant converter, can be integrated with the planar transformer by enhanced leakage inductance. In this chapter, all these issues of great concern will be covered.

TABLE 5.1 VOLUMES AND THERMAL RESISTANCES OF PLANAR CORES

Core	Volume (mm ³)	Thermal resistance (°C/W)
EELP14	296	105
EELP18	955	56
EELP22	2540	35
EELP32	5390	24
EELP38	10200	18
EELP43	13748	15
EELP58	25000	11
EELP64	41500	9
ER9.5/5	120	164
ER11/5	174	134
ER14.5/6	333	99

5.1 Planar Cores

Commercial planar cores include planar EE or EI cores, planar ER cores and other low profile versions of standard cores such as RM, PQ and port cores. The most commonly applied planar cores are planar EE and ER cores listed in Appendix A and their shapes are shown in Fig. A.1. The thermal resistances of planar cores are provided by the manufacturer and listed in Table 5.1. According to data fitting, as illustrated in Fig. 5.1, the thermal resistance of the planar transformer related to the volume is given by

$$R_{\theta} = \frac{0.056}{\sqrt{V_c}}, \quad (5.1)$$

where V_c is the planar core volume in unit of m³.

Due to the different cross-sectional shapes in Planar EE and ER cores, the winding configuration will vary. Fig. 5.2 shows the two winding configurations assembled with planar EE and ER cores, respectively. Assuming the two cores have exactly the same size which means the length and the width are identical as shown in the figure, the

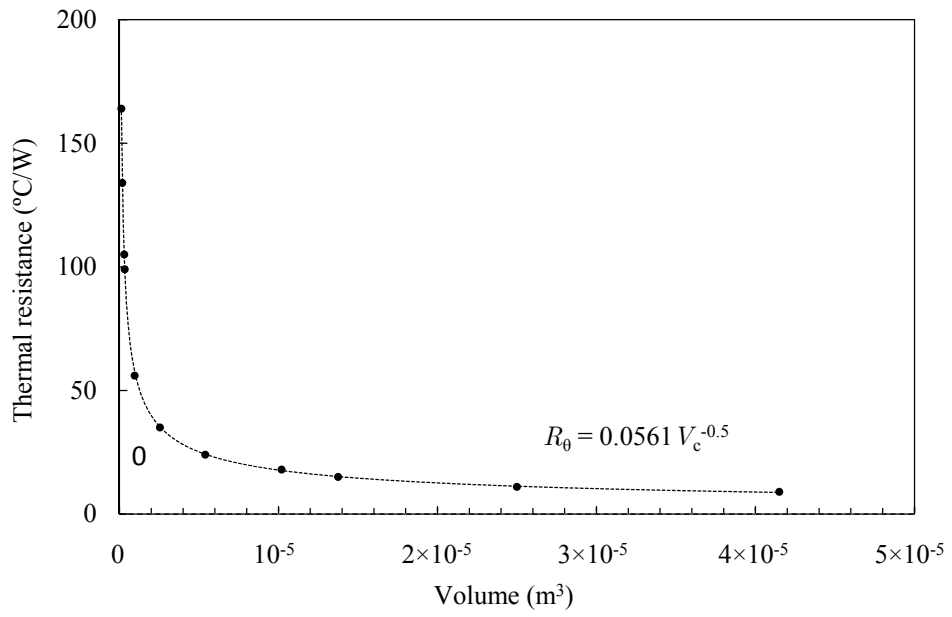


Fig. 5.1 Data fitting of thermal resistances versus planar core volume

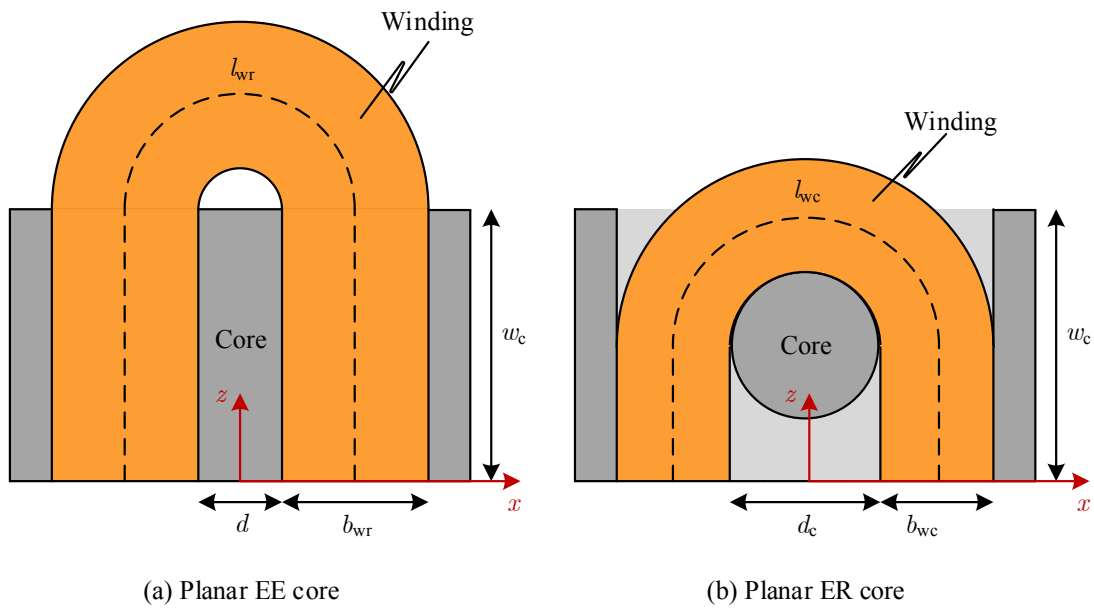


Fig. 5.2 Winding configurations assembled with planar EE and ER cores

diameter of the centre leg in the ER core will be related to the width of the centre leg in the EE core by

$$d_c = 2\sqrt{\frac{d \cdot w_c}{\pi}}, \quad (5.2)$$

where the symbols are shown in Fig. 5.2. The DC resistances and associated DC power losses of two winding configurations will be calculated as follows.

In the planar EE core, the conducting length of the segment at position x is obtained by

$$l_{wr_x} = 2w_c + \pi \left(\frac{d}{2} + x \right). \quad (5.3)$$

Assuming the DC voltage across two terminals is V_{dc} and the conductor thickness is t , the planar winding loss is given by

$$P_{cu_r} = \int_{\frac{d}{2}}^{\frac{d}{2}+b_{wr}} \frac{V_{dc}^2 t}{\rho_w l_{wr_x}} dx = \frac{V_{dc}^2 t}{\pi \rho_w} \ln \left[\frac{\pi d + \pi b_{wr} + 2w_c}{\pi d + 2w_c} \right]. \quad (5.4)$$

With the same principle, the winding loss for the planar ER core is obtained as

$$l_{wc_x} = w_c + \pi \left(\frac{d_c}{2} + x \right),$$

$$P_{cu_c} = \int_{\frac{d_c}{2}}^{\frac{d_c}{2}+b_{wc}} \frac{V_{dc}^2 t}{\rho_w l_{wc_x}} dx = \frac{V_{dc}^2 t}{\pi \rho_w} \ln \left[\frac{\pi d_c + \pi b_{wc} + w_c}{\pi d_c + w_c} \right]. \quad (5.5)$$

Due to the same length of planar EE and ER cores, we have

$$\frac{d}{2} + b_{wr} = \frac{d_c}{2} + b_{wc}. \quad (5.6)$$

In order to compare winding losses of planar EE core and ER cores, the normalized difference is defined as

$$\varepsilon = \frac{P_{cu_r} - P_{cu_c}}{P_{cu_r}}. \quad (5.7)$$

According to the dimensions of typical planar EE cores listed in the Appendix A, the calculation results of ε is shown in Fig. 5.3. It is indicated that the DC resistance of windings implemented in the planar ER core is much less than planar EE cores. Besides, the total footprint of planar ER core and winding is smaller.

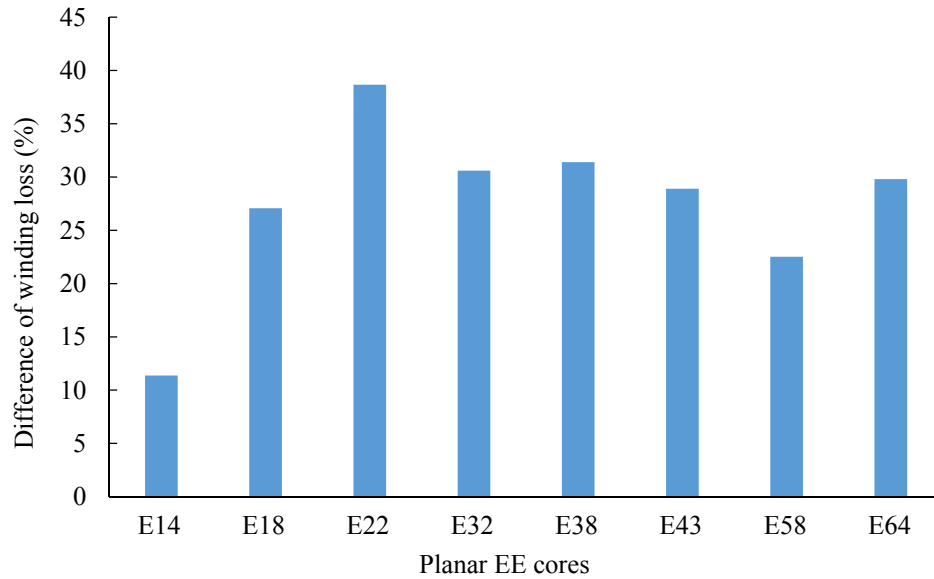


Fig. 5.3 Differences between winding losses of planar EE and ER cores

In practice, the selection of planar core shapes will take other factors into account, such as the assembly with PCB boards and cooling conditions, which means the planar ER cores are not always the prime choices other than planar EE cores. Referring to [201], the author found that the high frequency winding loss with ER core is bigger than EE core under the specific stated conditions. Consequently, the selection of planar core shapes needs comprehensive consideration.

5.2 Winding Loss Modelling of Planar Transformers

For the planar windings implemented by PCB copper tracks or copper foils, the winding configuration will differ from conventional ones. The planar winding generally has quite a big ratio of conductor width to thickness. Depending on the symmetrical characteristics, planar windings can be divided into strip conductors (based on the Cartesian coordinate system) and circular conductors (based on the Polar coordinate system), as shown in Fig. 5.4.

For the strip conductor, the current density distribution is uniform with low frequency excitation. The current density in the conductor will vary at high frequency due to eddy current effects. Nevertheless, the current density within the circular conductor is naturally non-uniform because the shorter path at the inner side of the conducting

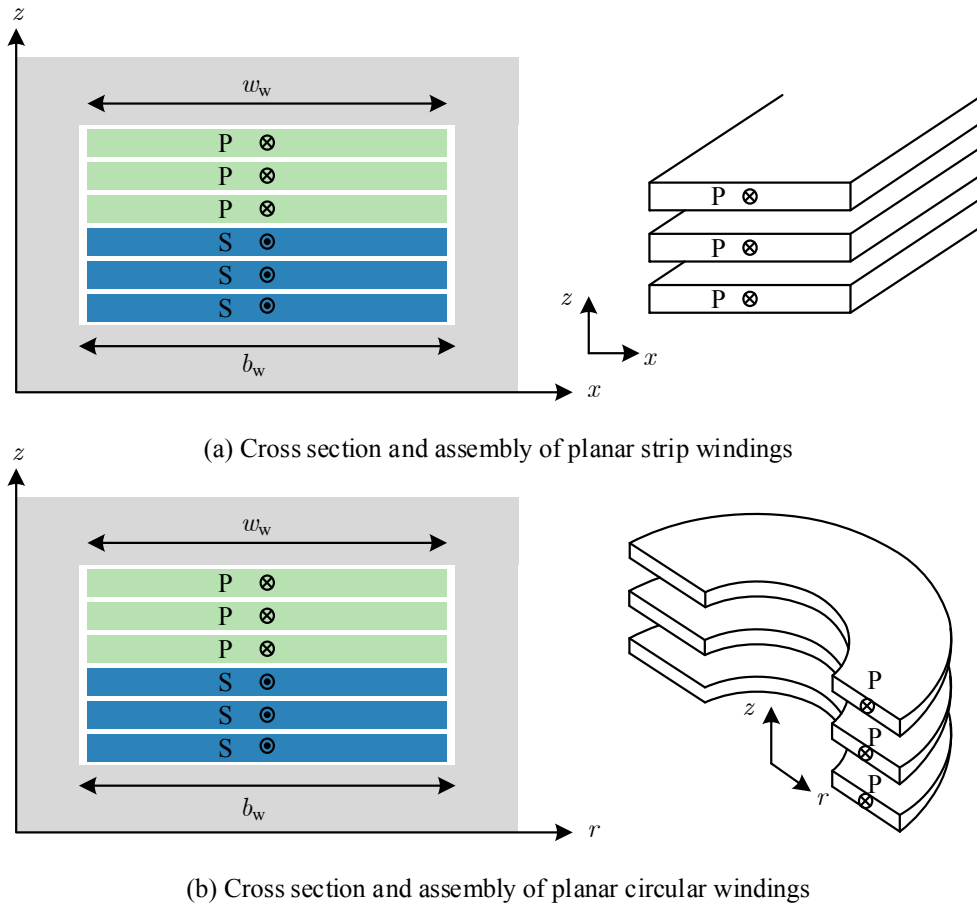


Fig. 5.4 Planar windings for strip conductors and circular conductors

section signifies lower resistance and the current density is therefore higher in the inner side than the outer side with DC excitation. The current distribution at higher frequency would be more complex.

5.2.1 Winding Loss for Strip Conductors

As shown in Fig. 5.4(a), Dowell's equation can be applied to obtain the high frequency winding loss with 1-D assumption for the magnetic field in the window area. However, the width of strip conductors w_w is practically smaller than the width of core window b_w . In some situations, a few turns will be implemented in one layer. The equivalent methodology proposed in [84] and [86] can be introduced to transfer the narrow strip conductor to the conductor filling the full window width. Fig. 5.5 illustrates the details of the equivalent transformation.

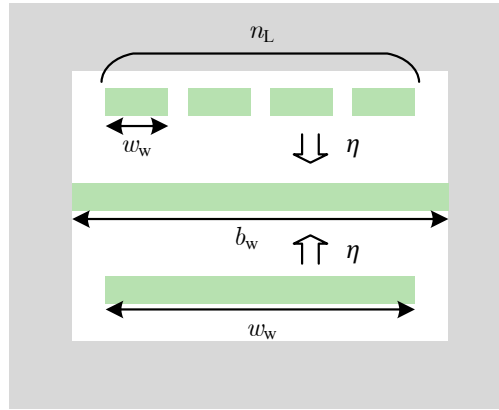


Fig. 5.5 Equivalent transformation for narrow strip conductor

The porosity factors are employed in the transformation process and defined as

$$\eta = \frac{n_L w_w}{b_w}, \quad (5.8)$$

where n_L and w_w are the number of turns per layer and the width of narrower conductor shown in the figure, respectively. The equivalent conductivity is defined as

$$\sigma' = \eta \sigma. \quad (5.9)$$

A series of simulations have been carried out for strip conductors with different widths and configurations. The thickness of conductors is fixed as 0.2 mm and the simulated frequencies of excitations are 100 kHz and 1 MHz. The selected planar core is EELP 64/10/50 and the window width is 21.8 mm. The winding length is 101.6 mm. The number of layers in the primary and secondary windings are both 2. The primary winding and secondary winding are non-interleaved. The insulation thickness between two layers is 0.1 mm. The number of turns in each layer is 1 and the values of porosity factors are assigned from 1 to 0.5. The simulated and calculated results of the ratio for the AC resistance R_{ac} to the DC resistance R_{dc} by Dowell's method are presented in Fig. 5.6.

It is illustrated that the calculation through porosity factor transformation method is accurate enough for high filling value. However, the calculated result will lead to big error when the conductor width is much shorter than the window width. The actual AC winding resistance is bigger than predicted value because the edge effect increases the losses due to the existence of vertical H field parallel to the conductor edge. In

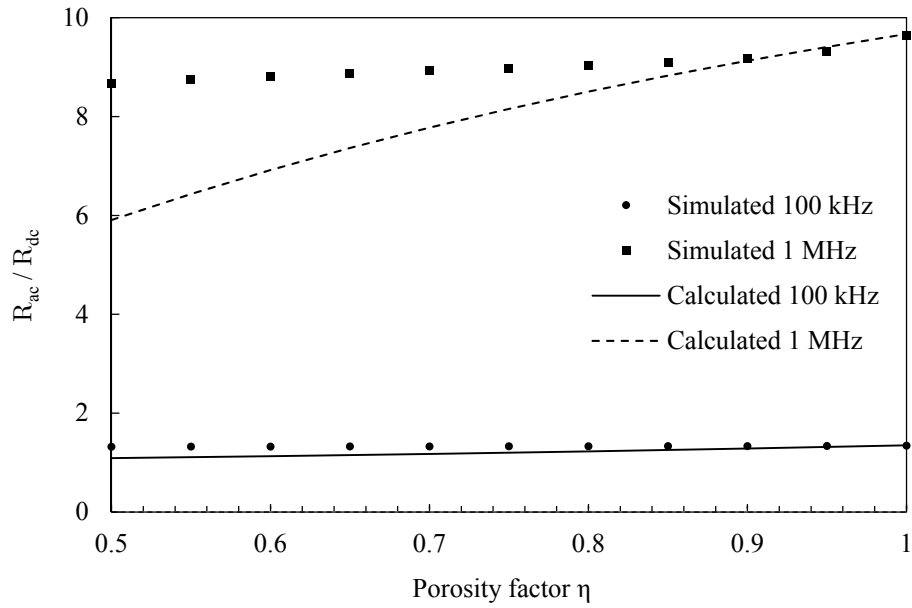
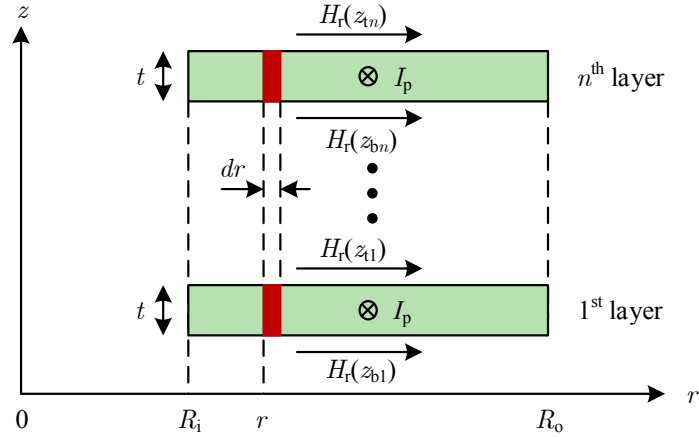


Fig. 5.6 Simulated and calculated results of R_{ac} / R_{dc} for strip conductors

particular, more conductor is allocated in the window area for the reduced DC resistance. Basically, the transformation method can be applied if the porosity factor is above 0.8. Otherwise, the FEA simulation tool is suggested to evaluate the accurate AC winding loss.

5.2.2 Winding Loss for Circular Conductors

If circular conductors are applied in the planar transformer, the wide and flat circular winding will perform differently compared to the conventional transformer. The polar coordination system is introduced to solve the field problem for this situation, as shown in Fig. 5.4(b). As the current flowing path at the inner side of the circular conductor is shorter than the outer side, the current density distribution will be non-uniform and related to the radius. The cross section of the circular conductor and the boundary conditions of the n^{th} primary layer applied in the following calculations is illustrated in Fig. 5.7. For a segment of $dr \times t$ in the conductor, it is reasonable to assume that the current flowing in the segment has an inverse relationship with r and it is given by


 Fig. 5.7 Boundary conditions of the n^{th} primary layer

$$\int_0^t J(r, z) dz = \frac{K}{r}, \quad (5.10)$$

where K is a constant. Supposing the total current flowing the primary winding is I_p , the current density is integrated along the whole conductor will attain

$$\int_{r_i}^{r_o} \int_0^t J(r, t) dz dr = I_p. \quad (5.11)$$

Therefore, the current in the segment is calculated by

$$\int_0^t J(r, t) dz = \frac{I_p}{r \ln\left(\frac{R_o}{R_i}\right)}. \quad (5.12)$$

The detailed derivation of the copper loss for planar circular conductors in the primary winding is given in Appendix D and the formula is presented as

$$R_{\text{acp}} = \frac{2\pi \rho_w n_p}{t \ln\left(\frac{R_o}{R_i}\right)} \cdot F_{R1}, \quad (5.13)$$

with

$$F_{R1} = \Delta \left[\frac{\sinh(2\Delta) + \sin(2\Delta)}{\cosh(2\Delta) - \cos(2\Delta)} + \frac{2(n_p^2 - 1)}{3} \frac{\sinh(\Delta) - \sin(\Delta)}{\cosh(\Delta) + \cos(\Delta)} \right] \quad (5.14)$$

and

$$\Delta = \frac{t}{\delta_0}, \quad (5.15)$$

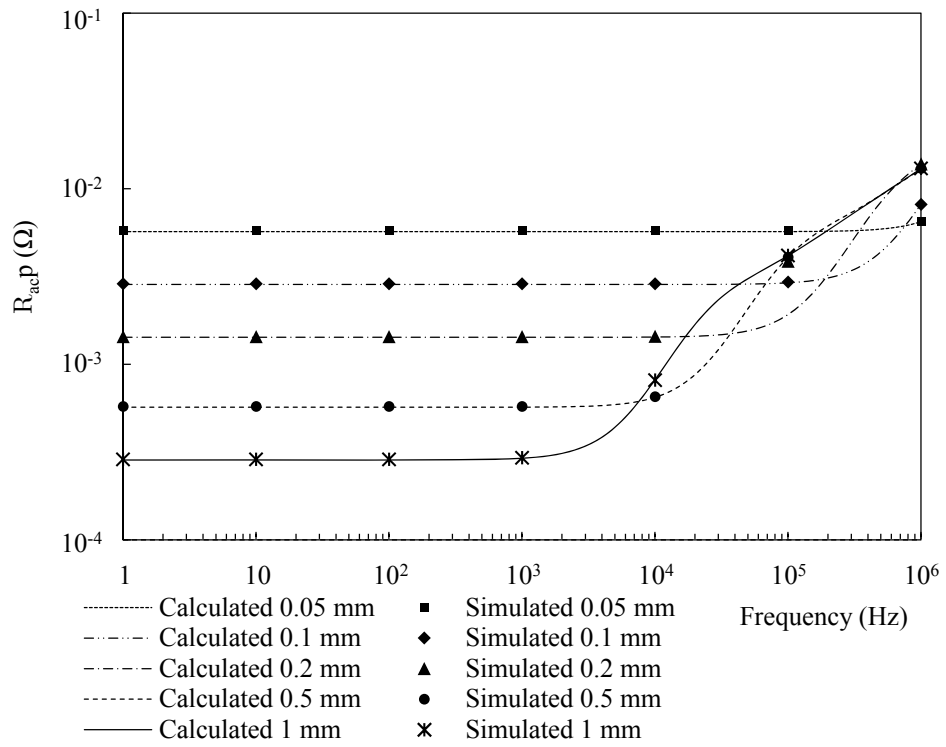
where n_p is the total number of layers in the primary winding and δ_0 is the skin depth.

For the interleaving of the primary and second windings, the value of n_p in (5.14) will be replaced by the number of layers in one winding portion with $n_p = n_{pp}$, as described in Chapter 4.

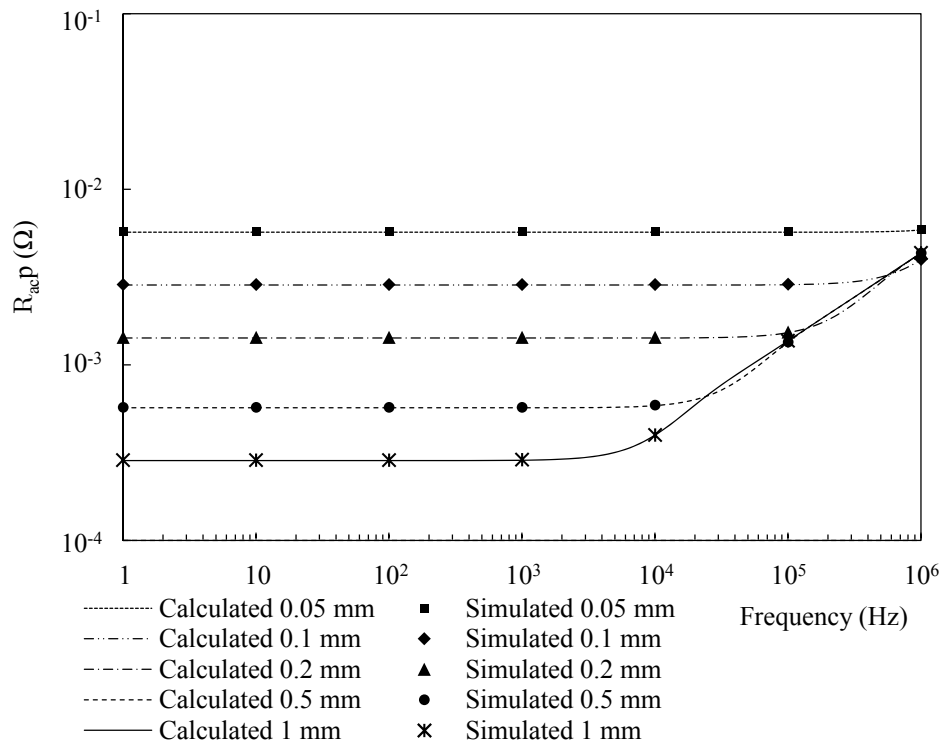
FEA simulations for several winding configurations have been carried out to verify the calculation results of (5.13). The planar core EER 41/7.6/32 is applied to complete the simulations. There are two layers of planar circular conductors in both the primary and secondary windings. The non-interleaved and interleaved winding configurations are simulated for different conductor thicknesses with varied frequencies of excitations. Fig. 5.8 shows the calculated and simulated total AC winding resistances for non-interleaved and interleaved winding configurations. The frequency is varied from 1 Hz to 1 MHz. The conductor thicknesses are assigned to be 0.05 mm, 0.1 mm, 0.2 mm, 0.5 mm and 1mm, respectively. The thickness of insulations between two layers is fixed as 0.1 mm. All windings are fully filling the window area.

Comparisons between the calculated and simulated results show that the evaluation formula for the winding loss of circular conductor is accurate. The winding loss at high frequency can be reduced by interleaving the primary and secondary windings. If the frequency is extremely high, the AC resistance of thick conductor will be dominated by the high frequency eddy current loss, where the skin depth is comparable to the conductor thickness.

The comparison of simulated current density distribution and calculated results based on (5.12) within one primary conductor for the case with $t = 0.5$ mm and frequency of 100 kHz is presented in Fig. 5.9. The results show that the preceding assumption of current distribution is valid.



(a) Calculated and simulated results for non-interleaved winding configuration



(b) Calculated and simulated results for interleaved winding configuration

Fig. 5.8 Comparisons of calculated and simulated AC winding resistance: (a) non-interleaved winding configuration; (b) interleaved winding configuration

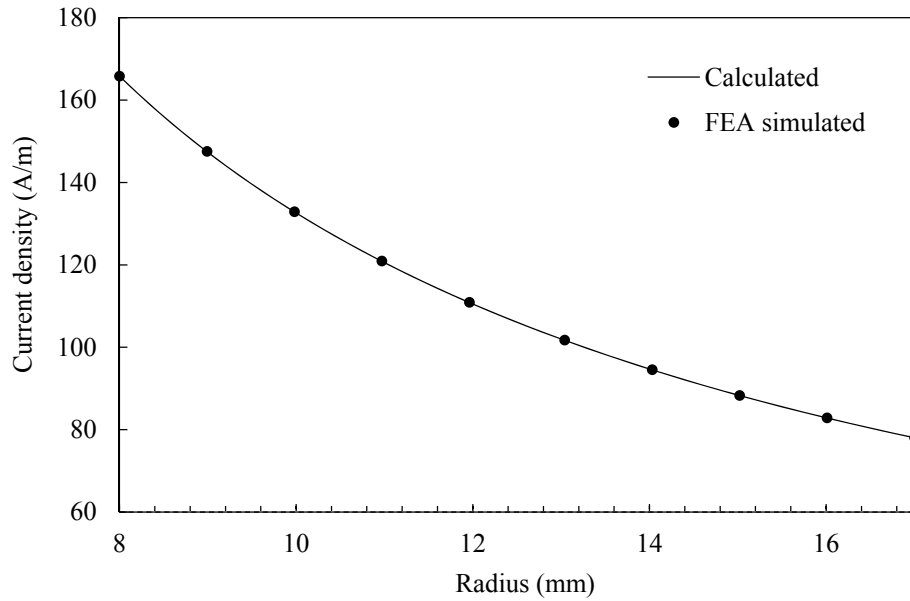


Fig. 5.9 Comparisons of simulated and calculated current density distribution within one circular conductor

It is also illustrated that the optimum thickness of the circular conductor can be found for the determined frequency. From Fig. 5.8(a), the AC winding resistance of 0.2 mm is the smallest value among all conductors with the listed five thicknesses at 100 kHz. However, the smallest value is achieved with the thickness of 0.5 mm for 100 kHz in the interleaving winding configuration, as shown in Fig. 5.8(b). It seems that the optimized thickness of the circular conductor varies with different winding configurations related to the number of layers in one interleaving portion, represented as n_{pp} .

For the fully interleaved winding configuration which is commonly applied in practice to eliminate the proximity effect, the formula of (5.13) becomes

$$R_{acp} = \frac{2\pi\rho_w n_p}{t \ln\left(\frac{R_o}{R_i}\right)} \cdot \Delta \frac{\sinh(2\Delta) + \sin(2\Delta)}{\cosh(2\Delta) - \cos(2\Delta)}. \quad (5.16)$$

Invoking the series expansions of the trigonometric and hyperbolic functions with terms up to the order of Δ^7 (the series expansions are improved for accuracy requirements by MATLAB data fitting tool)

$$\frac{\sinh(2\Delta) + \sin(2\Delta)}{\cosh(2\Delta) - \cos(2\Delta)} \approx \frac{1}{\Delta} + 0.074\Delta^3 - 0.001\Delta^7, \quad (5.17)$$

which is accurate enough for $\Delta < 2.5$. Thus, the optimum thickness of full interleaving circular conductor is given by

$$\Delta_{\text{opt}} = 1.527. \quad (5.18)$$

For the non-interleaved or partial interleaved winding configurations, the following approximation would be applied and it is accurate enough for $\Delta < 1.5$,

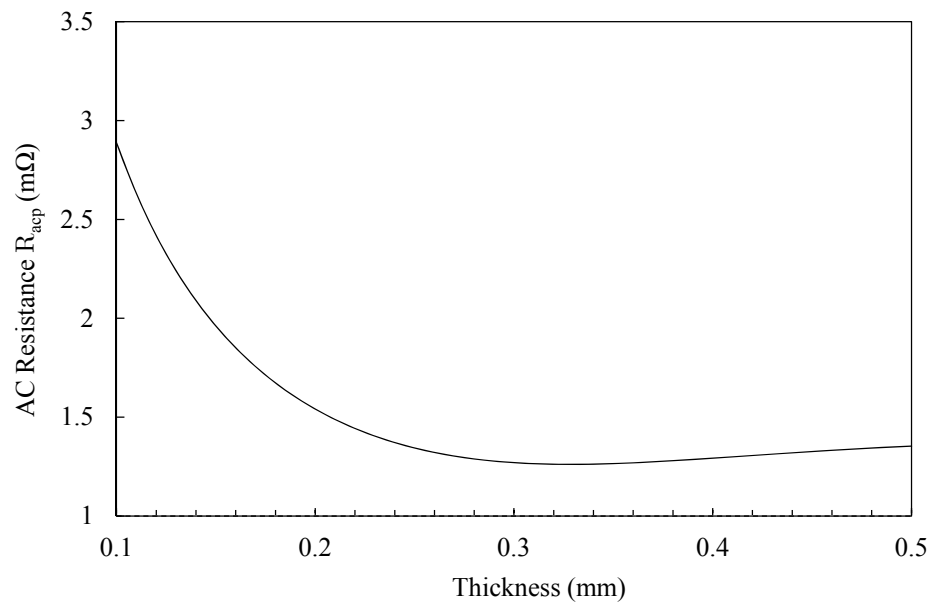
$$\frac{\sinh(\Delta) - \sin(\Delta)}{\cosh(\Delta) + \cos(\Delta)} \approx \frac{1}{6}\Delta^3 - 0.0058\Delta^7. \quad (5.19)$$

Consequently, we can obtain an approximation for (5.14) and the optimum value of Δ can be solved and the result is

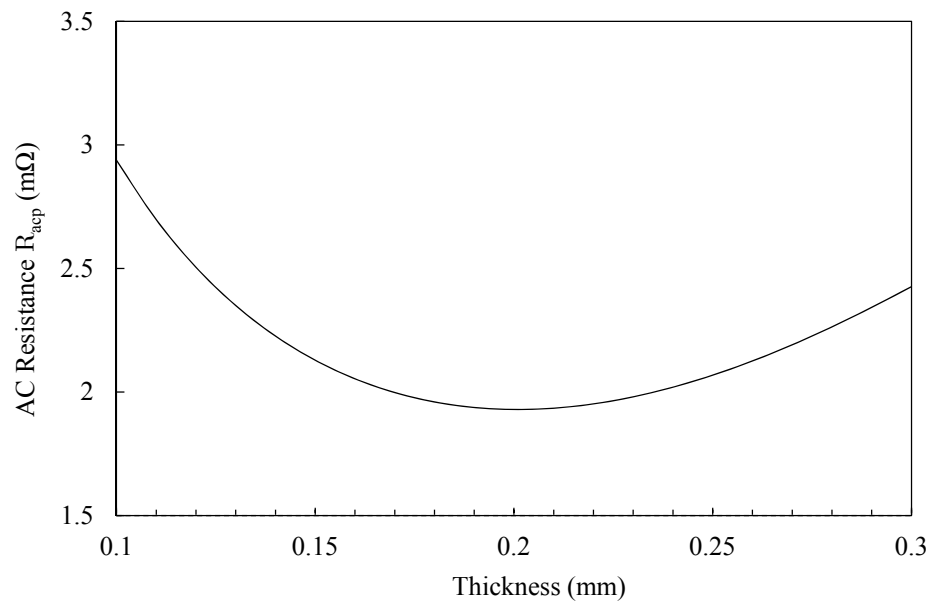
$$\Delta_{\text{opt}} = \left[\frac{\frac{1}{3}(n_{\text{pp}}^2 - 1) + 0.222 - \sqrt{\frac{1}{9}(n_{\text{pp}}^2 - 1)^2 + 0.04(n_{\text{pp}}^2 - 1) + 0.021284}}{0.054(n_{\text{pp}}^2 - 1) + 0.014}} \right]^{\frac{1}{4}}. \quad (5.20)$$

According to (5.20), the optimum copper thicknesses for 100 kHz with interleaved and non-interleaved winding configurations of 2 layers of circular conductors will be 0.32 mm and 0.20 mm, respectively. The FEA simulations with a series of copper thicknesses has been carried out and the AC winding losses of non-interleaved and interleaved structures are shown in Fig. 5.10. The results demonstrated the validity of proposed calculation method at 100 kHz.

Similar to the strip conductor, the width of a particular circular conductor is normally shorter than the window width of the planar core. The porosity factors can be employed in the transformation process. However, the definition will be different from (5.8). In order to maintain the same DC resistance, the porosity factor is given by



(a) interleaved case



(b) non-interleaved case

Fig. 5.10 FEA simulated AC conductor resistance of primary winding with interleaved and non-interleaved winding configurations at 100 kHz

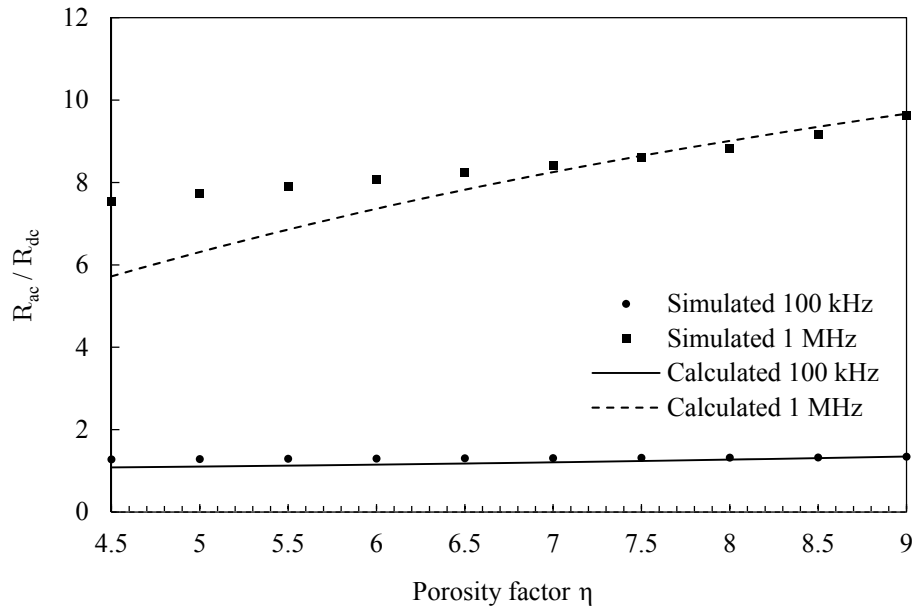


Fig. 5.11 Simulated and calculated results of R_{ac} / R_{dc} for circular conductors

$$\eta = \frac{\ln\left(\frac{R_{wo}}{R_{wi}}\right)}{\ln\left(\frac{R_o}{R_i}\right)}, \quad (5.21)$$

where R_{wo} and R_{wi} are the outer and inner radius of the shorter circular conductor, respectively, R_o and R_i are the outer and inner radius of the core window, respectively, as shown in Fig. 5.7. For the case of several turns of circular conductor placed in one layer, the porosity factor will be calculated to make sure the DC resistance remains the same for the transformation. The conductivity of the equivalent circular conductor is calculated by (5.9).

FEA simulations have been carried out to verify the accuracy of the equivalent transformation for circular conductors. The thickness of conductors is fixed as 0.2 mm and the simulated frequencies of excitations are 100 kHz and 1 MHz. The selected planar core is EER 41/7.6/32 and the window width is 9 mm. The number of layers in the primary and secondary windings are both 2. The primary winding and secondary winding are non-interleaved. The insulation thickness between two layers is 0.1 mm. The number of turns in each layer is 1 and the windings are placed in the middle of

the core window. The simulated winding width (equals $R_{wo} - R_{wi}$) are assigned to vary from 4.5 mm to 9 mm with the interval value of 0.5 mm. The simulated and calculated results of the ratio for the AC resistance R_{ac} to the DC resistance R_{dc} are presented in Fig. 5.11.

The results shows that the equivalent transformation based on the porosity factor at 100 kHz works well. However, the calculation results for 1 MHz at low porosity factor would lead an error up to 25%. It is caused by the edge effect of the conductor as the pure 1-D assumption is not sufficient. If the porosity factor is higher than 0.75, the equivalent transformation method can be applied to obtain the accurate result for the full range of frequencies.

5.2.3 Winding Loss with Phase Shifted Excitations

In some circuits, the currents through the primary winding and secondary winding have an inherent phase shift angle, such as the transformer in the LLC resonant converter and the coupled inductor in multi-phase converters. Actually, the phase shift of excitation currents will significantly affect the high frequency winding loss of magnetic components. Taking the full-interleaving winding configuration in the transformer as an example, the magnetic field will be totally different for phase-shifts of 0 and π between the primary and secondary currents. In the gapped transformer in a LLC resonant converter, the phase shift angle between the primary winding and the secondary winding will changes dynamically with load conditions based on the analysis in Chapter 2. In an attempt to achieve accurate analysis of the transformer power loss, it is paramount to consider the high frequency winding loss with phase shift. In [10], the resistance matrix was introduced to obtain the winding loss calculations. However, complex boundary magnetic field calculations are involved and the method has not been verified for the winding loss with phase-shifted excitation currents. The simple and easily computable evaluation methodology for the high frequency winding loss with phase-shifted currents has been proposed in [202]. The formula to calculate the total winding loss is given by

$$P_{cu,\theta} = I_{p_rms}^2 R_p + I_{s_rms}^2 R_s + 2I_{p_rms} I_{s_rms} R_{ps} \cos \theta_{ps}, \quad (5.22)$$

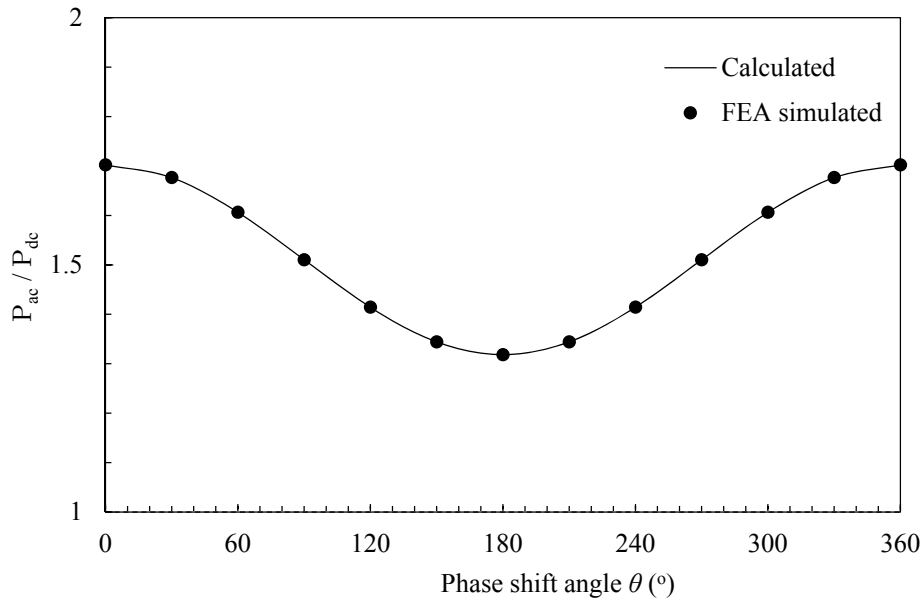


Fig. 5.12 Simulated and calculated results of P_{ac} / P_{dc} for different phase shift angles between primary and secondary currents

where I_{p_rms} and I_{s_rms} are the rms values of the primary and secondary currents, respectively. R_p , R_s and R_{ps} are the self resistance of the primary winding, self resistance of the secondary winding and the mutual resistance of the primary and secondary windings, respectively. θ_{ps} is the phase shift angle between the primary and secondary currents. Assuming the winding losses with the phase shift angles of 0 and π are $P_{cu,0}$ and $P_{cu,\pi}$, respectively, (5.22) can be rewritten as

$$P_{cu,\theta} = \frac{P_{cu,0} + P_{cu,\pi}}{2} + \frac{P_{cu,0} - P_{cu,\pi}}{2} \cos \theta_{ps}. \quad (5.23)$$

In practice, $P_{cu,0}$ and $P_{cu,\pi}$ are easily obtained and thus the winding loss with the phase angle of θ_{ps} will be obtained.

FEA simulations for the different phase shifts between the primary and secondary currents have been completed for the planar transformer applied in the 240 W LLC resonant converter, which will be introduced in Chapter 6, shown in Fig. 6.5. The results are shown in Fig. 5.12 and the calculation formula (5.23) is validated.

For the transformer with fully interleaved winding configurations, all transformer windings can be treated as one portion if the phase shift between the primary and secondary windings is 0. The high frequency proximity effect will distinctly increase the winding loss. On the other hand, the proximity effect on the winding loss will be eliminated if the primary and secondary currents have a phase shift angle of π . Combing the winding loss calculated by (5.23) with the phase shift angle of θ_{ps} and the winding losses for non-interleaved and full interleaved structure, the thickness of the circular conductors can be optimized.

For instance, supposing the currents in the primary and secondary windings are identical, the total AC winding resistance of the transformer, which has both n_p layers in the primary and secondary windings with the interleaved arrangement, can be calculated by

$$R_{cu,\theta} = \frac{4\pi\rho_w n_p}{t \ln\left(\frac{R_o}{R_i}\right)} F_{R\theta} \quad (5.24)$$

with

$$F_{R\theta} = \Delta \left[\frac{\sinh(2\Delta) + \sin(2\Delta)}{\cosh(2\Delta) - \cos(2\Delta)} + 2(1 + \cos\theta_{ps}) \frac{n_p^2 - 1}{3} \frac{\sinh(\Delta) - \sin(\Delta)}{\cosh(\Delta) + \cos(\Delta)} \right]. \quad (5.25)$$

5.3 Stray Capacitances of Planar Transformer

Stray capacitances in planar transformer is a concern because the overlap area of planar windings are normally bigger than that in the conventional wire wound transformer. Basically the parallel plate modelling method presented in Chapter 4 to calculate the stray capacitance can be applied properly for the planar transformer.

Consider the planar transformer shown in Fig. 5.13 and layout/construction in Fig. 5.14. The primary winding of the planar transformer is made by PCB board which has the thickness of 0.2 mm and the copper track on each side is 0.07 mm. The copper layers on the top and bottom sides of the PCB board are in parallel and the electric field inside the PCB board can be ignored, thus the total primary PCB board can be

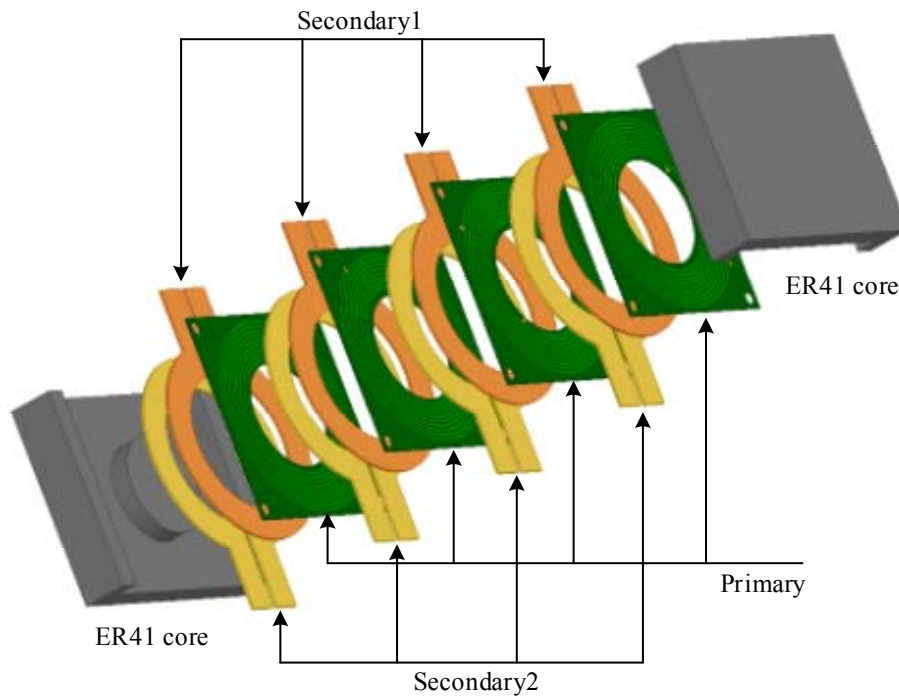
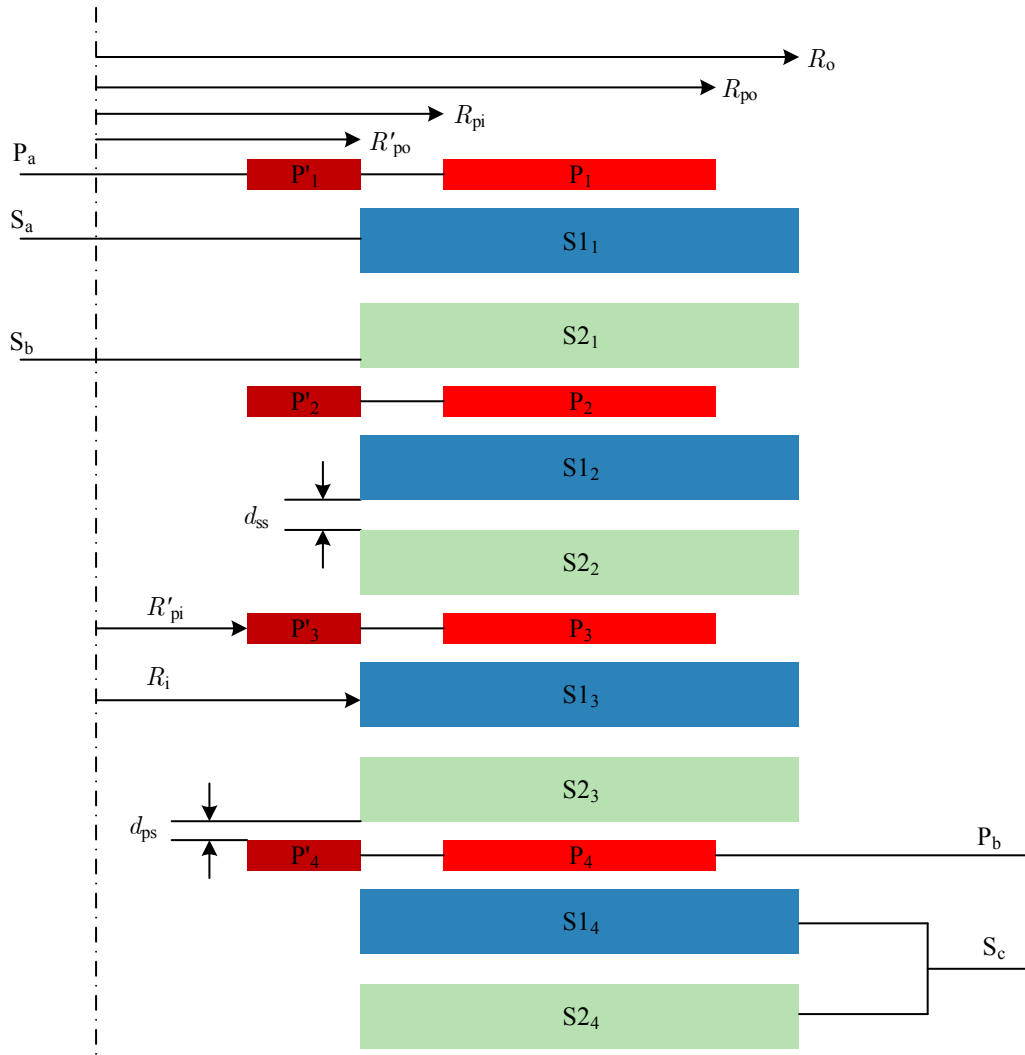


Fig. 5.13 Planar transformer for the capacitance calculation

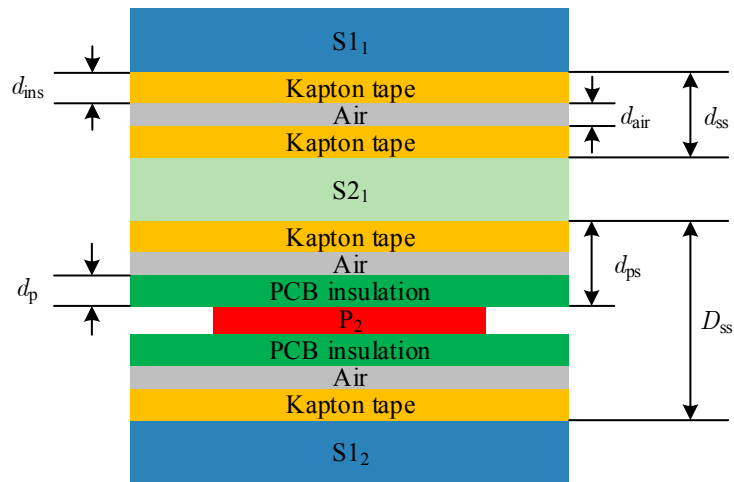
treated equivalently as the copper track with the thickness of 0.34 mm. The insulation of the PCB is 0.01 mm. The two secondary windings are copper foil and the thickness is 0.4 mm. Two layers of kapton tape are attached to both sides of the foil with 0.05 mm insulation achieved. The air gap between two kapton tape layers is assumed to be 0.05 mm.

The detailed cross section of the planar transformer windings is shown in Fig. 5.14. Each winding has four copper layers and they are labelled as presented in the figure. As only part of the primary PCB winding is exactly on top of the secondary winding, the effective copper foil is assumed to be placed overlapping the secondary conductor. The part of the primary winding which is away from the secondary winding can be assumed as the separate part sitting on the left-top corner.

Three basic kinds of adjacent capacitors will be evaluated including C_{ps} (primary layer and adjacent secondary layer), C_{ss} (two adjacent secondary layers) and C_{pp} (two adjacent primary layers). The insulation material and the detailed dimension are shown in Fig. 5.14(b) and Fig. 5.14(c). The list of symbols, their meanings and values



(a) Cross section of planar transformer windings



(b) Layers of different materials between windings

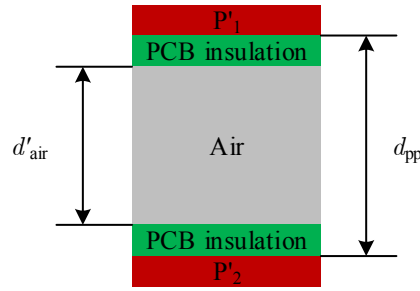

 (c) Layers of PCB insulations and air between P'_1 and P'_2

Fig. 5.14 Detailed cross section and insulation layers of planar transformer

are listed in Table 5.2. The relative dielectric constant of the PCB material and kapton tape are both 3.8.

According to Fig. 5.14(b), the adjacent capacitance between the primary layer and the secondary layer which is expressed as C_{ps} can be treated as three capacitances in series. If the effective relative dielectric constant ε_{ps} is applied, then

$$\frac{1}{C_{ps}} = \frac{d_{ps}}{\varepsilon_0 \varepsilon_{ps} A_{pri}} = \frac{d_p}{\varepsilon_0 \varepsilon_r A_{pri}} + \frac{d_{air}}{\varepsilon_0 A_{pri}} + \frac{d_s}{\varepsilon_0 \varepsilon_r A_{pri}}. \quad (5.26)$$

Following the similar principle, we have

$$\frac{1}{C_{ss}} = \frac{d_{ss}}{\varepsilon_0 \varepsilon_{ss} A_{sec}} = \frac{d_s}{\varepsilon_0 \varepsilon_r A_{sec}} + \frac{d_{air}}{\varepsilon_0 A_{sec}} + \frac{d_s}{\varepsilon_0 \varepsilon_r A_{sec}}, \quad (5.27)$$

$$\frac{1}{C_{pp}} = \frac{d_{pp}}{\varepsilon_0 \varepsilon_{pp} A'_{pri}} = \frac{d_p}{\varepsilon_0 \varepsilon_r A'_{pri}} + \frac{d'_{air}}{\varepsilon_0 A'_{pri}} + \frac{d_p}{\varepsilon_0 \varepsilon_r A'_{pri}}. \quad (5.28)$$

The calculated results are given by

$$\begin{aligned} C_{ps} &= 43.35 \text{ pF}, & \varepsilon_{ps} &= 1.792, \\ C_{ss} &= 56.63 \text{ pF}, & \varepsilon_{ss} &= 2.111, \\ C_{pp} &= 0.62 \text{ pF}, & \varepsilon_{pp} &= 1.013. \end{aligned} \quad (5.29)$$

Simulation models are built and the values obtained of C_{ps} , C_{ss} and C_{pp} are 43.17 pF, 53.14 pF and 0.61 pF, respectively. The calculated and simulated results are corresponding very well.

TABLE 5.2 SYMBOLS APPLIED IN THE CAPACITANCE CALCULATIONS

Symbols	Meaning	Value
R_{pi}	inner radius of the primary effective copper foil P_1	11.78 mm
R_{po}	outer radius of the primary effective copper foil P_1	15.22 mm
R'_{pi}	inner radius of the primary effective copper foil P'_1	9.8 mm
R'_{po}	outer radius of the primary effective copper foil P'_1	11 mm
R_{si}	inner radius of the secondary copper foil	11 mm
R_{so}	outer radius of the secondary copper foil	16 mm
A_{pri}	Area of the primary effective copper foil P_1	273.12 mm ²
A'_{pri}	Area of the primary effective copper foil P'_1	78.54 mm ²
A_{sec}	Area of the secondary copper foil	424.12 mm ²
d_{air}	thickness of the air between primary and secondary layer	0.04 mm
d'_{air}	thickness of the air between primary and primary layer	1.12 mm
d_p	thickness of the primary PCB insulation	0.01 mm
d_s	thickness of the secondary kapton tape insulation	0.05 mm
d_{pp}	distance between the adjacent primary windings	1.14 mm
d_{ps}	distance between the primary and secondary windings	0.1 mm
d_{ss}	distance between the adjacent secondary windings	0.14 mm
D_{ss}	distance between the distant secondary windings	0.54 mm
ϵ_r	relative dielectric constant of the kapton tape and PCB	3.8

As the two secondary windings is centre-tapped connected, the stray capacitance of terminal P_a and S_a is calculated by

$$C_{pasa} = 7C_{ps} = 305.31 \text{ pF}. \quad (5.30)$$

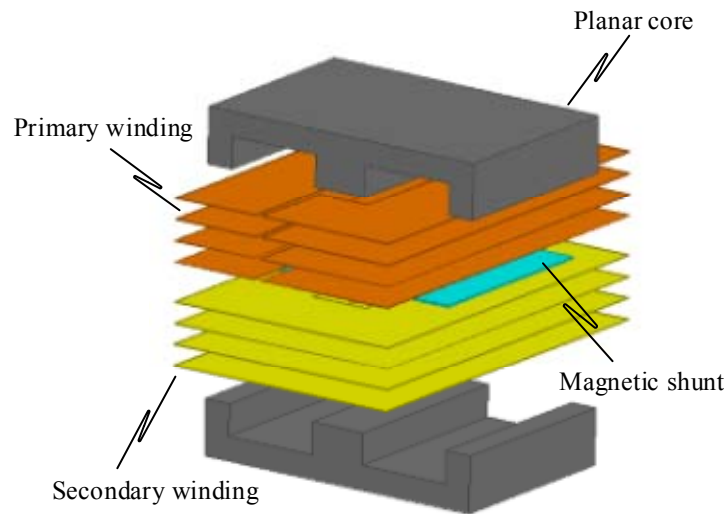


Fig. 5.15 Assembly of the planar transformer with magnetic shunt

The capacitance of C_{pasa} was measured by the impedance analyser of Agilent 4395 A with Agilent 4319A and 16092A. The measurement result is 332.79 pF which means the calculated result is close enough.

5.4 Leakage Inductance of Planar Transformer with Magnetic Shunt

The accurate prediction of leakage inductance in transformers is critical for power switching circuits, especially resonant converters because the resonant frequency should be well-matched and it will significantly affect the circuit operation and performance. Conventional wire wound transformer and the discrete inductor are normally implemented in the LLC resonant converter which will increase the overall volume of the converter. Aiming to minimize the size of magnetic components, many efforts have been carried out for LLC resonant converters including planar magnetics and integrated magnetics. High-efficiency low-profile transformer structures are described in [185], [186], [203] and [204]. In order to integrate the resonant inductor within the planar transformer, the leakage inductance should be achieved as large as the required value. The material with lower permeability is commonly inserted into the winding area to provide the shunt path for magnetic flux and it will increase the leakage inductance dramatically. Fig. 5.15 shows the implementation of the planar transformer with the magnetic shunt. For the purpose of modelling the leakage

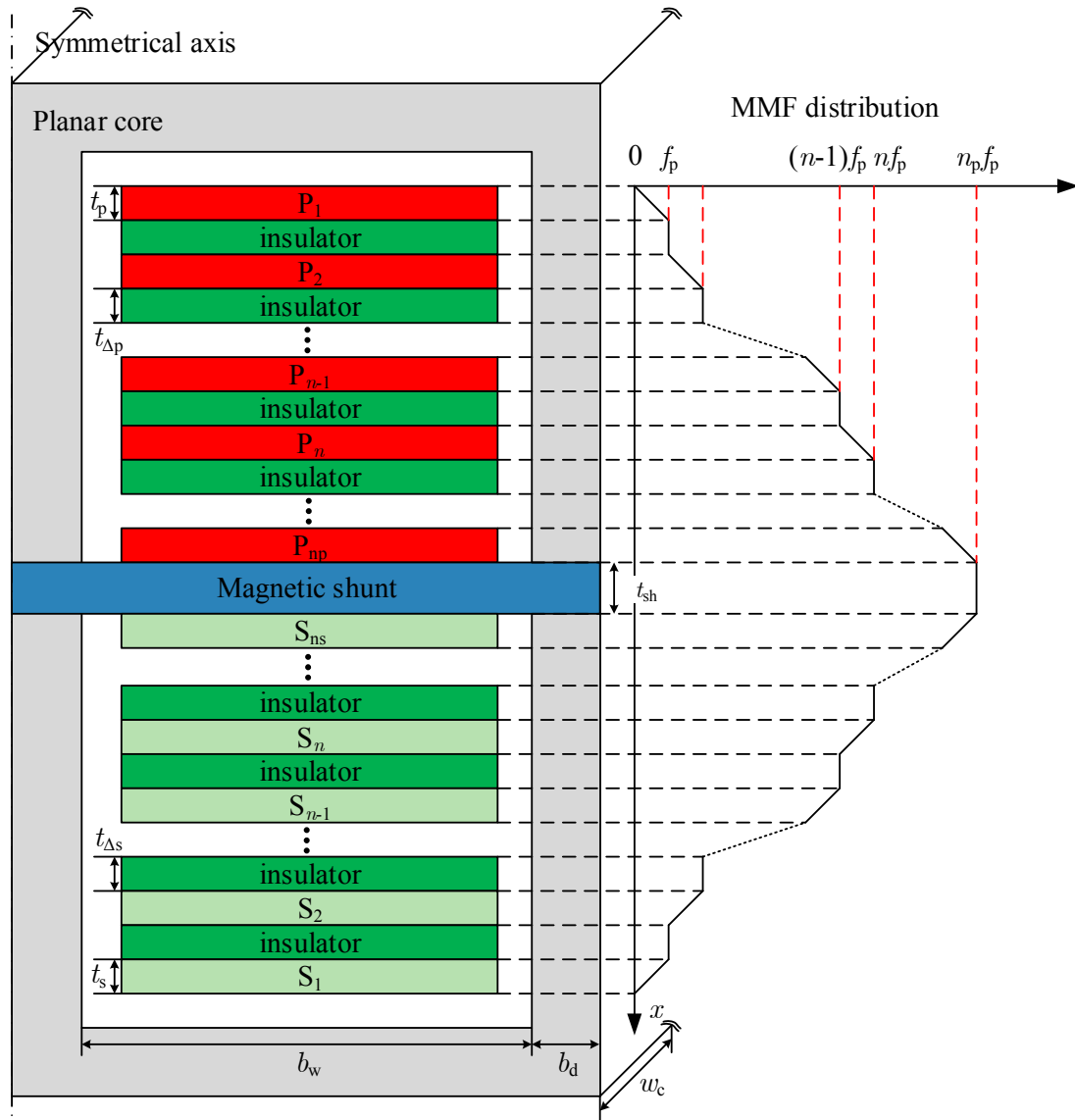


Fig. 5.16 Cross section of planar transformer with magnetic shunt and simplified analytical scheme of MMF distribution

inductance of the planar transformer involving the magnetic shunt, the calculation methodologies based on both the MMF and the reluctance model will be presented.

Fig. 5.16 illustrates the cross section of a typical planar transformer with the magnetic shunt placed in the middle across the window and core. The non-interleaved winding configuration is preferred for increasing the leakage inductance. In this figure, the simplified analytical scheme of MMF distribution along the window layers of the planar transformer are presented. The number of layers in the primary and secondary windings are n_p and n_s , respectively.

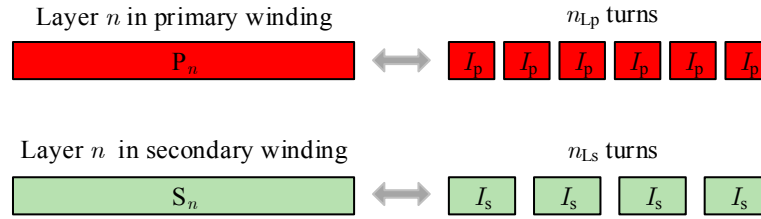
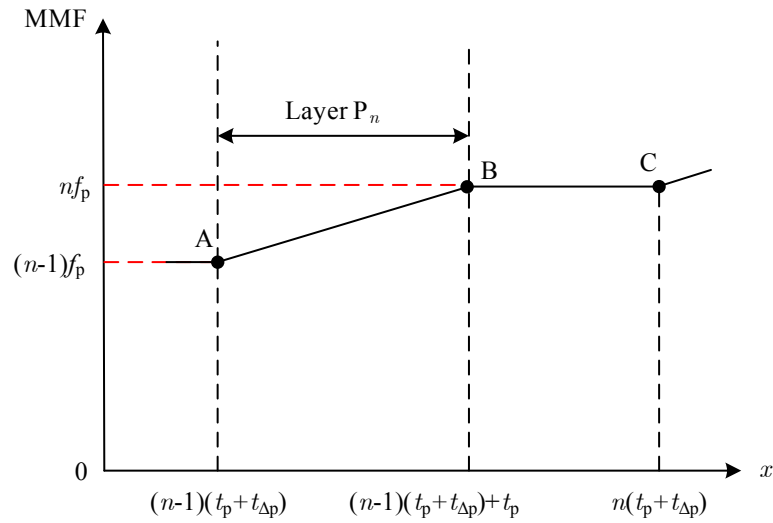


Fig. 5.17 Schematic diagram for the number of turns in each layer


 Fig. 5.18 MMF distribution in vicinity of the n^{th} layer

In the planar transformer with the windings implemented by PCB or copper foil, the numbers of turns in each layer of the primary and secondary winding are supposed to be n_{Lp} and n_{Ls} , respectively and the corresponding currents are represented as I_p and I_s , respectively, as shown in Fig. 5.17. Consequently, the total MMF in each layer of the primary and secondary windings is given by

$$f_p = n_{Lp}I_p, \quad f_s = n_{Ls}I_s. \quad (5.31)$$

The leakage inductance can be derived from the magnetic field energy with the total MMF of the primary and secondary sides cancelling. The magnetic field energy stored in the primary side (E_{pri}), the secondary side (E_{sec}) and the magnetic shunt (E_{shunt}) must be analysed and calculated.

E_{pri} can be obtained based on the analysis of the magnetic field intensity in the primary side and the used symbols appear in Fig. 5.16. Fig. 5.18 presents the MMF curve in vicinity of the n^{th} layer in the primary winding ($n=1,2,\dots,n_p$). The magnetic field intensity H at the geometric position x is given by

$$H(x) = \begin{cases} \left[\frac{(n-1)f_p}{b_w} + \frac{f_p}{t_p b_w} \left[x - (n-1)(t_p + t_{\Delta p}) \right] \right] \\ \text{when } (n-1)(t_p + t_{\Delta p}) < x \leq (n-1)(t_p + t_{\Delta p}) + t_p \\ \frac{n f_p}{b_w} \\ \text{when } (n-1)(t_p + t_{\Delta p}) + t_p < x \leq n(t_p + t_{\Delta p}) \end{cases}. \quad (5.32)$$

The stored energy E_{pri} can be calculated as

$$E_{\text{pri}} = 2 \cdot \frac{1}{2} \mu_0 w_c b_w \left[\sum_{n=1}^{n_p} \int_{(n-1)(t_p + t_{\Delta p})}^{(n-1)(t_p + t_{\Delta p}) + t_p} H^2(x) dx + \sum_{n=1}^{n_p-1} \int_{(n-1)(t_p + t_{\Delta p}) + t_p}^{n(t_p + t_{\Delta p})} H^2(x) dx \right], \quad (5.33)$$

where w_c is the depth of the magnetic core or the shunt. Combing (5.32) and (5.33), it can be obtained

$$E_{\text{pri}} = \frac{1}{6} \mu_0 \frac{w_c}{b_w} n_{Lp}^2 \left[2t_p n_p^3 + t_{\Delta p} (2n_p^3 - 3n_p^2 + n_p) \right] I_p^2. \quad (5.34)$$

Similarly, the energy stored in the secondary side E_{sec} is

$$E_{\text{sec}} = \frac{1}{6} \mu_0 \frac{w_c}{b_w} n_{Ls}^2 \left[2t_s n_s^3 + t_{\Delta s} (2n_s^3 - 3n_s^2 + n_s) \right] I_s^2. \quad (5.35)$$

The MMF in the magnetic shunt is supposed to be $n_p f_p$ and then,

$$H_s = \frac{n_p f_p}{b_w}. \quad (5.36)$$

The energy stored in the total magnetic shunt is

$$E_{\text{shunt}} = \mu_0 \mu_s \frac{t_{\text{sh}} w_c}{b_w} n_{Lp}^2 n_p^2 I_p^2, \quad (5.37)$$

where μ_s relative is the permeability of the magnetic shunt. Finally, the total leakage inductance based on the MMF analysis is calculated by

$$L_{lk} = \frac{\mu_0 w_c n_{lp}^2 n_p^2}{3b_w} \left\{ \sum_{i=p,s} \left[2n_i (t_i + t_{\Delta i}) - 3t_{\Delta i} + \frac{t_{\Delta i}}{n_i} \right] + 6\mu_s t_{sh} \right\}. \quad (5.38)$$

An alternative method to calculate the leakage inductance is based on the reluctance model of the planar transformer as the main magnetic flux path is changed with the shunt inserted as shown in Fig. 5.19. The MMF in the magnetic shunt may not be assumed as $n_p f_p$ under some conditions. Generally, the permeability of the magnetic shunt is substantially higher than the air, the leakage, magnetic field energy stored in the shunt will dominate the total energy. The reluctance model of leakage inductance calculation in the planar transformer incorporating magnetic shunt with the reluctance of winding ignored (since they are small) is shown in Fig. 5.20. The reluctances of the planar core R_{c1} and R_{c2} , the reluctances of the shunt R_{s1} and R_{s2} can be calculated respectively as follows,

$$\begin{aligned} R_{c1} + \frac{1}{2} R_{c2} &= \frac{l_c}{2\mu_0 \mu_r A_c}, \\ R_{s1} &= \frac{t_{sh}}{2\mu_0 \mu_s b_d w_c}, \quad R_{s2} = \frac{b_w}{\mu_0 \mu_s t_{sh} w_c}. \end{aligned} \quad (5.39)$$

where μ_r , μ_s are the relative permeability of the core and shunt respectively, A_c is the effective cross sectional area of the core, l_c is the effective length of the EE core set and other parameters are labelled in Fig. 5.19.

Based on the reluctance model, the magnetic flux in the shunt inside the core window is

$$\phi_s = \frac{n_p f_p}{R_{c1} + \frac{1}{2} R_{c2} + R_{s1} + R_{s2}}. \quad (5.40)$$

If a_R is defined as

$$a_R = \frac{R_{s2}}{R_{c1} + \frac{1}{2} R_{c2} + R_{s1} + R_{s2}}, \quad (5.41)$$

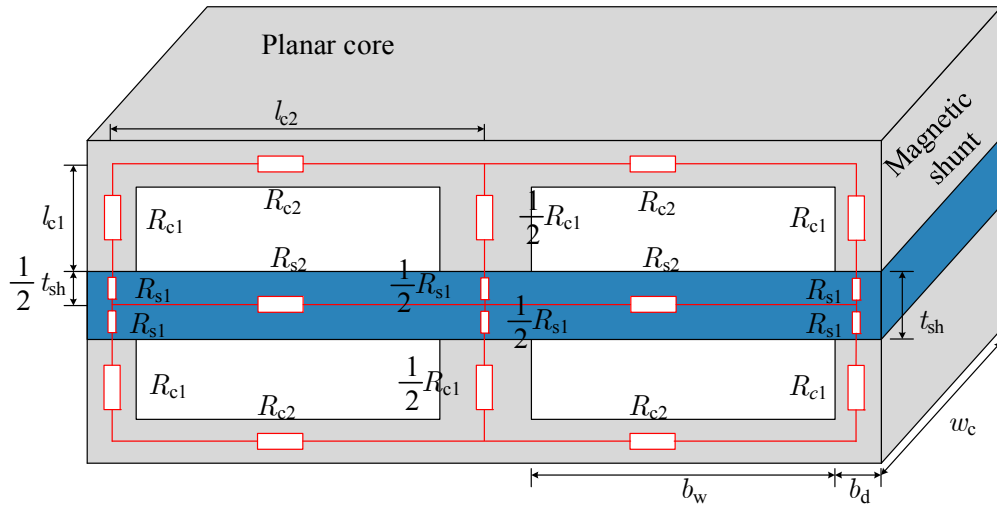


Fig. 5.19 Reluctances distributed in the integrated planar transformer

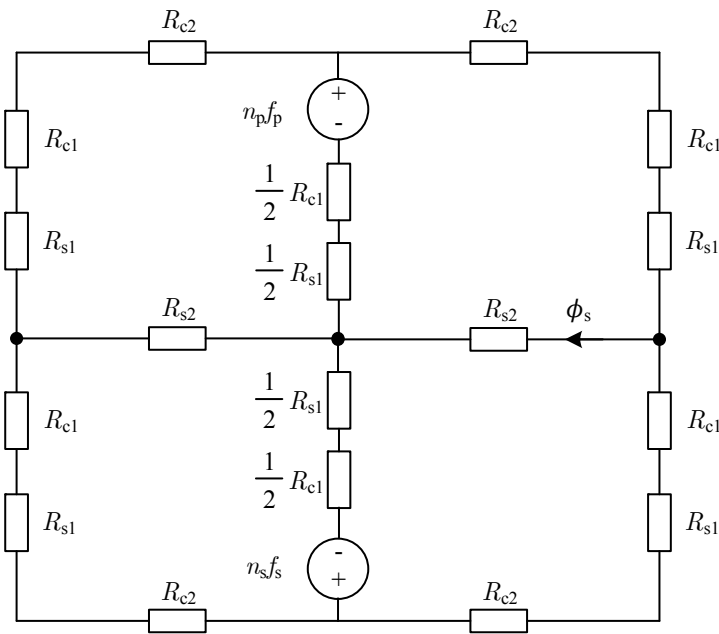


Fig. 5.20 Reluctance model of the integrated planar transformer

the magnetic field intensity of the shunt inside the core window is given by

$$H_{sw} = \frac{1}{b_w} a_R n_p f_p. \quad (5.42)$$

The H field of the shunt placed in the core leg is calculated as

$$H_{sc} = \frac{R_{s1}}{t_{sh} R_{s2}} a_R n_p f_p. \quad (5.43)$$

The magnetic field intensity in the planar core is

$$H_{\text{core}} = \frac{R_{c1} + \frac{1}{2}R_{c2}}{2l_c R_{s2}} a_R n_p f_p. \quad (5.44)$$

Consequently, the energies stored in the shunt and the planar core can be calculated as

$$E_{\text{shunt}} = \mu_0 \mu_s \left(\frac{t_{\text{sh}} w_c}{b_w} + \frac{2b_d w_c R_{s1}^2}{t_{\text{sh}} R_{s2}^2} \right) a_R^2 n_{Lp}^2 n_p^2 I_p^2, \quad (5.45)$$

$$E_{\text{core}} = \mu_0 \mu_r \frac{A_c}{8l_c R_{s2}^2} \left(R_{c1} + \frac{1}{2}R_{c2} \right)^2 a_R^2 n_{Lp}^2 n_p^2 I_p^2. \quad (5.46)$$

According to the MMF balance in the primary and secondary windings, we have

$$n_p n_{Lp} I_p = n_s n_{Ls} I_s. \quad (5.47)$$

Combing all these results, the total leakage inductance referred to the primary of the planar transformer with magnetic shunt can be expressed by

$$L_{lk} = \frac{1}{3} \mu_0 n_{Lp}^2 n_p^2 \frac{w_c}{b_w} \left\{ \begin{array}{l} \sum_{i=p,s} \left[2n_i (t_i + t_{\Delta i}) - 3t_{\Delta i} + \frac{t_{\Delta i}}{n_i} \right] + \\ 6\mu_s a_R^2 \left(t_{\text{sh}} + \frac{2b_d b_w R_{s1}^2}{t_{\text{sh}} R_{s2}^2} \right) + \\ \frac{3}{4} \mu_r a_R^2 \frac{b_w A_c}{w_c l_c R_{s2}^2} \left(R_{c1} + \frac{1}{2}R_{c2} \right)^2 \end{array} \right\}. \quad (5.48)$$

These two modelling methodologies for the leakage inductance of the integrated planar transformer will be compared and evaluated by the simulation and experimental results as described in the following sentences.

The 2-D FEA simulations for the planar core ELP 43/10/28 with shunts of different permeability and thicknesses have been performed. Table 5.3 lists out the detailed specifications of the planar PCB windings. The simulation results of the magnetic field intensity in the core window and the shunt is shown in Fig. 5.21. It is illustrated that the H field in the shunt is much higher than elsewhere, which means the leakage magnetic field energy is mainly stored in the shunt.

TABLE 5.3 SPECIFICATIONS OF THE PLANAR TRANSFORMER WITH SHUNT

Symbol	Meaning	Value
	Core material	N87
n_p	Layers of primary winding	4
n_{Lp}	Number of turns per primary layer	1
t_p	Thickness of each primary layer	0.15 mm
$t_{\Delta p}$	Separation of primary layers	0.4 mm
n_s	Layers of secondary winding	4
n_{Ls}	Number of turns per secondary layer	1
t_s	Thickness of each secondary layer	0.15 mm
$t_{\Delta s}$	Separation of secondary layers	0.4 mm

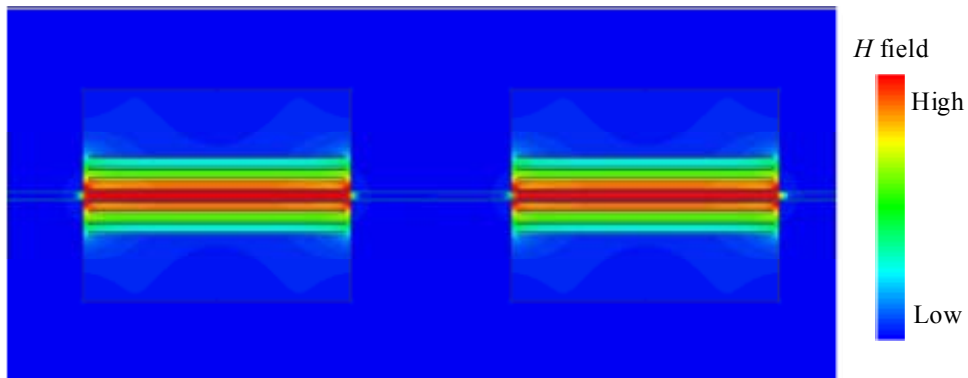


Fig. 5.21 Simulated magnetic intensity in the planar transformer with $\mu_r = 10$, $t_{sh} = 0.4$ mm

In an attempt to verify the proposed modelling methodologies of the leakage inductance and compare the two calculation methods, a series magnetic shunts are applied with different relative permeability: (1) $\mu_s = 10$; (2) $\mu_s = 40$; (3) $\mu_s = 100$; (4) $\mu_s = 150$; (5) $\mu_s = 200$. The thicknesses of the magnetic shunt vary from 0.1 mm to 2 mm. The calculated results based on the two proposed modelling methods are compared with FEA simulation results, as shown in Fig. 5.22. It is evident that the calculation method of the leakage inductance deduced by the reluctance model is more accurate.

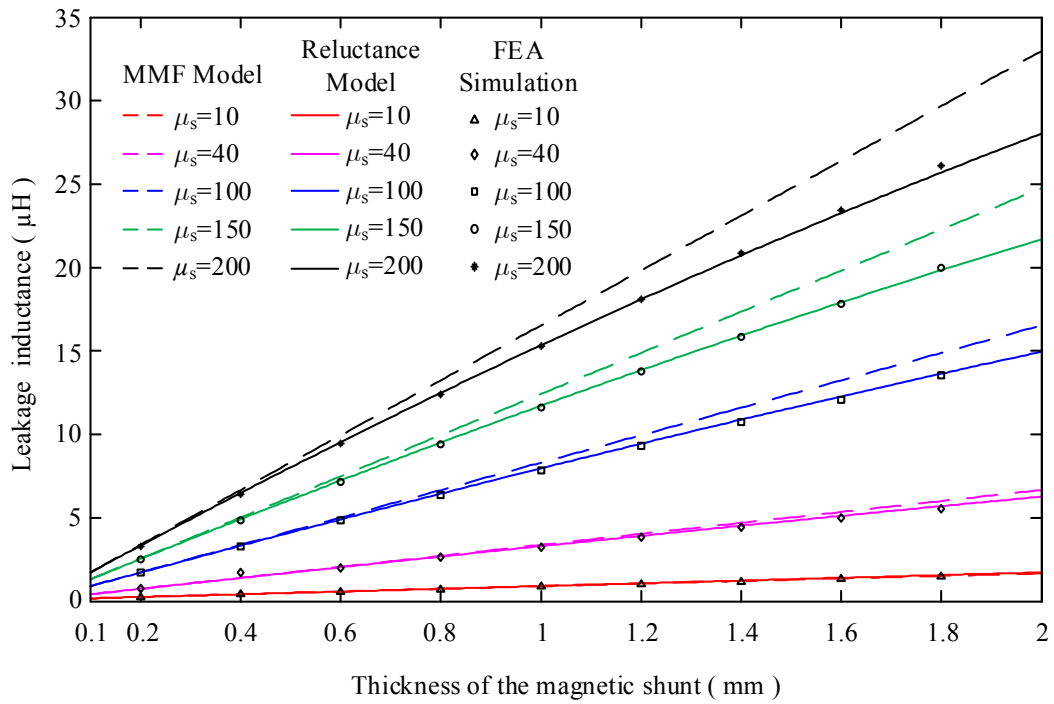


Fig. 5.22 Comparisons of the calculated and simulated results for the leakage inductance in the integrated planar transformer

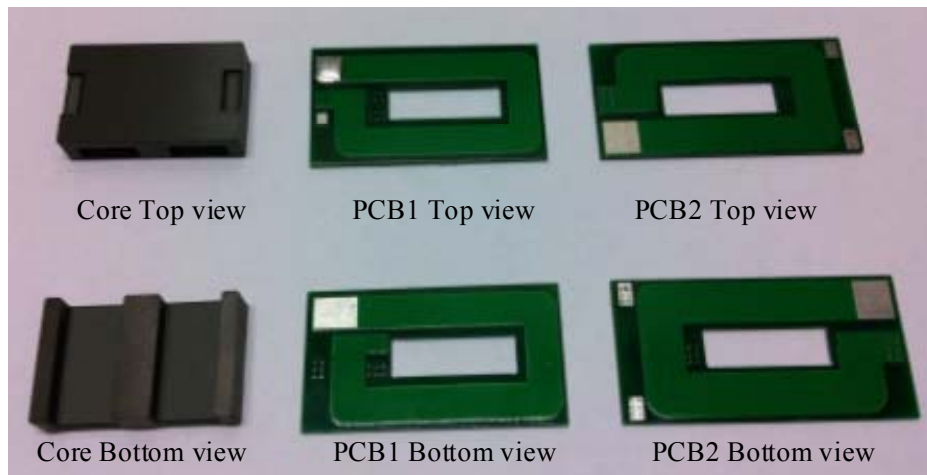


Fig. 5.23 PCB windings and planar core applied in the experimental test

Further experimental verification was carried out. Two kinds of PCB windings with different dimensions and patterns were fabricated to implement in the planar core ELP 43/10/28. Fig. 5.23 shows the PCB windings and planar core. The insulation thicknesses in PCB1 and PCB2 are 0.4 mm and 0.15 mm while the number of turns are 4 and 2, respectively. Three integrated planar transformer was built and their

TABLE 5.4 SPECIFICATIONS OF TESTED PLANAR TRANSFORMERS

Parameters	Trans1	Trans2	Trans3
Primary	PCB1	PCB2	PCB2
Secondary	PCB1	PCB1	PCB2
n_p	4	2	2
n_{Lp}	1	1	1
t_p	0.15 mm	0.15 mm	0.15 mm
$t_{\Delta p}$	0.4 mm	1.5 mm	1.5 mm
n_s	4	4	2
n_{Ls}	1	1	1
t_s	0.15 mm	0.15 mm	0.15 mm
$t_{\Delta s}$	0.4 mm	0.4 mm	1.5 mm

specifications are listed in Table 5.4. The thicknesses of magnetic shunt in the experiments are selected as 0.5 mm and 1mm with the relative permeability of 30. The leakage inductances of these six planar transformers with different magnetic shunts were measured using an Agilent 4395A impedance analyser with the secondary winding shorted. Fig. 5.24 shows the assembled planar transformer labelled as Trans. 1 in Table 5.4. The leakage inductances were measured at 100 kHz and the average value of 16 test results was selected as the final measured inductance.

Fig. 5.25 shows the calculation and experimental results for the three tested transformers with the thickness of the magnetic shunt 0.5 mm and 1 mm, respectively. The experimental results confirm that the proposed calculation method based on the reluctance model for the leakage inductance of the planar transformer with a magnetic shunt is valid.



Fig. 5.24 Photo of planar transformer with magnetic shunt (Trans1)

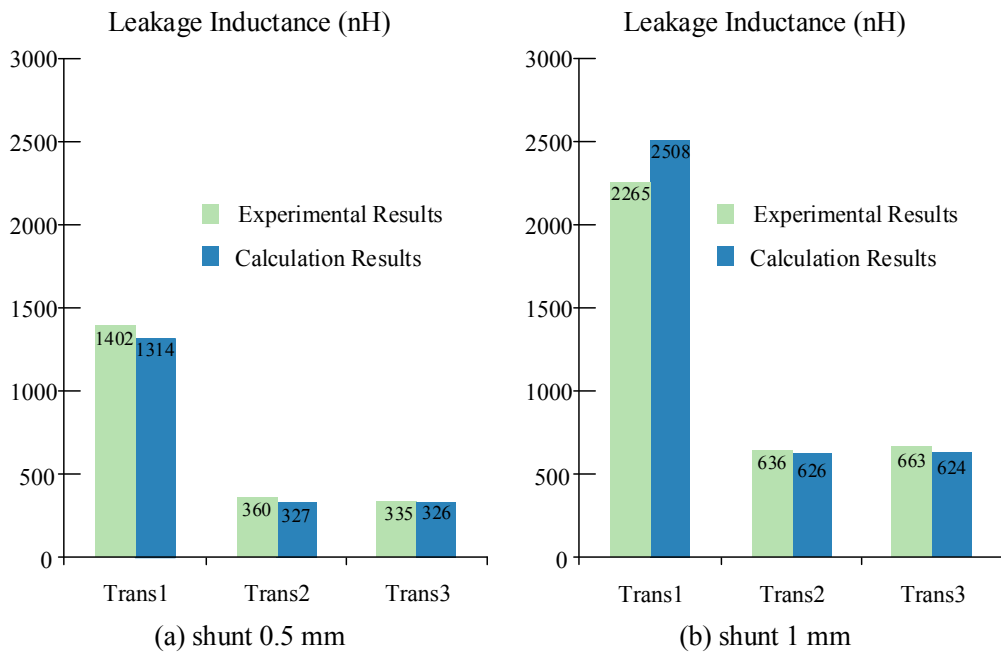


Fig. 5.25 Comparisons of the calculated and experimental results of the leakage inductance

5.5 Conclusions

Analysis and design of the planar transformer involving the planar core, the winding loss calculation and the stray capacitance have been presented. Basically, the planar EE and ER cores were investigated and compared in this chapter. For the planar windings with strip conductors and circular conductors, the high frequency winding loss calculation and the optimum design approach have been discussed. As the phase shift between the primary and secondary excitation currents significantly affect the winding loss, the associated evaluation method was proposed. In the aspect of the stray capacitance of the planar transformer, the calculation procedure for the specific planar transformer applied in the LLC resonant converter was presented. Finally, the leakage inductance of the integrated planar transformer incorporating a low permeability magnetic shunt was modelled and a calculation formula was proposed. The comprehensive FEA simulations and experimental results were carried out to validate the proposed calculations and all results corresponds well.

6

Gapped Planar Transformer in LLC Resonant Converters

In Chapter 3, the operation principle and the design methodology for the conventional gapped transformer in LLC resonant converters were proposed. On the other hand, the planar transformer has several advantages compared to conventional wire wound transformer as described in Chapter 5. The attempt to employ the gapped planar transformer in the LLC resonant converter will be discussed in this chapter.

6.1 Planar Core Selection

In the proposed design methodology for the gapped transformer described in Chapter 3, the A_p value of the magnetic core was used to select the proper core at first of the design process. In the design of the gapped planar transformer, the proposed design procedure will be introduced as the basic operating principle of the gapped transformer is identical.

In this chapter, we will focus on the gapped planar transformer design for one LLC resonant converter with the rated output power of 240 W, switching frequency of around 105 kHz. The input voltage and output voltage of the converter are 400 V and 24 V, respectively. The magnetizing inductance in the resonant tank is required around

TABLE 6.1 DESIGN SPECIFICATIONS OF THE PLANAR TRANSFORMER

Parameters	Symbols	Values
Output power	P_o	240 W
Switching frequency	f_s	105 kHz
Magnetizing inductance	L_m	420 μ H
Turns ratio	a	35:4:4
Maximum temperature rise	ΔT	60 $^{\circ}$ C
Ambient temperature	T_a	30 $^{\circ}$ C
Rms value of resonant current	I_{r_rms}	1.562 A
Peak value of magnetizing current	I_{Lm_pk}	1.138 A
Rms value of each secondary current	I_{s1_rms}	8.099 A

420 μ H. The turns ratio of the planar transformer is 35:4:4. The resonant inductance and the resonant capacitance in the resonant tank are 105 μ H and 20 nF, respectively. The detailed design specifications of the planar transformer are listed in Table 6.1, which is the same as the design specifications for the gapped conventional transformer as shown in Table 3.1. The peak value of the magnetizing current and RMS values of currents through the primary winding and secondary windings are calculated based on the formulas given in Section 2.1.2.

The ferrite material Ferroxcube 3C92 meets the application and the saturation flux density is 0.4 T. The parameters for the core loss calculation in the Steinmetz equation are obtained from the data given by the manufacturer as

$$K_c = 0.423, \quad \alpha = 1.618, \quad \beta = 3.114. \quad (6.1)$$

Considering the safety and insulation requirements, the initial window utilization factor is selected as 0.24. For the 3C92, select $B_{max} = 0.1$ T and the value of γ is taken as 1. The value of B_{max} is based on an iterative design and it was found that the value satisfies the constraint of the design while ensures that the maximum specifications not exceed. These parameters will be checked when the whole design is completed.

TABLE 6.2 DIMENSIONS AND PARAMETERS OF PLANAR EER 41/7.6/32 CORE

Parameters	Symbols	Values
Cross-sectional area	A_c	2.25 cm ²
Magnetic path length	l_c	5.7 cm
Window winding area	W_a	0.65 cm ²
Area product parameter of the core	A_p	1.463 cm ⁴
Volume of the core	V_c	12.9 cm ³
Mean length of a turn	MLT	8.48 cm
Height of the window of an ER core	h_{leg}	3.6 mm
Radius of the centre leg	g_r	8 mm

The required A_p value of the planar core is calculated by (3.22)

$$A_p = \left[\frac{\sqrt{k_u(1+\gamma)}L_m I_{r_rms} I_{Lm_pk}}{B_{max} k_{up} K_t \sqrt{\Delta T}} \right]^{\frac{8}{7}} = 1.304 \text{ cm}^4. \quad (6.2)$$

As we discussed in Section 5.1, the planar ER core is preferred to implement the planar transformer as the DC winding loss will be smaller than the planar ER core. Consequently, the EER41/7.6/32 planar core is suitable. Dimensions and parameters of the EER41/7.6/32 planar core are shown in Table 6.2. The thermal resistance of the core is calculated by (5.1)

$$T_\theta = \frac{0.056}{\sqrt{V_c}} = 15.6 \text{ }^\circ\text{C/W}. \quad (6.3)$$

6.2 Gap and Winding Design

Following the design procedure, the optimum permeability for the planar core with the gap will be obtained by (3.24)

$$\mu_{opt} = \frac{B_{max} l_c}{\mu_0 \sqrt{\frac{P_{cu_p} k_{up} W_a}{\rho_w MLT}}} \frac{I_{r_rms}}{I_{Lm_pk}} = 95. \quad (6.3)$$

The final gap length is selected to be 1 mm for the single gap placed in the centre leg. The numbers of turns in the primary winding and secondary winding are chosen as 35 and 4, respectively to meet the input/output voltage requirements. The calculated magnetizing inductance without considering the fringing effect is 333.7 μH .

If the fringing effect due to the air gap is considered, the inductance will be increased by the factor F_{Lm} and it is calculated by (3.12) with single gap in the centre leg

$$\sigma_r = \frac{1}{1 + \frac{g}{\pi g_r} \left(1 + \ln \frac{\pi h_{leg}}{2g} \right)} = 0.902, \quad (6.4)$$

and

$$F_{Lm} = \frac{L_m^f}{L_m} = \frac{g\mu_r + l_c}{\sigma_r^2 g\mu_r + l_c} = 1.219. \quad (6.5)$$

Thus, the magnetizing inductance is obtained as 406.8 μH which is close to the original design specification.

From the calculated current density given by (3.27), the required conduction areas of the primary winding and secondary winding are around 0.3 mm^2 and 1.5 mm^2 , respectively. The detailed design of the primary and secondary winding will be described next.

6.3 Windings Optimization

In the transformer, 35 turns in the primary winding and 8 turns in the two secondary windings are required. First of all, the full interleaving of these windings would be preferred to reduce the high frequency proximity effect and minimize the leakage inductance of the transformer. In the first step of the winding optimization, we will apply the method proposed in Chapter 5 and then the FEA simulation tool will be introduced to further optimize the winding arrangement with the fringing effect considered.

Referring the calculations of currents in the LLC resonant converter presented in Chapter 2, the phase shift angle φ between the resonant current and the current through the secondary winding 1 is given by (B3.5)

$$\varphi = -\tan^{-1} \frac{a^2 R_L T_r^2}{2\pi L_m T_s} = -0.545. \quad (6.6)$$

Considering the reference positive direction for the transformer winding, the phase shift angle between the currents through the primary and the secondary winding is $\varphi_{ps} = 211.2^\circ$. Consequently, the ratio of AC resistance to DC resistance of the planar transformer with circular winding and fringing effect ignored can be calculated by (5.25)

$$F_{R\varphi} = \Delta \left[\frac{\sinh(2\Delta) + \sin(2\Delta)}{\cosh(2\Delta) - \cos(2\Delta)} + 2(1 + \cos \varphi_{ps}) \frac{n_p^2 - 1}{3} \frac{\sinh(\Delta) - \sin(\Delta)}{\cosh(\Delta) + \cos(\Delta)} \right], \quad (6.7)$$

where n_p is the number of layers and it is given by half of the total winding layers because it is related to the case with the phase shift angle of the primary and secondary currents of 0 which means the transformer acts as the inductor. Based on (6.7), the optimum thickness of the circular conductor is calculated by (5.20) with

$$n_{pp} = \sqrt{(1 + \cos \varphi_{ps})(n_p^2 - 1)} + 1. \quad (6.8)$$

For this case, the optimum value of Δ is 0.77.

However, we need consider the porosity factor of windings filling in the window area. As the gap length placed in the centre leg is 1 mm, the winding would be placed away from the gap about 2.5 mm for initial design assumption to avoid the fringing effect. The outer edge of windings should also be placed away from the core for proper insulation. Thus, the porosity factor is calculated by

$$\eta = \frac{\ln\left(\frac{16 \text{ mm}}{10.5 \text{ mm}}\right)}{\ln\left(\frac{17 \text{ mm}}{8 \text{ mm}}\right)} = 0.56. \quad (6.9)$$

The equivalent skin depth is $\delta_{0\eta} = 0.27$ mm. Thus, the initial conductor thickness is chosen as 0.21 mm.

In an attempt to place more primary conductor in the windings, two layer of primary windings are attached together. In order to reduce the winding loss in the gapped planar transformer, FEA simulation was introduced and a series of simulations were carried out. The thickness of the circular conductor varies from 0.15 mm to 0.25 mm. The distance of the windings away from the gap is changed from 0.5 mm to 4 mm. The outer radius of the windings is fixed at 16 mm. The clearance in the primary layer is 0.4 mm. The simulation results are given in Fig. 6.1. The minimum winding loss can be achieved for the conductor thickness of 0.25 mm and it is also the available maximum value limited by the window height. The predicted optimum thickness is quite close, notwithstanding the error is due to the complex fringing field caused by the air gap.

Finally, the thickness of the conductor is determined to be 0.25 mm. Due to the fabrication implementation and capability, the width of the copper track of the primary winding is 0.75 mm and the clearance is 0.375 mm. The inner radius and outer radius if the secondary pattern are 11.5 mm and 16 mm, respectively.

The implementation for each layer of the primary winding is shown in Fig. 6.2. Both sides of the primary winding are covered by the kapton tape to ensure the proper insulation between the primary winding and secondary winding. Each secondary windings consists of 4 layers of the copper foil and the cutting patterns are shown in Fig. 6.3. The assembly drawing with interleaving is shown in Fig. 6.4.

For the designed gapped transformer, the core loss based on iGSE calculation method is $P_c = 0.083$ W based on (3.16). Combing the DC resistances of windings and the rms values of currents through windings, the DC winding loss can be calculated as

$$\begin{aligned} R_{p_dc} &= 35 \times (84.8 \times 10^{-3}) \times 0.092 \times [1 + 0.00393 \times (90 - 20)] = 0.347 \ \Omega, \\ R_{s1_dc} &= 4 \times (84.8 \times 10^{-3}) \times 0.015 \times [1 + 0.00393 \times (90 - 20)] = 0.007 \ \Omega, \quad (6.10) \\ P_{cu_dc} &= R_{p_dc} I_{r_rms}^2 + 2R_{s1_dc} I_{s1_rms}^2 = 1.714 \ \text{W}. \end{aligned}$$

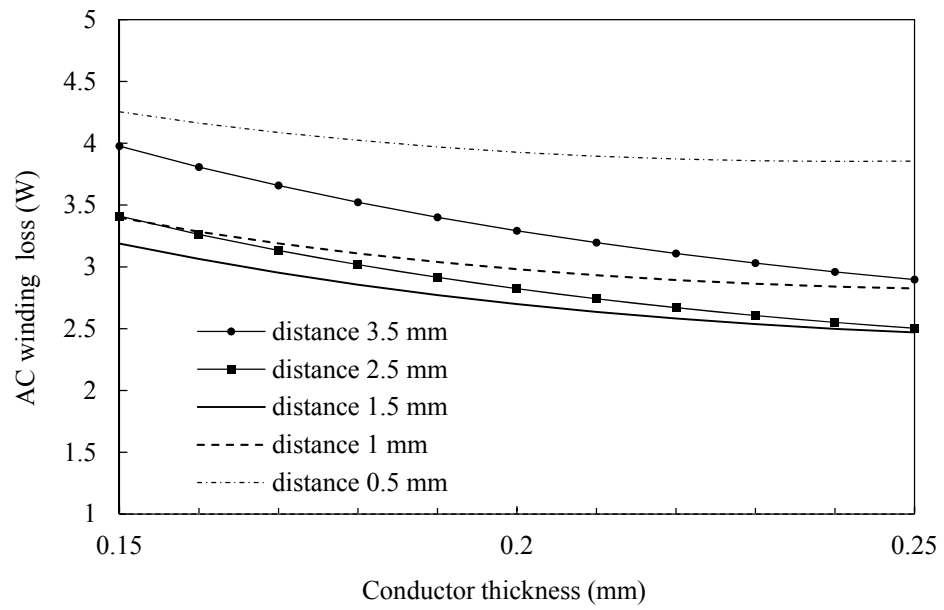


Fig. 6.1 Simulation results of winding loss in the gapped planar transformer with different thicknesses and distances away from the gap

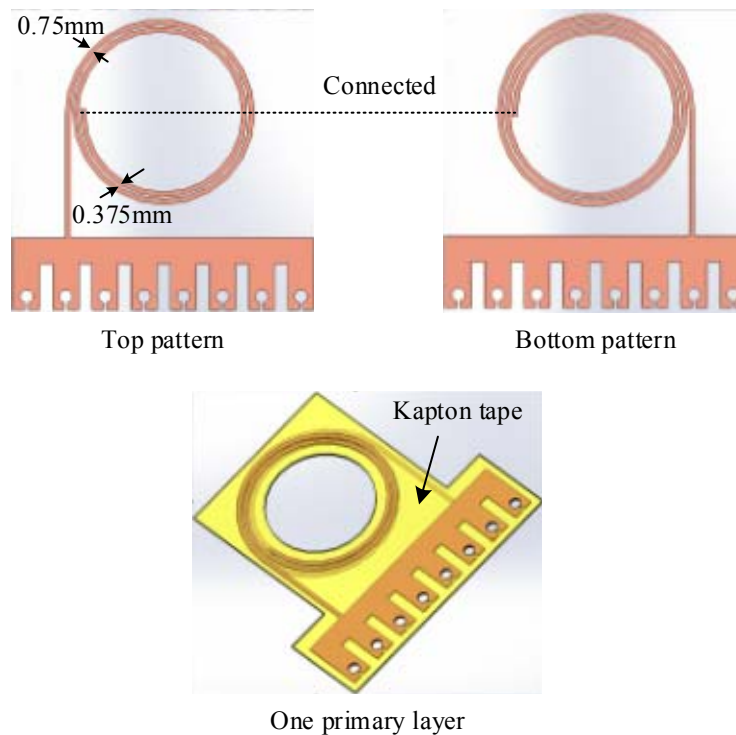


Fig. 6.2 Fabrication and assembly for the primary winding

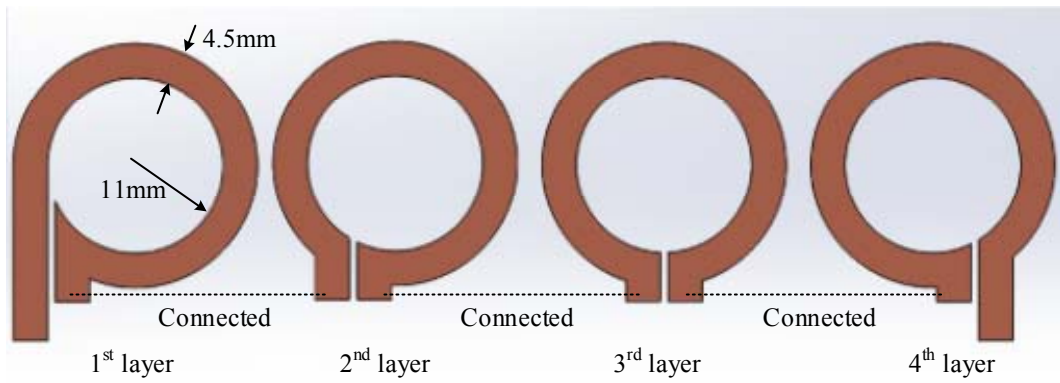


Fig. 6.3 Cutting patterns of the secondary winding

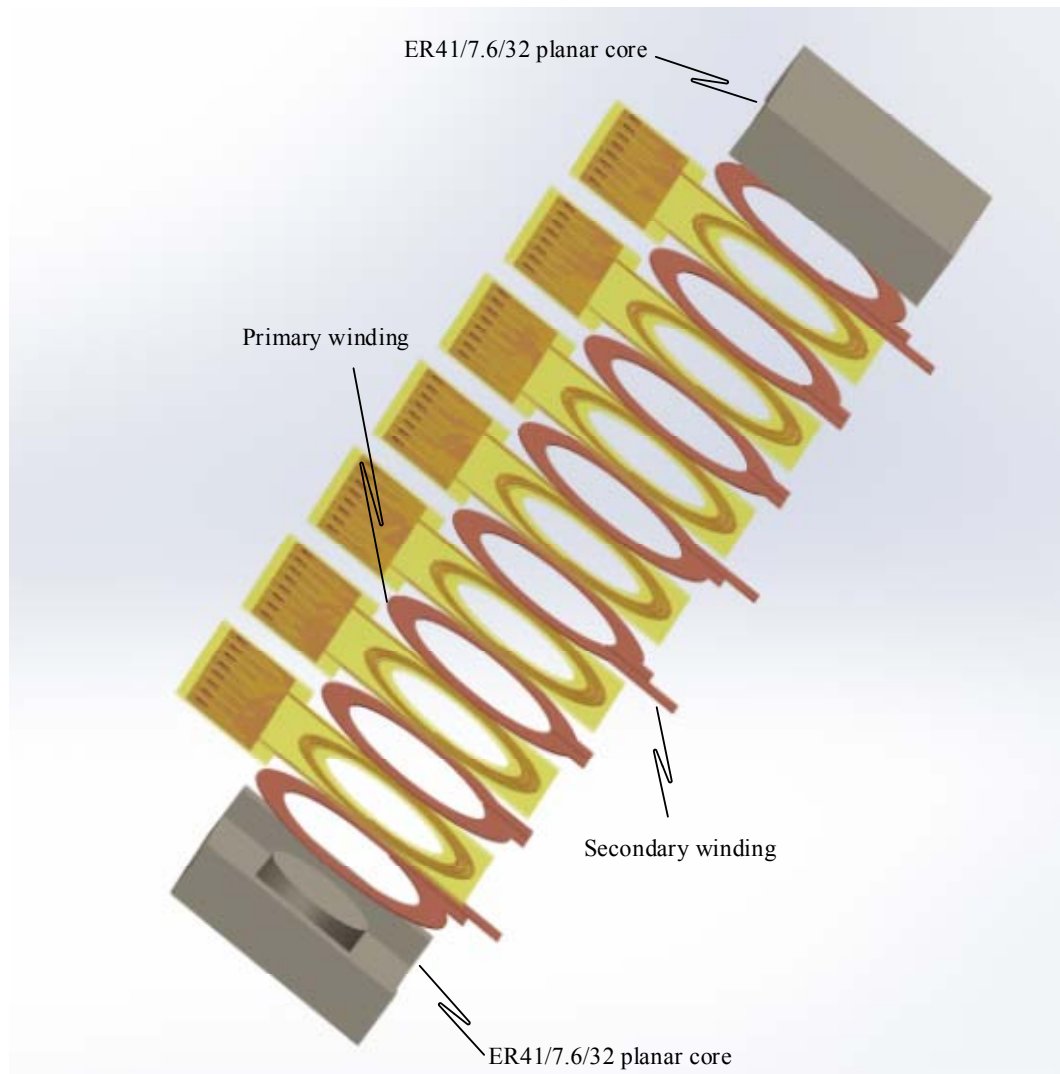


Fig. 6.4 Assembly drawing of the gapped planar transformer

TABLE 6.3 LOSSES BREAKDOWN OF THE PLANAR TRANSFORMER

Parameters	Symbols	Values
Maximum power loss	P_{\max}	3.592 W
DC winding loss	$P_{\text{cu_dc}}$	1.714 W
AC winding loss	$P_{\text{cu_ac}}$	3.382 W
Core loss	P_c	0.083 W
Total loss	P_{trafo}	3.465 W

FEA tools was applied to obtain the accurate winding loss of the gapped planar transformer as the fringing effect involved. The total AC winding loss was simulated to be 3.382 W. Individual losses are listed in Table 6.3. The maximum allowed power loss of the planar transformer based on thermal considerations is 3.592 W. The total loss for the designed gapped planar transformer is 3.465 W. It means the temperature rise of the transformer will not exceed the permissible range.

At the end of the design, the parameters including the window utilization factor and the value of γ should be checked. The total window utilization factor is

$$k_u = \frac{35 \times (1.875 \times 10^{-7}) + 2 \times 4 \times (1.125 \times 10^{-6})}{65 \times 10^{-6}} = 0.239. \quad (6.11)$$

The value of γ is given by

$$\gamma = \frac{P_{\text{trafo}} - P_{\text{cu_dc}}}{P_{\text{cu_dc}}} = 1.02. \quad (6.12)$$

These calculations correspond to the initial assumption values. According to the design result, the planar transformer was fabricated and the photo shown in Fig. 6.5.

6.4 Experimental Results of Gapped Planar Transformer

The designed planar transformer was embedded in the LLC resonant converter prototype. Fig. 6.6 shows the photo of the test set-up. The typical operating waveforms with the rated output current of 10 A are presented in Fig. 6.7. The waveforms show that the LLC resonant converter is operating as expected.



Fig. 6.5 Planar transformer fabricated based on the design results

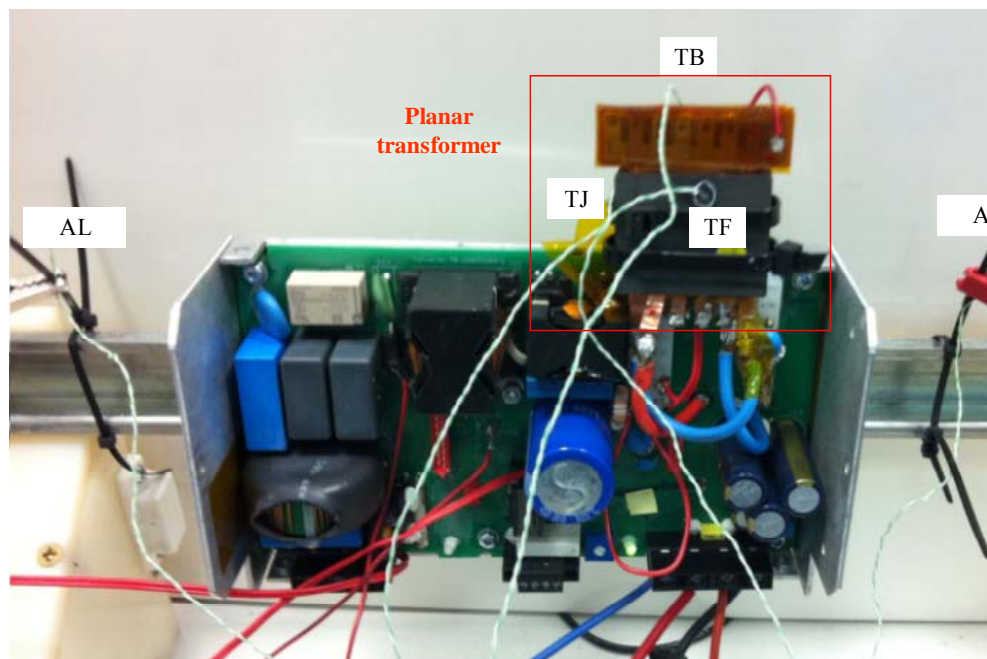


Fig. 6.6 Test set-up for the gapped planar transformer in the LLC resonant converter

The temperature was tested at three locations on the surface of the planar transformer: (1) TF is the centre point of the front surface of the magnetic core; (2) TB is the centre point of the back surface of the magnetic core; (3) TJ is the joint point between two EE cores. The ambient temperature was measured on both the left side (AL) and the right side (AR) of the planar transformer and the distance from the converter is about

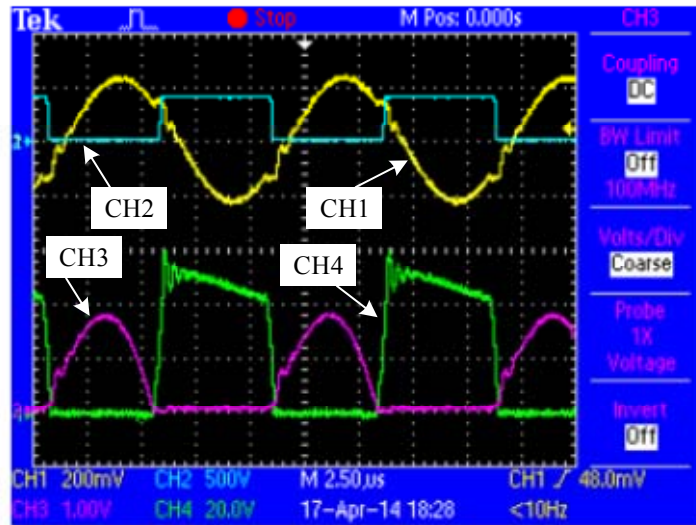


Fig. 6.7 Typical experimental waveforms (CH1: resonant current, 2 A/div; CH2: voltage of the resonant tank, 500 V/div; CH3: secondary current, 10 A/div; CH4: voltage of the secondary side, 20 V/div)

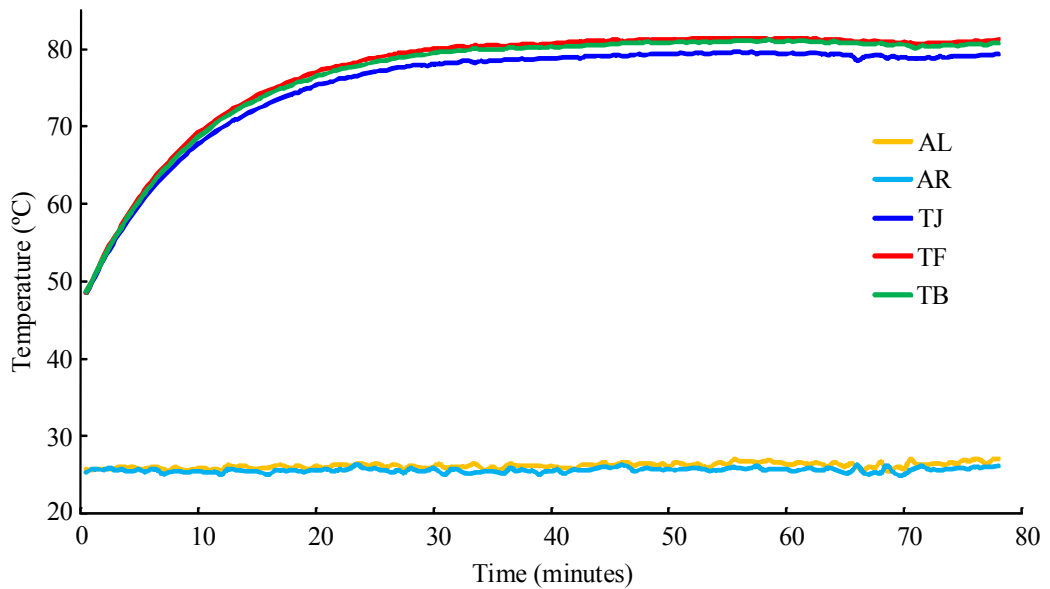


Fig. 6.8 Temperature rise of the gapped planar transformer tested at different places on the core surface

5 cm. The temperature rise curves at different points are shown in Fig. 6.8. The final temperature rise of the transformer is 53.7 °C and it meets the specified maximum of 60 °C.

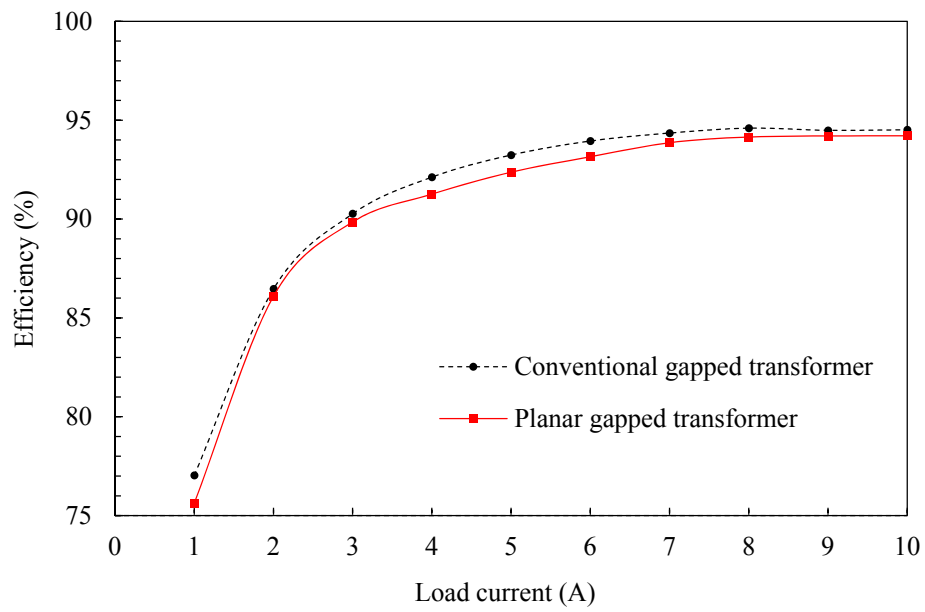
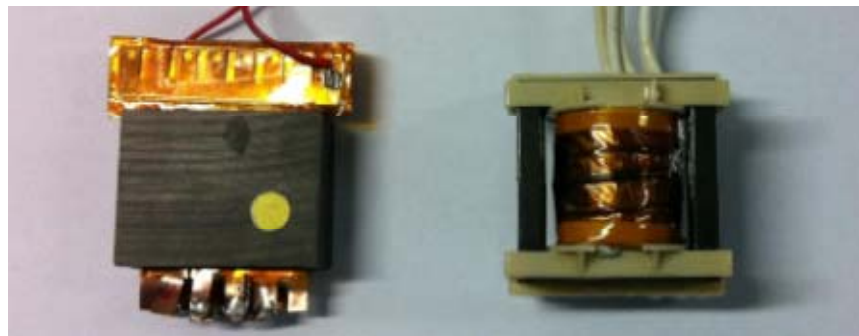
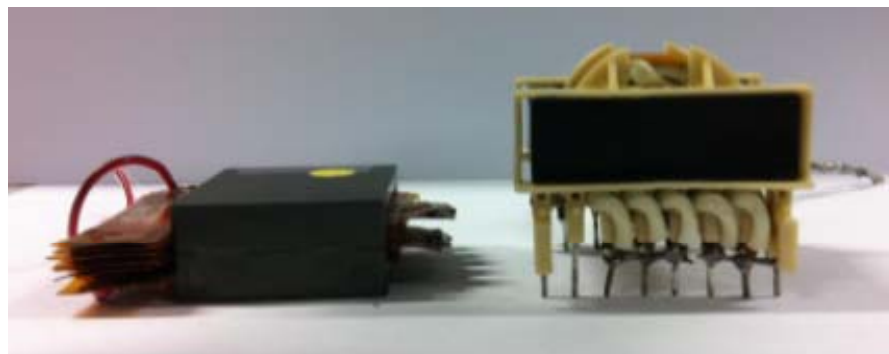


Fig. 6.9 Efficiencies of the LLC resonant converter incorporating designed planar gapped transformer and conventional gapped transformer



(a) Top view



(b) Side view

Fig. 6.10 Top view and side view of the designed planar gapped transformer and conventional transformer

The efficiency of the LLC resonant converter with a planar transformer under different currents is shown in Fig. 6.9 and it is compared with the efficiency of the LLC resonant converter incorporating the conventional gapped transformer designed in Chapter 3. It is shown that the efficiency with the planar gapped transformer is close to the conventional transformer. The experimental results show that the design methodology and the implementation method for the planar transformer works according to the specifications.

Fig. 6.10 shows the top view and side view of the designed planar gapped transformer and conventional gapped transformer. The height of the planar transformer is much lower than the conventional transformer. It is possible to use the low profile planar transformer in the LLC resonant converter to replace the conventional transformer.

6.5 Conclusions

In this chapter, the gapped planar transformer applied in the LLC resonant converter was designed based on the presented methodology. The winding configurations was optimum selected and the gapped planar transformer for the 240 W, 105 kHz LLC resonant converter has been fabricated. The experimental results for the planar transformer verified the design process and the assembly method. Comparison with the conventional transformer shows that successful operation is possible with the low profile core.

7

Conclusions and Future Work

7.1 Introduction

The LLC resonant converter is the preferred topology for power supplies because of the natural superiorities of soft switching within a wide range of the input voltage variation, the load conditions and the effective utilizations of stray parameters in the circuit, including the leakage inductance and the magnetizing inductance of the transformer. The design procedure of the LLC resonant converter, particularly the transformer was the main target of the thesis. The proper design methodologies for the LLC resonant converter and the gapped transformer for the purpose of integrating the magnetizing inductance are significant for the operation performance of the whole circuit. Meanwhile, the planar transformer was implemented with the power switching circuit to achieve lower profile and higher power density. The effort to involve the planar transformer with the LLC resonant converter was pursued and the associated design considerations were investigated. Basically, all the analysis and design issues were discussed in this thesis and the chief contributions may be summarised as follows.

7.2 Contributions to Gapped and Planar Transformers in LLC Resonant Converters

- The new design methodology for the main parameters in LLC resonant converters was presented.

- The design considerations include the power loss, the soft-switching requirement, the input voltage variation, the input voltage variations and the light load operation.
- The design procedure was shown in Fig. 2.8 and the related equations were given.
- The novel design methodology for the gapped transformer was proposed which can be applied to both conventional transformers and planar transformers.
 - The design considerations for the gapped transformer applied in the LLC resonant converter include the magnetizing inductance, the multi windings, the winding loss, the core loss and the temperature rise.
 - The design procedure was presented in Fig. 3.3 and the design equations were given.
- The modelling methodology for the planar transformer was proposed.
 - Calculation method for the high frequency winding loss of the planar transformer was presented.
 - Optimum selection of the conductor thickness of the planar winding was proposed.
 - Modelling of the winding loss with the phase shifted excitations was shown.
 - Stray capacitance calculation methodology was carried out.
- The calculation method for the leakage inductance in the integrated planar transformer with the magnetic shunt was proposed.

7.3 Future Work

On the progress and the related analysis in this thesis, prospective research on the optimization of LLC resonant converters and planar magnetics could be continued and possible future work includes:

(1) System optimization with the phase shift angle between the primary and secondary current through the transformer windings. As we found the high frequency AC winding loss is dramatically influenced by the phase shift angle, which is directly related to the resonant parameters in the circuit and the load condition, the overall investigation of the optimization of the LLC resonant converter considering the phase shift angle and the different load conditions will bring higher performance to the whole circuit.

(2) Integrated planar transformer with magnetic shunt. Based on the leakage inductance calculations proposed for the integrated planar transformer with the magnetic shunt, the resonant inductor in the LLC resonant converter can be replaced by the leakage inductance and thus the total volume of magnetic components would be minimized. The loss analysis of the integrated planar transformer with magnetic shunt would be interesting to show the optimum selection of the magnetic shunt material and implementation.

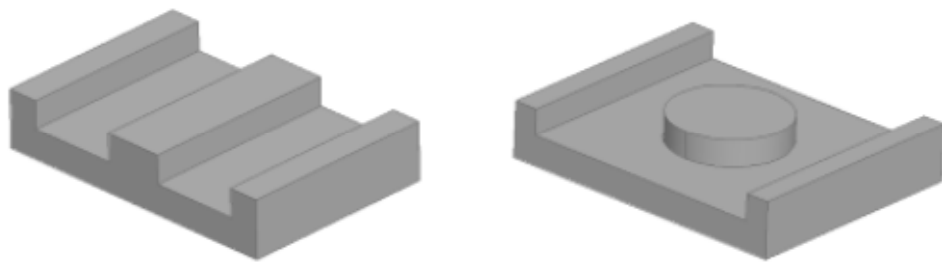
(3) GaN switches show the great promise in the LLC resonant converter. The switching frequency of the resonant converter with GaN devices can be much higher than the regular Silicon devices and it means the size of the converter can be significantly reduced. In [208], the role of GaN devices in LLC resonant converters were introduced in details. The reduced output capacitance of GaN leads to lower circulating current losses in the resonant tank and results in the possibility of applying larger magnetizing inductance which means lower fringing loss as the smaller gap can be used. For the planar transformer applied in the LLC resonant converter with GaN devices, the switching frequency will be extremely high and some other issues will come out including the connections of different layers in the planar windings and the stray leakage inductance due to the terminals of the planar windings.

Another advantage is that GaN devices have little to no reverse recovery charge and the failure operation of light load conditions can be eliminated. Thus, applying GaN switching device in high frequency LLC resonant converter has great potential.

Appendix A

Planar EE and ER Cores

In the planar magnetics, E and ER planar cores are widely applied and the basic shapes are shown in Fig. A.1. The low profile EQ cores can also be used in planar magnetics. They can be assembled as a set or with a flat block core. The commercial products manufactured by Ferroxcube [162] and TDK EPCOS [163] and their dimensions are listed in Table A.1 and Table A.2, respectively. EER41/7.6/32 was applied to fabricate the planar gapped transformer for the 240 W LLC resonant converter and EELP43 was applied to carry out the experiments of leakage inductance with the magnetic shunt.



(a) Planar E core

(b) Planar ER core

Fig. A.1 Shapes of planar E core and ER core

TABLE A.1 PLANAR EE CORES, ER CORES AND EQ CORES MANUFACTURED BY FERROXCUBE

Cores	l_c (mm)	A_c (mm ²)	Volume (mm ³)	Height (mm)	Window width (mm)	Window height (mm)	A_p (mm ⁴)
EER9.5/2.5/5	14.2	8.47	120	4.9	2	3.2	54.21
EER11/2.5/6	14.7	11.9	174	4.9	2.225	3	79.43
EER14.5/3/7	19.0	17.6	333	5.9	3.5	3.1	190.96
EER18/3.2/10	22.1	30.2	667	6.3	4.7	3.2	454.21
EER23/3.6/13	26.6	50.2	1340	7.2	6.1	3.2	979.90
EER32/6/25	38.2	141	5400	12	7.4	5.8	6051.72
*EER41/7.6/32	57.0	225	12900	15.2	9.02	7.2	14612.40
EER51/10/38	73.5	351	25800	20.32	10.9	9.9	37876.41
EER64/13/51	93.0	566	52600	25.4	14.05	12.5	99403.75
EE14/3.5/5	20.7	14.3	300	7	4	4	228.80
E14/3.5/5 PLT14/5/1.5	16.7	14.5	240	5	4	2	116
EE18/4/10	24.3	39.3	960	8	5	4	786
E18/4/10 PLT18/10/2	20.3	39.5	800	6	5	2	395
EE22/6/16	32.5	78.3	2550	11.4	5.9	6.4	2956.61
E22/6/16 PLT22/16/2.5	26.1	78.5	2040	8.2	5.9	3.2	1482.08
EE32/6/20	41.4	130	5380	12.7	9.275	6.36	7668.57
E32/6/20 PLT32/20/3.2	35.1	130	4560	10.16	9.275	3.18	3834.29
EE38/8/25	52.4	194	10200	16.52	11.315	8.9	19536.48
E38/8/25 PLT38/25/3.8	43.7	194	8460	12.07	11.315	4.45	9768.24
EE43/10/28	61.1	229	13900	19	13.3	10.8	32893.56
E43/10/28 PLT43/28/4.1	50.4	229	11500	13.6	13.3	5.4	16446.78
EE58/11/38	80.6	308	24600	21	20.95	13	83883.80

APPENDIX A. PLANAR EE AND ER CORES

(continued)

Cores	l_c (mm)	A_c (mm ²)	Volume (mm ³)	Height (mm)	Window width (mm)	Window height (mm)	A_p (mm ⁴)
E58/11/38 PLT28/38/4	67.7	310	20800	14.6	20.95	6.5	42214.25
EE64/10/50	79.9	519	40700	20.4	21.8	10.2	115404.84
E64/10/50 PLT64/50/5	69.7	519	35500	15.28	21.8	5.1	57702.42
EEQ13	17.5	19.9	348	5.7	3.1	3.5	215.92
EQ13 PLT13/9/1	15.9	19.8	315	3.95	3.1	1.75	107.42
EEQ20/R	33.2	59	1960	12.6	4.6	8.2	2225.48
EQ20/R PLT20/14/2/S	25.1	59.8	1500	8.6	4.6	4.1	1127.83
EQ25/LP PLT25/18/2	26.4	89.7	2370	11.2	5.5	6.4	3157.44
EEQ30	46.0	108	4970	16	7.5	10.6	8586
EQ30 PLT30/20/3	36.2	108	3910	10.7	7.5	5.3	4293
EEQ38/8/25	51.9	152	7900	16	9.55	10.6	15386.96
EQ38/8/25 PLT38/25/2.7	41.7	148	6190	10.7	9.55	5.3	7491.02

TABLE A.2 PLANAR EE CORES, ER CORES AND EQ CORES MANUFACTURED BY TDK EPCOS

Cores	l_c (mm)	A_c (mm ²)	Volume (mm ³)	Height (mm)	Window width (mm)	Window height (mm)	A_p (mm ⁴)	Thermal resistance (K/W)
EER9.5/5	13.6	8.81	120	5	2	3.2	56.38	164
EER11/5	14.1	12.4	174	5	2.225	3	82.77	134
EER14.5/6	19	17.6	333	5.9	3.55	3.3	206.18	99
EER18/3/10	22.1	30.2	667	6.3	4.7	3.1	440.01	
EER23/5/13	32.6	50.3	1640	10.2	6.1	6.2	1902.35	
ER23/5/13 I23/2/13	26.6	50.3	1335	7.2	6.1	3.1	951.17	
EER25/6/15	34.1	70.8	2414	11	6.15	6.2	2699.60	
ER 25/6/15 I25/3/15	28.1	70.4	1978	8	6.15	3.1	1342.18	
EER32/5/21	38.3	100.5	3847	10.2	9.25	5.4	5019.98	
EELP14	20.7	14.3	296	7	4	4	228.80	105
EILP14	16.7	14.5	242	5	4	2	116	116
EELP18	24.3	39.3	955	8	5	4	786.00	56
EILP18	20.3	39.5	802	6	5	2	395	61
EELP22	32.5	78.3	2540	11.4	5.9	6.4	2956.61	35
EILP22	26.1	78.5	2050	8.2	5.9	3.2	1482.08	38
EELP32	41.4	130	5390	12.7	9.525	6.4	7924.80	24
EILP32	35.1	130	4560	9.5	9.525	3.2	3962.4	26
EELP38	52.4	194	10200	16.5	11.6	8.9	20028.56	18
EILP38	43.6	194	8440	12.05	11.6	4.45	10014.28	20
*EELP43	61.6	225	13748	19	13.65	10.8	33169.50	15
EILP43	50.8	225	11430	13.6	13.65	5.4	16584.75	16
EELP58	80.7	310	25000	21.1	21.5	13	86645.00	11
EILP58	67.7	308	21000	14.6	21.5	6.5	43043	12
EELP64	79.9	519	41500	20.4	21.7	10.2	114875.46	9

(continued)

Cores	l_c (mm)	A_c (mm ²)	Volume (mm ³)	Height (mm)	Window width (mm)	Window height (mm)	A_p (mm ⁴)	Thermal resistance (K/W)
EILP58	67.7	308	21000	14.6	21.5	6.5	43043	12
EELP64	79.9	519	41500	20.4	21.7	10.2	114875.46	9
EILP64	69.7	519	36200	15.3	21.7	5.1	57437.73	9.5
EELP102	147.6	538	79410	40.6	36	26.6	511549.92	
EILP102	121.2	534.2	67745	27.3	36	13.3	255774.96	
EEQ13/3	17.5	19.8	347	5.7	1.075	3.5	74.50	
EQ13/3 I13/1	15.9	19.8	315	3.95	1.075	1.75	37.25	
EEQ20/6	33.2	59.0	1960	12.6	4.6	8.2	2225.48	
EQ20/6 I20/2	25.1	59.8	1550	8.6	4.6	4.1	1127.83	
EEQ25/6	32.95	93.51	3082	11.2	5.5	6.4	3291.55	
EQ25/6 I25/2	26.4	89.7	2370	7.9	5.5	3.2	1578.72	
EEQ30/8	46	108	4970	16	7.5	10.6	8586	
EQ30/8 I30/3	31.5	108	3400	10.7	7.5	5.3	4293	

Appendix B

Fundamental Frequency Analysis of LLC Resonant Converters

The fundamental frequency analysis of LLC resonant converters containing the transformer with secondary winding centre-tapped and the rectifier with diodes are summarised in this section. The output voltage characteristic and calculations for typical currents in the circuit have been sketched out in Chapter 2. As aforementioned, the switching frequency of the LLC resonant converter will vary according to the load condition and the input voltage in order to maintain the constant output voltage. Modelling of LLC resonant converter is complex and lots of effects in previous researchers' work focused to derive the accurate model which can be utilized to realise the control strategy. Among these analysis methodologies, the fundamental frequency analysis (FFA) is the most referenced and firstly applied to analysis the resonant converter by Steigerwald in [205]. Fig. B.1 presents the typical topology of the LLC resonant converter with the uncontrolled rectifier.

Referring to the FFA presented in [43] and [206], the DC voltage gain of LLC resonant converter will be derived firstly based on following assumptions:

(1) The resonant current in the resonant tank which consists of three components, the resonant inductor L_r , the resonant capacitor C_r and the magnetizing inductor L_m is assumed to be pure sinusoidal to simply the modelling of the circuit.

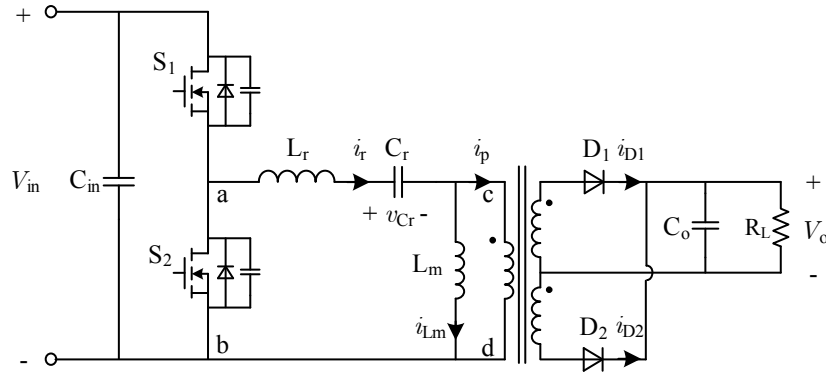


Fig. B.1 Half-bridge LLC resonant converter with the uncontrolled rectifier

- (2) Parasitic parameters of the transformer, for instance, leakage inductances and stray capacitances, are neglected.
- (3) The components are ideal and the efficiency of the circuit is $\eta = 100\%$.
- (4) The input voltage V_{in} and output voltage V_o are constant.

In the analysis, the equivalent resistance R_{eq} is calculated to replace the components in the secondary side of the transformer including the rectifier, the output filter and the load. Two main switches in the bridge, S_1 and S_2 , are complementarily conducting and the duty-cycle is supposed to be 0.5 with the dead time ignored as it is relatively small compared with the switching period. The output voltage of the half bridge, v_{tank} , has a rectangular waveform with two voltages, V_{in} and 0. The fundamental component at the switching frequency is calculated by

$$v_{tank1} = \frac{2V_{in}}{\pi} \sin(\omega_s t), \quad (B.1)$$

where ω_s is the angular switching frequency.

Two diodes, D_1 and D_2 , in the rectifier are complementarily forward biased. The output voltage of the resonant tank, v_p , owns a rectangular waveform. The higher and lower values are $a V_o$ and $-a V_o$ if the turns ratio of the transformer is $a:1:1$. The fundamental component of v_p is

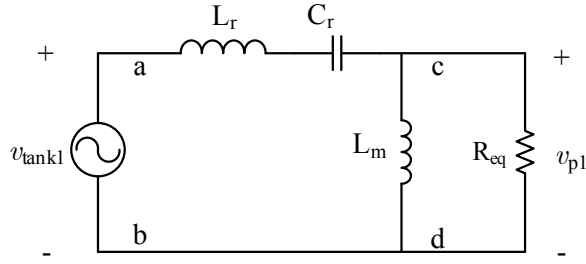


Fig. B.2 Equivalent circuit of the LLC resonant converter based on FFA

$$v_{p1} = \frac{4a V_o}{\pi} \sin(\omega_s t - \varphi_v), \quad (\text{B.2})$$

where φ_v represents the phase shift between v_{tank1} and v_{p1} .

At switching frequency, the equivalent resistance R_{eq} is the load resistance reflected to the primary side and the results is given by

$$R_{\text{eq}} = \frac{8a^2}{\pi^2} R_L, \quad (\text{B.3})$$

where R_L is the load resistance. The equivalent circuit based on FFA for the LLC resonant converter is shown in Fig. B.2.

From the equivalent circuit, we have the following relationship between the input voltage and output voltage of the resonant tank,

$$\left| \frac{v_{p1}}{v_{\text{tank1}}} \right| = \left| \frac{R_{\text{eq}} \parallel (j\omega_s L_m)}{j\omega_s L_r + \frac{1}{j\omega_s C_r} + R_{\text{eq}} \parallel (j\omega_s L_m)} \right|. \quad (\text{B.4})$$

Combing (B.1), (B.2), (B.3) and (B.4), we can obtain

$$\frac{2a V_o}{V_{\text{in}}} = \frac{1}{\left| 1 + \frac{L_r}{L_m} \left(1 - \left(\frac{\omega_r}{\omega_s} \right)^2 \right) + j \left(\frac{\omega_s}{\omega_r} - \frac{\omega_r}{\omega_s} \right) \frac{1}{R_{\text{eq}}} \sqrt{\frac{L_r}{C_r}} \right|}, \quad (\text{B.5})$$

where ω_r is the angular resonant frequency for L_r and C_r and the expression is

$$\omega_r = \frac{1}{\sqrt{L_r C_r}}. \quad (\text{B.6})$$

In order to simplify the result, some factors are introduced including the inductance ratio (k), the equivalent quality factor (Q) and normalized switching frequency (f_n). The definitions are

$$k = \frac{L_m}{L_r}, \quad (\text{B.7})$$

$$Q = \frac{\pi^2}{8a^2 R_L} \sqrt{\frac{L_r}{C_r}}, \quad (\text{B.8})$$

$$f_n = \frac{f_s}{f_r} = \frac{\omega_s}{\omega_r}, \quad f_n = \frac{f_s}{f_r} = \frac{\omega_s}{\omega_r}, \quad (\text{B.9})$$

where f_s and f_r are the switching frequency and the resonant frequency for L_r and C_r , respectively. Finally, the DC voltage gain of the LLC resonant converter, which is represented by M , is given as

$$M = \frac{V_o}{V_{in}} = \frac{1}{2a \sqrt{\left[1 + \frac{1}{k} \left(1 - \frac{1}{f_n^2}\right)\right]^2 + \left[Q \left(f_n - \frac{1}{f_n}\right)\right]^2}}. \quad (\text{B.10})$$

It is indicated that the output voltage of the LLC resonant converter is dependent on the switching frequency. Once the load or the input voltage varies, the switching frequency should be adapted to guarantee the unchanged output. For a certain LLC resonant converter, the parameter k in (B.10) will be fixed. The voltage gain will be related to the load and the normalized switching frequency f_n . Fig. B.3 shows a group of curves for the voltage gain with different values of Q ($Q = 0.1, 0.3, 0.5, 0.7, 1$ or 2) and $k = 10$.

In the LLC resonant converter, there are two associated resonant frequencies and they are

$$f_r = \frac{1}{2\pi \sqrt{L_r C_r}}, \quad f_{rm} = \frac{1}{2\pi \sqrt{(L_r + L_m) C_r}}. \quad (\text{B.11})$$

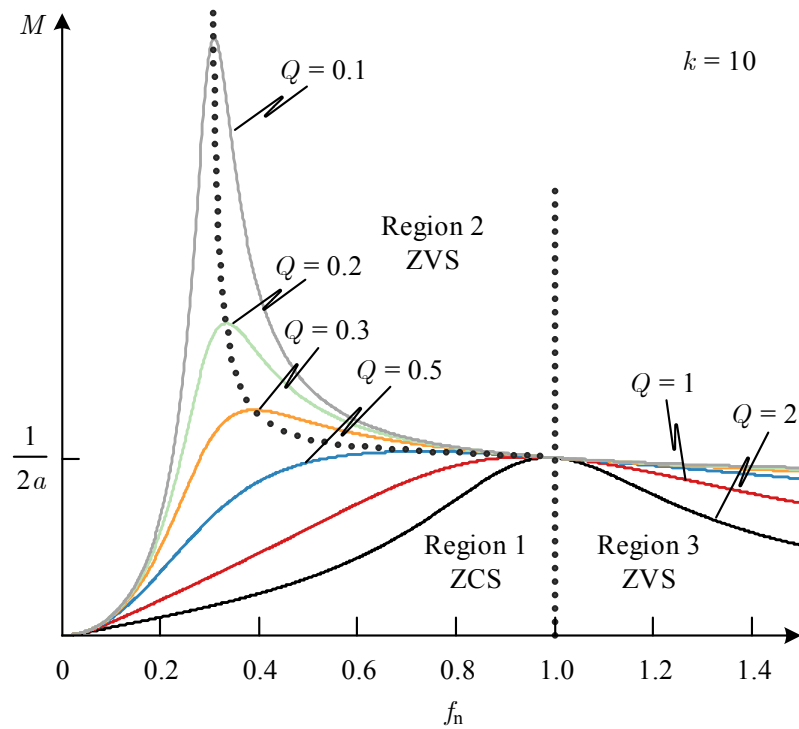


Fig. B.3 DC voltage gain of the LLC resonant converter

Due to the relative magnitude between f_s and f_r and f_{rm} , the whole plotting area in Fig. B.3 can be divided into three regions, region 1 ($f_s < f_{rm}$), region 2 ($f_{rm} < f_s < f_r$) and region 3 ($f_s > f_r$). In region 1, the resonant tank is capacitive and the resonant current leads the voltage. Thus, the zero current switching (ZCS) can be achieved for S_1 and S_2 . In region 2 and region 3, the input impedance of the resonant tank is inductive and the resonant current lags the voltage. The ZVS of S_1 and S_2 can be realised. The ZVS of MOSFETs will take more advantages than the ZCS which leads to the selection of operation at region 2 or 3 for the LLC resonant converter. Particularly, the ZCS switching off of the diodes at the secondary side is attained at region 2, where the switching frequency is lower than the resonant frequency, because the resonant current will oscillate to the magnetizing current (current through the magnetizing inductor L_m) before the driving signal for main switches. Consequently, the operation of LLC resonant converter is normally selected to be in region 2.

[206], [7] and [207] have done the operation analysis and calculations for the LLC resonant converter under region 2 ($f_{rm} < f_s < f_r$). The following derivation partly

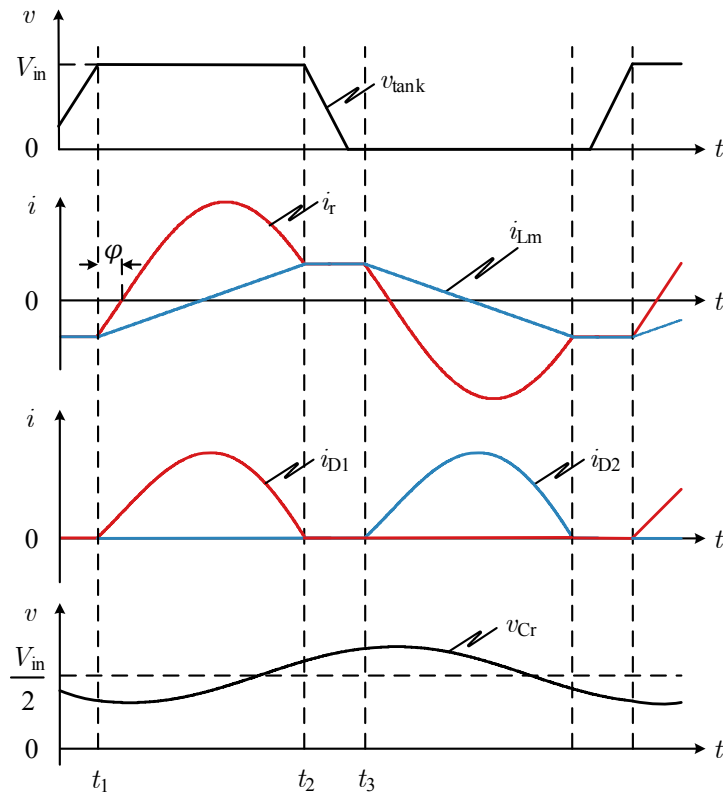


Fig. B.4 Waveforms of the LLC resonant converter

follows [7] and [207]. The modes operation and waveforms of the associated currents and voltages were already presented in Chapter 2. With the rated load, f_s is close to f_r . Meanwhile, L_m is quite bigger than L_r . It is reasonable to assume that the resonant current (i_r) and magnetizing current (i_{Lm}) maintain the same value during the dead time. The waveforms can be simplified as shown in Fig. B.4. i_{D1} and i_{D2} represent the currents through D1 and D2, respectively. The voltage of the resonant capacitor C_r is v_{Cr} .

The corresponding equivalent circuits for $t_1 \sim t_2$ and $t_2 \sim t_3$ are presented in Fig. B.5. Based on the calculation of each stage, we can obtain numerical values of currents on each side of the transformer.

In Stage 1 ($t_1 \sim t_2$):

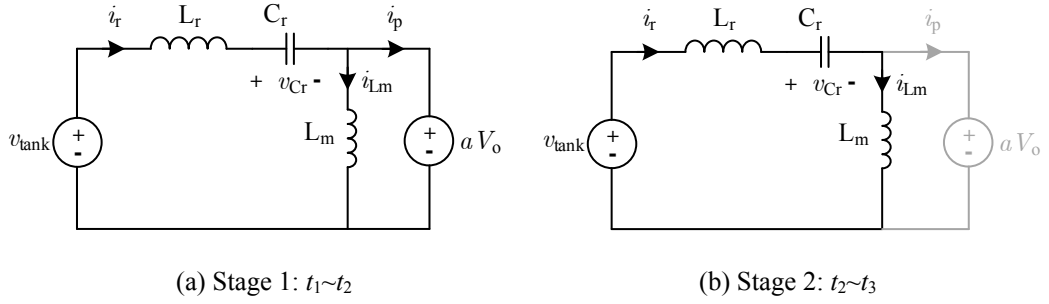


Fig. B.5 Equivalent circuits of the LLC resonant converter

The voltage supplied to the resonant tank is V_{in} . The voltage of L_m is clamped to $a V_o$.

The state equations are

$$\begin{cases} V_{in} = v_{Cr}(t) + L_r \frac{di_r(t)}{dt} + a V_o \\ i_r(t) = C_r \frac{dv_{Cr}(t)}{dt} \end{cases} \quad (\text{B.12})$$

The average value of i_{Lm} during the whole switching period is 0 and it is positive-negative symmetrical. We also have

$$\begin{cases} t_3 - t_1 = \frac{T_s}{2} \\ t_2 - t_1 = \frac{T_r}{2} \\ t_3 - t_2 = \frac{T_s - T_r}{2} \end{cases} \quad (\text{B.13})$$

Thus,

$$i_{Lm}(t_1) = -i_{Lm}(t_3). \quad (\text{B.14})$$

With the assumption

$$i_{Lm}(t_2) = i_{Lm}(t_3). \quad (\text{B.15})$$

Consequently,

$$i_{Lm}(t_1) = -i_{Lm}(t_2) = -i_{Lm}(t_3); \quad i_r(t_1) = i_{Lm}(t_1); \quad i_r(t_2) = i_{Lm}(t_2). \quad (\text{B.16})$$

During this stage, the variation of i_{Lm} is

$$i_{Lm}(t_2) - i_{Lm}(t_1) = \frac{a V_o T_r}{L_m} \frac{1}{2}. \quad (\text{B.17})$$

From (B.16) and (B.17), we can obtain

$$\begin{cases} i_r(t_1) = i_{Lm}(t_1) = -\frac{a V_o T_r}{4L_m} \\ i_r(t_2) = i_{Lm}(t_2) = \frac{a V_o T_r}{4L_m} \end{cases}. \quad (\text{B.18})$$

The DC components of v_{Cr} is half of V_{in} and the average value of the AC component of v_{Cr} is 0. Thus,

$$\frac{v_{Cr}(t_1) + v_{Cr}(t_3)}{2} = \frac{V_{in}}{2}. \quad (\text{B.19})$$

Based on (B.12), the variation of v_{Cr} during t_1 to t_3 is

$$v_{Cr}(t_3) - v_{Cr}(t_1) = \frac{1}{C_r} \int_{t_1}^{t_3} i_r(t) dt. \quad (\text{B.20})$$

On the other hand, during t_1 to t_3 ,

$$i_r(t) = i_{Lm}(t) + i_p(t) = i_{Lm}(t) + \frac{1}{a} i_{D1}(t), \quad (\text{B.21})$$

where i_p is the primary current of the ideal transformer which is shown in Fig. B.5.

And the integral of i_{Lm} within t_1 to t_3 is calculated by

$$\begin{aligned} \int_{t_1}^{t_3} i_{Lm}(t) dt &= \int_{t_1}^{t_2} i_{Lm}(t) dt + \int_{t_2}^{t_3} i_{Lm}(t) dt \\ &= 0 + (t_3 - t_2) \frac{a V_o T_r}{4L_m} = \frac{T_s - T_r}{2} \frac{a V_o T_r}{4L_m}. \end{aligned} \quad (\text{B.22})$$

The integral of i_{D1} within t_1 to t_3 is calculated by

$$\int_{t_1}^{t_3} i_{D1}(t) dt = (t_3 - t_1) I_o = \frac{T_s}{2} I_o, \quad (\text{B.23})$$

where I_o is the load current. Combing (B.20), (B.21), (B.22) and (B.23),

$$v_{Cr}(t_3) - v_{Cr}(t_1) = \frac{T_s I_o}{2a C_r} + \frac{a V_o (T_s - T_r) T_r}{8L_m C_r}. \quad (\text{B.24})$$

Based on (B.19) and (B.24), v_{Cr} at time t_1 can be solved by

$$v_{Cr}(t_1) = \frac{V_{in}}{2} - \frac{T_s I_o}{4a C_r} + \frac{a V_o (T_s - T_r) T_r}{16 L_m C_r}. \quad (B.25)$$

Thus, the differential equation (B.12) can be solved. The results are

$$\begin{cases} i_r(t) = I_{r_pk} \sin[\omega_r(t-t_1) + \varphi] \\ v_{Cr}(t) = V_{in} - a V_o - \omega_r L_r I_{r_pk} \cos[\omega_r(t-t_1) + \varphi] \end{cases} \quad (B.26)$$

where

$$I_{r_pk} = \sqrt{\left(\frac{a V_o T_r}{4 L_m}\right)^2 + \left(\left(\frac{V_{in}}{2} - a V_o\right) \frac{T_r}{2\pi L_r} + \frac{\pi I_o T_s}{2a T_r} - \frac{a V_o (T_s - T_r) T_r^2}{32\pi L_m L_r C_r}\right)^2}, \quad (B.27)$$

$$\varphi = \tan^{-1} \frac{-\frac{a V_o T_r}{4 L_m}}{\left(\frac{V_{in}}{2} - a V_o\right) \frac{T_r}{2\pi L_r} + \frac{\pi I_o T_s}{2a T_r} - \frac{a V_o (T_s - T_r) T_r^2}{32\pi L_m L_r C_r}}. \quad (B.28)$$

During stage 1, the magnetizing current i_{Lm} increases linearly and the expression is given by

$$i_{Lm}(t) = -\frac{a V_o T_r}{4 L_m} + \frac{a V_o}{L_m} (t - t_1). \quad (B.29)$$

In Stage 2 ($t_2 \sim t_3$):

Following the above-mentioned assumption, i_r and i_{Lm} are considered to maintain the constant value during this stage, thus

$$i_r(t) = i_{Lm}(t) = \frac{a V_o T_r}{4 L_m}, \quad (B.30)$$

$$v_{Cr}(t) = v_{Cr}(t_2) + \frac{1}{C_r} \frac{a V_o T_r}{4 L_m} (t - t_2). \quad (B.31)$$

Then v_{Cr} at time t_3 can be obtained by

$$\begin{aligned}
 v_{Cr}(t_3) &= V_{in} - a V_o - \omega_r L_r I_{r_pk} \cos[\omega_r (t_2 - t_1) + \varphi] + \frac{1}{C_r} \frac{a V_o T_r}{4L_m} (t_3 - t_2) \\
 &= \frac{3V_{in}}{2} - 2a V_o + \frac{\pi^2 I_o T_s L_r}{a T_r^2} + \frac{a V_o (T_s - T_r) T_r}{16L_m C_r}.
 \end{aligned} \tag{B.32}$$

Introducing (B.25) and (B.32) to (B.19), we can get

$$V_{in} = 2a V_o + \frac{a V_o (T_s - T_r) T_r}{8L_m C_r}. \tag{B.33}$$

Using (B.33), all results can be simplified. If we set t_1 to be the initial time of the calculation, i.e. $t_1 = 0$, the calculation results of i_r , i_{Lm} , v_{Cr} , i_{D1} and i_{D2} during half of the switching period are listed as follows.

(1) Resonant current through L_r (i_r)

$$i_r(t) = \begin{cases} I_{r_pk} \sin[\omega_r t + \varphi] & 0 < t < \frac{T_r}{2} \\ \frac{a V_o T_r}{4L_m} & \frac{T_r}{2} < t < \frac{T_s}{2} \end{cases}, \tag{B.34}$$

where

$$I_{r_pk} = \sqrt{\left(\frac{a V_o T_r}{4L_m}\right)^2 + \left(\frac{\pi I_o T_s}{2a T_r}\right)^2}, \quad \varphi = -\tan^{-1} \frac{a^2 R_L T_r^2}{2\pi L_m T_s}. \tag{B.35}$$

(2) Magnetizing current through L_m (i_{Lm})

$$i_{Lm}(t) = \begin{cases} -\frac{a V_o T_r}{4L_m} + \frac{a V_o}{L_m} t & 0 < t < \frac{T_r}{2} \\ \frac{a V_o T_r}{4L_m} & \frac{T_r}{2} < t < \frac{T_s}{2} \end{cases}. \tag{B.36}$$

(3) Voltage of resonant capacitor C_r (v_{Cr})

$$v_{Cr}(t) = \begin{cases} V_{in} - a V_o - \omega_r L_r I_{r_pk} \cos[\omega_r t + \varphi] & 0 < t < \frac{T_r}{2} \\ V_{in} - a V_o + \frac{\pi^2 I_o T_s L_r}{a T_r^2} + \frac{1}{C_r} \frac{a V_o T_r}{4L_m} \left(t - \frac{T_r}{2}\right) & \frac{T_r}{2} < t < \frac{T_s}{2} \end{cases}, \tag{B.37}$$

(4) Current through D_1 (i_{D1})

$$i_{D1}(t) = \begin{cases} aI_{r_pk} \sin[\omega_r t + \varphi] + \frac{a^2 V_o T_r}{4L_m} - \frac{a^2 V_o}{L_m} t & 0 < t < \frac{T_r}{2} \\ 0 & \frac{T_r}{2} < t < \frac{T_s}{2} \end{cases}, \quad (\text{B.38})$$

(5) Current through D₂ (i_{D2})

$$i_{D2}(t) = 0 \quad 0 < t < \frac{T_s}{2}. \quad (\text{B.39})$$

Appendix C

Design Equations for Gapped Transformers

The magnetizing inductance is given by

$$L_m = \frac{\mu_0 \mu_{\text{eff}} N_p^2 A_c}{l_c}. \quad (\text{C.1})$$

Following the operation principle of the gapped transformer in the LLC resonant converter, the maximum magnetic field in the core is

$$H_{\text{max}} = \frac{N_p I_{L_m_pk}}{l_c}. \quad (\text{C.2})$$

The maximum flux density in the core will be

$$B_{\text{max}} = \mu_0 \mu_{\text{eff}} H_{\text{max}} = \frac{\mu_0 \mu_{\text{eff}} N_p I_{L_m_pk}}{l_c}. \quad (\text{C.3})$$

The peak value of the magnetizing current is

$$I_{L_m_pk} = \frac{B_{\text{max}} l_c}{\mu_0 \mu_{\text{eff}} N_p}. \quad (\text{C.4})$$

Combing (C.1) and (C.4), gives

$$\frac{1}{2} L_m I_{L_m_pk}^2 = \frac{1}{2} \frac{A_c l_c B_{\text{max}}^2}{\mu_0 \mu_{\text{eff}}}. \quad (\text{C.5})$$

On the other hand, the DC winding loss of the primary winding is given by

$$P_{\text{cu}_p} = \rho_w \frac{l_{\text{wp}}}{A_{\text{wp}}} I_{\text{r}_\text{rms}}^2, \quad (\text{C.6})$$

where ρ_w is the conductivity of the copper, l_{wp} and A_{wp} are the length and conduction area of the primary winding, respectively. The length of the winding can be expressed by

$$l_{\text{wp}} = N_p M L T, \quad (\text{C.7})$$

where $M L T$ is the mean length of one turn. Based on (C.6) and (C.7), the rms value of the resonant current is

$$I_{\text{r}_\text{rms}} = \sqrt{\frac{P_{\text{cu}_p} A_{\text{wp}}}{\rho_w N_p M L T}}. \quad (\text{C.8})$$

Combing (C.1) and (C.8), yields

$$\frac{1}{2} L_m I_{\text{r}_\text{rms}}^2 = \frac{1}{2} \frac{\mu_0 \mu_{\text{eff}} N_p P_{\text{cu}_p} A_c A_{\text{wp}}}{\rho_w l_c M L T}. \quad (\text{C.9})$$

Based on (C.5) and (C.9), the ratio of I_{r_rms} to I_{Lm_pk} is

$$\frac{I_{\text{r}_\text{rms}}}{I_{Lm_pk}} = \frac{\mu_0 \mu_{\text{eff}}}{B_{\text{max}} l_c} \sqrt{\frac{N_p P_{\text{cu}_p} A_{\text{wp}}}{\rho_w M L T}}. \quad (\text{C.10})$$

Thus, the relative permeability is

$$\mu_{\text{opt}} = \frac{B_{\text{max}} l_c}{\mu_0 \sqrt{\frac{N_p P_{\text{cu}_p} A_{\text{wp}}}{\rho_w M L T}}} \frac{I_{\text{r}_\text{rms}}}{I_{Lm_pk}}. \quad (\text{C.11})$$

Invoking the definitions of the window utilization factor,

$$N_p A_{\text{wp}} = k_{\text{up}} W_a. \quad (\text{C.12})$$

Thus,

$$\mu_{\text{opt}} = \frac{B_{\text{max}} l_c}{\mu_0 \sqrt{\frac{P_{\text{cu}_p} k_{\text{up}} W_a}{\rho_w M L T}}} \frac{I_{\text{r}_\text{rms}}}{I_{Lm_pk}}. \quad (\text{C.13})$$

The maximum dissipation of the transformer, P_D , is related to the temperature rise and the thermal resistance as given by

$$\Delta T = R_{\theta} P_D. \quad (C.14)$$

The thermal resistance of the magnetic core will be obtained by the data curves supplied by the manufacturer or the empirical data. The approximate calculation method for the thermal resistance of the core with the volume V_c is given by

$$R_{\theta} = \frac{0.06}{\sqrt{V_c}}. \quad (C.15)$$

The total power loss will be dissipated through the surface of the transformer. Based on Newton's equation of convection, we have

$$P_D = h_c A_t \Delta T, \quad (C.16)$$

where h_c is the coefficient of heat transfer and A_t is the surface area of the core. The typical value of h_c without the air force cooling condition is around 10 W/m²°C.

For the current density in the windings, the expression is given by

$$J_0 = \frac{I_{r_rms}}{A_{wp}}. \quad (C.17)$$

Thus, the dc copper loss of the primary winding is

$$\begin{aligned} P_{cu_p} &= \rho_w \frac{l_{wp}}{A_{wp}} I_{r_rms}^2 = \rho_w \frac{N_p M L T (J_0 A_{wp})^2}{A_{wp}} \\ &= \rho_w M L T (N_p A_{wp}) J_0^2 = \rho_w M L T W_a k_{up} J_0^2 \\ &= \rho_w V_w k_{up} J_0^2, \end{aligned} \quad (C.18)$$

where V_w is the volume of the winding for the magnetic core.

Similarly, for each secondary winding, the dc winding loss is

$$\begin{aligned} P_{cu_s1} &= \rho_w \frac{l_{ws1}}{A_{ws1}} I_{s1_rms}^2 = \rho_w \frac{N_{s1} M L T (J_0 A_{ws1})^2}{A_{ws1}} \\ &= \rho_w M L T (N_{s1} A_{ws1}) J_0^2 = \rho_w M L T W_a k_{us1} J_0^2 \\ &= \rho_w V_w k_{us1} J_0^2. \end{aligned} \quad (C.19)$$

Thus, the total dc winding loss of the transformer is expressed by

$$P_{\text{cu_dc}} = P_{\text{cu_p}} + 2P_{\text{cu_s1}} = \rho_w V_w (k_{\text{up}} + 2k_{\text{us1}}) J_0^2 = \rho_w V_w k_u J_0^2. \quad (\text{C.20})$$

From (3.19)

$$P_{\text{trafo}} = (1 + \gamma) P_{\text{cu_dc}}, \quad (\text{C.21})$$

the following equation will be established combining (C.16), (C.20) and (C.21).

$$(1 + \gamma) \rho_w V_w k_u J_0^2 = h_c A_t \Delta T. \quad (\text{C.22})$$

Consequently, the current density is

$$J_0 = \sqrt{\frac{h_c A_t \Delta T}{(1 + \gamma) \rho_w k_u V_w}}. \quad (\text{C.23})$$

The physical quantities A_t and V_w in (C.23) may be related to the product of the core window area and the cross-sectional area, represented as A_p value of the core, and it follows the equations as

$$A_t = k_{\text{at}} A_p^{\frac{1}{2}}, \quad (\text{C.24})$$

$$V_w = k_{\text{vw}} A_p^{\frac{3}{4}}, \quad (\text{C.25})$$

where k_{at} and k_{vw} are the coefficients. Based on the data fit for several core types and sizes, the values of k_{at} and k_{vw} for typical wire wound cores are 40 and 10, respectively. The equations for the current density can be rewritten as

$$J_0 = K_t \sqrt{\frac{\Delta T}{k_u (1 + \gamma)}} \frac{1}{\sqrt[8]{A_p}}, \quad (\text{C.26})$$

with

$$K_t = \sqrt{\frac{h_c k_{\text{at}}}{\rho_w k_{\text{vw}}}}, \quad (\text{C.27})$$

and the typical value is $K_t = 48.2 \times 10^3$.

Combining (C.3) and (C.5), we have

$$L_m I_{\text{Lm_pk}}^2 = N_p A_c B_{\text{max}} I_{\text{Lm_pk}}, \quad (\text{C.28})$$

and

$$N_p I_{Lm_pk} = N_p I_{r_rms} \frac{I_{Lm_pk}}{I_{r_rms}} = N_p J_0 A_{wp} \frac{I_{Lm_pk}}{I_{r_rms}} = k_{up} W_a \frac{I_{Lm_pk}}{I_{r_rms}} J_0. \quad (C.29)$$

Thus taking the definition of $A_p = W_a A_c$,

$$L_m I_{Lm_pk}^2 = B_{max} k_{up} \frac{I_{Lm_pk}}{I_{r_rms}} J_0 A_p. \quad (C.30)$$

Combing (C.26) and (C.30), the A_p value of the magnetic core is

$$A_p = \left[\frac{\sqrt{k_u (1 + \gamma)} L_m I_{r_rms} I_{Lm_pk}}{B_{max} k_{up} K_t \sqrt{\Delta T}} \right]^{\frac{8}{7}}. \quad (C.31)$$

Appendix D

Planar Winding Loss of Circular Conductors

For the circular conductors applied in the planar transformer, the polar coordination system is introduced to calculate the high frequency winding loss. The cross section of circular conductor and boundary conditions of the n^{th} primary layer applied in the following calculations is illustrated in Fig. 5.7. For a segment of $dr \times t$ in the conductor, it is reasonable to assume that the current flowing in the segment has an inverse relationship with r and the current in the segment is calculated by

$$\int_0^t J(r, t) dz = \frac{I_p}{r \ln\left(\frac{R_o}{R_i}\right)}. \quad (\text{D.1})$$

For the planar circular winding, the width of the conductor is generally much bigger than the thickness and the H field would be approximately along the r axis. As the 1st layer of primary conductor is closed to the ideal magnetic core, the boundary condition of H field at the bottom of 1st layer is given by

$$H_r(r, z_{b1}) = 0. \quad (\text{D.2})$$

Invoking Amperes' law for the segment of $dr \times t$, we have

$$H_r(r, z_{t1}) \cdot dr = \int_r^{r+dr} \int_0^t J(r, z) dz dr. \quad (\text{D.3})$$

Thus, the boundary condition at the top of 1st layer is obtained by

$$H_r(r, z_{t1}) = \frac{I_p}{r \ln\left(\frac{R_o}{R_i}\right)}. \quad (\text{D.4})$$

As the magnetic and electric fields contains only r and θ components, respectively, the Maxwell's equations under polar coordinate system in phasor forms are expressed as

$$-\frac{dE_\theta(r, z)}{dz} = -j\omega\mu_0 H_r(r, z), \quad (\text{D.5})$$

$$\frac{dH_r(r, z)}{dz} = J_\theta(r, z) = \sigma E_\theta(r, z). \quad (\text{D.6})$$

The solution of the magnetic field intensity is given in [115] as

$$H_r(r, z) = A_1 e^{\lambda z} + A_2 e^{-\lambda z}, \quad (\text{D.7})$$

with

$$\lambda = \frac{1+j}{\delta_0}. \quad (\text{D.8})$$

The boundary conditions for the top and bottom sides are presented by

$$H_r(r, z_{tn}) = n H_r(r, z_{t1}) = n \frac{I_p}{r \ln\left(\frac{R_o}{R_i}\right)}, \quad (\text{D.9})$$

$$H_r(r, z_{bn}) = (n-1) H_r(r, z_{t1}) = (n-1) \frac{I_p}{r \ln\left(\frac{R_o}{R_i}\right)}. \quad (\text{D.10})$$

Consequently, the magnetic field intensity in the n^{th} primary layer is calculated by

$$H_r(r, z) = \frac{I_p}{r \ln\left(\frac{R_o}{R_i}\right)} \frac{n \sinh[\lambda(z - z_{bn})] + (n-1) \sinh[\lambda(z_{tn} - z)]}{\sinh(\lambda t)}. \quad (\text{D.11})$$

Substitution of (D.11) into (D.6) yields the electric field intensity in the n^{th} primary layer as

$$E_{\theta}(r, z) = \frac{I_p}{r \ln\left(\frac{R_o}{R_i}\right)} \frac{\lambda}{\sigma} \frac{n \cosh[\lambda(z - z_{bn})] - (n-1) \cosh[\lambda(z_{tn} - z)]}{\sinh(\lambda t)}. \quad (\text{D.12})$$

The AC current density in the n^{th} layer is given by

$$J_{\theta}(r, z) = \frac{\lambda I_p}{r \ln\left(\frac{R_o}{R_i}\right)} \frac{n \cosh[\lambda(z - z_{bn})] - (n-1) \cosh[\lambda(z_{tn} - z)]}{\sinh(\lambda t)}. \quad (\text{D.13})$$

Based on the Poynting vector theorem, the complex power of the n^{th} layer is

$$\begin{aligned} P_{Zn} &= \int_0^{2\pi} \int_{R_i}^{R_o} E_{\theta}(r, z_{tn}) H_r(r, z_{tn}) r dr d\theta - \int_0^{2\pi} \int_{R_i}^{R_o} E_{\theta}(r, z_{bn}) H_r(r, z_{bn}) r dr d\theta \\ &= \frac{2\pi I_p^2 \lambda}{\sigma \ln\left(\frac{R_o}{R_i}\right)} \left[2n(n-1) \tanh \frac{\lambda t}{2} + \coth(\lambda t) \right]. \end{aligned} \quad (\text{D.14})$$

Combing (D.8) and (D.14), the AC resistance of n^{th} layer can be obtained by

$$R_{acn} = \frac{2\pi \rho_w}{t \ln\left(\frac{R_o}{R_i}\right)} \cdot \Delta \left[\frac{\sinh(2\Delta) + \sin(2\Delta)}{\cosh(2\Delta) - \cos(2\Delta)} + 2n(n-1) \frac{\sinh(\Delta) - \sin(\Delta)}{\cosh(\Delta) + \cos(\Delta)} \right]. \quad (\text{D.15})$$

If the total number of layers in the primary winding is n_p , the total AC resistance of the primary winding is given by

$$R_{acp} = \frac{2\pi \rho_w n_p}{t \ln\left(\frac{R_o}{R_i}\right)} \cdot F_{R1} \quad (\text{D.16})$$

with

$$F_{R1} = \Delta \left[\frac{\sinh(2\Delta) + \sin(2\Delta)}{\cosh(2\Delta) - \cos(2\Delta)} + \frac{2(n_p^2 - 1)}{3} \frac{\sinh(\Delta) - \sin(\Delta)}{\cosh(\Delta) + \cos(\Delta)} \right], \quad (\text{D.17})$$

which is actually the increasing factor of AC resistance due to eddy current effect as the same result given by Dowell's equation shown in [84].

Appendix E

Publications

Journal Papers

[J.1] **J. Zhang**, Z. Ouyang, M. C. Duffy, M. A. E. Andersen and W. G. Hurley, “Leakage Inductance Calculation for Planar Transformers With a Magnetic Shunt,” *IEEE Trans. Ind. Appl.*, vol. 50, no. 6, pp. 4107-4112, Nov.-Dec. 2014.

Abstract: The magnetic shunt is generally inserted in a planar transformer to increase the leakage inductance which can be utilized as the series inductor in resonant circuits such as the LLC resonant converter. This paper presents a calculation methodology for the leakage inductance of the transformer with a magnetic shunt by means of the stored magnetic energy in the primary and secondary sides of the transformer using the magnetomotive force (MMF) variation method, as well as the stored energy in the shunt based on the reluctance model. The detailed calculation method is described. Both the FEA simulation and the experimental results have proven the validity of the proposed calculation method for leakage inductance.

[J.2] Z. Ouyang, **J. Zhang** and W. G. Hurley, “Calculation of Leakage Inductance for High Frequency Transformers,” *IEEE Trans. Power Electron.*, PP(99):1. (In press)

Abstract: Frequency dependent leakage inductance is often observed. High frequency eddy current effects cause a reduction in leakage inductance. The proximity effect between adjacent layers is responsible for the reduction of leakage inductance. This paper gives a detailed analysis of high frequency leakage inductance and

proposes an accurate prediction methodology. High frequency leakage inductances in several interleaved winding configurations are also discussed. Interleaved winding configurations actually give a smaller degree of reduction of leakage induction at high frequency. Finite Element Analysis (FEA) simulation and measurement validate the models.

[J.3] C. Feeney, **J. Zhang** and M. Duffy, “Ac Winding Loss of Phase-Shifted Coupled Windings”, *IEEE Trans. Power Electron.*, 2015. (In press)

Abstract: In circuits where there is an inherent phase shift angle between coupled winding currents such as in coupled inductors, it is important to accurately calculate the ac winding loss at the correct phase shift and frequency. Phase shift between winding currents can cause the ac winding loss to vary significantly due to changes in the magnetic field distribution. This paper presents an analysis of winding loss for the general case of coupled windings with arbitrary phase shifted currents and its effect in a number of practical devices. A detailed approach to analytically calculate ac winding loss in microfabricated coupled stripline inductors is presented along with a derivation of the resistance matrix for the device. The analysis and methodology is then validated using finite element analysis and experimental results.

[J.4] W. G. Hurley, M. C. Duffy, **J. Zhang**, I. Lope, B. Kunz and W. H. Wölfle, “A Unified Approach to the Calculation of Self and Mutual Inductance for Coaxial Coils in Air”, *IEEE Trans. Power Electron.*, 2015. (In press)

Abstract: This paper extends a previous formula for the mutual inductance between single turn coils to include all coils in air with rectangular cross-sections, without any restrictions on the dimensions (including overlapping coils). The formula is compared with a wide spectrum of examples from the literature and agreement is excellent in every case. Experimental results are presented to validate the formula for both solenoid and disk coils. The formula is relevant to coreless transformers, inductive coupling, wireless power transfer and leakage inductance in resonant converters.

Conference Papers

[C.1] **J. Zhang**, W. G. Hurley, W. H. Wolfle and M. C. Duffy, "Optimized design of LLC resonant converters incorporating planar magnetics," in *Proc. IEEE Appl. Power Electron. Conf. Expo. (APEC)*, 2013, pp. 1683-1688.

Abstract: The LLC resonant converter is widely applied as front-end dc-dc conversion for distributed power system and intermediate conversion for renewable energy power generation systems. A continuous miniaturization of LLC resonant converter incorporating planar magnetics is leading to higher performance, higher efficiency and decreasing costs. This paper outlines an improved design methodology for LLC resonant converters based on judicious choice of the circuit components including the resonant inductor, the transformer magnetizing inductor and the resonant capacitor as well as the dead time. Planar magnetics are playing a significant role in the low profile DC/DC converter applications. With the planar transformer employed, the parameters can be controlled precisely which is of great importance to the operating performance of the converter. Several structures of the planar transformer applied in LLC resonant converter are investigated. Finally, the comparison of the proposed structures basis on the ac resistance and the winding losses are presented

[C.2] **J. Zhang**, Z. Ouyang, M. C. Duffy, M. A. E. Andersen and W. G. Hurley, "Leakage inductance calculation for planar transformers with a magnetic shunt," in *Proc. IEEE Energy Convers. Congr. Expo. (ECCE)*, 2013, pp. 643-648.

Abstract: The magnetic shunt is generally inserted in a planar transformer to increase the leakage inductance which can be utilized as the series inductor in resonant circuits such as the LLC resonant converter. This paper presents a calculation methodology for the leakage inductance of the transformer with a magnetic shunt by means of the stored magnetic energy in the primary and secondary sides of the transformer using the magnetomotive force (MMF) variation method, as well as the stored energy in the shunt based on the reluctance model. The detailed calculation method is described. Both the FEA simulation and the experimental results have proven the validity of the proposed calculation method for leakage inductance.

[C.3] **J. Zhang**, W. G. Hurley and W. H. Wolfle, “Gapped transformer design methodology and implementation for LLC resonant converters,” in *Proc. IEEE Appl. Power Electron. Conf. Expo. (APEC)*, 2014, pp. 726-731.

Abstract: In the LLC resonant converter, the air gap is generally positioned in the core of the transformer for proper magnetizing inductance. Traditional transformer design methods assume infinite permeability of the core and no energy stored in the core. The improved design methodology for the gapped transformer is proposed with the optimum relative permeability and gap selection to meet the temperature rise and the magnetizing inductance requirements. The magnetizing current influences the magnetic flux in the core leading to the core saturation and core loss, while the resonant current contributes to the winding loss. The transformer design for a 200 W, 90 kHz LLC resonant converter is presented and experimental results validate the proposed methodology.

[C.4] **J. Zhang**, W. G. Hurley and W. H. Wolfle, “Design of the planar transformer in llc resonant converters for micro-grid applications,” in *Proc. IEEE Power Electron. Distributed Generation Systems (PEDG)*, 2014, pp. 1-7.

Abstract: LLC resonant converters may be applied as an intermediate converter in low power level micro-grid systems. The field of planar magnetics is continuously pushing its utilization in resonant converters as higher power densities and lower profiles are achieved. The design process for the planar transformer is significant due to the gap being placed on the magnetic core for the proper magnetizing inductance requirement. The optimum design methodology for the conventional transformer has been extended to the planar transformer. Design considerations and equations are presented. The planar transformer for a 240 W, 105 kHz LLC resonant converter was fabricated. The experiments were carried out and the results verify the design methodology and the implementation method.

[C.5] I. Lope, W. G. Hurley and **J. Zhang**, “Common-mode choke design considerations applied to domestic induction heating,” in *Proc. Int. Universities' Power Eng. Conf. (UPEC)*, 2013, pp. 1-5.

Abstract: In this work, a design calculation method for common-mode chokes (CMC) is presented. With this purpose, a similar method to the employed in a typical inductor design where the input current characteristics define both the maximum magnetic flux and the winding losses has been adapted. In order to get a suitable design that provides a CMC optimization, considerations with regard to both current components, the common-mode (CM) and the differential-mode (DM) current, have been taken into account. Therefore, the CM current contributes to the magnetic flux in the core, which is associated to the core saturation and core losses, whereas the DM current generates the copper losses. Finally, a CMC for domestic induction heating appliances is designed.

References

- [1] T. G. Wilson, "The evolution of power electronics," *IEEE Trans. Power Electron.*, vol. 15, no. 3, pp. 439-446, May 2000.
- [2] B. K. Bose, "The past, present, and future of power electronics," *IEEE Ind. Electron. Mag.*, vol. 3, no. 2, pp. 7-11, 14, Jun. 2009.
- [3] R. W. Erickson and D. Maksimovic, *Fundamentals of Power Electronics*, 2nd ed. Norwell, MA: Kluwer, 2001.
- [4] M. M. Jovanovic, "Technology drivers and trends in power suppliers for computer/telecom," in *Proc. IEEE Appl. Power Electron. Conf. Expo. (APEC)*, Plenary session presentation, 2006.
- [5] F. C. Lee, P. Barbosa, P. Xu, J. Zhang, B. Yang and F. Canales, "Topologies and design considerations for distributed power system applications," *Proceedings of the IEEE*, vol. 89, no. 6, pp. 939-950, Jun. 2001.
- [6] U. Badstübner, "Ultra-high performance telecom DC-DC converter," *PhD dissertation*, Swiss Federal Institute of Technology Zürich (ETH), Zürich, Switzerland, 2012.
- [7] D. Fu, "Topology investigation and system optimization of resonant converters," *PhD dissertation*, Virginia Polytechnic Institute and State University, Blacksburg, Virginia, 2010.
- [8] Z. Ouyang, "Advances in planar and integrated magnetics," *PhD dissertation*, Technical University of Denmark, Kgs. Lyngby, Denmark, 2011.
- [9] I. D. Jitaru, "High efficiency converter using current shaping and synchronous rectification," in *Proc. International Telecommun. Energy Conf. (INTELEC)*, 2002, pp. 48-54.
- [10] B. R. Lin, J. J. Chen, Y. E. Lee and H. K. Chiang, "Analysis and implementation of a bidirectional ZVS dc-dc converter with active clamp," in *Proc. IEEE Conf. Ind. Electron. Appl. (ICIEA)*, 2008, pp. 382-387.
- [11] M. Cacciato, A. Consoli, V. Crisafulli, G. Vitale and N. Abbate, "A new resonant active clamping technique for bi-directional converters in HEVs," in *Proc. IEEE Energy Convers. Congr. Expo. (ECCE)*, 2010, pp. 1436-1441.
- [12] S. Gui-Jia, F. Z. Peng and D. J. Adams, "Experimental evaluation of a soft-switching DC/DC converter for fuel cell vehicle applications," in *Proc. IEEE*

- Workshop Power Electron. Transp. (WPET)*, 2002, pp. 39-44.
- [13] F. Liu, Y. Chen, G. Hu and X. Ruan, "Modified three-phase three-level DC/DC converter with zero-voltage-switching characteristic-adopting asymmetrical duty cycle control," *IEEE Trans. Power Electron.*, vol. 29, no. 12, pp. 6307-6318, Dec. 2014.
- [14] B. Yang, F. C. Lee, A. J. Zhang and G. Huang, "LLC resonant converter for front end DC/DC conversion," in *Proc. IEEE Appl. Power Electron. Conf. Expo. (APEC)*, 2002, pp. 1108-1112.
- [15] R. Chen, J. T. Strydom and J. D. van Wyk, "Design of planar integrated passive module for zero-voltage-switched asymmetrical half-bridge PWM converter," *IEEE Trans. Ind. Appl.*, vol. 39, no. 6, pp. 1648-1655, Nov.-Dec. 2003.
- [16] L. Il-Oun and M. Gun-Woo, "A new asymmetrical half-bridge converter with zero DC-offset current in transformer," *IEEE Trans. Power Electron.*, vol. 28, no. 5, pp. 2297-2306, May 2013.
- [17] T. Kuo-Ching, C. Fenf-Jie, C. Jyun-Ze and K. Jia-Huei, "Study and implementation of asymmetrical half-bridge converter," in *Proc. IEEE International Symposium Next-Generation Electron. (ISNE)*, 2013, pp. 502-505.
- [18] L. Ching-Shan and C. Ming-Hung, "Asymmetrical half-bridge converter with input current ripple reduction," in *Proc. International Conf. Intelligent Green Building Smart Grid (IGBSG)*, 2014, pp. 1-5.
- [19] K. Jin-Tae and S. Li, "A hold-up time extending method for asymmetrical half-bridge converter," in *Proc. IEEE European Conf. Power Electron. Appl. (EPE)*, 2011, pp. 1-7.
- [20] F. Liu, Z. Wang, Y. Mao and X. Ruan, "Asymmetrical Half-Bridge Double-Input DC/DC Converters Adopting Pulsating Voltage Source Cells for Low Power Applications," *IEEE Trans. Power Electron.*, vol. 29, no. 9, pp. 4741-4751, Sept. 2014.
- [21] L. Bor-Ren and C. Chia-Hung, "Interleaved ZVS DC/DC converter with high input voltage," in *Proc. IEEE International Symposium Ind. Electron. (ISIE)*, 2012, pp. 360-365.
- [22] L. Bor-Ren and C. Chia-Hung, "Soft-switching converter with two series half-bridge legs to reduce voltage stress of active switches," *IEEE Trans. Ind. Electron.*, vol. 60, no. 6, pp. 2214-2224, Jun. 2013.
- [23] W. Li, Y. He, X. He, Y. Sun, F. Wang and L. Ma, "Series asymmetrical half-bridge converters with voltage autobalance for high input-voltage applications," *IEEE Trans. Power Electron.*, vol. 28, no. 8, pp. 3665-3674, Aug. 2013.
- [24] R. Sharma and H. Gao, "Low cost high efficiency DC-DC converter for fuel cell powered auxiliary power unit of a heavy vehicle," *IEEE Trans. Power Electron.*, vol. 21, no. 3, pp. 587-591, May 2006.
- [25] M. Nowak, J. Hildebrandt and P. Luniewski, "Converters with AC transformer intermediate link suitable as interfaces for supercapacitor energy storage," in *Proc. IEEE Power Electron. Specialists Conf. (PESC)*, 2004, pp. 4067-4073.

- [26] W. Chen, F. C. Lee, M. M. Jovanovic and J. A. Sabate, "A comparative study of a class of full bridge zero-voltage-switched PWM converters," in *Proc. IEEE Appl. Power Electron. Conf. Expo. (APEC)*, 1995, pp. 893-899.
- [27] Y. Zhong, "Dual-bridge DC/DC converter with wide-range ZVS and zero circulating current," in *Proc. IEEE Energy Convers. Congr. Expo. (ECCE)*, 2009, pp. 1353-1361.
- [28] C. Zhao, X. Wu, P. Meng and Z. Qian, "Optimum design consideration and implementation of a novel synchronous rectified soft-switched phase-shift full-bridge converter for low-output-voltage high-output-current applications," *IEEE Trans. Power Electron.*, vol. 24, no. 2, pp. 388-397, Feb. 2009.
- [29] Z. Guo, D. Sha, X. Liao and J. Luo, "Input-series-output-parallel phase-shift full-bridge derived DC-DC converters with auxiliary LC Networks to achieve wide zero-voltage switching range," *IEEE Trans. Power Electron.*, vol. 29, no. 10, pp. 5081-5086, Oct. 2014.
- [30] D. Sha, K. Deng and X. Liao, "Duty cycle exchanging control for input-series-output-series connected two PS-FB DC-DC converters," *IEEE Trans. Power Electron.*, vol. 27, no. 3, pp. 1490-1501, Mar. 2012.
- [31] W. Li, Q. Jiang, Y. Mei, C. Li, Y. Deng and X. He, "Modular multilevel DC/DC converters with phase-shift control scheme for high-voltage DC-based systems," *IEEE Trans. Power Electron.*, vol. 30, no. 1, pp. 99-107, Jan. 2015.
- [32] Z. Zhang, Z. Ouyang, O. C. Thomsen and M. A. E. Andersen, "Analysis and Design of a Bidirectional Isolated DC-DC Converter for Fuel Cells and Supercapacitors Hybrid System," *IEEE Trans. Power Electron.*, vol. 27, no. 2, pp. 848-859, Feb. 2012.
- [33] A. Rodriguez, A. Vazquez, D. G. Lamar, M. M. Hernando and J. Sebastian, "Different purpose design strategies and techniques to improve the performance of a dual active bridge with phase-shift control," *IEEE Trans. Power Electron.*, vol. 30, no. 2, pp. 790-804, Feb. 2015.
- [34] S. W. Anderson, R. W. Erickson and R. A. Martin, "An improved automotive power distribution system using nonlinear resonant switch converters," *IEEE Trans. Power Electron.*, vol. 6, no. 1, pp. 48-54, Jan. 1991.
- [35] G. Hua, F. C. Lee and M. M. Jovanovic, "An improved full-bridge zero-voltage-switched PWM converter using a saturable inductor," *IEEE Trans. Power Electron.*, vol. 8, no. 4, pp. 530-534, Oct. 1993.
- [36] C. Bo-Yuan and L. Yen-Shin, "Switching control technique of phase-shift-controlled full-bridge converter to improve efficiency under light-load and standby conditions without additional auxiliary components," *IEEE Trans. Power Electron.*, vol. 25, no. 4, pp. 1001-1012, Apr. 2010.
- [37] C. Je-Hyung, P. Ki-Bum, P. Jin-Sik, M. Gun-Woo and Y. Myung-Joong, "Design of a digital offset compensator eliminating transformer magnetizing current offset of a phase-shift full-bridge converter," *IEEE Trans. Power Electron.*, vol. 27, no. 1, pp. 331-341, Jan. 2012.
- [38] K. Jong-Woo, K. Duk-You, K. Chong-Eun and M. Gun-Woo, "A simple

- switching control technique for improving light load efficiency in a phase-shifted full-bridge converter with a server power system,” *IEEE Trans. Power Electron.*, vol. 29, no. 4, pp. 1562-1566, Apr. 2014.
- [39] K. Duk-You, K. Chong-Eun and M. Gun-Woo, “Variable delay time method in the phase-shifted full-bridge converter for reduced power consumption under light load conditions,” *IEEE Trans. Power Electron.*, vol. 28, no. 11, pp. 5120-5127, Nov. 2013.
- [40] L. Yen-Shin, S. Zih-Jie and C. Wen-Shyue, “New hybrid control technique to improve light load efficiency while meeting the hold-up time requirement for two-stage server power,” *IEEE Trans. Power Electron.*, vol. 29, no. 9, pp. 4763-4775, Sep. 2014.
- [41] K. Young-Do, C. Kyu-Min, K. Duk-You and M. Gun-Woo, “Wide-range ZVS phase-shift full-bridge converter with reduced conduction loss caused by circulating current,” *IEEE Trans. Power Electron.*, vol. 28, no. 7, pp. 3308-3316, Jul. 2013.
- [42] Z. Chen, S. Liu and L. Shi, “A soft switching full bridge converter with reduced parasitic oscillation in a wide load range,” *IEEE Trans. Power Electron.*, vol. 29, no. 2, pp. 801-811, Feb. 2014.
- [43] R. L. Steigerwald, “A comparison of half-bridge resonant converter topologies,” *IEEE Trans. Power Electron.*, vol. 3, no. 2, pp. 174-182, Apr. 1988.
- [44] J. P. Vandelac and P. D. Ziogas, “A DC to DC PWM series resonant converter operated at resonant frequency,” *IEEE Trans. Ind. Electron.*, vol. 35, no. 3, pp. 451-460, Aug. 1988.
- [45] D. James, “A constant power rectifier for telecommunications using a novel variable turns ratio transformer,” in *Proc. International Telecommun. Energy Conf. (INTELEC)*, 1997, pp. 251-256.
- [46] L. Bor-Ren and C. Po-Jen, “New ZVS DC-DC converter with series-connected transformers to balance the output currents,” *IEEE Trans. Power Electron.*, vol. 29, no. 1, pp. 246-255, Jan. 2014.
- [47] H. B. Kotte, R. Ambatipudi and K. Bertilsson, “High-speed (MHz) series resonant converter (SRC) using multilayered coreless printed circuit board (PCB) step-down power transformer,” *IEEE Trans. Power Electron.*, vol. 28, no. 3, pp. 1253-1264, Mar. 2013.
- [48] M. M. Swamy and A. K. S. Bhat, “A comparison of parallel resonant converters operating in lagging power factor mode,” *IEEE Trans. Power Electron.*, vol. 9, no. 2, pp. 181-195, Mar. 1994.
- [49] R. Petkov, D. Chapman and D. James, “A comparative study of two DC/DC converter topologies for telecommunications,” in *Proc. International Telecommun. Energy Conf. (INTELEC)*, 1996, pp. 279-288.
- [50] H. Sheng, W. Shen, H. Wang, D. Fu, Y. Pei, X. Yang, F. Wang, D. Boroyevich, F. C. Lee and C. W. Tipton, “Design and implementation of a high power density three-level parallel resonant converter for capacitor charging pulsed-power supply,” *IEEE Trans. Plasma Sci.*, vol. 39, no. 4, pp. 1131-1140, Apr.

- 2011.
- [51] H. Sheng, F. Wang and C. W. Tipton, "A fault detection and protection scheme for three-level DC-DC converters based on monitoring flying capacitor voltage," *IEEE Trans. Power Electron.*, vol. 27, no. 2, pp. 685-697, Feb. 2012.
 - [52] A. K. S. Bhat, "A 48 V output DC-to-DC resonant converter suitable for telecommunication applications," in *Proc. International Telecommun. Energy Conf. (INTELEC)*, 1989, pp. 20-24.
 - [53] G. A. Ward and A. J. Forsyth, "Topology selection and design trade-offs for multi-kW telecoms DC power supplies," in *Proc. International Conf. Power Electron. Machines Drives*, 2002, pp. 439-444.
 - [54] M. S. Agamy and P. K. Jain, "A three-level resonant single-stage power factor correction converter: analysis, design, and implementation," *IEEE Trans. Ind. Electron.*, vol. 56, no. 6, pp. 2095-2107, Jun. 2009.
 - [55] R. L. Steigerwald, R. W. De Doncker and M. H. Kheraluwala, "A comparison of high-power DC-DC soft-switched converter topologies," *IEEE Trans. Ind. Appl.*, vol. 32, no. 5, pp. 1139-1145, Sep. 1996.
 - [56] A. Suk-Ho, R. Hong-Je, G. Ji-Woong and J. Sung-Roc, "Low-ripple and high-precision high-voltage DC power supply for pulsed power applications," *IEEE Trans. Plasma Sci.*, vol. 42, no. 10, pp. 3023-3033, Oct. 2014.
 - [57] R. Yang, H. Ding, Y. Xu, L. Yao and Y. Xiang, "An analytical steady-state model of LCC type series-parallel resonant converter with capacitive output filter," *IEEE Trans. Power Electron.*, vol. 29, no. 1, pp. 328-338, Jan. 2014.
 - [58] Q. Yang, B. Lu, B. Yang, D. Fu, F. C. Lee, F. Canales, R. Gean and W. C. Tipton, "A high-frequency high-efficiency three-level LCC converter for high-voltage charging applications," in *Proc. IEEE Power Electron. Specialists Conf. (PESC)*, 2004, pp. 4100-4106.
 - [59] D. Fu, F. C. Lee, Q. Yang and F. Wang, "A novel high-power-density three-level LCC resonant converter with constant-power-factor-control for charging applications," *IEEE Trans. Power Electron.*, vol. 23, no. 5, pp. 2411-2420, Sep. 2008.
 - [60] A. K. S. Bhat, "Analysis and design of LCL-type series resonant converter," in *Proc. International Telecommun. Energy Conf. (INTELEC)*, 1990, pp. 172-178.
 - [61] B. Yang, R. Chen and F. C. Lee, "Integrated magnetic for LLC resonant converter," in *Proc. IEEE Appl. Power Electron. Conf. Expo. (APEC)*, 2002, pp. 346-351.
 - [62] B. Wang, X. Xin, S. Wu, H. Wu and J. Ying, "Analysis and implementation of LLC burst mode for light load efficiency improvement," in *Proc. IEEE Appl. Power Electron. Conf. Expo. (APEC)*, 2009, pp. 58-64.
 - [63] H. de Groot, E. Janssen, R. Pagano and K. Schetters, "Design of a 1-MHz LLC resonant converter based on a DSP-driven SOI half-bridge power MOS module," *IEEE Trans. Power Electron.*, vol. 22, no. 6, pp. 2307-2320, Nov. 2007.
 - [64] R. Yu, G. K. Y. Ho, B. M. H. Pong, B. W. K. Ling and J. Lam, "Computer-aided

- design and optimization of high-efficiency LLC series resonant converter,” *IEEE Trans. Power Electron.*, vol. 27, no. 7, pp. 3243-3256, Jul. 2012.
- [65] W. Feng, F. C. Lee, P. Mattavelli and D. Huang, “A universal adaptive driving scheme for synchronous rectification in LLC resonant converters,” *IEEE Trans. Power Electron.*, vol. 27, no. 8, pp. 3775-3781, Aug. 2012.
- [66] W. Feng, P. Mattavelli and F. C. Lee, “Pulsewidth locked loop (PWLL) for automatic resonant frequency tracking in LLC DC-DC transformer (LLC-DCX),” *IEEE Trans. Power Electron.*, vol. 28, no. 4, pp. 1862-1869, Apr. 2013.
- [67] I. Demirel and B. Erkmén, “A very low-profile dual output LLC resonant converter for LCD/LED TV applications,” *IEEE Trans. Power Electron.*, vol. 29, no. 7, pp. 3514-3524, Jul. 2014.
- [68] W. Feng, F. C. Lee and P. Mattavelli, “Optimal trajectory control of burst mode for LLC resonant converter,” *IEEE Trans. Power Electron.*, vol. 28, no. 1, pp. 457-466, Jan. 2013.
- [69] D. Fu, S. Wang, P. Kong, F. C. Lee and D. Huang, “Novel techniques to suppress the common-mode EMI noise caused by transformer parasitic capacitances in DC-DC converters,” *IEEE Trans. Ind. Electron.*, vol. 60, no. 11, pp. 4968-4977, Nov. 2013.
- [70] D. Wang and Y. Liu, “A zero-crossing noise filter for driving synchronous rectifiers of LLC resonant converter,” *IEEE Trans. Power Electron.*, vol. 29, no. 4, pp. 1953-1965, Apr. 2014.
- [71] D. Huang, S. Ji and F. C. Lee, “LLC resonant converter with matrix transformer,” *IEEE Trans. Power Electron.*, vol. 29, no. 8, pp. 4339-4347, Aug. 2014.
- [72] W. Feng and F. C. Lee, “Optimal trajectory control of LLC resonant converters for soft start-up,” *IEEE Trans. Power Electron.*, vol. 29, no. 3, pp. 1461-1468, Mar. 2014.
- [73] F. Musavi, M. Craciun, D. S. Gautam and W. Eberle, “Control strategies for wide output voltage range LLC resonant DC-DC converters in battery chargers,” *IEEE Trans. Veh. Technol.*, vol. 63, no. 3, pp. 1117-1125, Mar. 2014.
- [74] Z. Hu, Y. Liu and P. C. Sen, “Bang-bang charge control for LLC resonant converters,” *IEEE Trans. Power Electron.*, vol. 30, no. 2, pp. 1093-1108, Feb. 2015.
- [75] D. Fu, Y. Liu, F. C. Lee and M. Xu, “A novel driving scheme for synchronous rectifiers in LLC resonant converters,” *IEEE Trans. Power Electron.*, vol. 24, no. 5, pp. 1321-1329, May 2009.
- [76] R. Beiranvand, B. Rashidian, M. R. Zolghadri and S. M. H. Alavi, “A design procedure for optimizing the LLC resonant converter as a wide output range voltage source,” *IEEE Trans. Power Electron.*, vol. 27, no. 8, pp. 3749-3763, Aug. 2012.
- [77] F. Musavi, M. Craciun, D. S. Gautam, W. Eberle and W. G. Dunford, “An LLC resonant DC-DC converter for wide output voltage range battery charging applications,” *IEEE Trans. Power Electron.*, vol. 28, no. 12, pp. 5437-5445,

- Dec. 2013.
- [78] G. Yang, P. Dubus and D. Sadarnac, "Double-phase high-efficiency, wide load range high-voltage/low-voltage LLC DC/DC converter for electric/hybrid vehicles," *IEEE Trans. Power Electron.*, vol. 30, no. 4, pp. 1876-1886, Apr. 2015.
- [79] L. Il-Oun, C. Shin-Young and M. Gun-Woo, "Three-level resonant converter with double LLC resonant tanks for high-input-voltage applications," *IEEE Trans. Ind. Electron.*, vol. 59, no. 9, pp. 3450-3463, Sep. 2012.
- [80] L. Il-Oun and M. Gun-Woo, "Analysis and design of a three-level LLC series resonant converter for high- and wide-input-voltage applications," *IEEE Trans. Power Electron.*, vol. 27, no. 6, pp. 2966-2979, Jun. 2012.
- [81] W. T. Chi, M. P. Foster, D. A. Stone and D. T. Gladwin, "Analysis and design of LLC resonant converters with capacitor-diode clamp current limiting," *IEEE Trans. Power Electron.*, vol. 30, no. 3, pp. 1345-1355, Mar. 2015.
- [82] T. Jiang, J. Zhang, X. Wu, K. Sheng and Y. Wang, "A bidirectional LLC resonant converter with automatic forward and backward mode transition," *IEEE Trans. Power Electron.*, vol. 30, no. 2, pp. 757-770, Feb. 2015.
- [83] Z. Hu, Y. Qiu, L. Wang and Y. Liu, "An interleaved LLC resonant converter operating at constant switching frequency," *IEEE Trans. Power Electron.*, vol. 29, no. 6, pp. 2931-2943, Jun. 2014.
- [84] W. G. Hurley and W. H. Wölfle, *Transformers and Inductors for Power Electronics: Theory, Design and Applications*, Chichester: Wiley, 2013.
- [85] A. M. Urling, V. A. Niemela, G. R. Skutt and T. G. Wilson, "Characterizing high-frequency effects in transformer windings-a guide to several significant articles," in *Proc. IEEE Appl. Power Electron. Conf. Expo. (APEC)*, 1989, pp. 373-385.
- [86] P. L. Dowell, "Effects of eddy currents in transformer windings," *Proc. Institution Electr. Engineers*, vol. 113, no. 8, pp. 1387-1394, Aug. 1966.
- [87] M. P. Perry, "Multiple layer series connected winding design for minimum losses," *IEEE Trans. Power Apparatus and Systems*, vol. PAS-98, no. 1, pp. 116-123, Jan. 1979.
- [88] P. S. Venkatraman, "Winding eddy current losses in switch mode power transformers due to rectangular wave current," in *Proc. Powercon II*, 1984, pp. 1-11.
- [89] B. Carsten, "High frequency conductor losses in switchmode magnetics," in *Proc. HPFC*, 1986, pp. 155-176.
- [90] J. P. Vandelac and P. D. Ziogas, "A novel approach for minimizing high-frequency transformer copper losses," *IEEE Trans. Power Electron.*, vol. 3, no. 3, pp. 266-277, Jul. 1988.
- [91] W. G. Hurley, E. Gath and J. G. Breslin, "Optimizing the AC resistance of multilayer transformer windings with arbitrary current waveforms," *IEEE Trans. Power Electron.*, vol. 15, no. 2, pp. 369-376, Mar. 2000.

- [92] R. L. Stoll. *The Analysis of Eddy Currents*. Clarendon: Press. Oxford, 1974.
- [93] J. A. Ferreira, "Improved analytical modeling of conductive losses in magnetic components," *IEEE Trans. Power Electron.*, vol. 9, no. 1, pp. 127-131, Jan. 1994.
- [94] M. Bartoli, N. Noferi, A. Reatti and M. K. Kazimierczuk, "Modeling litz-wire winding losses in high-frequency power inductors," in *Proc. IEEE Power Electron. Specialists Conf. (PESC)*, 1996, pp. 1690-1696.
- [95] J. A. Ferreira. *Electromagnetic Modelling of Power Electronic Converters*. Dordrecht, Netherlands: Kluwer Academic Publishers, 1989.
- [96] N. Xi and C. R. Sullivan, "Simplified high-accuracy calculation of eddy-current loss in round-wire windings," in *Proc. IEEE Power Electron. Specialists Conf. (PESC)*, 2004, pp. 873-879.
- [97] F. Robert, P. Mathys and J. P. Schauwers, "A closed-form formula for 2D ohmic losses calculation in SMPS transformer foils," in *Proc. IEEE Appl. Power Electron. Conf. Expo. (APEC)*, 1999, pp. 199-205.
- [98] M. Vitelli, "Numerical evaluation of 2-D proximity effect conductor losses," *IEEE Trans. Power Del.*, vol. 19, no. 3, pp. 1291-1298, Jul. 2004.
- [99] F. Robert, P. Mathys, B. Velaerts and J. P. Schauwers, "Two-dimensional analysis of the edge effect field and losses in high-frequency transformer foils," *IEEE Trans. Magn.*, vol. 41, no. 8, pp. 2377-2383, Aug. 2005.
- [100] D. R. Zimmanck and C. R. Sullivan, "Efficient calculation of winding-loss resistance matrices for magnetic components," in *Proc. IEEE Control and Modeling Power Electron. (COMPEL)*, 2010, pp. 1-5.
- [101] C. R. Sullivan, "Computationally efficient winding loss calculation with multiple windings, arbitrary waveforms, and two-dimensional or three-dimensional field geometry," *IEEE Trans. Power Electron.*, vol. 16, no. 1, pp. 142-150, Jan. 2001.
- [102] O. Moreau, L. Popiel and J. L. Pages, "Proximity losses computation with a 2D complex permeability modelling," *IEEE Trans. Magn.*, vol. 34, no. 5, pp. 3616-3619, Sep. 1998.
- [103] A. T. Phung, G. Meunier, O. Chadebec, X. Margueron and J. P. Keradec, "High-frequency proximity losses determination for rectangular cross-section conductors," *IEEE Trans. Magn.*, vol. 43, no. 4, pp. 1213-1216, Apr. 2007.
- [104] N. Xi and C. R. Sullivan, "A two-dimensional equivalent complex permeability model for round-wire windings," in *Proc. IEEE Power Electron. Specialists Conf. (PESC)*, 2005, pp. 613-618.
- [105] N. Xi and C. R. Sullivan, "An equivalent complex permeability model for litz-wire windings," *IEEE Trans. Ind. Appl.*, vol. 45, no. 2, pp. 854-860, Mar. 2009.
- [106] C. R. Sullivan, "Optimal choice for number of strands in a litz-wire transformer winding," *IEEE Trans. Power Electron.*, vol. 14, no. 2, pp. 283-291, Mar. 1999.
- [107] C. R. Sullivan and R. Y. Zhang, "Simplified design method for litz wire," in *Proc. IEEE Appl. Power Electron. Conf. Expo. (APEC)*, 2014, pp. 2667-2674.

- [108] R. Y. Zhang, J. K. White, J. G. Kassakian and C. R. Sullivan, "Realistic litz wire characterization using fast numerical simulations," in *Proc. IEEE Appl. Power Electron. Conf. Expo. (APEC)*, 2014, pp. 738-745.
- [109] A. M. Lockie, "Transformers with interleaved windings," *IEEE Trans. Power Apparatus and Systems*, vol. 83, no. 9, pp. 914-918, Sep. 1964.
- [110] R. van Nuys, "Interleaved high-voltage transformer windings," *IEEE Trans. Power Apparatus and Systems*, vol. PAS-97, no. 5, pp. 1946-1954, Sep. 1978.
- [111] L. Satish and A. Jain, "Structure of transfer function of transformers with special reference to interleaved windings," *IEEE Trans. Power Del.*, vol. 17, no. 3, pp. 754-760, Jul. 2002.
- [112] M. Pavlovsky, S. W. H. de Haan and J. A. Ferreira, "Partial interleaving: a method to reduce high frequency losses and to tune the leakage inductance in high current, high frequency transformer foil windings," in *Proc. IEEE Power Electron. Specialists Conf. (PESC)*, 2005, pp. 1540-1547.
- [113] J. Mühlethaler, "Modeling and multi-objective optimization of inductive power components," *PhD dissertation*, Swiss Federal Institute of Technology Zürich (ETH), Zürich, Switzerland, 2012.
- [114] A. Balakrishnan, W. T. Joines and T. G. Wilson, "Air-gap reluctance and inductance calculations for magnetic circuits using a Schwarz-Christoffel transformation," *IEEE Trans. Power Electron.*, vol. 12, no. 4, pp. 654-663, Jul. 1997.
- [115] M. K. Kazimierczuk. *High-Frequency Magnetic Components (Second Edition)*. Chichester: Wiley, 2014.
- [116] N. Mohan, T. M. Undeland and W. P. Robbins. *Power Electronics - Converters, Applications and Design*. Chichester: Wiley, 2003.
- [117] A. Van den Bossche and V. C. Valchev. *Inductors and Transformers for Power Electronics*. Boca Raton: Taylor & Francis, 2005.
- [118] P. Wallmeier, "Improved analytical modeling of conductive losses in gapped high-frequency inductors," *IEEE Trans. Ind. Appl.*, vol. 37, no. 4, pp. 1045-1054, Jul. 2001.
- [119] C. J. Carpenter, "The application of the method of images to machine end-winding fields," *Proc. IEE - Part A: Power Engineering*, vol. 107, no. 35, pp. 487-500, Oct. 1960.
- [120] W. Chen, X. Huang and J. Zheng, "Improved winding loss theoretical calculation of magnetic component with air-gap," in *Proc. IEEE Power Electron. Motion Control Conf. (IPEMC)*, 2012, pp. 471-475.
- [121] W. A. Roshen, "Winding loss from an air-gap," in *Proc. IEEE Power Electron. Specialists Conf. (PESC)*, 2004, pp. 1724-1730.
- [122] W. A. Roshen, "Fringing field formulas and winding loss due to an air gap," *IEEE Trans. Magn.*, vol. 43, no. 8, pp. 3387-3394, Aug. 2007.
- [123] W. A. Roshen, "High-frequency fringing fields loss in thick rectangular and round wire windings," *IEEE Trans. Magn.*, vol. 44, no. 10, pp. 2396-2401, Oct.

- 2008.
- [124] A. Stadler, R. Huber, T. Stolzke and C. Gulden, "Analytical calculation of copper losses in litz-wire windings of gapped inductors," *IEEE Trans. Magn.*, vol. 50, no. 2, pp. 81-84, Feb. 2014.
- [125] L. Wei and R. A. Lukaszewski, "Analysis of strap losses for high power high frequency inductors," in *Proc. IEEE Industry Appl. Conf.*, 2007, pp. 1802-1809.
- [126] J. Hu and C. R. Sullivan, "AC resistance of planar power inductors and the quasidistributed gap technique," *IEEE Trans. Power Electron.*, vol. 16, no. 4, pp. 558-567, Jul. 2001.
- [127] M. Albach, "Two-dimensional calculation of winding losses in transformers," in *Proc. IEEE Power Electron. Specialists Conf. (PESC)*, 2000, pp. 1639-1644.
- [128] J. Hu and C. R. Sullivan, "Optimization of shapes for round-wire high-frequency gapped-inductor windings," in *Proc. IEEE Industry Appl. Conf.*, 1998, pp. 907-912.
- [129] J. D. Pollock and C. R. Sullivan, "Gapped-inductor foil windings with low AC and DC resistance," in *Proc. IEEE Industry Appl. Conf.*, 2004, pp. 557.
- [130] W. Lundquist, V. Yang and C. Castro, "Low AC resistance foil cut inductor," in *Proc. IEEE Energy Convers. Congr. Expo. (ECCE)*, 2014, pp. 2182-2186.
- [131] K. D. Papastergiou and D. E. Macpherson, "Air-gap effects in inductive energy transfer," in *Proc. IEEE Power Electron. Specialists Conf. (PESC)*, 2008, pp. 4092-4097.
- [132] N. H. Kutkut and D. M. Divan, "Optimal air-gap design in high-frequency foil windings," *IEEE Trans. Power Electron.*, vol. 13, no. 5, pp. 942-949, Sep. 1998.
- [133] V. Leonavicius, M. Duffy, U. Boeke and S. C. O. Mathuna, "Comparison of realization techniques for PFC inductor operating in discontinuous conduction mode," *IEEE Trans. Power Electron.*, vol. 19, no. 2, pp. 531-541, Mar. 2004.
- [134] D. C. Jiles and J. B. Thoenke, "Theory of ferromagnetic hysteresis: determination of model parameters from experimental hysteresis loops," *IEEE Trans. Magn.*, vol. 25, no. 5, pp. 3928-3930, Sep. 1989.
- [135] D. C. Jiles, J. B. Thoenke and M. K. Devine, "Numerical determination of hysteresis parameters for the modeling of magnetic properties using the theory of ferromagnetic hysteresis," *IEEE Trans. Magn.*, vol. 28, no. 1, pp. 27-35, Jan. 1992.
- [136] A. Rezaei-Zare, R. Iravani, M. Sanaye-Pasand, H. Mohseni and S. Farhangi, "An accurate hysteresis model for ferroresonance analysis of a transformer," *IEEE Trans. Power Del.*, vol. 23, no. 3, pp. 1448-1456, Jul. 2008.
- [137] W. A. Roshen, "A practical, accurate and very general core loss model for nonsinusoidal waveforms," *IEEE Trans. Power Electron.*, vol. 22, no. 1, pp. 30-40, Jan. 2007.
- [138] C. P. Steinmetz, "On the law of hysteresis," *Proc. IEEE*, vol. 72, no. 2, pp. 197-221, Feb. 1984.
- [139] I. Villar, U. Viscarret, I. Etxeberria-Otadui and A. Rufer, "Global loss

- evaluation methods for nonsinusoidally fed medium-frequency power transformers,” *IEEE Trans. Ind. Electron.*, vol. 56, no. 10, pp. 4132-4140, Oct. 2009.
- [140] J. Reinert, A. Brockmeyer and R. W. A. A. De Doncker, “Calculation of losses in ferro- and ferrimagnetic materials based on the modified Steinmetz equation,” *IEEE Trans. Ind. Appl.*, vol. 37, no. 4, pp. 1055-1061, Jul. 2001.
- [141] J. Li, T. Abdallah and C. R. Sullivan, “Improved calculation of core loss with nonsinusoidal waveforms,” in *Proc. IEEE Industry Appl. Conf.*, 2001, pp. 2203-2210.
- [142] K. Venkatachalam, C. R. Sullivan, T. Abdallah and H. Tacca, “Accurate prediction of ferrite core loss with nonsinusoidal waveforms using only Steinmetz parameters,” in *Proc. IEEE Workshop Computers Power Electron.*, 2002, pp. 36-41.
- [143] J. Muhlethaler, J. Biela, J. W. Kolar and A. Ecklebe, “Improved core-loss calculation for magnetic components employed in power electronic systems,” *IEEE Trans. Power Electron.*, vol. 27, no. 2, pp. 964-973, Feb. 2012.
- [144] A. Van den Bossche, V. C. Valchev and G. B. Georgiev, “Measurement and loss model of ferrites with non-sinusoidal waveforms,” in *Proc. IEEE Power Electron. Specialists Conf. (PESC)*, 2004, pp. 4814-4818.
- [145] D. Lin, P. Zhou, W. N. Fu, Z. Badics and Z. J. Cendes, “A dynamic core loss model for soft ferromagnetic and power ferrite materials in transient finite element analysis,” *IEEE Trans. Magn.*, vol. 40, no. 2, pp. 1318-1321, Mar. 2004.
- [146] W. Shen, F. Wang, D. Boroyevich and C. W. Tipton, “Loss characterization and calculation of nanocrystalline cores for high-frequency magnetics applications,” *IEEE Trans. Power Electron.*, vol. 23, no. 1, pp. 475-484, Jan. 2008.
- [147] Z. Ouyang, O. C. Thomsen and M. A. E. Andersen, “The analysis and comparison of leakage inductance in different winding arrangements for planar transformer,” in *Proc. International Conf. Power Electron. Drive Systems (PEDS)*, 2009, pp. 1143-1148.
- [148] W. Hurley and D. J. Wilcox, “Calculation of leakage inductance in transformer windings,” *IEEE Trans. Power Electron.*, vol. 9, no. 1, pp. 121-126, Jan. 1994.
- [149] J. Biela and J. W. Kolar, “Using transformer parasitics for resonant converters- A review of the calculation of the stray capacitance of transformers,” *IEEE Trans. Ind. Appl.*, vol. 44, no. 1, pp. 223-233, Jan. 2008.
- [150] A. Massarini and M. K. Kazimierczuk, “Self-capacitance of inductors,” *IEEE Trans. Power Electron.*, vol. 12, no. 4, pp. 671-676, Jul. 1997.
- [151] Y. L. Hai, J. G. Zhu and S. Y. R. Hui, “Experimental determination of stray capacitances in high frequency transformers,” *IEEE Trans. Power Electron.*, vol. 18, no. 5, pp. 1105-1112, Sep. 2003.
- [152] L. Dalessandro, F. Da Silveira Cavalcante and J. W. Kolar, “Self-capacitance of high-voltage transformers,” *IEEE Trans. Power Electron.*, vol. 22, no. 5, pp. 2081-2092, Sep. 2007.

- [153] Z. Ouyang, O. C. Thomsen and M. A. E. Andersen, "Optimal design and tradeoff analysis of planar transformer in high-power DC-DC converters," *IEEE Trans. Ind. Electron.*, vol. 59, no. 7, pp. 2800-2810, Jul. 2012.
- [154] N. Dai, A. W. Lofti, G. Skutt, W. Tabisz and F. C. Lee, "A comparative study of high-frequency, low-profile planar transformer technologies," in *Proc. IEEE Appl. Power Electron. Conf. Expo. (APEC)*, 1994, pp. 226-232.
- [155] K. D. T. Ngo, R. P. Alley and A. J. Yerman, "Fabrication method for a winding assembly with a large number of planar layers," *IEEE Trans. Power Electron.*, vol. 8, no. 1, pp. 55-61, Jan. 1993.
- [156] E. J. Meurer and S. W. H. de Haan, "On the common mode resonant frequency of transformers," in *Proc. European Conf. Power Electron. Appl. (EPE)*, 2007, pp. 1-6.
- [157] E. C. W. de Jong, E. C. W. de Jong, B. J. A. Ferreira and P. Bauer, "Toward the Next Level of PCB Usage in Power Electronic Converters," *IEEE Trans. Power Electron.*, vol. 23, no. 6, pp. 3151-3163, Nov. 2008.
- [158] C. K. Lee, Y. P. Su and S. Y. R. Hui, "Printed spiral winding inductor with wide frequency bandwidth," *IEEE Trans. Power Electron.*, vol. 26, no. 10, pp. 2936-2945, Oct. 2011.
- [159] D. Yao, C. G. Levey and C. R. Sullivan, "Microfabricated V-groove power inductors using multilayer Co-Zr-O thin films for very-high-frequency DC-DC converters," in *Proc. IEEE Energy Convers. Congr. Expo. (ECCE)*, 2011, pp. 1845-1852.
- [160] C. Quinn, K. Rinne, T. O'Donnell, M. Duffy and C. O. Mathuna, "A review of planar magnetic techniques and technologies," in *Proc. IEEE Appl. Power Electron. Conf. Expo. (APEC)*, 2001, pp. 1175-1183.
- [161] Z. Ouyang and M. A. E. Andersen, "Overview of planar magnetic technology-fundamental properties," *IEEE Trans. Power Electron.*, vol. 29, no. 9, pp. 4888-4900, Sep. 2014.
- [162] Ferroxcube, www.ferroxcube.com.
- [163] TDK EPCOS, www.epcos.com.
- [164] R. Prieto, O. Garcia, R. Asensi, J. A. Cobos and J. Uceda, "Optimizing the performance of planar transformers," in *Proc. IEEE Appl. Power Electron. Conf. Expo. (APEC)*, 1996, pp. 415-421.
- [165] S. Wang, M. A. de Rooij, W. G. Odendaal, J. D. van Wyk and D. Boroyevich, "Reduction of high-frequency conduction losses using a planar litz structure," *IEEE Trans. Power Electron.*, vol. 20, no. 2, pp. 261-267, Mar. 2005.
- [166] Z. Ouyang, O. C. Thomsen, M. A. E. Andersen, X. Bjo and T. Rklund, "Low profile, low cost, new geometry integrated inductors," in *Proc. IEEE Appl. Power Electron. Conf. Expo. (APEC)*, 2011, pp. 150-156.
- [167] W. G. Hurley and M. C. Duffy, "Calculation of self and mutual impedances in planar magnetic structures," *IEEE Trans. Magn.*, vol. 31, no. 4, pp. 2416-2422, Jul. 1995.

- [168] W. G. Hurley and M. C. Duffy, "Calculation of self- and mutual impedances in planar sandwich inductors," *IEEE Trans. Magn.*, vol. 33, no. 3, pp. 2282-2290, May 1997.
- [169] W. G. Hurley, M. C. Duffy, S. O'Reilly and S. C. O'Mathuna, "Impedance formulas for planar magnetic structures with spiral windings," *IEEE Trans. Ind. Electron.*, vol. 46, no. 2, pp. 271-278, Apr. 1999.
- [170] S. R. Cove, M. Ordonez, F. Luchino and J. E. Quaioco, "Applying response surface methodology to small planar transformer winding design," *IEEE Trans. Ind. Electron.*, vol. 60, no. 2, pp. 483-493, Feb. 2013.
- [171] D. V. Harburg, J. Qiu and C. R. Sullivan, "An improved AC loss model for the optimization of planar-coil inductors," in *Proc. IEEE Control and Modeling Power Electron. (COMPEL)*, 2012, pp. 1-7.
- [172] I. Lope, C. Carretero, J. Acero, R. Alonso and J. M. Burdio, "AC power losses model for planar windings with rectangular cross-sectional conductors," *IEEE Trans. Power Electron.*, vol. 29, no. 1, pp. 23-28, Jan. 2014.
- [173] M. Chen, M. Araghchini, K. K. Afridi, J. H. Lang, C. R. Sullivan and D. J. Perreault, "A systematic approach to modeling impedances and current distribution in planar magnetics," in *Proc. IEEE Control and Modeling Power Electron. (COMPEL)*, 2014, pp. 1-17.
- [174] W. Chen, Y. Yan, Y. Hu and Q. Lu, "Model and design of PCB parallel winding for planar transformer," *IEEE Trans. Magn.*, vol. 39, no. 5, pp. 3202-3204, Sep. 2003.
- [175] X. Margueron, A. Besri, Y. Lembeye and J. P. Keradec, "Current sharing between parallel turns of a planar transformer: prediction and improvement using a circuit simulation software," *IEEE Trans. Ind. Appl.*, vol. 46, no. 3, pp. 1064-1071, May 2010.
- [176] R. Prieto, R. Asensi and J. A. Cobos, "Selection of the appropriate winding setup in planar inductors with parallel windings," in *Proc. IEEE Energy Convers. Congr. Expo. (ECCE)*, 2010, pp. 4599-4604.
- [177] N. H. Kutkut, "A simple technique to evaluate winding losses including two-dimensional edge effects," *IEEE Trans. Power Electron.*, vol. 13, no. 5, pp. 950-958, Sep. 1998.
- [178] N. Wang, T. O'Donnell and C. O'Mathuna, "An improved calculation of copper losses in integrated power inductors on silicon," *IEEE Trans. Power Electron.*, vol. 28, no. 8, pp. 3641-3647, Aug. 2013.
- [179] G. S. Dimitrakakis and E. C. Tatakis, "High-frequency copper losses in magnetic components with layered windings," *IEEE Trans. Magn.*, vol. 45, no. 8, pp. 3187-3199, Aug. 2009.
- [180] B. W. Carsten, "The low leakage inductance of planar transformers; fact or myth?" in *Proc. IEEE Appl. Power Electron. Conf. Expo. (APEC)*, 2001, pp. 1184-1188.
- [181] I. W. Hofsjager, J. A. Ferreira and J. Daan Van Wyk, "Design and analysis of planar integrated L-C-T components for converters," *IEEE Trans. Power*

- Electron.*, vol. 15, no. 6, pp. 1221-1227, Nov. 2000.
- [182] M. Meinhardt, M. Duffy, T. O'Donnell, S. O'Reilly, J. Flannery and C. O Mathuna, "New method for integration of resonant inductor and transformer-design, realisation, measurements," in *Proc. IEEE Appl. Power Electron. Conf. Expo. (APEC)*, 1999, pp. 1168-1174.
- [183] J. T. Strydom and J. D. van Wyk, "Electromagnetic modeling for design and loss estimation of resonant integrated spiral planar power passives (ISP³)," *IEEE Trans. Power Electron.*, vol. 19, no. 3, pp. 603-617, May 2004.
- [184] W. Liu, J. D. van Wyk and B. Lu, "In-circuit loss measurement of a high-frequency integrated power electronics module," *IEEE Instrum. Meas. Mag.*, vol. 57, no. 7, pp. 1394-1402, Jul. 2008.
- [185] S. R. Cove, M. Ordonez, F. Luchino and J. E. Quaicoe, "Integrated magnetic design of small planar transformers for LLC resonant converters," in *Proc. IEEE Energy Convers. Congr. Expo. (ECCE)*, 2011, pp. 1839-1844.
- [186] K. Duk-You, K. Chong-Eun and M. Gun-Woo, "High-efficiency slim adapter with low-profile transformer structure," *IEEE Trans. Ind. Electron.*, vol. 59, no. 9, pp. 3445-3449, Sep. 2012.
- [187] K. Eun-Soo, N. Young-Jae, L. Seung-Min, C. Bong-Gun, L. Jae-Sam, P. Min-Soo and H. Dong-Young, "A low profile LLC resonant converter using novel planar transformer," in *Proc. IEEE Appl. Power Electron. Conf. Expo. (APEC)*, 2012, pp. 1307-1312.
- [188] K. Eun-Soo, L. Seung-Min, S. Phum, C. Bong-Gun and L. Kwang-Ho, "A novel planar transformer for low profile LLC resonant converter," in *Proc. IEEE Appl. Power Electron. Conf. Expo. (APEC)*, 2012, pp. 2234-2239.
- [189] D. Fu, F. C. Lee and S. Wang, "Investigation on transformer design of high frequency high efficiency dc-dc converters," in *Proc. IEEE Appl. Power Electron. Conf. Expo. (APEC)*, 2010, pp. 940-947.
- [190] J. Wang, X. Yang, H. Niu, Z. Wang and J. Liu, "PCB integrated transformer composed with ferrite mosaics for LLC resonant converter," in *Proc. IEEE Energy Convers. Congr. Expo. (ECCE)*, 2009, pp. 1032-1038.
- [191] B. Yang, "Topology investigation for front end DC/DC power conversion for distributed power system," *PhD dissertation*, Virginia Polytechnic Institute and State University, Blacksburg, Virginia, 2003.
- [192] Y. Liu, "High efficiency optimization of LLC resonant converter for wide load range," *Master dissertation*, Virginia Polytechnic Institute and State University, Blacksburg, Virginia, 2007.
- [193] J. Biela and J. W. Kolar, "Electromagnetic integration of high power resonant circuits comprising high leakage inductance transformers," in *Proc. IEEE Power Electron. Specialists Conf. (PESC)*, 2004, pp. 4537-4545.
- [194] A. Stadler and M. Albach, "The influence of the winding layout on the core losses and the leakage inductance in high frequency transformers," *IEEE Trans. Magn.*, vol. 42, no. 4, pp. 735-738, Apr. 2006.
- [195] C. Jung-Muk, B. Byeng-Joo, L. Yong-Jin, H. Dong-Hwa, K. Hyeong-Seog and

- C. Gyu-Ha, "Design of leakage inductance in resonant DC-DC converter for electric vehicle charger," *IEEE Trans. Magn.*, vol. 48, no. 11, pp. 4417-4420, Nov. 2012.
- [196] K. S. Muhammad and D. D. C. Lu, "Magnetically isolated gate driver with leakage inductance immunity," *IEEE Trans. Power Electron.*, vol. 29, no. 4, pp. 1567-1572, Apr. 2014.
- [197] J. Jee-Hoon, "Bifilar winding of a center-tapped transformer including integrated resonant inductance for LLC resonant converters," *IEEE Trans. Power Electron.*, vol. 28, no. 2, pp. 615-620, Feb. 2013.
- [198] X. Margueron, J. P. Keradec and D. Magot, "Analytical calculation of static leakage inductances of HF transformers using PEEC formulas," *IEEE Trans. Ind. Appl.*, vol. 43, no. 4, pp. 884-892, Jul. 2007.
- [199] M. Lambert, F. Sirois, M. Martinez-Duro and J. Mahseredjian, "Analytical calculation of leakage inductance for low-frequency transformer modeling," *IEEE Trans. Power Del.*, vol. 28, no. 1, pp. 507-515, Jan. 2013.
- [200] F. de Leon, S. Purushothaman and L. Qaseer, "Leakage inductance design of toroidal transformers by sector winding," *IEEE Trans. Power Electron.*, vol. 29, no. 1, pp. 473-480, Jan. 2014.
- [201] R. Pittini, Z. Zhang, Z. Ouyang, M. A. E. Andersen and O. C. Thomsen, "Analysis of planar E+I and ER+I transformers for low-voltage high-current DC/DC converters with focus on winding losses and leakage inductance," in *Proc. IEEE Power Electron. Motion Control Conf. (IPEMC)*, 2012, pp. 488-493.
- [202] C. Feeney, J. Zhang and M. Duffy, "Ac winding loss of phase-shifted coupled windings," *IEEE Trans. Power Electron.*, 2015, pp. 99.
- [203] W. Liu and J. D. van Wyk, "Design of integrated LLCT module for LLC resonant converter," in *Proc. IEEE Appl. Power Electron. Conf. Expo. (APEC)*, 2005, pp. 362-368.
- [204] D. Fu and S. Wang, "Novel concepts for high frequency high efficiency transformer design," in *Proc. IEEE Energy Convers. Congr. Expo. (ECCE)*, 2011, pp. 3800-3807.
- [205] R. King and T. A. Stuart, "A normalized model for the half-bridge series resonant converter," *IEEE Trans. Aerosp. Electron. Syst.*, vol. AES-17, no. 2, pp. 190-198, Mar. 1981.
- [206] Y. Zhang, D. Xu, M. Chen, Y. Han and Z. Du, "LLC resonant converter for 48 V to 0.9 V VRM," in *Proc. IEEE Power Electron. Specialists Conf.*, 2004, pp. 1848-1854.
- [207] Y. Shi, "Research of high frequency DC/DC converter," *Master dissertation*, Zhejiang University, Hangzhou, China, 2010.
- [208] M. D. Seeman, "GaN Devices in resonant LLC converters: system-level considerations," *IEEE Power Electron. Magazine*, vol. 2, no. 1, pp. 36-41, Mar. 2015.